University of Exeter
College of Engineering, Mathematics and Physical Sciences

Magnetic Field Effects in Quantum Biology: Beyond the Radical Pair Mechanism

Robert H. Keens

Submitted by Robert H. Keens, to the University of Exeter as a thesis for the degree of Doctor of Philosophy in Physics, 9th August 2021.

I certify that all material in this thesis which is not my own work has been identified and that any material that has previously been submitted and approved for the award of a degree by this or any other University has been acknowledged.

Signed: .....

Abstract

The effects of weak magnetic fields on biological systems have become an area of burgeoning research and interest in recent years. Specifically, the Radical Pair Mechanism (RPM) has been quite successful at beginning to explain phenomena such as avian magnetoreception, the magnetosensitivity of lipid peroxidation reactions and other such biological magnetic field effects (MFEs) - but there are still many questions to answer. This thesis addresses such questions, by proposing a new mechanism (D3M) to offer a new perspective on radical spin dynamics, and methods for amplifying biological MFEs.

0.1 List of Abbreviations:

- MFE: Magnetic Field Effect
- RPM: Radical Pair Mechanism
- LFE: Low-Field Effect
- D3M: New mechanism proposed to move beyond the RPM, which centres on the electron-electron dipolar interactions between three radicals.
- DnM: Extension of D3M to many spins
- HFI: Hyperfine Interaction
- CRY: Cryptochrome
- EED: Electron-Electron Dipolar (couplings/interactions)
- MCWF: Monte-Carlo Wave Function

Acknowledgements

I would like to thank Dr. Daniel Kattnig, Dr. Chris Sampson and Dr. Janet Anders, without whom this project would not have been possible.

I would also like to thank Dr George De Ath for making the LaTeX template for a University of Exeter regulation-compliant PhD thesis available in the public domain. The master repository can be found (correct at time of writing) here: *https://github.com/georgedeath*.

Contents

List of Figures

List of Tables

1. Introduction

There is growing excitement about the possibility of quantum coherence and entanglement underpinning the optimal functioning of biological processes (Lambert et al., 2013; Brookes, 2017; Scholes et al., 2017; Kim et al., 2021). A notable example is the avian inclination compass (Hore and Mouritsen, 2016; Hiscock et al., 2016; Gauger et al., 2011; Clausen et al., 2014; Pauls et al., 2013; Hogben, Biskup and Hore, 2012; Cai et al., 2012; Ritz, Adem and Schulten, 2000; Tiersch and Briegel, 2012; Xu et al., 2013; Kattnig et al., 2016a), which has recently been realised as a truly quantum-biological process (Hiscock et al., 2016), and has likely been optimised through evolution (Melkikh and Khrennikov, 2015). The leading explanation of this phenomenon utilizes the Radical Pair Mechanism (RPM), which describes the unitary evolution of singlet-triplet (S-T) coherences in systems comprising two radicals, i.e. two electron spins (Hore and Mouritsen, 2016; Rodgers and Hore, 2009; Steiner and Ulrich, 1989). The avian compass has received the most high-profile attention in the literature, and has thus been afforded significant attention in the motivation for this thesis. However, as this chapter hints at, and later chapters expand upon, there is in fact a much more general argument in place from a theoretical perspective and a far wider-reaching range of applications than just magnetoreception. For instance, the RPM has also been suggested to underpin controversial health-related implications of exposure to weak electromagnetic fields, such as cellular lipid peroxidation reactions (Ghodbane et al., 2013b; Lalo, Pankratov and Mykhaylyk, 1994; Kabuto et al., 2001; Juutilainen et al., 2018a). These have direct applications to possible new technological advances in both quantum navigation and "magnetoceuticals" - the envisaged use of new non-invasive therapies based on the targeted application of sub-mT magnetic fields. For these phenomena, the so-called low-field effect (LFE)

is essential for facilitating the sensitivity to magnetic fields of intensity comparable to the geomagnetic field (i.e. approximately 50 μT) (Timmel et al., 1998; Maeda et al., 2008; Maeda et al., 2012; Suzuki et al., 2005; Pauls et al., 2013; Kattnig et al., 2016b; Kattnig, 2017b; Timmel and Henbest, 2004).

This chapter will first motivate the discussion by briefly reviewing the progress in the field of spin physics relevant to biological systems. Then, the Radical Pair Mechanism will be introduced (with the main mathematical discussion saved for chapter 2), followed by a discussion of the background for some of its more successful applications aside from magnetoreception - including lipid peroxidation, and other effects in enzymatic systems. Subsequently, the motivation for a new theory, a new perspective on the magnetosensitivity of biological spin physics, is provided along with a qualitative discussion of symmetry and its ubiquity in natural systems. Finally, the overall structure of the thesis will be detailed.

1.1 Biological spin physics: past, present and future developments

1.1.1 Magnetoreception

The phenomenon of avian magnetoreception has been avidly discussed in recent literature from a range of fields, and would appear to require interdisciplinary research in order to fully elucidate the mystery. It seems to be generally agreed that migratory birds have a magnetic compass by which they navigate (see refs. Ritz, Adem and Schulten, 2000; Solov'yov, Mouritsen and Schulten, 2010; Dodson, Hore and Wallace, 2013, for example), yet the precise mechanism by which it operates remains elusive. The leading hypothesis is the Radical-Pair Mechanism (RPM), as first proposed by Schulten (Schulten, Swenberg and Weller, 1978), with this claim based upon the body of evidence that exists in its favour (see refs. Hore and Mouritsen, 2016; Kim et al., 2021 for a comprehensive review). However, the magnetite hypothesis, as first proposed by Lowenstam (Lowenstam, 1962) and later applied in the context of more complex organisms by Kirschvink (Kirschvink, 1981) also has some support from the

community.

While neither idea has been unequivocally proven experimentally, recent studies suggest that both mechanisms are simultaneously present in various species. Different sensory modalities appear to map to the two mechanisms: magnetite, a map sense, and the radical pairs, a compass (Munro et al., 1997; Ritz, Adem and Schulten, 2000). Below is a brief summary of the two ideas.

Magnetite: There exist magnetic nanoparticles in the upper beaks of many species of bird (Falkenberg et al., 2010; Kirschvink, 1981; Munro et al., 1997) - they are seemingly led by the nose through the geomagnetic field to their destinations. It has been suggested that birds can use the magnetisation brought about by these particles to form a kind of 'magnetic map' by which they navigate. It was argued that they gain experience using this over time, gradually building up this picture over several migrational seasons, as juvenile *Zosterops lateralis* (Australian Silveryes) were shown not to orient with this technique (Munro et al., 1997).

While there exists some support for this hypothesis (Wiltschko and Wiltschko, 2013), experimental evidence is not abundant. Most notable is the fact that a receptor for this 'magnetic sense' has yet to be found in experiment (Nordmann, Hochstoeger and Keays, 2017), making it difficult to reconcile the mechanism with any kind of signalling pathway that would actually allow organisms to utilise this magnetic information. There also exists evidence showing that magnetite alone cannot be responsible in a recent study by Wiltschko et al. (Wiltschko et al., 2015), where they anaesthetised the upper beaks (wherein navigational magnetite is believed to be found) of their subjects as a control. Despite the anaesthesia, they reported still seeing a preferred direction presented by their test subjects, which could be interfered with by radio-frequency irradiation. This further suggests that multiple mechanisms may be in play synchronously for magnetoreception. It should be noted, however, that this experimental methodology has been disputed with the claim that the anaesthetic used may be artificially biasing the organisms to behave differently than they would under natural circumstances, and also that is cannot be guaranteed that the effects of said anaesthetic would last for the full duration of the study

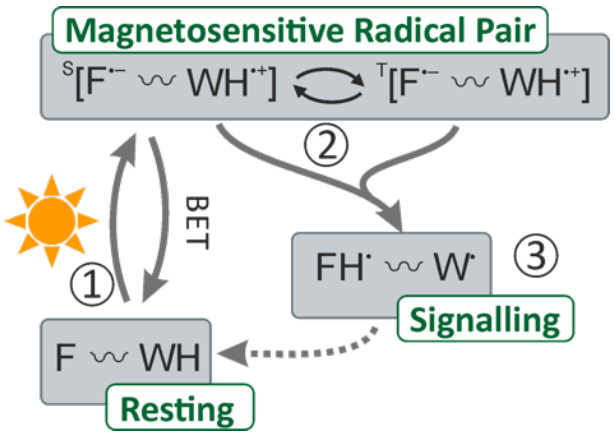

Figure 1.1: A schematic of the photocycle of the radical-pair mechanism, assuming the participant species to be flavin adenine dinucleotide, here abbreviated as F, and the amino acid tryptophan (abbreviated as WH) The reaction pathways shown are back electron transfer (BET), which accounts for the geminate recombination, and reaction to form the signalling state. The circled numbers refer to the stages of the mechanism: stage 1 is photo-excitation, stage 2 is singlet-triplet inter-conversion and stage 3 is the formation of the signalling product.

(Engels et al., 2018). As such, there are many uncertainties still surrounding this question and one cannot claim conclusive proof either way at present.

Radical Pair Mechanism: Fig. 1.1 shows schematically how the RPM proceeds. The initial precursor state is photo-excited by an incoming photon of sufficient energy and the radical pair is formed in a coherent and entangled superposition of spin-up and spin-down: a pure singlet state; this can later evolve into a coherent superposition of the singlet (S) and triplet (T) spin states. There exist two distinct reaction pathways: the first is via back electron transfer (BET), thus reforming the precursor state, and the second is the formation of a signalling product state; this is sometimes called an 'escape product', as (for mobile reactants) the geminate pair either recombines or escapes to the bulk, where it gives rise to free ions.

The reason that a magnetic field effect can occur is the spin-selective recombination exhibited in this set of reactions - the differing chemical fates of radicals in the singlet and triplet states permits the possibility of affecting the respective product formation rates/yields. Hence, by altering the conversion dynamics with an applied magnetic field (Schulten, 1982) one can tune the yield of the signalling state. The singlet yield, as shown in Fig. 1.2, is an oft-calculated quantity used to demonstrate these magnetic field effects. The complement of this quantity, the triplet yield, can also be readily calculated.

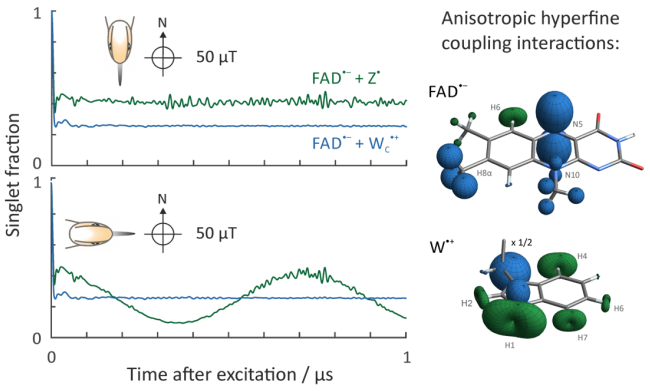

Figure 1.2: A depiction of how a bird might interpret its orientation to the applied weak magnetic field; here shown as approximately the strength of the geomagnetic field. The fraction of radical pairs in the singlet state after photo-excitation is shown as a function of the time elapsed thereafter, and can be seen to oscillate when aligned parallel to the field, but this is much less pronounced when perpendicular thereto. This variation could provide the basis for magnetoreception by the RPM if the singlet-fraction is linked to the recombination yield of the reaction and thus, indirectly, the signalling state to show that it could be directly affected by a magnetic field comparable to that of Earth. The structures on the right represent the anisotropic hyperfine couplings present. The colour represents the sign thereof; blue is positive, green is negative. The meanings of the colours in the singlet fraction are: green for the FAD (flavin adenine dinucleotide) anion radical and a hypothetical radical devoid of hyperfine couplings; blue for the FAD anion radical and the W_C cation radical.

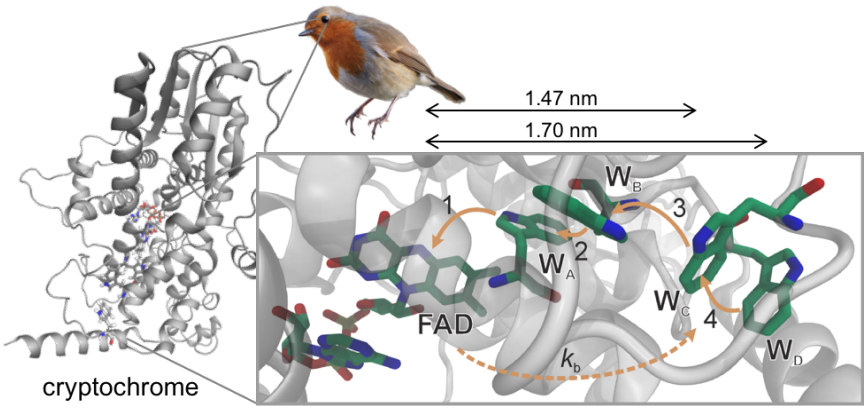

Figure 1.3: Structural representation of a typical cryptochrome, located in the avian retina (shown: *E. Rebecula*). Shown are an electron transfer pathway involving three highly conserved tryptophan residues, and the flavin adenine dinucleotide structure; widely believed to be contenders for the magnetosensitive radicals involved in the radical pair mechanism of avian magnetoreception. The distances shown are the edge-to-edge distances of $FAD - W_C$ and $FAD - W_D$, respectively.

The chemical compass, involving transient reaction intermediates known as radical pairs, is said to provide information about the inclination to the geomagnetic field but to be insensitive to the polarity of the field (Wiltschko and Wiltschko, 1972; Hiscock et al., 2016; Rodgers and Hore, 2009). This is achieved through the presence of anisotropy in the hyperfine interactions of the radical-pair system, as shown schematically in Fig. 1.2. A detailed explanation of the mechanism can be found in references (Rodgers and Hore, 2009; Hore and Mouritsen, 2016), for example.

This inclination compass has been speculated to be found in the cryptochromes of the avian retinae and to couple to the visual transduction pathway (Ritz, Adem and Schulten, 2000), allowing the magnetic information produced to be interpreted neurologically, and the Mouritsen group has tracked this information to cluster N in the forebrain (Liedvogel et al., 2007b; Zapka et al., 2010). Several behavioural studies exist that show evidence for the plausibility of the radical-pair mechanism, and provide motivation for further scrutiny of this pathway (Wiltschko et al., 2014; Zhang, Berman and Kais, 2015; Wiltschko and Wiltschko, 2014; Engels et al., 2014). Fig. 1.3 shows a structural representation of a cryptochrome, a blue-light photoreceptor protein (Lin and Todo, 2005) and the putative receptor for magnetoreception (Liedvogel and Mouritsen, 2010; Hore and Mouritsen, 2016; Ritz, Adem and Schulten, 2000; Solov'yov, Chandler and Schulten, 2008). The FAD (flavin adenine dinucleotide) of a cryptochrome can exist in several states: its fully oxidised form (FAD), semiquinone form ($FADH^{\bullet}$), anionic semiquinone form ($FAD^{\bullet-}$) and the fully-reduced hydroquinone ($FADH^{-}$), which could allow it to participate in many types of redox reaction. Radical pairs that could form the basis of a magnetic sensor can be generated by the oxidation of the fully reduced form or the photo-reduction of the oxidised form by suitable electron donors such as aromatic amino acids.

One bone of contention where this mechanism is concerned is the precise nature of the radicals involved. It is currently widely believed that one of the radicals is a radical derived from FAD but the identity of the other is as yet uncertain. A popular controversial suggestion for the second radical is superoxide (Cai, Caruso and Plenio, 2012; Cai, Guerreschi and Briegel, 2010; Solov'yov and Schulten, 2009;

Niessner et al., 2013), but discussions involving this choice often fail to take into account spin relaxation. Spin relaxation in the radical pair formalism is the process whereby the excited radicals revert, over a timescale denoted the relaxation time, to thermal equilibrium with their surroundings (Rodgers and Hore, 2009; Hayashi and Nagakura, 1984). As a result, doubt is cast upon the choice of superoxide as the partner radical for FAD since it has a very short relaxation time (< 1 ns) relatively to the reaction timescale (Hogben et al., 2009); it would need to be of the order of a microsecond to be sensitive to the geomagnetic field.

Fig. 1.2 shows how the singlet fraction (discussed in more mathematical detail in chapter 2) can be affected by a magnetic field of strength comparable to the geomagnetic field which, when considered with the reaction pathway shown in Fig. 1.1, shows that the applied magnetic field can affect the signalling state of the protein. The low-field effect (LFE), a feature in the singlet yield facilitated by the lifting of level degeneracy owing to the Zeeman effect (Cintolesi et al., 2003; Solov'yov, Chandler and Schulten, 2008; Timmel et al., 1998), is central to the phenomenon. Further, these magnetic field effects can be perturbed by the application of a low-intensity (as weak as tens of nT (Kavokin, 2009), or even less (Engels et al., 2014; Schwarze et al., 2016)) magnetic field in the megahertz regime (Hogben et al., 2009; Efimova and Hore, 2008; Evans et al., 2016), which is further evidence for the RPM as such an effect could not be predicted by a magnetite-based model, because the torques involved would be so small as to be both unable to rotate biological macromolecules and imperceptible to the organism (Kabuto et al., 2001). The LFE has been observed for radical reactions involving FAD (Evans et al., 2016), and in *in vitro* studies of cryptochromes, but not yet for any where its partner radical was superoxide (Kattnig, 2017b; Maeda et al., 2012).

The tryptophan radical has long since been the strongest contender (Kattnig and Hore, 2017a; Wiltschko et al., 2015; Solov'yov, Chandler and Schulten, 2007; Cintolesi et al., 2003) but this idea has been challenged recently by suggesting that in fact the step in the reaction that governs magnetoreceptive ability occurs later than originally thought - in the dark reoxidation of $FADH^{-}$ (Gegear et al., 2010;

Niessner et al., 2014; Wiltschko et al., 2015; Wiltschko et al., 2014; Wiltschko et al., 2016; Pooam et al., 2019). Parallel to this, Cry4, a weakly oscillating protein hitherto only found in vertebrates that exhibit magnetic compass behaviour, has been found to bind flavins and also to contains the Trp tetrad present in DmCry (Müller et al., 2015; Nohr et al., 2016; Zoltowski et al., 2011; Levy et al., 2013), which is considered critical for its activation (Günther et al., 2018). Given that, relatively to the strong, robust, circadian oscillations of Cry1a, Cry1b and Cry2, Cry4 is weakly oscillating, this suggests that upregulation of Cry4 does something else entirely, which can be done irrespective of the time of day, such as migration and thus that it may play a part in the magnetosensitive step of avian navigation, whether this be dark-state or otherwise (Günther et al., 2018; Niessner et al., 2014; Wiltschko et al., 2016).

Several comprehensive reviews exist that cover the biophysical and physiological aspects of the RPM (Johnsen and Lohmann, 2005; Kishkinev and Chernetsov, 2015; Hore and Mouritsen, 2016; Brocklehurst and McLauchlan, 1996; Jones, 2016; Fay et al., 2019) and describe magnetic effects in chemical systems (Steiner and Ulrich, 1989; Kim et al., 2021), but the aim of the present work is to address the progress that has been made in theoretically modelling the problem and, ultimately, to make a more general remark upon the utility of weak magnetic fields in influencing and amplifying quantum effects in biological systems (i.e. not only limited to magnetoreception). The main common problems to theoretical treatments at present are in trying to predict and justify the remarkable acuity that the avian compass demonstrates in experiment (Hiscock et al., 2016; Akesson et al., 2001; Lefeldt et al., 2015), while also creating a model system that is sensitive to weak, oscillating, radio-frequency magnetic fields and remains sensitive even in low-light conditions (Gauger et al., 2011; Hiscock et al., 2017; Solov'yov, Mouritsen and Schulten, 2010). This final point, about dark-state reactions, has been addressed briefly above, but is still listed here because further evidence is required for conclusivity. Thus, with these issues in mind, some proposed refinements to the original formulation shall be presented and discussed herein.

Model systems currently in frequent experimental use for magnetreception

studies are a photolyase from the bacterium Escherichia coli, and the related (and structurally very similar) cryptochrome proteins from the plant Arabidopsis thaliana, fly Drosophila melanogaster (AtCry1 and DmCry, respectively) (Ritz, Adem and Schulten, 2000; Kattnig and Hore, 2017a), and recently birds Xu et al., 2021. Theoretical models in the literature have been mostly fuelled by the crystal structures of *At*Cry and *Dm*Cry. Although this class of protein is highly conserved among species, (Lin and Todo, 2005; Solov'yov, Chandler and Schulten, 2007), this introduces additional ambiguity in model calculations since, while they may be similar structures in terms of conservedness they are not identical to those found in avian retinae. Recently, however, the structure of pigeon Cry4 has been resolved (Zoltowski et al., 2019), which could allow more realistic simulations of magnetoreceptive systems to be undertaken.

Research into the avian magnetic compass is exciting and relevant because once the mechanism is understood it could be mimicked and harnessed by the technological industries. Quantum navigation could be applied in many ways. Perhaps the most intuitive example of use would be sensory applications - for example allowing purely organic magnetic sensors with applications to the navigational, archaeological and medical imaging of magnetic fields. One example of such a medical application is the detection of prenatal congenital heart defects using magnetocardiography (Kahler et al., 2001). This technique works by detecting changes in the cardiac magnetic field and thus, if such changes could be detected more sensitively by using techniques inspired by magnetoreception this would improve non-invasive diagnostic capability. There is also applicability to quantum information, as one may think of the entangled (Zhang, Berman and Kais, 2015; Gauger et al., 2011; Cai, Guerreschi and Briegel, 2010) spin states accessible to radical-pairs as being analogous to qubits. If resilience to relaxation, and hence prolonged coherence lifetimes, as described above, can be learned from the biological model this would provide motivation for further attempts to realise it in quantum devices.

While avian magnetoreception is certainly a hot topic in the literature, much of the more direct evidence in support of cryptochrome having a role in biological

magnetoreception in fact comes from experiments using Drosophila flies and Monarch butterflies. For example, flight simulator studies have been performed to show that Monarch butterflies have an inclination compass and, further, that this compass appears to be light-dependent in the same wavelength regime as for CRY Guerra, Gegear and Reppert, 2014. This, coupled with previous behavioural (binary-choice assay) work showing that Drosophila have a blue-light dependent navigational ability Gegear et al., 2008; Gegear et al., 2010, forms part of the foundation for the suggestion that the same protein could be in use for a similar function in birds, as cryptochromes are highly-conserved between species. Further evidence for CRY's proposed relevance in biological magnetoreception can be seen in experiments by the Philips group, where they show marked difference in the orientational behaviour of Drosphila (and even a type of salamander) in the presence of blue light when compared with its absence Phillips and Borland, 1992; Phillips and Sayeed, 1993. While CRY was not explicitly referenced in the initial work, the link was made more concretely in a later review Phillips, Jorge and Muheim, 2010.

Seizure response to blue light in Drosophila has been investigated, that was not observed in those flies in which DmCRy had been knocked out Marley et al., 2014. Importantly, the authors found that repeating their experiment in the presence of a 100mT magnetic field significantly increased the magnitude of the seizures induced by blue light. This is important because it establishes another link between magnetism and CRY. Further work by the same group studied the blue-light dependent electrochemical response of (Drosophila) larval membranes, wherein they showed that magnetic field exposure increased the level of action potential firing, and thus provides direct evidence that a magnetic field may indeed be able to influence animal behaviour Giachello et al., 2016. These experimental results, and other insights from this group, have been summarised in a recent review Bradlaugh et al., 2021. The Kyriacou group provides some of the first evidence that the classical tryptophan-mediated RPM may be insufficient to model the animal magnetosensitive behaviour, even though the presence of CRY and blue light has been established to be important, as they show that an isolated CRY C-terminus (which does not encode

tryptophan) is apparently still able to mediate electromagnetic field response in Drosophila Fedele et al., 2014a; Fedele et al., 2014b. This is important in particular because it suggests that other partner radicals for the well-established FAD should certainly be studied, and also that the theoretical basis for magnetoreception is far from complete - even though the RPM represents an important building block.

However, though magnetoreception is a hot topic at the moment, with much attention in the literature, the avian compass is not the only interesting application of biological MFEs. The following two subsections will briefly summarise some other very interesting and relevant uses of the same fundamental theoretical principles.

1.1.2 Lipid Peroxidation

Many review articles describe lipid autoxidation in great detail and the reader is referred to those for an in-depth discussion of the phenomenon itself (Spiteller, 1998; F. Benzie, 1996; Farmer and Mueller, 2013; Yin, Xu and A. Porter, 2011; Ghodbane et al., 2013b), however a brief summary shall be provided below.

Lipid peroxidation proceeds by a free-radical chain mechanism that involves peroxyl radicals as the main chain carriers (Spiteller, 1998; Mylonas and Kouretas, 1999; Doktorov, N. Lukzen and Pedersen, 2008; Lalo, Pankratov and Mykhaylyk, 1994; Ciejka and Goraca, 2008; Novitskii et al., 2015). The chain reaction is initiated by a surplus of oxidising agents such as reactive oxygen species (ROS), which include superoxide $O_2^{\bullet -}$ and the hydroxyl radical $OH^{\bullet}$ (Giorgio et al., 2007; Gaschler and Stockwell, 2017; Hogg and Kalyanaraman, 1999; Tejero et al., 2007). The latter species can be formed, through a Fenton reaction, using hydrogen peroxide H_2O_2 (Gutteridge, 1986). At a high level of concentration, ROS can cause severe oxidative stress and damage in otherwise healthy cells, and can even sometimes lead to the death of the cell (Kannan and Jain, 2000; Ryter et al., 2007). It is, however, worth noting that reactions involving ROS can be magnetosensitive (Usselman et al., 2014; Usselman et al., 2016), so there exists the possibility that magnetism could be used therapeutically one day to mitigate the aforementioned damaging effects. The reaction scheme shown in Fig.1.4A, summarises the most important reactions that

account for initiation, propagation, termination and degenerate chain branching (Doktorov, N. Lukzen and Pedersen, 2008). Since abstracting bis-allylic hydrogen atoms is energetically easy, poly un-saturated fatty acids are particularly susceptible to radical attack and, thus, are key to the process. As detailed in the reaction scheme in Fig. 1.4A, the chain-carrying peroxyl radicals are typically formed through the reaction of highly reactive carbon-centred radicals with molecular oxygen or through degenerate chain-branching (reactions III and IV in Fig. 1.4A). Though it can be slow, the degenerate chain branching step presents interesting non-linear dynamics. If its rate approaches the rate of termination, this can result in a strong increase in radical concentrations, which is often vividly referred to as "chain ignition" (Emanuel and Gagarina, 1966). Kipriyanov *et al.* (Kipriyanov Jr., Doktorov and Purtov, 2015) have suggested that small alterations made to the radical recombination efficiency could induce bifurcation transitions between bi-stable steady states. As a consequence, a small effect putatively exerted by magnetic fields on the chain branching reaction has the potential to induce huge (i.e. three orders of magnitude) changes in radical concentrations. It has been argued that the RPM cannot predict MFEs on the symmetric recombination of peroxyl radicals, because $\Delta g = 0$ and no hyperfine interactions could be expected, as the spin density of peroxyl radicals centres on the terminal oxygen, for which all magnetic isotopes have insignificant natural abundance (for ^{17}O, $I = 5/2$, but its abundance is only 0.037%). Consequently, previous studies have associated magnetosensitivity with reactions other than the recombination of such peroxyl radicals (Lalo, Pankratov and Mykhaylyk, 1994; Kipriyanov Jr., Doktorov and Purtov, 2015; Pliss et al., 2017). The same ideas appear to be implicated in the oxidation of hydrocarbons by molecular oxygen (Pliss et al., 2017). In Chapter 4 is presented a theoretical study of the RPM and the D3M in the context of lipid autoxidaton and, for reasons that will become more apparent therein, a focus on the recombination of the main chain carriers, the lipid peroxyl radicals, is taken.

Many experimental studies have demonstrated that lipid peroxidation reactions are magnetosensitive, and a correlation between the MFE and levels of oxidative

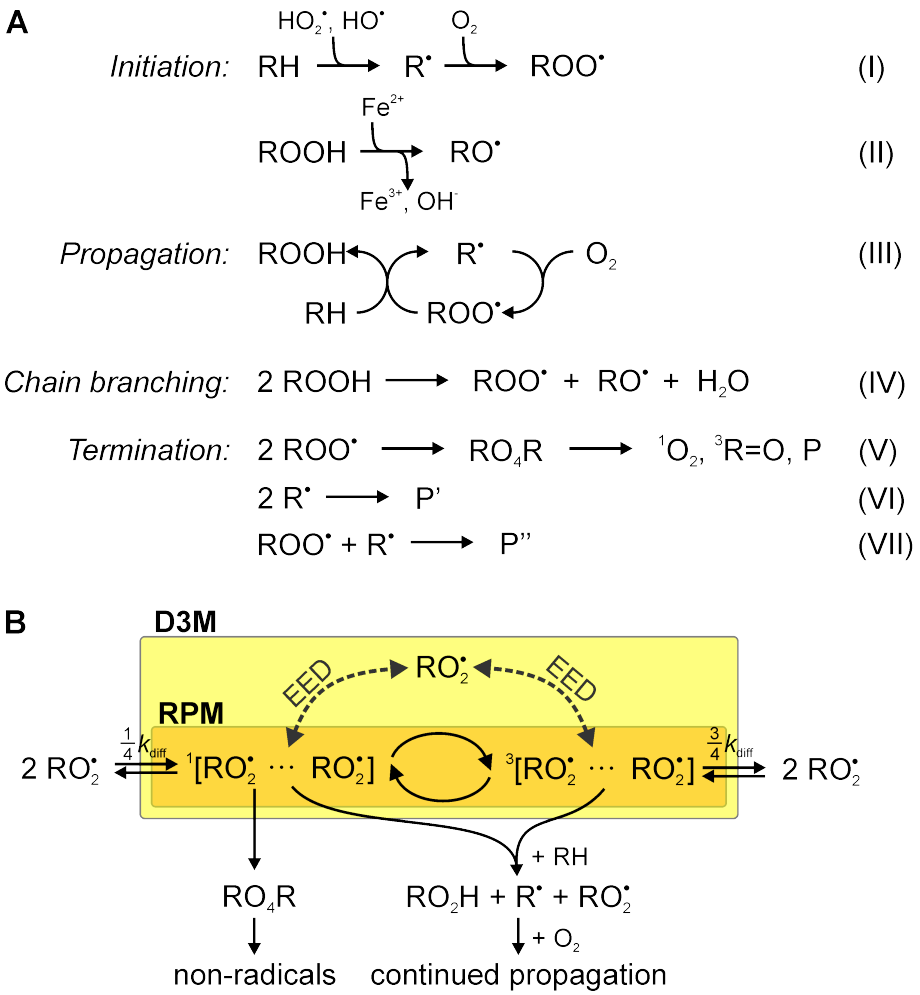

Figure 1.4: A: Key reaction steps in lipid peroxidation: initiation (I and II), propagation (III), degenerate-chain branching (IV) and termination (V-VII). The different Ps stand for diamagnetic termination products. R represents a lipid backbone. B: The radical pair mechanism (orange section) specifically linked to lipid peroxidation in this example. The dashed arrows indicate the action of the electron-electron dipolar interaction with a third radical, which may induce MFEs via the D3M. k_{diff} indicates the diffusive encounter rate constant. For random encounters of radicals, the ratio of triplet to singlet encounter is 3:1.

stress has been determined to exist (Okano, 2008; Ghodbane et al., 2013a; Pratt, Tallman and Porter, 2011; Lukzen et al., 2020; Mattsson and Simkó, 2014). The body of evidence includes the level of lipid peroxidation in rats' blood (Ciejka and Goraca, 2008), brains (Ciejka et al., 2011), and lymphocytes (Zmyslony et al., 2004; Jajte et al., 2002), as well as guinea pigs (Coşkun et al., 2008), mouse brains (Lee et al., 2004; Kabuto et al., 2001), and in radish seeds (Novitskii et al., 2015). Some *in vitro* studies have been conducted on simpler model systems, yet the mechanistic details behind the results have remained elusive. Landoulsi *et al.* (Hanini et al., 2017) have used bacterial strain *P. aeruginosa* and mutants thereof, and found that the level of lipid peroxidation increased when the bacteria were exposed to a 200 mT

static magnetic field. Ding *et al.* (Ding et al., 2004) found that exposing HL-60 cells to a combination of H_2O_2 and a weak (5 mT) magnetic field promotes cell death. Furthermore, it has been shown that by applying a steady magnetic field of 8 mT to liposomes from 1,2-dioleoylphosphatidylcholine, the rate of lipid peroxidation can be increased (Lalo, Pankratov and Mykhaylyk, 1994). Kabuto et al. (Kabuto et al., 2001) showed that, for field strengths between 2 and 4 mT, static magnetic fields had an inhibitory effect on iron-induced lipid peroxidation, however, the autoxidation of linoleic acid was increased in a high field of 9.4 T (Inotani, Fukuyoshi and Kusumi, 2001). These fields are evidently stronger than most of the weak background fields of everyday surroundings. However, even background fields can cause an increase in oxidative stress (Kıvrak et al., 2017).

1.1.3 Other Biological MFEs

While lipid peroxidation and avian magnetoreception are the two major biological applications that the publications stemming from the research detailed herein make reference to, they are by no means the only situations in which MFEs manifest in biological systems. Indeed, significant research has been undertaken on the presence of radicals and radicals generations in adenosylcobalamin enzymes (Jones et al., 2007; Jones et al., 2011a; Chagovetz and Grissom, 1993), and MFEs have been detected in photo-induced radical pairs generated from adenosylcobalamin reactions (Messiha et al., 2015; Jones, Woodward and Scrutton, 2009). These enzymes serve as a general model for how enzymes produce, and regulate, free radicals *in vivo* and their control thereof is considered one of the underpinning factors contributing to their catalytic efficiency of 'unusual' reconstruction and elimination reactions. See Ref. (Marsh and Meléndez, 2012) for a review.

While some doubt has been cast on exactly how relevant the RPM might be to redox enzyme reactions, it would be interesting to know whether the DnM mechanism, proposed herein to move beyond the conventional RPM model of radical-pair magnetosensitivity, could provide a theoretical backing to experimental data that seem to be highly dependent on experimental conditions. The many-radical effects

considered in the work leading up to the DnM mechanism behave quite distinctly from a traditional RPM-style reaction, showing the RPM to be a very special case, albeit a useful one, rather than an exhaustive paradigm to describe magnetic effects in biological systems.

It is also worth noting that the effects of weak magnetic fields upon reactions involving organic molecules is primarily the focus of the research presented herein, so effects that require the presence of high field (e.g. the Δg mechanism (Karogodina et al., 2011b; Hughes et al., 2019)), while certainly interesting, are not discussed here in detail.

1.1.4 Physical origins of Magnetic Field Effects

Broadly speaking, there are three distinct regimes where magnetic field effects may manifest. These are low-field (comparable to the geomagnetic field of approximately 50 μT), moderate field ($1-10$mT) and high field (fields in excess of 100mT) Hayashi and Sakaguchi, 2005. Distinction should be drawn between these regions, because the physical basis of the MFEs observed therein differs.

The low-field effect can be attributed to symmetry-breaking transitions between the S and T_0 states (i.e. where the application of a weak field lifts the degeneracies between zero-field eigenstates and increases the number of pathways for singlet-triplet inter-conversion) Lewis et al., 2018b.

Moderate field effects typically occur in radicals pairs due to the hyperfine coupling mechanism, i.e. hyperfine driven singlet-triplet conversion whereby the intereconversion efficiency is modulated by the magnetic field through impacting on energy level spacings.

In the high-field regime, MFEs arise because the strength of the field serves to energetically decouple the T_+ and T_- states, reducing the number of pathways by which singlet-triplet inter-conversion can take place (i.e. only $S-T_0$ inter-conversion happens appreciably) Jones et al., 2007; Hayashi and Sakaguchi, 2005.

The magnetic field effects on the spin conversion are revealed through the different chemical fates of singlet and triplet states of the radical pair. This is true

for both singlet- and triplet-born radicals pairs, though in slightly different ways. For triplet-born pairs, however, spin-selectivity is typically provided by spin-selective recombination via the singlet state, leaving the remaining radical pairs in the triplet state Timmel et al., 1998. It should also be noted that, while singlet-born radical pairs form the primary focus of the work detailed herein, triplet-born pairs are not an esoteric special case - they are just as common as singlet-born pairs, but primarily observed in different contexts to those presented herein. For example, random radical encounters in solution are a prime example giving rise to triplet-born-like behaviour, when the singlet recombination quickly depopulates the singlet encounter pairs.

1.1.5 Beyond the conventional Radical Pair Mechanism

In this subsection, some results of the work detailed in this thesis shall be briefly highlighted.

Remarkable magnetosensitive phenomena can emerge from systems comprising *three* radicals instead of the conventionally considered radical pair. If the dominant interaction among the radicals is their exchange coupling, this brings one to the field of spin catalysis, which has been reviewed in (Buchachenko and Berdinsky, 2002). If, on the other hand, the function of the third radical is predominantly to scavenge one of the radicals of the original pair in a spin-selective side reaction, the "chemical Zeno effect" becomes observable, which has recently been hypothesised to enhance the sensitivity of the avian magnetic compass (Kattnig and Hore, 2017b; Kattnig, 2017a; Letuta and Berdinskii, 2015). As the scavenging reaction immunises the dynamics to one of the radicals being quickly-relaxing, this scavenging mechanism provides more realistic prospects for MFEs from systems involving swiftly relaxing species, such as superoxide, which, in radical pair reactions, preclude magnetosensitivity in the regime of moderate intensities (i.e. the mT-range) (Hogben et al., 2009; Karogodina et al., 2011a; Kattnig, 2017a). In Chapter 3, it is shown that for systems of three or more radicals, MFEs can also result from the mutual electron-electron dipolar coupling alone (Keens, Bedkihal and Kattnig, 2018). This is noteworthy as this process could, thus, elicit MFEs in the absence of hyperfine interactions and differences in radical

g-factors, which are the corner stones of the dyadic RPM. Furthermore, the MFE can persist in this new formalism for fields comparable to the geomagnetic field. This mechanism is termed D3M.

A recently-proposed modification to the RPM is that introducing a third reactant could provide the amplification required to give sensitivity predictions closer to the experimentally observed values (Kattnig and Hore, 2017a). In contrast to the two-electron spin systems of the conventional RPM, larger systems have attracted comparably little attention. To the authors' knowledge, three-spin systems have only been discussed in the biological context at time of writing in (Salikhov, Golbeck and Stehlik, 2007; Kattnig, 2017b; Kattnig and Hore, 2017c). All models mentioned in this context have disregarded the effects of electron-electron dipolar interactions. Further afield, systems of three electron spins have been discussed in the contexts of spin catalysis (Buchachenko and Berdinsky, 1996), the chemical Zeno effect (Letuta and Berdinskii, 2015; Kattnig, 2017b), quantum teleportation (Salikhov, Golbeck and Stehlik, 2007), and as a decoherence pathway (Borovkov et al., 2013). In spin catalysis, the exchange coupling of the radical pair with the spin catalyst is the main effectual interaction. As the Zeeman part of the Hamiltonian commutes with the exchange Hamiltonian, it cannot produce MFEs by itself. However, the exchange interaction can allow for near level-crossings at certain magnetic field intensities, such that hyperfine-driven spin conversion can proceed efficiently (Magin et al., 2004; Magin et al., 2005), and may also transmit the effect of a quickly-relaxing third radical (Hore et al., 1988). Spin coherence transfer in the three-radical system has been recently realized experimentally (Rugg et al., 2019), so three-spin systems are certainly worth exploring in more detail.

A schematic of the reaction pathways envisioned from the addition of a third radical into the RPM framework is shown in the lower half of Fig. 1.5; the upper half is the original mechanism, by way of contrast. From this, one can see that the presence of the scavenger opens a new spin-selective channel along which the radical interactions may progress. This new addition to the system, termed a 'scavenger', seems to work in a similar way to the spin catalysis discussed by Berdinskii, (Letuta

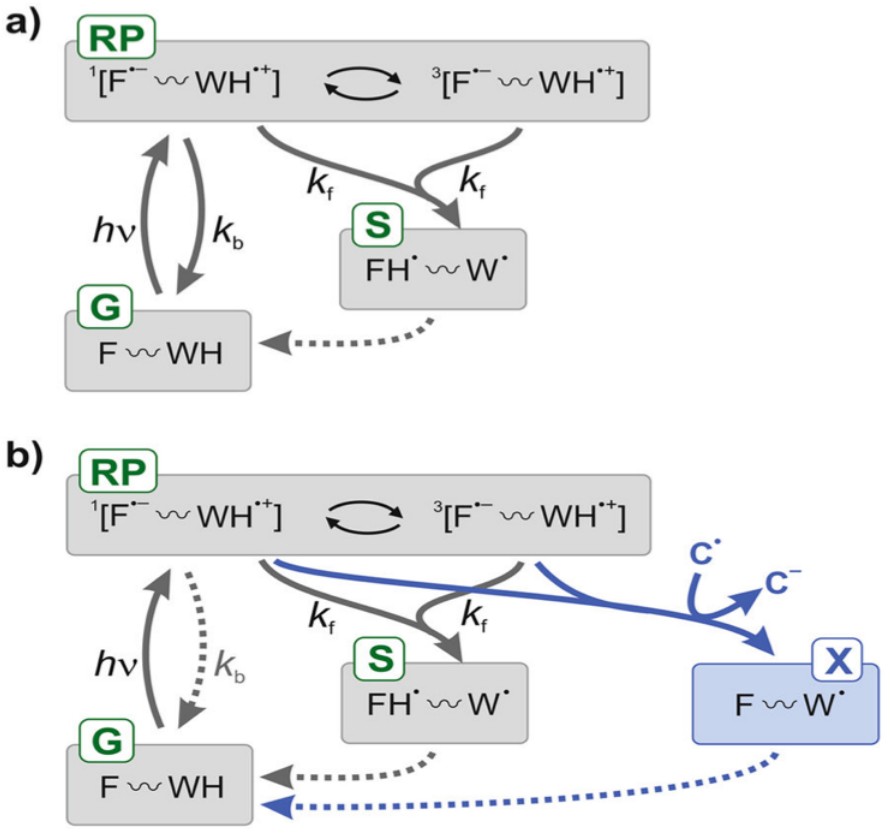

Figure 1.5: Cryptochrome reaction schemes for magnetoreception. (a) The photocycle that accounts for the magnetic field effect on AtCry1. (b) The same reaction scheme augmented by a spin-selective reaction of the flavin radical with a scavenger, $C^{\bullet}$. Abbreviations used for different states of the protein are: RP, radical pair state; **G**, ground state; **S**, signalling state; **X**, scavenging product state. Abbreviations used for reaction partners: **F**, flavin adenine dinucleotide; WH, terminal residue of the tryptophan triad/tetrad. Superscript dots indicate radicals. Superscript numbers are spin multiplicities. $FH^{\bullet}$ and $W^{\bullet}$ are (de)protonated forms of the initially formed radicals, $F^{\bullet-}$ and $WH^{\bullet+}$. The dashed arrows indicate processes that regenerate **G**, typically on a slow timescale, but which are not essential for the function of the sensor. The photo-excited singlet state of the FAD is not shown. Image and caption adapted from reference (Kattnig and Hore, 2017a).

and Berdinskii, 2015), but in the presence of anisotropic hyperfine interactions. The spin-selective reaction of a radical pair with a third scavenger has been shown to boost anisotropic magnetic field effects (Kattnig and Hore, 2017c) and provide resilience to spin relaxation in one of the radicals of the triad (Kattnig, 2017b), thereby providing decisive advantages over the conventional RPM model of magnetoreception.

The exploration of systems with more than two reactive radicals forms a significant part of the present work, as the realisation that the RPM is in fact a very special case, as opposed to the general case, lead the author and group members to re-examine of some fundamental assumptions of the RPM and to propose a new model, called D3M, that moves beyond the conventional RPM and is detailed fully in

chapter 3. A resulting insight of the research undertaken is that D3M could underpin the putative magnetosensitivity of lipid autoxidation, i.e. the oxidative degradation of lipids, which is covered in chapter 4 (Keens, Bedkihal and Kattnig, 2018). Another major point of note from this work is that it is shown that the hyperfine interaction is not categorically required for the observation of MFEs in biological systems comprising more than two radicals, unlike for the conventional RPM, showing that the conventional RPM is indeed a very special case. The core distinct ingredient of D3M is the electron-electron dipolar interaction. This interaction is often neglected when addressing MFEs within the RPM framework. It is worth noting that the dipolar interaction is averaged to zero in freely diffusing systems, as is hyperfine coupling anisotropy, by rapid molecular tumbling (Cintolesi et al., 2003; Lewis, Manolopoulos and Hore, 2014; Rodgers and Hore, 2009). However, other preliminary explorations have been conducted and found that electron-electron dipolar coupling is expected to resemble the exchange coupling, which, as the dominant interaction in close proximity, suppresses S-T inter-conversion by lifting the near-degeneracy of triplet and singlet states, reducing their susceptibility to mixing by weak hyperfine interactions (Zarea et al., 2014), and quenching the LFE (O'Dea et al., 2005). Efimova et al. proposed that the dipolar interaction could be partly compensated by the exchange interaction, thereby allowing high sensitivity to the geomagnetic field despite sizeable electron-electron dipolar coupling interactions (Efimova and Hore, 2008), but this has been shown not to be applicable (Nohr et al., 2017).

Following on from this notion of the dipolar interaction's importance in radical reactions for more than two spins, one may ask why this is not so in the special case of the conventional RPM; the answer: symmetry. Within a radical pair, there is an obvious permutation symmetry between the interacting radicals, and the presence of this does not allow the dipolar interaction to take hold. In systems of more than two spins, however, such permutation symmetries are not so obvious - and indeed are often absent. It is this absence of symmetry that can lead to many interesting new MFEs, as is explored in more detail in Chapter 3. Thus, permutation symmetry is central. In addition, recent work by the author and group members suggests that the

geometrical symmetry of the radical system can also have significant effects (Keens, Sampson and Kattnig, 2021). A brief summary of this idea follows.

Symmetry Considerations

One aim of *D3M* is to relax, or outright remove, some of the stringent assumptions inherent to the standard RPM, and to provide a new perspective on MFEs in quantum biology (Keens, Bedkihal and Kattnig, 2018). In order to fully understand why this might be so, a discussion of symmetry is required.

In many respects, symmetry appears to be fundamental to important processes in nature. For example, in organisms and structures where maximum macroscopic efficiency or aesthetic appeal is required, perfectly regular geometry is advantageous. Symmetry is also central to many branches of mathematics and theoretical physics, because the discovery (or imposition) of certain symmetries upon a system under consideration can serve to dramatically reduce the complexity of the required mathematical analysis. Thus, symmetry is often the first tool employed when tackling problems of significant mathematical difficulty, and indeed many such problems are considered only in special, high-symmetry, configurations due to the analytical and computational intractability of the general case. This also applies to the spin dynamics of systems of radicals, which until recently have required a high level of abstraction and/or symmetry to be tractable (Timmel et al., 1998; Gauger et al., 2011). Technological advances, such as the creation of more powerful hardware, are one way in which previously intractable problems can become soluble without the need for extra assumptions of impositions. Another is the introduction of more efficient computational methods, such as the MCWF method detailed in Chapter 7, which does not require external symmetry impositions upon the system.

Though symmetry itself can be a powerful tool, the breaking of symmetry can produce new and often interesting results. *Spontaneous* symmetry-breaking is a widely known phenomenon, fundamental to the Ginzburg-Landau theory of phase transitions, systems described by the so-called 'Mexican Hat' potential, semiconductor quantum device proposals and indeed present even in some everyday situations (Shaver et al.,

2007; Rosenstein and Li, 2010; Frost, Pienta and Coffey, 2018).

The above examples shows how technological applications, e.g. in sensing, can be revolutionised by deliberately breaking symmetries, and the work reported here suggests that Nature might have done the same for magnetic sensing as it e.g. pertains to avian magnetoreception (Maeda et al., 2012; Tiersch and Briegel, 2012) and more generally to spin chemistry (Kattnig, Solov'yov and Hore, 2016; Kattnig, 2017b). In particular, it is argued that a natural symmetry absence may go some way to explaining the remarkable sensitivity of these systems to weak magnetic fields, and also how such a truly quantum effect can still be reliably persistent in the 'hot, noisy environment' that is a biological system.

Natural symmetry absence is not a special-case phenomenon. Rather, it is present in a broad spectrum of fields, from condensed matter physics to medicine and to the author's knowledge has never before been studied in this context nor in explicit and focused detail. A fundamental example of this phenomenon from both medical biochemistry and anatomy and physiology is that of chirality. This is essentially the natural absence of a reflection symmetry between two otherwise atomically identical structures - an intuitive example of a chiral structure is the human hand. Chirality appears in medical biochemistry because different optical isomers of the same compound are known to have different pharmacological profiles (Chhabra, Aseri and Padmanabhan, 2013; Krasulova et al., 2016). More recently, chirality has been making waves in spin chemistry circles, with the introduction of the CISS effect (Naaman and Waldeck, 2015), which comes from essentially the same premise: symmetry (or the lack thereof) is something that is chemically paramount and its inclusion in theoretical treatment can produce fascinating results.

As such, being able to take advantage of the geometric distinctions between compounds could allow for the design of organic molecular filters to increase the potency of drugs that are currently delivered in racemic mixtures (McConathy and Owens, 2003; Nguyen, He and Pham-Huy, 2006). Experimental procedures to iteratively test the geometry of a solution already exist and are in wide use, so this theory could be quickly and readily tested experimentally. The circular dichroism

technique is one such example, found in both biological and technological applications (Kelly, Jess and Price, 2005; Wei et al., 2016).

The author and group members have recently shown that natural symmetry absence can be observed in dipolarly coupled three-spin systems (discussed in chapter 3). The missing symmetry here is a permutation symmetry of two electron spins poised to recombine to form a diamagnetic state (Keens, Bedkihal and Kattnig, 2018). In the conventional Radical Pair Mechanism, this symmetry is broken by hyperfine interactions with magnetic nuclei. Going beyond this well-established mechanism, it was shown that this symmetry is also naturally broken by the dipolar interaction in systems of more than two radicals, and that remarkable MFEs result from this symmetry absence. As such, given that the absence or breaking of symmetries can produce new and amplified magnetic effects in radical systems, it would be interesting to see whether the RPM or DnM model could be combined with the symmetry-breaking inherent to the CISS effect to yield even larger results.

Metastability has also been recently demonstrated biologically, and the metastability of microbiology can be understood intuitively from one of the oldest biological and medical precedents: *homeostasis*. Biological systems have a range of optimality within which they can function, for example the size and shape of a protein's active site, the concentrations of respective ions across cell membranes, or even the core temperature of the human body. Should this optimality be impinged upon by some external interference, the system adapts its internal processes in order to restore ideal function under the newly imposed set of external conditions. However, the trouble with anything that is metastable is that it, by definition, can only handle *small* perturbations to its optimal conditions (Baldwin et al., 2011). Beyond a certain level, which is system-specific, no sustainable alteration of internal processes can restore the homeostatic balance quickly enough and so the system starts to fail. Some human examples of this are: Alzheimers' disease, diabetic ketoacidosis and cancer (Baldwin et al., 2011; Córdova-Palomera et al., 2017). These are macroscopic diseases, with microscopic origin. The aim of any therapeutic intervention is to provide an external stimulus that aids the immune response to restore the homeostatic balance

and combat the disease before irreparable damage is done. Medicine continues to advance, but the advent of quantum biology hints at a completely new form of non-invasive treatment which one may describe as 'magnetoceuticals'. Given the effect of weak magnetic fields upon lipid peroxidation reactions, reactions which themselves, when the homeostatic balance is broken, have been implicated in several human diseases, one may begin to wonder how this could be amplified to produce a potent therapeutic effect (Barnes and Greenebaum, 2018; Kabuto et al., 2001; Lalo, Pankratov and Mykhaylyk, 1994; Ghodbane et al., 2013b; Juutilainen et al., 2018b). It has been long said that noise and imperfections dampen, and render insignificant, the quantum biological effects of magnetism. Therapeutically, this would render any derived treatment no better than placebo. Finding a way to amplify these quantum effects is the first step toward realizing this new branch of medicine. This is where symmetry comes to the fore. Or rather, this is where *broken* symmetries, and indeed noise in the system, play their role.

It is herein proposed (Chapters 5 and 6), with calculations based on the recently suggested *DnM* model, that broken symmetries allow weak magnetic fields to have far more significant biological effects than have been previously postulated (Keens, Bedkihal and Kattnig, 2018). It is shown that biologically pertinent spin-systems can display MFEs which are stronger in cases where a geometric symmetry has been broken. The model also predicts that noise in the system can *enhance* biological MFEs, and offers results that are consistent with some recent experimental studies on the effects of noise in photosynthetic transport chains. It is shown that noise is not always detrimental to quantum effects in biological systems, contrary to popular belief, and also the distortion-dephasing effect shows not only this, but that combined with the relaxation of geometric symmetry one can observe effects that are amplified. This is especially remarkable, because the noise source that achieves this is singlet-triplet dephasing - one of the central concerns people have regarding the efficacy of the RPM for use in biology, and indeed for the whole idea of quantum biology in itself. Remarkably, this combined distortion-dephasing consideration shows a further enhancement to the MFEs over either taken individually. It is encouraging

that the type of noise which leads to the most pronounced display of this effect is singlet-triplet dephasing, because this is one of the most biologically and physically relevant types of noise that can influence radical dynamics. It is hoped that this work will inspire new theoretical approaches into the relaxation of symmetries in new and established models. It is further hoped that these results will provide proof-of-principle to inspire significant new experimental and clinical research into the widespread effects of weak magnetic fields *in vivo*.

1.2 Outline of the Thesis

In Chapter 2, fundamental concepts from spin chemistry, quantum mechanics, and the underpinning equations of radical pair dynamics are introduced. These are contextualised via their use in the Radical Pair Mechanism (RPM) and the currently available treatments of the systems described in this chapter. The RPM is discussed in detail, and the main metric used to measure the magnetosensitivity of a biological or chemical system in this formalism, the magnetic field effect, is then defined. The chapter concludes with a discussion of how magnetic field effects can be measured experimentally, providing the motivation for the theoretical treatment of radical pair dynamics.

Chapter 3 begins with a discussion of the limitations of the RPM introduced in Chapter 2. Then, moving beyond this model, the D3M model is introduced and it is used to show that some of the basic assumptions of the conventional RPM do not hold for systems of three or more radicals, i.e. interesting new pathways to magnetic field effects appear possible beyond the notions of the RPM. Results obtained using the D3M mechanism are presented, and it is shown that in many circumstances the dipolar and exchange terms are far more important to radical dynamics than anyone had previously given them credit for. A crucial result of this chapter is the breaking of one of the axioms of the conventional RPM: that hyperfine interactions, or differences in g-factors, are categorically required to see biological magnetic field effects; they are not. This work has been published in PRL (Keens, Bedkihal and Kattnig, 2018).

Chapter 4 uses the proposed D3M model to model the reaction dynamics of lipid autoxidation, and it is found that the model predicts both known results and the new result that radical recombination depends on radical concentration; this fact is only apparent once one considers the dipolar interaction within the Hamiltonian, and so is not predicted by the conventional RPM. Further, it is shown that the inclusion of the hyperfine interaction within the D3M model (noting that in chapter three the model was defined in the absence of hyperfine terms) does not lead to the abolition of effects predicted by D3M and so strengthens D3M as a more viable model for biological MFEs. This work has been published in PCCP (Sampson, Keens and Kattnig, 2019).

Chapter 5 introduces a generalisation of the D3M model to DnM, where $n \geq 3$, and considers the effects of spin-system geometry on radical dynamics. The motivation for this idea was that symmetry is usually imposed upon systems under theoretical treatments in order to simplify the mathematics, but that in biological contexts the dynamic form of the protein (or equivalent source of radicals) may have some bearing on the nature of the MFEs observable. Interestingly, it turns out that this is true and that distorting the geometry of the system slightly can give rise to markedly increased MFEs. This was explored for both linear and planar geometries of up to six spins, in the presence of all terms of the DnM Hamiltonian. This work has been published in JCP (Keens, Sampson and Kattnig, 2021).

Chapter 6 takes a similar approach to its preceding chapter, but with the further realisation of the system with the introduction of noise (singlet-triplet dephasing as the physically relevant test case, and also uncorrelated noise on one spin, then all spins, for control purposes). This was done for both distorted and perfectly regular geometries, with the surprising result that geometric distortion and singlet-triplet dephasing taken together produce an overall enhancement to the MFEs available for exploitation. This distortion-dephasing effect could challenge the paradigm that the noise inherent to biological systems is always detrimental to quantum effects, and this work is currently in preparation for publication.

Chapter 7 introduces a computational method to make the simulations required

to computationally explore the theoretical systems outlined in previous chapters more tractable. The method is an extension of the Monte-Carlo Wavefunction approach to include non-Lindbladian dynamics of the type encountered within the Haberkorn approach to radical recombination dynamics. This work has been published in New J. Phys (Keens and Kattnig, 2020).

Finally, Chapter 8 offers an executive summary and overview of the work presented by way of a conclusion to the thesis.

2. Theory

Radicals are, often highly reactive, chemical species with an unpaired electron and are integral to many biological processes (Halliwell and Gutteridge, 2015). The Radical pair Mechanism (RPM) is a canonical model for the magnetosensitivity of chemical reaction processes involving such species. For a review of how radical pair reactions can be affected by magnetic fields, see (Steiner and Ulrich, 1989; Woodward, 2002; Rodgers, 2009). In weak fields, the key ingredient of this model is the hyperfine interaction that induces a coherent mixing of singlet and triplet electron spin states in pairs of radicals, thereby facilitating magnetic field effects (MFEs) on reaction yields through spin-selective reaction channels.

The RPM involves the formation of a radical pair, which can be geminate, i.e. formed in an elementary reaction from (typically) diamagnetic precursors, or as a so-called F-pair, i.e. resulting from a random encounter of radicals (Hore and Mouritsen, 2016; Rodgers and Hore, 2009; Steiner and Ulrich, 1989; Hayashi, 2004a; Steiner, 1984; Timmel et al., 1998; Lewis et al., 2018a; Brocklehurst, 2002; Rodgers and Hore, 2009). Once formed, these radical pairs are generally short-lived, but exhibit reactivity that is controlled by spin dynamics. They can coherently inter-convert between the electronic singlet and triplet states under the influence of magnetic interactions and inter-radical interactions such as the exchange coupling. Specifically, the mixing of the electron spin states can be instantiated from a difference in the Zeeman precession frequency (Δg mechanism) or the interaction with intra-radical magnetic nuclei (hyperfine mechanism). This proceeds most efficiently if the singlet and triplet energy levels become quasi degenerate, e.g. for distances at which the exchange coupling has decayed. As an external magnetic field can impact the relative energy of the energy levels or, in the case of the Δg mechanism, impact directly upon

the mixing term, the population of the spin states and their coherent inter-conversion becomes magnetosensitive. Due to spin-selective recombination reactions, these MFEs on spin dynamics can eventually be reflected in product/recombination yields. More details are found in (Hore and Mouritsen, 2016; Rodgers and Hore, 2009; Steiner and Ulrich, 1989; Hayashi, 2004a; Steiner, 1984; Timmel et al., 1998; Lewis et al., 2018a; Brocklehurst, 2002; Rodgers and Hore, 2009).

In this section, some fundamental theoretical concepts underpinning this model, and all of the coming chapters, will be presented. More specialised derivations will be presented as necessary within the pertinent chapters, as they are more valuable in context.

Specifically, this chapter will outline existing interpretations and implementations of this model, giving a general overview of the idea followed by a more detailed exposition of the constituent parts and the fundamental concepts from spin chemistry that underpin the idea. In this exposition, the distinct parts of the RPM Hamiltonian will be introduced, as well as the Haberkorn approach to modelling recombination, culminating in the master equation used to describe radical-pair spin dynamics. The solution of this equation will be discussed, and outlook provided for moving beyond the currently accepted models. This provides the motivation for chapter 3, where the new D3M model is introduced to provide a new perspective on biologically relevant spin systems.

2.1 Theoretical Approaches

The Hamiltonians used to treat the magnetoreceptive systems described in chapter 1 vary among different groups, but it is generally agreed that the hyperfine interaction is essential if one works within the current formalism of the radical-pair mechanism, as it drives the singlet-triplet inter-conversion required to observe a magnetic field effect in weak fields. In the recently suggested three-radical models, such inter-conversion can also be induced by the Chemical Zeno effect; within this effect, the third radical is referred to as a spin catalyst (Letuta and Berdinskii, 2015), or scavenger (Kattnig and Hore, 2017b). Hyperfine couplings are still required to elicit a magnetic field

dependence in the reaction yield, however. The electron Zeeman interaction is generally included, though in the geomagnetic field it is typically weaker than the hyperfine interaction terms by an order of magnitude or more. The nuclear Zeeman interaction is generally neglected by order-of-magnitude arguments (Schulten, 1982). The exchange and dipolar interactions are also often removed from calculations by imposing that the radicals are 'far enough apart' that they are insignificant in magnitude, or that the radicals are freely tumbling in solution which averages the dipolar interaction to zero. For protein-bound radicals, radical separations of less than 2.0 nm are typically assumed, suggesting that this assumption is violated for at least the electron-electron dipolar coupling (Kattnig and Hore, 2017a; Efimova and Hore, 2008). One suggested justification for the removal of both of these terms is that there may exist conditions under which the exchange and dipolar interactions cancel each other, at least partially (Efimova and Hore, 2008). However this has been shown recently not to be applicable, at least for DmCry (Nohr et al., 2017; Babcock and Kattnig, 2020). Furthermore, radicals may not be separated indefinitely. A spin-selective reaction is required for this mechanism, meaning that the radicals must be close enough to actually react; edge-to-edge distances of about 1.5nm are typical for cryptochrome-bound magnetosenstive radical pairs (Kattnig and Hore, 2017a).

A general Hamiltonian for a radical-pair system is:

$$\hat{H} = \sum_{i=1,2} \sum_{j_i}^{N_i} \hat{\mathbf{S}}_i \cdot \mathbf{A}_{j_i} \cdot \hat{\mathbf{I}}_{j_i} - \gamma_e \sum_{i=1,2} \mathbf{B} \cdot \hat{\mathbf{S}}_i - \hat{\mathbf{S}}_1 \cdot \mathbf{D}_{12} \cdot \hat{\mathbf{S}}_2 - J_{1,2} \left(\frac{1}{2} + 2\hat{\mathbf{S}}_1 \cdot \hat{\mathbf{S}}_2 \right) \tag{2.1}$$

where $\hat{\mathbf{S}}_i$ are the spin angular momentum vector operators for each electron in the radical pair, $\mathbf{A}$ is a hyperfine coupling tensor and the sum over the subscript j_i accounts for the N_i nuclei that have appreciable hyperfine interactions. γ_e is the gyromagnetic ratio and $\mathbf{B}$ is the applied magnetic field. $\mathbf{D}_{ij}$ and $\mathbf{J}_{ij}$ are the dipolar coupling tensor and the exchange interaction of electron spin i and j, respectively. Thus, in order of appearance, this Hamiltonian shows the contributions of the hyperfine, Zeeman, dipolar and exchange interactions.

To actually measure these quantities experimentally, the most common technique in use is EPR (electron paramagnetic resonance) spectroscopy, detailed comprehensively in (Orton, 1969; Drago, 1992), for example. This method allows one to measure the splittings induced by magnetic interactions in radicals by measuring the absorption of microwave radiation of the samples polarized in an external magnetic field, i.e. by detecting shifts in the transitions of the spin states split by the Zeeman effect.

When considering the evolution of the system dynamics in time, however, it becomes necessary to think in terms of density operators and model this evolution with a master equation. The most common choice is of the form given below. It combines an expression for the spin-selective recombination due to Haberkorn (Haberkorn, 1976) with a Lindblad form to account for decoherence effects.

$$\frac{d\hat{\rho}}{dt} = -\frac{i}{\hbar}\left[\hat{H},\hat{\rho}\right] + \sum_j \gamma_j \left[\hat{L}_j\hat{\rho}\hat{L}_j^\dagger - \frac{1}{2}\left\{\hat{L}_j^\dagger\hat{L}_j,\hat{\rho}\right\}\right] - \frac{1}{2}k_b\left[\hat{P}_S,\hat{\rho}\right] - k_f\hat{\rho} \quad (2.2)$$

where $\hat{H}$ is the Hamiltonian, $\hat{\rho}$ is the spin density operator, γ_j is the decoherence rate (defined in integral form in reference (Brasil, Fanchini and Napolitano, 2013)) and the L_j operators are Lindblad operators; these are a combination of spin operators for the system, and act to include decoherence. k_f and k_b are the forward and backward reaction rate constants as introduced by reference (Haberkorn, 1976). An instructive derivation of Eq. (2.2) is given by reference (Brasil, Fanchini and Napolitano, 2013).

The Haberkorn form underpins the so-called 'standard approach' to modelling radical-pair dynamics, and has garnered much support from the community, but other approaches do exist. A recent example is the Jones-Hore reaction model (Jones and Hore, 2010a). This is not vastly dissimilar to the standard Haberkorn approach, but introduces an extra factor of two into the reaction-induced singlet-triplet dephasing rate. In essence they have introduced more noise into the system, as other noise sources are expected to exist in biological environments that exert a similar effect to those already accounted for. Members of the same group have said, however, that they do not reject the standard Haberkorn approach and that it should continue to

be used until a discrepancy is experimentally observed (Maeda et al., 2013).

One major shortcoming of all hitherto proposed models is an inability to predict the level of sensitivity that the *in vivo* avian compass demonstrates. Simulations performed to date (Evans et al., 2016; Kattnig and Hore, 2017a) have shown that many symmetry-unrelated hyperfine interactions, as well as inter-radical interactions, tend to reduce the magnitude of the magnetic field effect. From the practical point of view, this suggests that the least realistic models (i.e. the ones that leave out the most interactions) would actually give predictions closest in magnitude to what is required to give sensitive compass navigation (Hiscock et al., 2019) and that the extra analytical and computational effort required to solve the more complicated problem of a realistic Hamiltonian may in fact be somewhat wasted within this formalism as it stands, or at least not supporting of the premise.

Assuming that the mechanism is not wholly incorrect, while acknowledging that this is of course a possibility, a potential source of the shortcomings is the use of a faulty assumption. Many assumptions are made when modelling spin-systems of the kind encountered in the radical-pair mechanism, sometimes without much real physical justification but for the purpose of simplifying the mathematical task from computationally nigh-impossible to merely daunting.

A common assumption used is, as briefly mentioned above, that the reacting radicals are 'far enough apart' for the duration of their time interacting coherently (the coherence lifetime) that the exchange and dipolar terms in the spin Hamiltonian can be safely ignored. This is often coupled with the assumption that the system is static, hence this separation is maintained (Lambert et al., 2013). These conditions could be difficult to realise in the 'wet, noisy' environment that is a biological system but, even if the protein backbone were to well-confine the radicals in space, fluctuations of dihedral angles and libration motions will induce spin relaxation (Hayashi and Nagakura, 1984; Kattnig, Solov'yov and Hore, 2016) which will, in most cases, deteriorate the observed magnetosensitivity.

The coherence lifetime of the radical pair is usually assumed to be of the order of microseconds (Cai, Guerreschi and Briegel, 2010; Rodgers and Hore, 2009),

while for freely-diffusing radicals relaxation times in the range 100-500 ns are often postulated (Jones and Hore, 2010a; Evans et al., 2016). Coherence lifetimes of the order of 1 μs are necessary to give the external magnetic field enough time to have a significant effect on the spins. The relaxation issue still needs to be overcome, but progress is being made (Kattnig, 2017b).

Anomalous coherence lifetimes, closer to the order of milliseconds, have been proposed as an attempt to fit the experimental data with the current model (Gauger et al., 2011; Liedvogel et al., 2007a) and many have speculated as to effects that may cause the coherence of the system to persist for so long. Such ideas include interactions between the radical pair's electron spins and an effective spin bath (the other moieties of the molecules involved) (Lambert et al., 2013) and the application of pulses over a static magnetic field to try and mimic an oscillating field (Cai, Guerreschi and Briegel, 2010). It remains to be seen whether or not this assumed value range is attainable in reality.

Many assume that the singlet and triplet states of the radical pair decay into their respective products at the same rate, k rather than distinct rates (cf. Fig. 1.1) Hiscock et al., 2017; Cai, Caruso and Plenio, 2012; Lewis et al., 2018b. While this significantly simplifies the mathematics of the calculations, and is certainly convenient, the author can see no general physical basis for this assumption.

Canfield has attempted to apply perturbation theory to this problem (Canfield et al., 1994; Canfield et al., 1995), but for larger spin systems with more realistic interactions this approach may be computationally prohibitive to evaluate. Density functional theory has been employed to provide numerical values for parameters such as the hyperfine coupling constant (Cintolesi et al., 2003; Efimova and Hore, 2008; Solov'yov, Chandler and Schulten, 2008). The most common package used is Gaussian, with some iteration of the B3LYP functional, though many others exist. Variation exists in the values of hyperfine constant acquired, and the neglect of the protein environment in such calculations may be the primary cause. This is discussed in detail in a recent paper by Ritz and coworkers (Procopio and Ritz, 2016).

2.2 Fundamental concepts underpinning quantum radical dynamics

2.2.1 Spin

Spin is a fundamental property of particles, characterised by an intrinsic angular momentum, and is a truly quantum property - that is, it has no precise analogue in classical mechanics. It is for this reason that spin chemistry (and hence magnetosensitive radical pair effects) can said to be truly quantum in nature, at least in a trivial sense. The electronic spin degree of freedom has the same operatorial properties as those in the orbital angular momentum algebra, but differs in that its associated quantum number has a fixed magnitude of $\frac{1}{2}$, which can be projected as positive or negative with respect to an arbitrary axis (known as the quantisation axis, where traditionally the z-axis is used) and was experimentally verified in the famous Stern-Gerlach experiment.

For a system of N spins, the total spin S takes a maximal value of $\frac{N}{2}$, and its projection as composed from the $\pm\frac{1}{2}$ from each spin, ranges from $-S$ to S in unit steps; there are $2S+1$ such unique values.

As radicals are defined by their unpaired electron, it is the electron spin that will form the primary focus of radical interactions. Spin can be fully represented by the set of operators $\{\hat{S}_x, \hat{S}_y, \hat{S}_z\}$, where $\hat{S}_\alpha, \alpha \in \{x, y, z\}$ represent the individual components of the Lie group $SU(2)$ that is commonly written, with $\hbar = 1$, as:

$$\hat{S}_x = \frac{1}{2}\begin{pmatrix} 0 & 1 \\ 1 & 0 \end{pmatrix}, \hat{S}_y = \frac{1}{2}\begin{pmatrix} 0 & -i \\ i & 0 \end{pmatrix}, \hat{S}_z = \frac{1}{2}\begin{pmatrix} 1 & 0 \\ 0 & -1 \end{pmatrix}. \tag{2.3}$$

Equipping this group with the Lie bracket, allows the commutation relations between these operators to be defined:

$$\left[\hat{S}_x, \hat{S}_y\right] = i\hat{S}_z, \left[\hat{S}_y, \hat{S}_z\right] = i\hat{S}_x, \left[\hat{S}_z, \hat{S}_x\right] = i\hat{S}_y. \tag{2.4}$$

The total spin operator, denoted $\hat{\mathbf{S}}^2$, commutes with each element of the algebra

formed from the $SU(2)$ group and the Lie bracket, and is defined as:

$$\hat{\mathbf{S}}^2 = \hat{S}_x \cdot \hat{S}_x + \hat{S}_y \cdot \hat{S}_y + \hat{S}_z \cdot \hat{S}_z. \tag{2.5}$$

This is useful because it allows one to construct simultaneous eigenstates of $\hat{\mathbf{S}}^2$ and $\hat{S}_z$ (the latter chosen due to the convention of the quantisation axis), which can then be used to fully describe a set of spin-S particles. Since there are $2S+1$ unique values that m can take, there are $2S+1$ simultaneous eigenstates, which satisfy the relations (again, with $\hbar$ set to unity for convenience):

$$\begin{aligned} \hat{\mathbf{S}}^2 \left|S, \pm\right\rangle &= S(S+1) \left|S, \pm\right\rangle \\ \hat{S}_z \left|S, \pm\right\rangle &= \pm \left|S, \pm\right\rangle . \end{aligned} \tag{2.6}$$

The creation and annihilation operators for quanta of S are:

$$\hat{S}_\pm = \hat{S}_x \pm i\hat{S}_y, \tag{2.7}$$

which will be convenient when evaluating expressions between the spin operators later.

Given that the values of spin projection are $\pm\frac{1}{2}$ for an electron, it is also possible to construct composite states for the proximity of two such electron spins. These composite states are the fundamental building block for the discussion of magnetosensitive radical dynamics, and are the singlet and triplet states. Essentially, these states are the combinatorial possibilities of the projections of the individual spins and are given as:

$$\begin{aligned} \left|S\right\rangle &= \frac{1}{\sqrt{2}} \left(\left|+,-\right\rangle - \left|-,+\right\rangle\right), S = 0, M = 0 \\ \left|T_0\right\rangle &= \frac{1}{\sqrt{2}} \left(\left|+,-\right\rangle + \left|-,+\right\rangle\right), S = 1, M = 0 \\ \left|T_+\right\rangle &= \left|+,+\right\rangle, S = 1, M = 1 \\ \left|T_-\right\rangle \left|-,-\right\rangle, S &= 1, M = -1 \end{aligned} \tag{2.8}$$

where S is the total spin quantum number, M is the sum of the total individual

projected components, and the + and − states represent the sign of the projected spin for each individual electron in the composite state. These four individual states are the singlet state and the three triplet states, respectively.

2.2.2 Zeeman Interaction

Electrons, by virtue of their spin, have magnetic dipole moments that can interact with an external magnetic field. As itinerant and relativistic electrons are not the focus of this thesis, but rather those bound in biological compounds, orbital angular momentum (and hence spin-orbit coupling) will be neglected from the discussion of the magnetic interactions; the notion of the $\Delta - g$ mechanism manifesting in the geomagnetic field shall, thus, also not be mentioned further (Uhrig, 2008). This is a valid approximation to make in the context of the RPM, because the differences in relativistic scalar quantities within the valence levels of interest to quantum chemistry (i.e. concerning organic radicals in biological systems) are negligible (Visscher, 2002). Thus the magnetic moment operator for the electron can be simply written as:

$$\hat{\mu} = \gamma_e \hat{S}, \tag{2.9}$$

where γ_e is the gyromagnetic ratio: $-\mu_B g_e/\hbar$, μ_B is the Bohr magneton and g_e is the electron g-factor. The interaction of this operator for an arbitrary electron labelled i and an external (applied) magnetic field $\vec{B}$ is:

$$\hat{H}_{zee,i} = \frac{\mu_B g_e}{\hbar} \vec{\hat{S}}_i \cdot \vec{B}. \tag{2.10}$$

Nuclear spins can also interact in this way with an applied magnetic field but, due to the inverse proportionality relation between the gyromagnetic ratio and particle mass, the contribution to the system Hamiltonian due to a nuclear spin is several orders of magnitude smaller than that of an electron and is thus neglected.

While the effects of weak fields are those in primary focus in the present work, it is worth noting that very different behaviour can be observed at higher fields (i.e. hundreds of mT and above). In particular, the Zeeman interaction can cause the $T_{\pm}$

states to be energetically removed from the mixing that the hyperfine interaction can drive (Kim et al., 2021).

2.2.3 Hyperfine Interactions

While orbital angular momentum, and spin-orbit coupling, can be neglected, the interaction between the electronic spin angular momentum and the magnetic field induced by nuclear spin operators cannot. In the case of radical pairs in weak magnetic fields, this is in fact the dominant contribution to the Hamiltonian. This can be notationally inconvenient as it requires a formal representation of the nuclear spin operators, and so to differentiate between the nuclear and electronic spin operators it is customary in this field to introduce the symbol $\hat{I}$ for nuclear spin operators, while maintaining S for the electronic spin operators. Due to the unfortunate conflict of this notation with the more standard use of I to refer to the identity operator, the symbol $\mathbb{1}$ is used throughout this work to avoid duplication of definition. The nuclear spin operators obey the same commutation relations as derived above, so they will not be re-stated here.

The interaction specified above is termed the hyperfine interaction, and can be written as:

$$H_{hyp} = \sum_{i,j}^{N_i} \hat{\mathbf{S}}_i \cdot \mathbf{A}_{i,j} \cdot \hat{\mathbf{I}}_j, \tag{2.11}$$

where $\mathbf{A}_{i,j}$ is the hyperfine tensor of coupling components between a given nuclear spin and electron spin. In situations where the point-dipole approximation breaks down, i.e. when electrons and nuclei can no longer be considered "sufficiently separated", it becomes necessary to add the Fermi contact interaction into the above equation (Fermi, 1930). This, and spin-orbit coupling contributions, can be accommodated within the hyperfine part of the RPM Hamiltonian but for sufficiently separated S and I the anisotropic contribution results from the point-dipole approximation; the isotropic part is due to the Fermi contact interaction, and spin-orbit contributions are usually negligible for the radicals studied here.

In general this interaction is anisotropic, but for radicals in solution rapid mo-

lecular tumbling may cause the rotational averaging of the anisotropic contributions if the tumbling is sufficiently fast compared to the timescale of the interaction. In this case, the hyperfine Hamiltonian reduces to:

$$H_{hyp} = \sum_j a_{i,j} \hat{\mathbf{S}}_i \cdot \hat{\mathbf{I}}_j, \tag{2.12}$$

where $a_{i,j}$ are the isotropic hyperfine coupling constants (the average of the diagonal terms of the hyperfine tensor given above).

2.2.4 Dipolar Interactions

Within the point-dipole approximation, electron-electron magnetic interactions can be understood by considering the interaction energies between their respective magnetic fields if the dipoles are a distance r apart. The quantum mechanical picture of interaction energy between two such electrons is given by the Hamiltonian:

$$\hat{H}_{dip} = \frac{\mu_0 \gamma_1 \gamma_2}{4\pi r^3} \left(\hat{S}_1 \cdot \hat{S}_2 - \frac{3(\hat{S}_2 \cdot \vec{r})(\hat{S}_1 \cdot \vec{r})}{r^2} \right), \tag{2.13}$$

where $\hat{S}_i$ represents an electronic spin operator as previously defined, and γ_i the corresponding gyromagnetic ratio. (Carrington and McLachlan, 1967). This equation can be more conveniently expressed by isolating the coupling tensor and writing it in a form similar to the hyperfine Hamiltonian shown previously:

$$\begin{aligned} \hat{H}_{dip} &= \hat{S}_1 \cdot \left(\frac{\mu_0 \gamma_1 \gamma_2}{4\pi r^3} \left(\mathbb{1} - \frac{3r \otimes r}{r^2} \right) \right) \cdot \hat{S}_2 \\ &= \hat{S}_1 \cdot \hat{\mathcal{D}} \cdot \hat{S}_2, \end{aligned} \tag{2.14}$$

where $\mathbb{1}$ is the identity matrix. This is the form that will be used in later chapters.

For organic molecules involved in magnetosensitive reactions, the HFCs are typically within the range of tens of MHz (Woodward, 2002; Steiner and Ulrich, 1989). For many of the systems studied in the present work, however, the dipolar interaction strength is greater than this ($\approx 15MHz$) - making this the dominant interaction and one that thus may not be neglected by assumption.

2.2.5 Exchange Interactions

The final part of the interaction Hamiltonian is the exchange interaction, arising from correlations between the electron spins themselves and owing to their fermionic nature. The strength of this interaction is conventionally represented by the parameter J which coincides with the exchange integral (Van Vleck, 1932):

$$J_{ex} = \frac{e^2}{4\pi\epsilon_0} \langle \psi_a(r_1)\psi_b(r_2)| \frac{1}{|r_1 - r_2|} |\psi_b(r_1)\psi_a(r_2)\rangle \,, \tag{2.15}$$

where ψ_i represents a solution to the time-independent Schrodinger equation for the one-electron problem. The basis states for the representation that follows correspond to the symmetric and antisymmetric combinations of the orbitals ψ_i:

$$\begin{aligned} \Psi_+ &= \frac{1}{\sqrt{2}}\psi_a(r_1)\psi_b(r_2) + \psi_b(r_1)\psi_a(r_2) \\ \Psi_- &= \frac{1}{\sqrt{2}}\psi_a(r_1)\psi_b(r_2) - \psi_b(r_1)\psi_a(r_2). \end{aligned} \tag{2.16}$$

For derivational convenience, let E_i be defined as the corresponding energy eigenvalue of the solution ψ_i and $E_0 = E_1 + E_2$. The degeneracy of the ground state of the potential well for the two electron problem is lifted by the Coulomb interaction which, if introduced according to first-order perturbation theory, yields the energies of the now non-degenerate states from the solutions to the equations arising from the secular determinant of (Atkins and Friedman, 2011):

$$\begin{pmatrix} E_0 + K - \epsilon & J_{ex} \\ J_{ex} & E_0 + K - \epsilon \end{pmatrix} = 0 \tag{2.17}$$

where ϵ is the energy adjusted for lifted degeneracy and K denotes the Coulomb interaction (Weil and Bolton, 2007):

$$\begin{aligned} K &= \frac{e^2}{4\pi\epsilon_0} \langle \psi_a(r_1)\psi_b(r_2)| \frac{1}{|r_1 - r_2|} |\psi_a(r_1)\psi_b(r_2)\rangle \\ &= \frac{e^2}{4\pi\epsilon_0} \langle \psi_b(r_1)\psi_a(r_2)| \frac{1}{|r_1 - r_2|} |\psi_b(r_1)\psi_a(r_2)\rangle \end{aligned} \tag{2.18}$$

with all terms as previously defined.

Two solutions exist for ϵ, which correspond to symmetric and anti-symmetric combinations of the spatial electron wavefunctions ψ_i:

$$\begin{aligned} \epsilon_+ &= E_0 + K + J_{ex} \\ \epsilon_- &= E_0 + K - J_{ex}. \end{aligned} \tag{2.19}$$

Given that the total electronic (i.e. spin and spatial) wavefunction must be anti-symmetric under permutation of spins, one can associate the previously defined singlet state (i.e. anti-symmetric spin function) with the symmetric spatial term (ϵ_+) and vice-versa for the triplet state. This gives an overall energy difference between the singlet and triplet states as:

$$E_S - E_T = 2J_{ex}. \tag{2.20}$$

Knowing this overall energy contribution, one can now write a Heisenberg-type Hamiltonian to describe this interaction (Weil and Bolton, 2007; Van Vleck, 1932):

$$\hat{H}_{ex} = -2J\hat{S}_1 \cdot \hat{S}_2. \tag{2.21}$$

The form that will be used herein, however, differs from this slightly as an extra diagonal term is added into this for convenience as prescribed by Hayashi (Hayashi, 2004b). Thus the form that shall be considered is:

$$\hat{H}_{ex} = -J\left(2\hat{S}_1 \cdot \hat{S}_2 + \frac{1}{2}\right). \tag{2.22}$$

The addition of this extra term is valid as, because it is diagonal, it will not affect the equations of motion by more than a systematic global shift in energy and so will identically describe the evolution of the systems under consideration.

2.2.6 Recombination

Due to the rules regarding allowed transitions between spin states (i.e. selection rules), radical pair recombination is a spin-selective process. This necessitates a

non-unitary contribution to any master equation governing the dynamics, in the form of a recombination superoperator - traditionally labelled $\hat{\hat{K}}$.

The action of $\hat{\hat{K}}$ on the density matrix of the system is given by the anti-commutator:

$$\hat{\hat{\mathcal{K}}}\rho = \left\{\hat{K}, \rho\right\}. \tag{2.23}$$

The original formulation of this superoperator was proposed by Haberkorn (Haberkorn, 1976) and, although there have been attempts at redefining it in recent years, no other approach has yet significantly and reliably outperformed it. Therefore, it is the Haberkorn approach that will be followed when discussing recombination.

Recombination is considered between nearest-neighbour spins in the proposed model, with the recombination dissipator given by:

$$\hat{K} = \sum_{i,j} \frac{k_S\left(|\mathbf{r_{ij}}|\right)}{2} \hat{P}^{(S)}_{i,j}, \tag{2.24}$$

where $k_S\left(|\mathbf{r}|_{\mathbf{ij}}\right)$ represents the singlet recombination rate constant between radicals i and j; exponential scaling assumed. $\hat{P}^{(S)}_{i,j}$ is the projection operator onto the singlet subspace of radicals i and j, with functional form:

$$\hat{P}^{(S)}_{i,j} = \frac{1}{4}\mathbb{1} - \hat{S}_i \cdot \hat{S}_j. \tag{2.25}$$

The form of $\hat{K}$ for a radical pair is:

$$\hat{K} = \frac{k_S}{2}\hat{P}^{(S)}_{1,2} + \frac{k_T}{2}\hat{P}^{(T)}_{1,2}, \tag{2.26}$$

where $k_{S,T}$ are the reaction rate constants (often assumed equal in the literature for mathematical convenience) for the singlet and triplet states respectively, and $\hat{P}^{(S)}_{1,2}$ and $\hat{P}^{(T)}_{1,2}$ are the projection operators onto the singlet and triplet subspaces of the system. $\hat{P}^{(T)}_{1,2}$ is given by:

$$\hat{P}^{(T)}_{1,2} = \mathbb{1} - \hat{P}^{(S)}_{1,2}. \tag{2.27}$$

With this information, one can now solve the Liouville - von Neumann equation of motion:

$$\frac{d\hat{\rho}}{dt} = -i[\hat{A}, \hat{\rho}(t)] - k\hat{\rho}(t), \tag{2.28}$$

with $\hat{A}$ being the effective Hamiltonian:

$$\hat{A} = \hat{H} - i\hat{K}. \tag{2.29}$$

In the absence of decoherence/dissipation, this allows one to formulate the time-dependent density matrix as:

$$\rho(t) = exp(-k_f t)exp(-i\hat{A}t)\rho(0)exp(i\hat{A}^{\dagger}t), \tag{2.30}$$

where k_e is the escape rate constant. Reactions yields resulting from eq. 2.30 can be evaluated by finding the eigenvalues and eigenvectors of the effective Hamiltonian, denoted by λ and T respectively, and then computing the following integral:

$$\begin{aligned} &\int_0^{\infty} \rho_{ij}(t) = \\ &\sum_{k,l,m,n} T_{i,k}T^{-1}_{k,l}\rho(0)_{l,m}(T^{-1})^*_{k,m}T^*_{j,n}\frac{1}{k_e + i(\lambda_k - \lambda^*_k)}. \end{aligned} \tag{2.31}$$

Taking these quantities together the singlet recombination yield can be calculated:

$$\varphi_S = 2Tr\left[\hat{K}\int \rho(t)dt\right], \tag{2.32}$$

where the time-integrated density operator follows from eq. 2.31.

The measure used to quantify the magnetosensitivity of a biological system, or chemical reaction, is termed the magnetic field effect (MFE) and is defined as the affectation of the rate of singlet-triplet inter-conversion and product yield subsequent to the field's application (Grissom, 1995)). An instructive derivation, for toy radical pairs, of this quantity was presented by Timmel (Timmel et al., 1998). Eq. 2.32 can be used to quantify the effect that the applied magnetic field has upon the

recombination yield, which hence allows one to define the MFE as:

$$\chi_S(B_0) = \frac{\varphi_S(B_0) - \varphi_S(0)}{\varphi_S 0}, \tag{2.33}$$

where $\varphi_S(B_0)$ is the singlet yield at an applied field of intensity B_0, and $\varphi_S(0)$ is the same quantity at zero field.

In general, the MFE is position-dependent with respect to the recombining radicals due to the distance-dependence of the dipolar interaction and of the parameters k_S and J. For the latter parameters, both can often be assumed to have an exponential fall-off. These take the form:

$$k_S(|\mathbf{r}_{ij}|) = k_S(0)exp(-\beta(|\mathbf{r}_{ij}| - 2R)), \tag{2.34}$$

and:

$$J(|\mathbf{r}_{ij}|) = J(0)exp(-\beta(|\mathbf{r}_{ij}| - 2R)). \tag{2.35}$$

In both of the above, the same decay rate, β, has been used and R is representative of the finite radical radius.

Simulations to further test this model for larger, more intricate, spin systems than have previously been explored were carried out using local HPC computing facilities based on code written by the author and group members. This code has been extensively tested against known, and previously derived, results in order to ensure the validity and consistency of the acquired new results and conclusions. The specific methods used were MKL-based calculations of the eignevalues of non-Hermitian matrices and their eigenvalues.

Solving the master equation is at best difficult and at worst intractable, due to the nature of the exponential scaling of the Hilbert space with respect to system size. Even in the special case of radical pairs, one is limited by the number of coupled nuclei that can be considered. As a result, there are some common assumptions that are made when addressing biological systems under the RPM formalism:

- Each electron spin has only a few coupled nuclei.

- Dipolar and Exchange terms should be neglected.

- Singlet and triplet recombination proceeds at the same rate.

While these assumptions may sometimes be considered necessary to make the problem soluble, there are some flaws in the methodology that need to be addressed. The most egregious, one may argue, is the neglect of the dipolar and exchange terms. The argument usually given for this is that the radicals are far enough apart that their magnitudes do not matter. Challenging this assumption, and presenting an alternative model that challenges a fundamental requirement of the RPM, is what the following chapter will address, and the argument proceeds as follows:

Chapter 3 shows that the inclusion of these two terms, in particular the dipolar term, gives rise to brand new effects that the traditional RPM misses. The reason for this, is that the two-radical case (i.e. the RPM) is a very special case with a global symmetry that is not disrupted by the addition of the dipolar term and hence no MFEs are observed in the absence of hyperfine interactions or difference in g-factors. However, Chapter 3 shows that for systems of three or more spins this does not hold and the dipolar interaction causes some fundamental differences in the mathematical description of the radical dynamics.

3. Moving beyond the Radical Pair Mechanism: The D3M Model

The work presented in this chapter is adapted from the following publication: Keens, R.H., Bedkihal, S. and Kattnig, D.R., 2018. Magnetosensitivity in dipolarly coupled three-spin systems. Physical review letters, 121(9), p.096001, with permission from PRL.

Applied to low magnetic fields, for which differences in g-factors/matrices and thus Larmor precession frequencies are negligible, a key ingredient of the RPM is the hyperfine interaction that coherently mixes singlet and triplet electron spin states in pairs of radicals, facilitating magnetic field effects (MFEs) on reaction yields via spin-selective reaction channels. This chapter shows that the hyperfine interaction is not a categorical requirement for the magnetosensitivity of radical reactions, especially to weak magnetic fields. It is proposed that, in systems comprising three (rather than two) radicals, dipolar interactions provide an alternative pathway for MFEs. By considering the role of symmetries and energy level crossings, a model is presented that demonstrates a directional sensitivity to fields weaker than the geomagnetic field and remarkable spikes in the reaction yield as a function of the magnetic field intensity; these effects can further be tuned by the exchange interaction.

Here, it is shown that MFEs are absent for a system of two radicals coupled by electron dipole-dipole interactions alone, i.e. without hyperfine interactions or g-factor differences. It is then shown that MFEs are absent in a purely exchange coupled isotropic linear N-spin system on account of $SU(2)$ symmetry. The relevant commutators are evaluated to demonstrate the $SU(2)$ symmetry of an isotropic, exchange coupled, linear spin system. It is further shown that the $SU(2)$ symmetry

is broken when dipole-dipole interactions are included. The necessary and sufficient conditions to realize magnetic field effects are obtained, and it is shown that the dipolar interaction mixes singlet-triplet states for most configurations of spin-triad; there exist only two special cases where no MFEs are observed. Finally, MFEs are shown for the equilateral triangular and general geometries, and the bond-angle dependence in isosceles triangular triads.

Thus, simply by including the dipolar and exchange terms alongside the Zeeman contribution, one can see remarkable MFEs, which suggests that the assumption that dipolar and exchange terms can be neglected is indeed an assumption that does not generally hold, and that interesting new MFEs are predicted beyond the convectional RPM if they are included. The D3M model is the first step in this new paradigm.

3.1 The D3M model

A toy model of three spins in an external magnetic field is considered and subsequently the MFEs that arise as a consequence of inter-radical interactions are investigated. The model Hamiltonian is given (in angular frequency units) by

$$\begin{aligned}\hat{H} &= \hat{H}_0 + \hat{H}_1 = \hat{H}_{dd} + \hat{H}_{ex} + \hat{H}_1 \\ &= \sum_{i<j}^{N} \hat{\mathbf{S}}_i \cdot \mathbf{D}_{i,j} \cdot \hat{\mathbf{S}}_j - \sum_{i<j}^{N} J_{i,j} \left(\tfrac{1}{2} + 2\hat{\mathbf{S}}_i \cdot \hat{\mathbf{S}}_j \right) + \gamma \vec{\mathbf{B_0}} \cdot \sum_{i}^{N} \hat{\mathbf{S}}_i \end{aligned} \tag{3.1}$$

The individual summands account for the electron-electron dipolar ($\hat{H}_{dd}$), exchange ($\hat{H}_{ex}$) and Zeeman interactions ($\hat{H}_1$). $\vec{\mathbf{B_0}}$ denotes the applied magnetic field, B_0 its intensity and $\gamma = \frac{g\mu_B}{\hbar}$. Here, it has been assumed that the Zeeman interaction is isotropic and identical for all radicals on account of the focus on the MFEs of organic radicals in weak magnetic fields, i.e. $g \approx 2$ and the anisotropies are negligible for moderate B_0. The electron-electron dipolar interactions are treated in the point-dipole limit. The interaction energy is related to the (supra)-molecular structure of the spin-triad by

$$\hat{\mathbf{S}}_i \cdot \mathbf{D}_{i,j} \cdot \hat{\mathbf{S}}_j = d_{i,j}(r_{i,j}) \left[\hat{\mathbf{S}}_i \cdot \hat{\mathbf{S}}_j - 3 \left(\hat{\mathbf{S}}_i \cdot \vec{\mathbf{e}}_{i,j} \right) \left(\hat{\mathbf{S}}_j \cdot \vec{\mathbf{e}}_{i,j} \right) \right]. \tag{3.2}$$

In the above equation, $\vec{\mathbf{e}}_{i,j} = \frac{\vec{\mathbf{r}}_{i,j}}{|\vec{\mathbf{r}}_{i,j}|}$ where $\vec{\mathbf{r}}_{i,j}$ is the vector connecting radical centres i and j, $d_{i,j} = \frac{d_0}{|\vec{\mathbf{r}}_{i,j}|^3}$, and $d_0 = \frac{\mu_0}{4\pi\hbar} g^2 \mu_B^2$. It is assumed that the three-radical system is generated in the singlet state of radicals 1 and 2 with the third radical uncorrelated to the others, i.e. the initial density operator obeys $\hat{\rho}(t=0) = \frac{1}{2}\hat{P}_s^{(1,2)}$ where $\hat{P}_s^{(i,j)} = \frac{1}{4} - \hat{\mathbf{S}}_i \cdot \hat{\mathbf{S}}_j = \frac{1}{2}(1 - \hat{P}_{i,j})$ is the singlet projection operator on the i,j- subspace, and $\hat{P}_{i,j}$ is the permutation operator for spins i and j. Assuming that radicals 1 and 2 recombine with equal rate constant k in the singlet and triplet configurations, the equation of motion for the spin-triad density matrix becomes

$$\frac{d\hat{\rho}}{dt} = -i[\hat{H}, \hat{\rho}(t)] - k\hat{\rho}(t). \tag{3.3}$$

The quantum yield of the singlet recombination product of radicals 1 and 2 is $\varphi_s = k\int_0^\infty d\tau Tr[\hat{P}_s^{(1,2)}\hat{\rho}(\tau)]$, and the powder-averaged singlet yield is $\langle\varphi_s\rangle = \frac{1}{4\pi}\int_0^{2\pi} d\phi \int_0^{\pi} d\vartheta \sin(\vartheta)\varphi_s(B_0(\vartheta,\phi))$. The MFEs can then be quantified by $\chi_s = \frac{\varphi_s(B_0)}{\varphi_s(0)} - 1$; analogous definitions apply to the orientation-averaged yield. In the eigenbasis of the Hamiltonian, $\hat{H}$, it is such that $\varphi_s = \frac{1}{2}\sum_{i,j}\left|\langle i|\hat{P}_s^{(1,2)}|j\rangle\right|^2 f(k, \omega_i - \omega_j)$, where $f(k,\Delta\omega) = \frac{k^2}{k^2+\Delta\omega^2}$, and $|i\rangle$, $|j\rangle$ are the eigenstates of $\hat{H}$.

The magnetic field independent part of the Hamiltonian ($\hat{H}_0$) is invariant under time reversal symmetry, i.e. it commutes with the time reversal operator $\hat{\Theta} = e^{i\pi\hat{S}_y}\hat{\mathcal{K}}$ where $\hat{\mathcal{K}}$ denotes complex conjugation in the standard basis, and $\hat{S}_y$ is the y-component of the total spin-angular momentum operator $\hat{\mathbf{S}} = \sum_j \hat{\mathbf{S}}_j$. As $\hat{\Theta}^2 = -1$, the eigenstates of $\hat{H}_0$ are (at least) two-fold degenerate (Kramers degeneracy (Klein, 1952)). Furthermore, as $\hat{\Theta}$ maps $|S^{(1,2)}\pm\rangle$ into $\pm|S^{(1,2)}\mp\rangle$, pairwise degenerate states ($|i\rangle$, $\hat{\Theta}|i\rangle$) yield the same expectation value of $\hat{P}_s^{(1,2)}$. Note however, that $|S^{(1,2)}\pm\rangle$ is not an eigenstate of the Hamiltonian, in stark contrast to the well-studied scenarios of pairs of radicals. This Kramers degeneracy, in spin triads, is broken by an external magnetic field. Consequently, the energy levels split and, depending on symmetry properties, can cross and/or anti-cross as a function of the applied field. This gives rise to prominent MFEs by impacting upon the coupling matrix elements $\langle i|\hat{P}_s^{(1,2)}|j\rangle$ and $f(k,\Delta\omega)$ (through altered energy differences). An example of such degeneracy-lifting is shown schematically in Fig. 3.1(a). The necessary and sufficient conditions

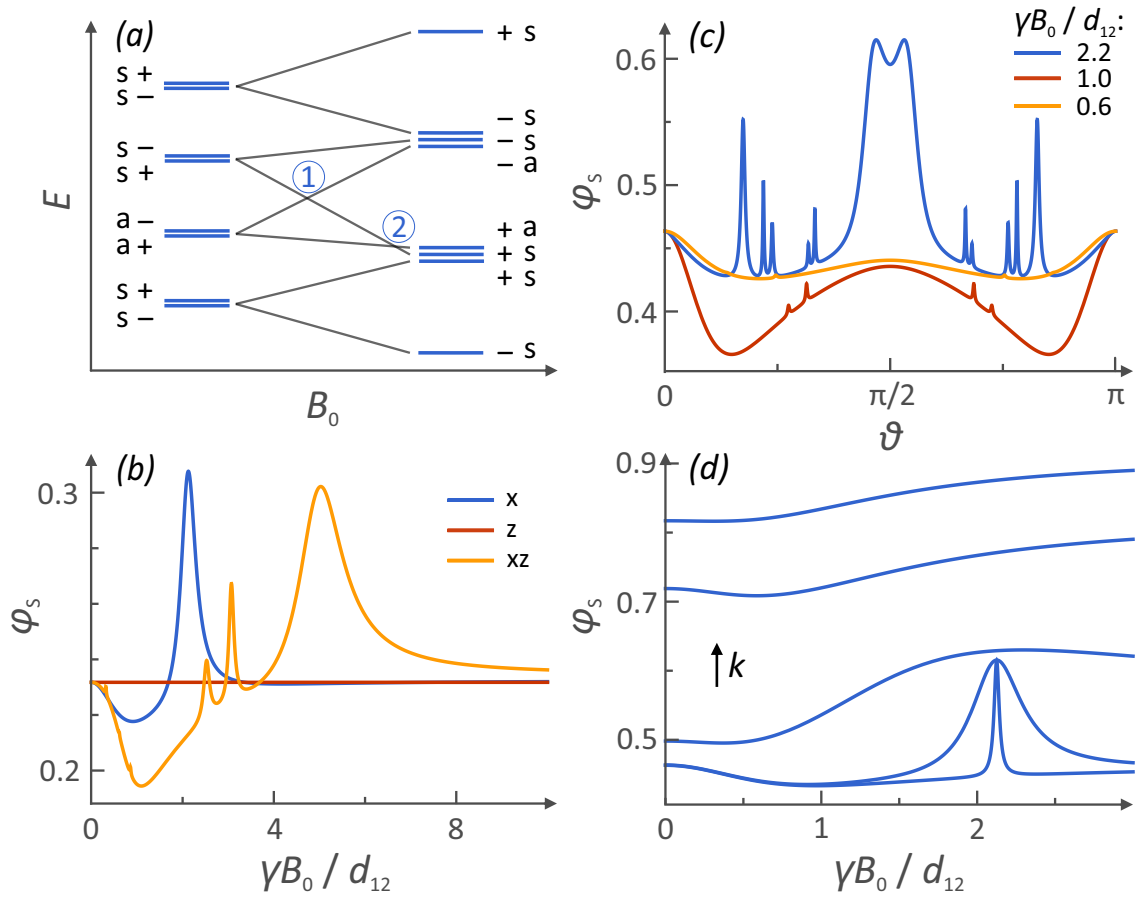

Figure 3.1: (a) Schematic correlation diagram of energy level crossings as a function of the applied field, B_0. The labels classify the (anti-)symmetry of the states under $\hat{P}_{1,3}$. (b) Yield vs orientation for selected values of B_0. Here, the recombination constant $k/d_{1,2}$ is 0.01. (c) Yield vs B_0 for selected orientations; here $k/d_{1,2}$ is 0.01. (d) Yield vs B_0 for $k/d_{1,2} = 0.001, 0.01, 0.1, 0.5, 1$, respectively, and in ascending order. Here the Zeeman field is along the x-direction. In all of the above figures, $J = 0$.

to observe MFEs are that (i) $[\hat{P}_s^{(1,2)}, \hat{H}_0] \neq 0$ and (ii) $\hat{H}_0$ does not possess the $SU(2)$ spin rotation symmetry.

For a radical *pair* (with the Hamiltonian as given in eq. 3.1, i.e. with no hyperfine interactions), $\hat{H}$ always commutes with $\hat{P}_s^{(1,2)}$, and no MFEs are observed due to inter-radical interactions alone. Here, it is argued that dipolarly-coupled spin triads give rise to MFEs for all configurations except for a peculiar one with the third (inert) radical placed midway between the recombining radicals (and in the limit that radical 3 is so remote that it does not affect the spin-evolution of the dyad on the timescale of its lifetime). On the contrary, a purely exchange-coupled isotropic spin system does not exhibit magnetosensitivity as a consequence of the retained $SU(2)$ symmetry of $\hat{H}_0$.

First a situation is considered where there is a system of two radicals coupled

by dipole-dipole and exchange interactions. The Hamiltonian is given by

$$\hat{H} = \hat{H}_0 + \hat{H}_1,$$

with:

$$\hat{H}_0 = \hat{\mathbf{S}}_1 \cdot \mathbf{D}_{1,2} \cdot \hat{\mathbf{S}}_2 - J_{1,2} \left(\frac{1}{2} + 2\hat{\mathbf{S}}_1 \cdot \hat{\mathbf{S}}_2 \right), \tag{3.4}$$

and:

$$\hat{H}_1 = \gamma \vec{\mathbf{B}}_0 \cdot \Big(\hat{\mathbf{S}}_1 + \hat{\mathbf{S}}_2 \Big),$$

where $D_{1,2}$ is the dipole-dipole tensor coupling spins 1 and 2, $J_{1,2}$ is the exchange coupling strength and B_0 is the intensity of an applied magnetic field. Noting that among the commutators between the two-spin operators, only those that can be represented by $\left[2\hat{S}_{1,i}\hat{S}_{2,k}, 2\hat{S}_{1,j}\hat{S}_{2,k}\right] = \varepsilon_{i,j,m}\, i\, \hat{S}_{1,m}\hat{S}_{2,k}$ and $\left[2\hat{S}_{1,k}\hat{S}_{2,i}, 2\hat{S}_{1,k}\hat{S}_{2,l}\right] = \varepsilon_{i,l,m}\, i\, \hat{S}_{1,k}\hat{S}_{2,m}$ are non-zero, with $\varepsilon_{i,j,m}$ denoting the Levi-Civita symbol and the summation over m being implied, the singlet projection operator $\hat{P}_S^{(1,2)} = \frac{1}{4} - \hat{S}_1 \cdot \hat{S}_2$ commutes with the field-independent Hamiltonian $\hat{H}_0$. Furthermore, as $\hat{H}_1$, and consequently $\hat{H}$, commutes with $\hat{P}_S^{(1,2)}$, the singlet state is a field-independent eigenstate of the Hamiltonian and no MFEs on the singlet yield are observed (in the absence of additional interactions).

Here, the necessary and sufficient conditions to realize MFEs in a system of $N > 2$ spins are examined. First, consider a purely exchange coupled isotropic spin system given by the following Hamiltonian,

$$\hat{H}_0 = \sum_{i<j}^{N} J_{i,j}[\hat{S}_{i,x}\hat{S}_{j,x} + \hat{S}_{i,y}\hat{S}_{j,y} + \hat{S}_{i,z}\hat{S}_{j,z}]. \tag{3.5}$$

Let the total spin operator along the respective direction be denoted as $\hat{S}_i = \sum_m \hat{S}_{m,i}$

where $i \in \{x, y, z\}$. Then, one can evaluate the following commutator

$$\begin{aligned}\left[\hat{H}_0, \hat{S}_z\right] &= \sum_{i,j} J_{i,j} \sum_m [\hat{S}_{i,x}\hat{S}_{j,x} + \hat{S}_{i,y}\hat{S}_{j,y} + \hat{S}_{i,z}\hat{S}_{j,z}, \hat{S}_{m,z}] \\ &= \sum_{i,j} J_{i,j} \sum_m \left([\hat{S}_{i,x}\hat{S}_{j,x}, \hat{S}_{m,z}] + [\hat{S}_{i,y}\hat{S}_{j,y}, \hat{S}_{m,z}] + [\hat{S}_{i,z}\hat{S}_{j,z}, \hat{S}_{m,z}]\right).\end{aligned} \tag{3.6}$$

The above commutator can be further reduced to

$$\begin{aligned}\left[\hat{H}_0, \hat{S}_z\right] = \sum_{i,j}^{N} J_{i,j}([\hat{S}_{i,x}\hat{S}_{j,x}, \hat{S}_{i,z}] + [\hat{S}_{i,y}\hat{S}_{j,y}, \hat{S}_{i,z}] + [\hat{S}_{i,z}\hat{S}_{j,z}, \hat{S}_{i,z}] \\ + [\hat{S}_{i,x}\hat{S}_{j,x}, \hat{S}_{j,z}] + [\hat{S}_{i,y}\hat{S}_{j,y}, \hat{S}_{j,z}] + [\hat{S}_{i,z}\hat{S}_{j,z}, \hat{S}_{j,z}]).\end{aligned} \tag{3.7}$$

The first term can be written as

$$\left[\hat{S}_{i,x}\hat{S}_{j,x}, \hat{S}_{i,z}\right] = -i\hat{S}_{i,y}\hat{S}_{j,x}. \tag{3.8}$$

Likewise the remaining commutators in Eq. 3.7 can be simplified to obtain,

$$\begin{aligned}\left[\hat{H}_0, \hat{S}_z\right] &= \sum_{i<j}^{N} J_{i,j}([\hat{S}_{i,x}, \hat{S}_{i,z}]\hat{S}_{j,x} + [\hat{S}_{i,y}, \hat{S}_{i,z}]\hat{S}_{j,y} + [\hat{S}_{i,z}, \hat{S}_{i,z}]\hat{S}_{j,z} \\ &\quad + \hat{S}_{i,x}[\hat{S}_{j,x}, \hat{S}_{j,z}] + \hat{S}_{i,y}[\hat{S}_{j,y}, \hat{S}_{j,z}] + \hat{S}_{i,z}[[\hat{S}_{j,z}, \hat{S}_{j,z}]) \\ &= i\sum_{i<j}^{N} J_{i,j}(-\hat{S}_{i,y}\hat{S}_{j,x} + \hat{S}_{i,x}\hat{S}_{i,y} + 0 + \hat{S}_{i,y}\hat{S}_{j,x} - \hat{S}_{i,x}\hat{S}_{j,y} + 0) \\ &= 0.\end{aligned}$$

Similarly it can be shown that $[\hat{H}_0, \hat{S}_x] = [\hat{H}_0, \hat{S}_y] = 0$. This implies that an isotropic exchange coupled spin model has $SU(2)$ symmetry and the eigenstates can be arranged as $SU(2)$ multiplets. As $\hat{H}_1$ commutes with $\hat{P}_S^{(1,2)}$, thus MFEs are not observed for this scenario.

Next, these commutators are examined by adding dipole-dipole interactions of the form $\hat{H}_0 = \sum_{i<j} \hat{\mathbf{S}}_i \cdot \mathbf{D}_{i,j} \cdot \hat{\mathbf{S}}_j$. In this case it is found that in general $[\hat{H}_0, \hat{S}_i] \neq 0$, and MFEs are observed if $[\hat{P}_S^{(i,j)}, \hat{H}_0] \neq 0$. Typically, $[\hat{H}_0, \hat{S}_i] \neq 0$, but it is remarked that this is in particular not true for a linear triad aligned along x, with the magnetic field aligned along the triad axis. In the next section the geometric conditions that

have to be fulfilled (see below for details) in order to observe MFEs in dipolarly coupled three-spin systems are discussed.

3.2 MFEs without hyperfine interactions using D3M

In this section, the dipolar interaction is examined in detail in the context of the D3M model. Here it is shown that the dipolar interaction induces magnetic field dependent singlet-triplet mixing in all spin configurations except for one special case. Without loss of generality, it is assumed that the three spins are located at the origin, displaced along the z-axis (spin 1) and along an arbitrary direction in the x,z-plane that is inclined with respect to the z-axis by an angle θ (spin 3), respectively. In units of $d_{1,2}$, the dipolar coupling tensors are then given by

$$D_{1,2} = \begin{pmatrix} 1 & 0 & 0 \\ 0 & 1 & 0 \\ 0 & 0 & -2 \end{pmatrix} \tag{3.9}$$

$$D_{2,3} = \frac{1}{r^3} \begin{pmatrix} \frac{[3\cos(2\theta)-1]}{2} & 0 & -3\cos(\theta)\sin(\theta) \\ 0 & 1 & 0 \\ -3\cos(\theta)\sin(\theta) & 0 & -\frac{[1+3\cos(2\theta)]}{2} \end{pmatrix} \tag{3.10}$$

and

$$D_{1,3} = \frac{1}{f(r,\theta)^3} \begin{pmatrix} 1 - G_1(r,\theta) & 0 & G_2(r,\theta) \\ 0 & 1 & 0 \\ G_2(r,\theta) & 0 & G_1(r,\theta) \end{pmatrix} \tag{3.11}$$

where $f(r,\theta) = (1 + r^2 - 2r\cos(\theta))^{\frac{1}{2}}$, $G_1(r,\theta) = 2 - 3\left(\frac{r\sin\theta}{f(r,\theta)}\right)^2$, and $G_2(r,\theta) = \frac{3r(1-r\cos\theta)\sin\theta}{f(r,\theta)^2}$, and it is assumed that there are no stacked spins (i.e. excluding the case $r = 1$ and $\theta = 0$).

With this, the dipolar Hamiltonian becomes

$$\hat{H}_0 = \hat{S}_1 D_{1,2} \hat{S}_2 + \hat{S}_2 D_{2,3} \hat{S}_3 + \hat{S}_1 D_{1,3} \hat{S}_3. \tag{3.12}$$

Next, examine the commutator $[\hat{P}_S^{(1,2)}, \hat{H}] = [\hat{P}_S^{(1,2)}, \hat{H}_0]$. Using the commutator identities of the form $[\hat{A}\hat{B}, \hat{C}\hat{D}] = \hat{A}[\hat{B}, \hat{C}]\hat{D} + \hat{A}\hat{C}[\hat{B}, \hat{D}] + [\hat{A}, \hat{C}]\hat{D}\hat{B} + \hat{C}[\hat{A}, \hat{D}]\hat{B}$ and using angular momentum algebra, the above commutators can be written in the form of triple products of spin operators,

$$\begin{aligned} -i[\hat{P}_S^{(1,2)}, \hat{H}_0] = &\left[\frac{1}{r^3} - \frac{1}{f(r,\theta)^5}\right]\left(\hat{S}_{1,z}\hat{S}_{2,x}\hat{S}_{3,y} - \hat{S}_{1,x}\hat{S}_{2,z}\hat{S}_{3,y}\right) \\ &+ \lambda(r,\theta)(\hat{S}_{1,y}\hat{S}_{2,x}\hat{S}_{3,x} + \hat{S}_{1,z}\hat{S}_{2,y}\hat{S}_{3,z} \\ &- \hat{S}_{1,x}\hat{S}_{2,y}\hat{S}_{3,x} - \hat{S}_{1,y}\hat{S}_{2,z}\hat{S}_{3,z}) + ..., \end{aligned} \tag{3.13}$$

where

$$\lambda(r,\theta) = \frac{3\cos\theta\sin\theta}{r^3} - \frac{3r\sin\theta(r\cos\theta - 1)}{f^5}. \tag{3.14}$$

The sum on the right hand side of Eq. 3.13 comprises a total of 10 different triple products of the spin operators of radical 1, 2 and 3, which can be collected in 4 groups of unique dependence on r and θ. The spin evolution mixes singlet and triplet states unless the singlet states are the eigenstates of the Hamiltonian $\hat{H}_0$, which requires the commutator $[\hat{P}_S^{(1,2)}, \hat{H}_0]$ to vanish; one can now seek the conditions on r and θ for which this occurs.

The first set of terms vanishes for $\theta = \pm\arccos\left(\frac{1}{2r}\right)$. Inserting this into the second term gives a non-zero contribution except for $r = 1/2$, which stipulates that $\theta = 0, \pi/2, \pi$ on account of the first condition. Indeed, only for $\theta = 0$ do all terms in the commutator vanish simultaneously. Thus, it can be concluded that the dipolar interaction mixes singlet and triplet terms except for one peculiar configuration, for which the third (unreactive) radical is placed half-way between the recombining radicals. Obviously, this corresponds to a scenario that might be difficult to realize in practice. If, additionally, one takes the exchange interaction into account, an analogous treatment reveals that the same products of spin operators appear in the commutator. The coefficients are, however, in part augmented by the difference of $J_{1,3}$ and $J_{2,3}$. A detailed analysis reveals that the commutator vanishes if the above conditions are fulfilled ($r = 1/2$, $\theta = 0$) and additionally $J_{1,3} = J_{2,3}$.

This exploration is continued by showing that the dipolar interaction gives rise to a

magnetic field dependence of the singlet recombination yield for most configurations of three spins. The reaction yield varies with the intensity of magnetic field if $\hat{H}_0$ does not commute with the singlet projection operator, as established above, and $\hat{H}_0$ does not commute with $\hat{H}_1$. The focus shall now be on this second condition for the dipolar Hamiltonian. The relevant commutator becomes

$$\begin{aligned} -i[\hat{H}_{dd}, \hat{H}_1] = &-3\omega_{0,x}(\hat{S}_{1,z}\hat{S}_{2,y} + \hat{S}_{1,y}\hat{S}_{2,z}) \\ &+3\omega_{0,y}(\hat{S}_{1,z}\hat{S}_{2,x} + \hat{S}_{1,x}\hat{S}_{2,z}) + ... \end{aligned} \tag{3.15}$$

The right hand side of above equation contains 20 summands, which are bilinear in spin operators; $\omega_{0,i}$, with $i \in \{x, y, z\}$, denotes the Larmor precession frequency associated with field-component i, and $\vec{\omega}_0 = \gamma\vec{\mathbf{B}}_0$. The form of Eq. 3.15 suggests that the commutator can only vanish if $\omega_{0,x} = \omega_{0,y} = 0$. Assuming this condition holds one arrives at the simpler expression

$$\begin{aligned} -i[\hat{H}_{dd}, \hat{H}_1] = &\omega_{0,z}\frac{3\sin\theta\cos\theta}{r^3}(\hat{S}_{2,z}\hat{S}_{3,y} + \hat{S}_{2,y}\hat{S}_{3,z}) \\ &+\omega_{0,z}\frac{3r(r\cos\theta - 1)\sin\theta}{f^5}(\hat{S}_{1,z}\hat{S}_{3,y} + \hat{S}_{1,y}\hat{S}_{3,z}) \\ &+\omega_{0,z}\frac{3\sin^2\theta}{r^3}(\hat{S}_{2,y}\hat{S}_{3,x} + \hat{S}_{2,x}\hat{S}_{3,y}) \\ &+\omega_{0,z}\frac{3r^2\sin^2\theta}{f^5}(\hat{S}_{1,y}\hat{S}_{3,x} + \hat{S}_{1,x}\hat{S}_{3,y}). \end{aligned} \tag{3.16}$$

It can be seen that all the terms in the above equations are proportional to $\sin\theta$ and vanish for $\theta = 0$ or $\theta = \pi$. As a result the singlet yield is insensitive to the magnetic field for a linear configuration of three radicals (including asymmetric configuration) if the magnetic field is parallel to the distinguished axis. For these orientations, the Hamiltonian has $U(1)$ symmetry and the magnetization along the distinguished axis is a conservative quantity. Conversely, except for this peculiar scenario and the configuration discussed above, MFEs are generally predicted.

3.3 Specific example cases

In this section, a few specific geometries are considered and their available MFEs evaluated wihin the framework of the D3M model.

First, a linear symmetric triad is considered, for which $d_{1,2} = d_{2,3} = 8\ d_{1,3}$; the effect of changes to this geometry can be seen below. For a radical *pair*, $\hat{H}$ always commutes with $\hat{P}_s^{(1,2)}$, and no MFEs are observed due to inter-radical interactions. For the linear case with negligible exchange couplings ($J_{i,j} = 0$), Figs. 3.1 (b-d) show the singlet yield as a function of the magnetic field for selected orientations or as a function of orientation for selected fields.

3.3.1 Analytical results for the linear geometry

In the case with the magnetic field parallel to the symmetry axis, no MFEs are observed. The eigenstates and associated energies, which depend linearly on the field intensity (see Fig. 3.1) can be readily evaluated for this scenario. Further, the singlet yield can be calculated analytically following the approach as outlined previously. The following dependence upon the recombination rate constant k is obtained:

$$\begin{aligned}\varphi_S =& \frac{841}{1816} + \frac{147}{908} f\left(\frac{\sqrt{681}}{16} d_{1,2}, k\right) \\ &+ \frac{\left(681 + 17\sqrt{681}\right)}{3632} f\left(\frac{1}{32}\left(\sqrt{681} - 17\right) d_{1,2}, k\right) \\ &+ \frac{\left(681 - 17\sqrt{681}\right)}{3632} f\left(\frac{1}{32}\left(\sqrt{681} + 17\right) d_{1,2}, k\right)\end{aligned} \tag{3.17}$$

where, $f(\Delta\omega, k) = \frac{k^2}{k^2+\Delta\omega^2}$ as previously. Fig. 3.2(b) shows the dependence of yield on the recombination rate constant.

For general orientations, an analytical calculation is impractical. An exception is the high-field scenario ($\gamma B_0 >> d_{1,2}$) with the magnetic field oriented perpendicular to the distinguished axis, which allows an approximate solution by degenerate perturbation theory. By representing the Hamiltonian in the eigenbasis of $\hat{H}_1$, followed by diagonalising the degenerate sub-blocks, the following approximate

expression for the singlet yield can be obtained:

$$\begin{aligned}\varphi_S \approx & \frac{841}{1816} + \frac{147}{908} f\left(\frac{\sqrt{681}}{32} d_{1,2}, k\right) \\ & + \frac{\left(681 + 17\sqrt{681}\right)}{3632} f\left(\frac{1}{64}\left(\sqrt{681} - 17\right) d_{1,2}, k\right) \\ & + \frac{\left(681 - 17\sqrt{681}\right)}{3632} f\left(\frac{1}{64}\left(\sqrt{681} + 17\right) d_{1,2}, k\right).\end{aligned} \tag{3.18}$$

Together with Eq. 3.17 this allows one to approximately calculate the MFE for $B_0 >> d_{1,2}$ and with the magnetic field at a perpendicular orientation. Fig. 3.3 illustrates this MFE as a function of the recombination rate constant. Remarkably, large MFEs can be realized for recombination rates of the order of 0.1 to 1 $d_{1,2}$, i.e. under conditions of relatively fast recombination. In fact, this high-field procedure can be applied for an arbitrary orientation of the magnetic field. Denoting the angle between the axis of the three-spin system and the magnetic field by θ, we obtain:

$$\begin{aligned}\varphi_S \approx & \frac{841}{1816} + \frac{147}{908} f\left(\frac{1}{64}\sqrt{681}\, h(\vartheta)\, d_{1,2}, k\right) \\ & + \frac{681 + 17\sqrt{681}}{3632} f\left(\frac{1}{128}\left(\sqrt{681} - 17\right)\, h(\vartheta)\, d_{1,2}, k\right) \\ & + \frac{681 - 17\sqrt{681}}{3632} f\left(\frac{1}{128}\left(\sqrt{681} + 17\right) h(\vartheta)\, d_{1,2}, k\right),\end{aligned} \tag{3.19}$$

where $h(\vartheta) = 1 + 3\cos(2\vartheta)$. It is noteworthy that the singlet yield is equal to 1 for the magic angle, $\vartheta = \frac{1}{2}\arccos\left(-\frac{1}{3}\right)$, for which the secular terms of the dipole-dipole coupling (cf. below) vanish and thus no singlet-triplet mixing is induced in high field. Fig. 3.4 shows the directional dependence of the singlet yield as given by Eq. 3.19 and the dependence of the average singlet yield on k. Fig. 3.5 illustrates the anisotropy of the singlet yield through polar plots of the deviation of the singlet yield from the spherical mean. Note that remarkably spiky changes in the singlet yield can appear at the magic angle if the lifetime is long. For long lifetimes away from the magic angle, φ_S approaches $\frac{841}{1816}$; for fast recombination no spin mixing is realised and φ_S approaches 1. Even in the presence of exchange interactions, no MFEs are observed when the field is along the symmetry axis. For this scenario, and

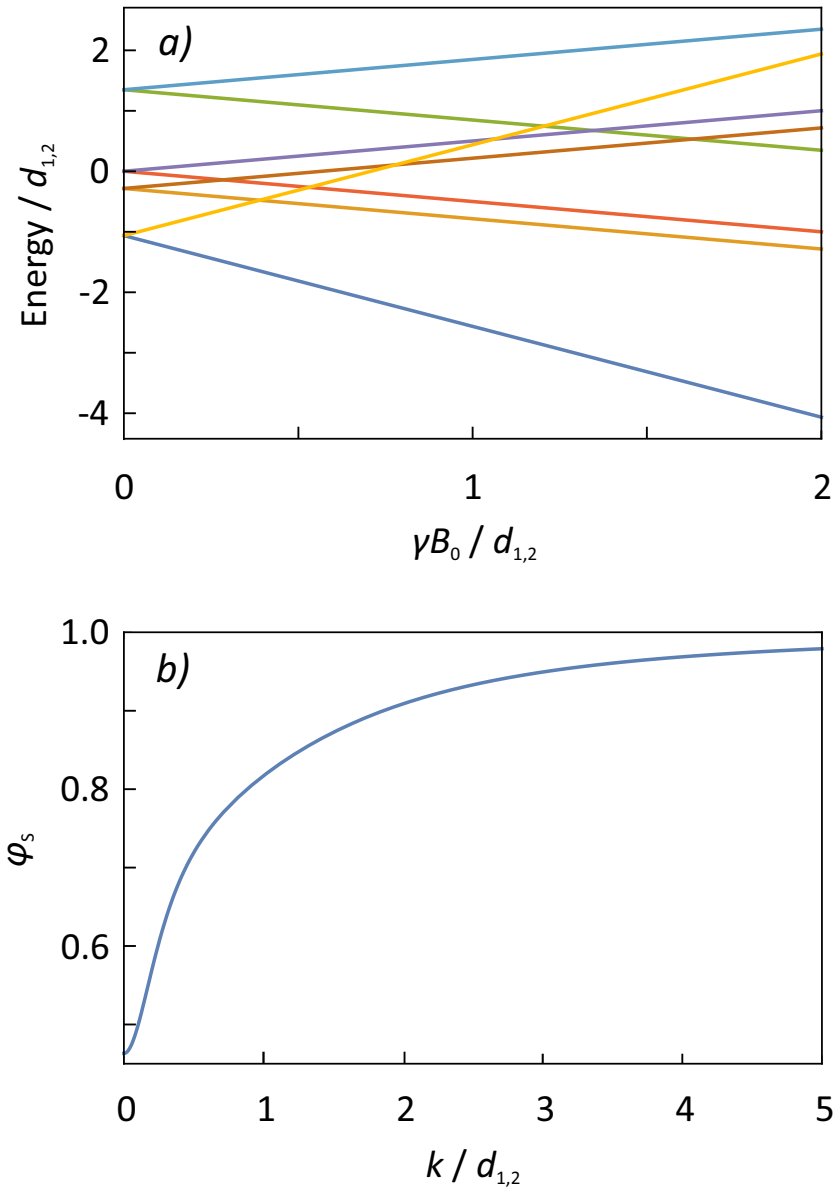

Figure 3.2: A linear spin triad with no exchange interaction. a) Energy level scheme for the field parallel to the molecular axis. b) Dependence of the singlet yield on the recombination rate constant k for the magnetic field parallel to the z-axis (any field intensity).

$j_{1,2} = j_{2,3} = j\ d_{1,2}$, and $j_{1,3} = 0$, the analytic dependence reads

$$\varphi_S = \frac{1}{s(j)}\left[2\left(841 + 160j\left(24j - 17\right)\right) + d(j)\left(17 - 48j + d(j)\right) f\left(\frac{1}{32}\upsilon d_{1,2}, k\right)\right] - \frac{1}{s(j)}\left[d(j)\left(17 - 48j - d(j)\right) f\left(\frac{1}{32}\upsilon d_{1,2}, k\right) + 588\, f\left(\frac{d(j)}{16}d_{1,2}, k\right)\right] \tag{3.20}$$

where $s(j) = 16(227 + 32j(24j - 17))$, $d(j) = \sqrt{3}\sqrt{227 - 544j + 768j^2}$, and $\upsilon = \sqrt{\left(d(j) - 17 - 16j\right)^2}$.

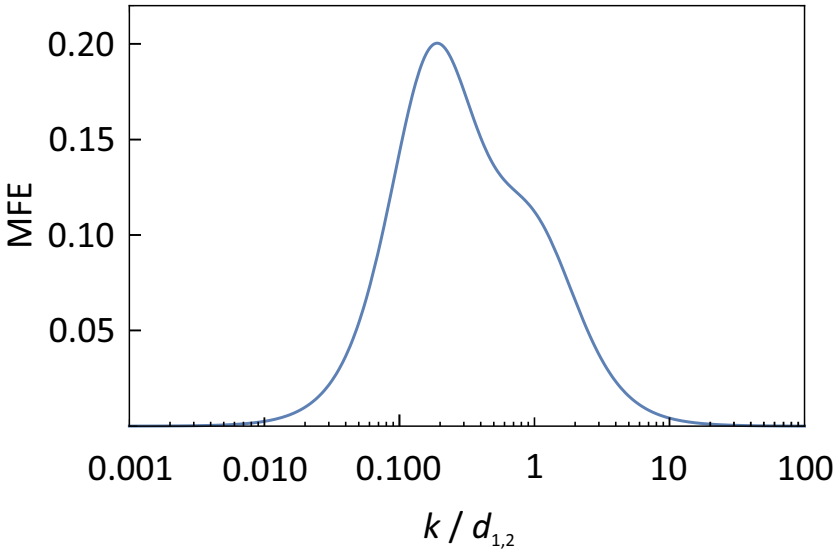

Figure 3.3: MFE of the linear spin-triad with the field perpendicular to the triad-axis as a function of the recombination rate constant k; no exchange; analytical result.

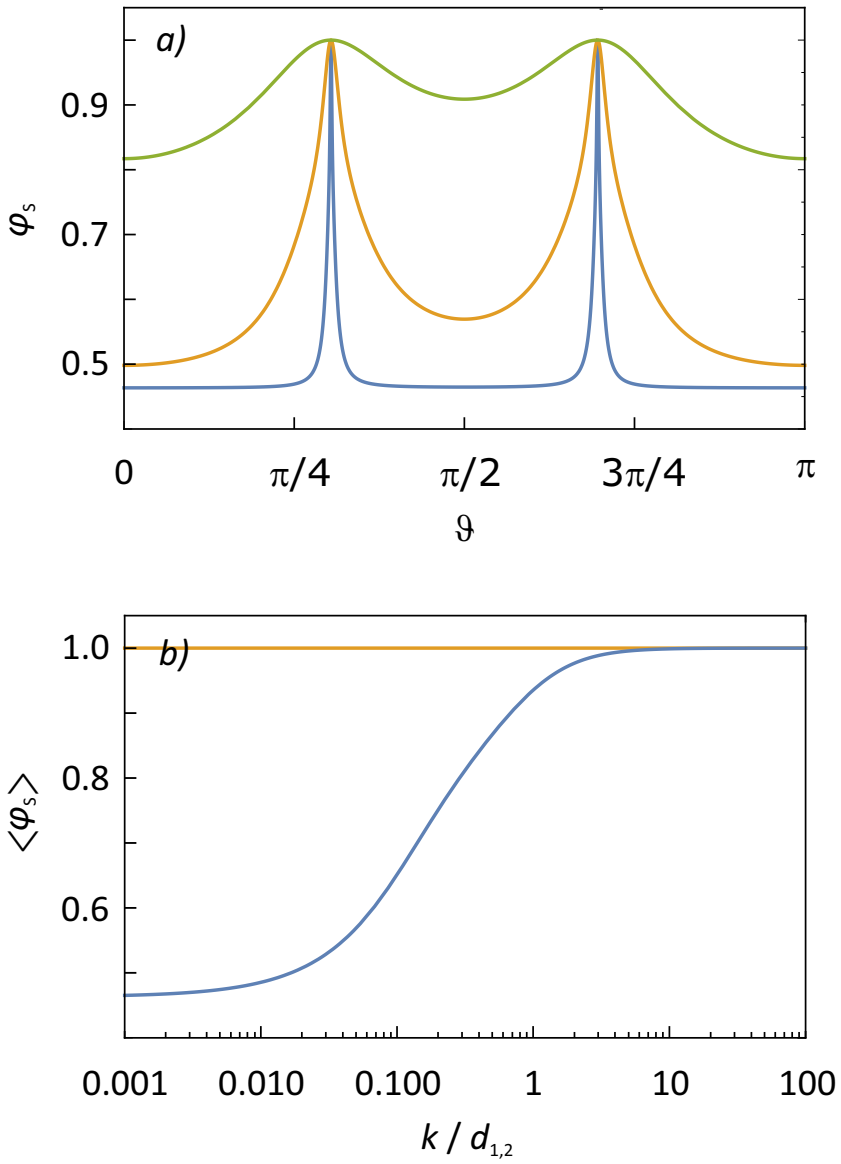

Figure 3.4: Linear geometry with no exchange; analytical results. a) Directional dependence of the singlet yield, $k = \{0.01, 0.1, 1\}$ $d_{1,2}$. b) Powder-averaged singlet yield as a function of $k/d_{1,2}$.

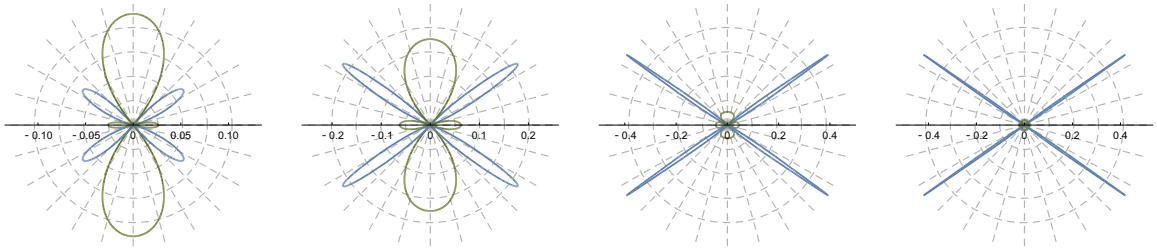

Figure 3.5: Polar plots of the anisotropy of the singlet yield for the linear geometry in the high-field limit. No exchange was used, and $k = \{0.01, 0.025, 0.25, 1\}d_{1,2}$.

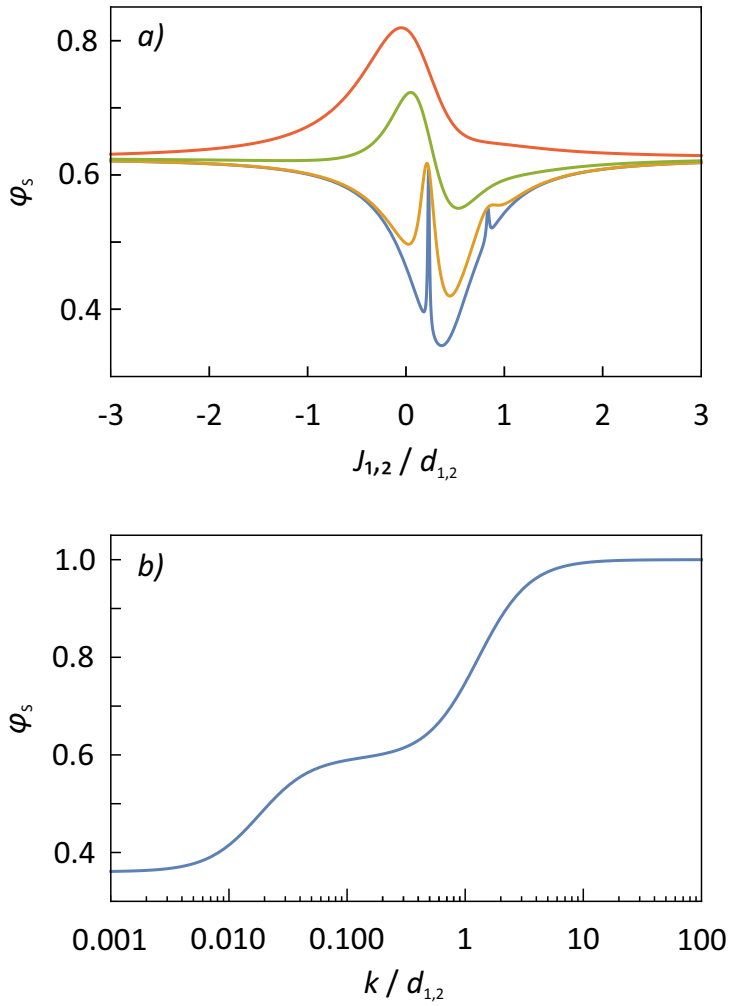

Figure 3.6: Linear spin triad with exchange, $J_{1,2} = J_{2,3}$, and $J_{1,3} = 0$. a) Singlet yield as a function of $J_{1,2} = J_{2,3}$ for the magnetic field parallel to the molecular axis (any intensity). $k = \{0.01$ (blue), $0.1, 0.5, 1$ (red)$\}$ $d_{1,2}$. b) Dependence of the singlet yield on k for $J_{1,2} = J_{2,3} = \frac{1}{4} d_{1,2}$.

In the case where the magnetic field is parallel to the molecular symmetry axis, z, $[\hat{H}_{dd}, \hat{H}_1] = 0$, i.e. the z-component of the total magnetization is conserved and no MFE arises. An analytic calculation shows the dependence of the singlet yield on k.

3.4 Further results for the linear geometry

A remarkable sensitivity to k is recognized for j in the range $(-1,1)$, as is shown in Fig. 3.6. Fig. 3.7 shows the yield as a function of magnetic field for different k values when the magnetic field is along a perpendicular direction so that $[\hat{H}_0, \hat{H}_1] \neq 0$. It can be seen that the width of the low field peak broadens as k increases.

In the limit of slow recombination, the yield approaches $\frac{841}{1816}$; for fast recombination no spin conversion is observed ($\varphi_S = 1$) as expected. For any other

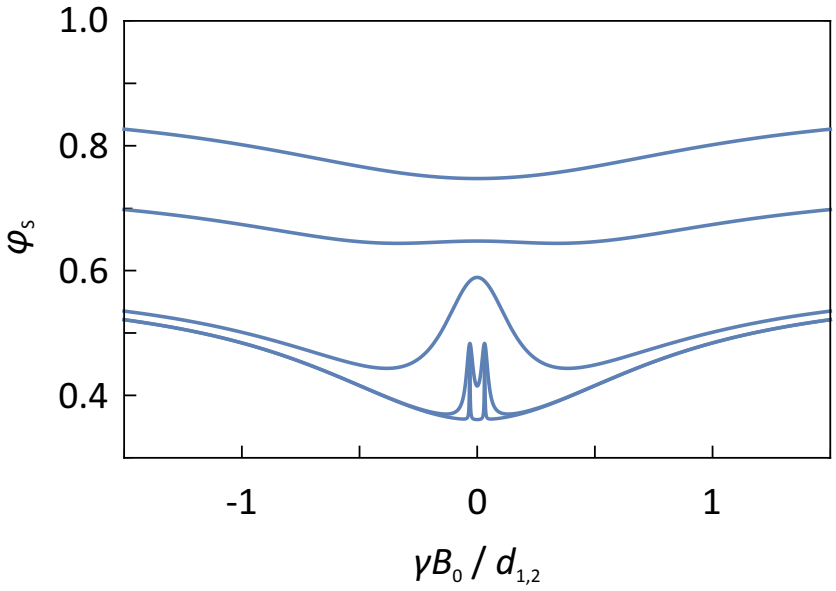

Figure 3.7: Linear spin triad with $J_{1,2} = J_{2,3} = \frac{1}{4}d_{1,2}$ and the field perpendicular to the molecular axis. $k = \{0.001, 0.01, 0.1, 0.5, 1\}\ d_{1,2}$.

orientation of the magnetic field, the Zeeman Hamiltonian does not commute with the dipolar part and pronounced MFEs can be observed, as demonstrated in Fig. 3.1(b). With $B_0||x$, a marked spike is observed for $B_0 \approx 2.1\ d_{1,2}$. This peak is the consequence of the crossing of two energy levels, with different permutation symmetries but the same spin-inversion symmetry, as is schematically illustrated in the correlation diagram in Fig. 3.1(a). $\hat{H}$ is symmetric with respect to the interchange of spins 1 and 3. Consequently, six of the eigenstates are symmetric and two are anti-symmetric with respect to $\hat{P}_{1,3}$. For $B_0||x$, the latter two are proportional to $|\alpha\alpha\beta\rangle \pm |\alpha\beta\beta\rangle - |\beta\alpha\alpha\rangle \mp |\beta\beta\alpha\rangle$. These two states cross one of the states of the symmetric representation at $B_0 \approx 0.3812\ d_{1,2}$ and $B_0 = \frac{17}{8}\ d_{1,2}$. The spike results from the second of these crossings involving the anti-symmetric state with lower signs (labelled (2) in Fig. 3.1(a)); for the first one, the matrix element of $\langle i|\hat{P}_s^{(1,2)}|j\rangle$ vanishes by symmetry. This is so because, for $B_0||x$, $\hat{X} = \otimes_i \hat{\sigma}_{i,x}$, which exchanges α and β states, provides another symmetry element. Since $\left[\hat{X}, \hat{P}_s^{(1,2)}\right] = 0$, only crossings of the same $\hat{X}$-symmetry can alter the MFE. As such, sharp changes in the reaction yield result from the level crossings between states of different symmetry provided that the off-diagonal matrix elements of the singlet projection operator do not vanish.

3.4.1 On the origin of sharp spikes in the MFE of linear spin chains

The spin Hamiltonian of linear spins chains with a transverse magnetic field can be approximately cast into the form of the XXZ model, for which

$$\begin{aligned}\hat{H}_{XXZ} &= \hat{H}_0 + \hat{H}_1 \\ &= \sum_{i=1}^{N}[J_{i,i+1}\hat{S}_{i,x}\hat{S}_{j,x} + J_{i,i+1}\hat{S}_{i,y}\hat{S}_{j,y} + J_{i,i+1}\delta J_{i,i+1}\hat{S}_{i,z}\hat{S}_{j,z}] + \gamma B_0 \sum_{i}^{N}\hat{S}_{i,x}\end{aligned} \tag{3.21}$$

where $J_{i,i+1}$ is a coupling parameter and $\delta J_{i,i+1}$ evaluates the anisotropy of this nearest-neighbour coupling. For $\delta J_{i,i+1} \neq 1$ the SU(2) symmetry of $\hat{R}^x_\pi$ is broken and the model resembles the dipole-dipole coupled spin chain. Then, magnetic field effects are observed if the singlet projection operator does not commute with $\hat{H}_0$.

The sharp peak in reaction yield as a function of magnetic field is a consequence of crossings of eigenstates with different permutation symmetries. The linear spin model exhibits rich symmetries such as reflection symmetries and symmetries under global π rotation around the x axis. The presence of such symmetries may give rise to sharp peaks in the reaction yield for linear spin systems. For example, a linear four spin system described by $\hat{H}_{XXZ}$ has a global π rotation symmetry about the x-axis, i.e $[\hat{H}_{XXZ}, \hat{R}^x_\pi] = 0$, where $\hat{R}^x_\pi = \hat{\sigma}^1_x\hat{\sigma}^2_x\hat{\sigma}^3_x\hat{\sigma}^4_x$. The eigenstate

$$\left|\psi^{(i)}\right\rangle = c^i_1\left|\alpha\alpha\beta\beta\right\rangle + c^i_2\left|\alpha\beta\alpha\beta\right\rangle + c^i_3\left|\alpha\beta\beta\alpha\right\rangle + c^i_4\left|\beta\alpha\alpha\beta\right\rangle + c^i_5\left|\beta\alpha\beta\alpha\right\rangle + c^i_6\left|\beta\beta\alpha\alpha\right\rangle \tag{3.22}$$

has $c^i_1 = c^i_6$, $c^i_2 = c^i_5$, $c^i_3 = c^i_4$, corresponding to an eigenvalue of $\hat{R}^x_\pi$ $E_1 = +1$, or $c^i_1 = -c^i_6$, $c^i_2 = -c^i_5$, $c^i_3 = -c^i_4$, corresponding to an eigenvalue of $\hat{R}^x_\pi$ $E_2 = -1$. Furthermore, one can define a parity operator for linear spin systems as

$$\hat{P} = \hat{P}_{1,N}\hat{P}_{2,N-1}...\hat{P}_{\frac{N}{2},\frac{N+2}{2}} \tag{3.23}$$

for even N, and

$$\hat{P} = \hat{P}_{1,N}\hat{P}_{2,N-1}...\hat{P}_{\frac{N-1}{2},\frac{N+3}{2}} \tag{3.24}$$

for odd N. If $[\hat{H}, \hat{P}] = 0$, then the parity is conserved and the eigenstates of the Hamiltonian can be classified as even or odd. For example, an eigenstate $\left|\psi^{(i)}\right\rangle = c_1^i \left|\alpha\beta\beta\beta\right\rangle + c_2^i \left|\beta\alpha\beta\beta\right\rangle + c_3^i \left|\beta\beta\alpha\beta\right\rangle + c_4^i \left|\beta\beta\beta\alpha\right\rangle$ the even parity gives $c_1^i = c_4^i$, $c_2^i = c_3^i$ and odd parity gives $c_1^i = -c_4^i$, $c_2^i = -c_3^i$. If an eigenstate of a certain symmetry (e.g. with respect to parity or the global x-rotation), $|i\rangle$ undergoes crossing with another eigenstate $|j\rangle$ with different symmetry properties such that $\langle i| \hat{P}_s^{(i,j)} |j\rangle \neq 0$, the sharp spikes occur in the reaction yield. It is indeed interesting that such an interplay of symmetries, level crossings and many-body interactions can lead to pronounced MFEs at fields lower than the geomagnetic field.

For arbitrary magnetic field and orientation, the singlet yield has to be evaluated numerically. For high fields, all but the secular parts of $\hat{H}_{dd}$ can be neglected and a perturbation-theoretical treatment yields an analytic expression of the singlet yield and its orientational dependence as shown above. Its most obvious feature is the cessation of spin evolution for the magic angle.

3.4.2 Blocked singlet-triplet conversion in the high-field limit

In the high-field limit, the quantisation axis of the spins corresponds to the direction of the magnetic field. It is then possible to simplify the Hamiltonian $\hat{H}_0$ to only include the secular terms:

$$\hat{H}'_{dd} = \frac{1}{2} \sum_{i<j} d_{i,j}(r_{i,j})(3\cos\theta_{i,j} - 1) \left(3\hat{S}_{i,z}\hat{S}_{j,z} - \hat{\mathbf{S}}_i \cdot \hat{\mathbf{S}}_j\right) \tag{3.25}$$

where $\theta_{i,j}$ is the angle between the magnetic field and the vector connecting spins i and j. The individual terms vanish for the magic angle $\theta_{i,j} = 54.7°$, which for the linear configuration can be used to simultaneously suppress all dipolar couplings, i.e. $\hat{H}'_{dd} = 0$ and thus the singlet-triplet mixing vanishes (*vide supra*). For general geometries it is not possible to simultaneously fulfil the three magic-angle conditions. Nonetheless, the more broad condition $[\hat{P}_S^{(1,2)}, \hat{H}'_{dd}] = 0$ can be realized for certain field orientations for which consequently $\varphi_S = 1$. Assuming an isosceles triangular arrangement with bond angle α it can be shown that $\hat{H}'_{dd}$ and $\hat{P}_S^{(1,2)}$ commute if the following condition is satisfied:

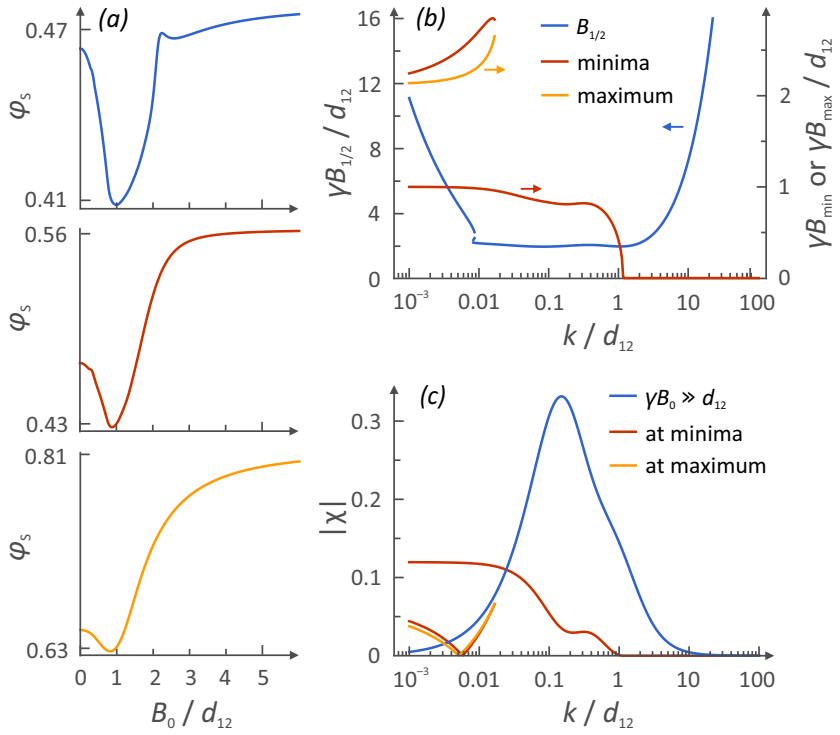

Figure 3.8: (a) Powder averages for $k/d_{1,2} = 6.86 \cdot 10^{-3}$, 0.047 and 0.322, respectively. (b) MFE characterized by half saturation $B_{\frac{1}{2}}$, and the locations of minima (B_{min}) and maxima (B_{max}), as a function of $k/d_{1,2}$. (c) Absolute MFE vs $k/d_{1,2}$. In all of the above figures $J = 0$.

$$\begin{aligned}
&\frac{1}{8}\csc^3\left(\tfrac{\alpha}{2}\right)\left((1+3\cos(2\vartheta))\left(2-6\sin\left(\tfrac{\alpha}{2}\right)+7\sin\left(\tfrac{3\alpha}{2}\right)-3\sin\left(\tfrac{5\alpha}{2}\right)\right)\right)\\
&+\frac{1}{8}\csc^3\left(6\cos(2\phi)\left(10\sin\left(\tfrac{\alpha}{2}\right)-5\sin\left(\tfrac{3\alpha}{2}\right)+\sin\left(\tfrac{5\alpha}{2}\right)-2\right)\sin^2(\vartheta)\right)\\
&\quad+12\cos(\phi)\sin(\alpha)\sin(2\vartheta)=0
\end{aligned} \tag{3.26}$$

Here, the spin-triad has been placed in the x,z-plane ($z \leq 0$) and ϕ and θ are the polar and azimuthal angle specifying the direction of the magnetic field vector. Typically, Eq. 3.26 defines 2 closed contours on the θ, ϕ-sphere. For the linear configuration ($\alpha = \pi$), Eq. 3.26 is tantamount to the vanishing of the three dipolar couplings. For $\alpha < \pi$, the dipolar coupling gives rise to large anisotropies of the MFE, which typically exceed the anisotropies from hyperfine-induced singlet-triplet mixing, because the latter lacks this unique switching property.

3.4.3 Persistence of the effect even within a powder average

For a disordered system, the observed singlet yield represents the average over all possible orientations of the external magnetic field vector B_0, with respect to the molecular axes of the system. Fig. 3.8(a) shows this powder average of the singlet yield for the linear, symmetric spin triad over a range of k-values. Interestingly, the recombination yield does not average to zero even though the average dipolar interaction of a pair of spins vanishes. The field-dependence is characterized by a minimum at $B_0 \approx d_{1,2}$, which is the dominant feature at small k. The field-effect can be characterised by established measures such as the field of half-saturation $B_{\frac{1}{2}}$ (the field for which $\langle\varphi_s(B_0)\rangle$ equals $\frac{1}{2}(\langle\varphi_s(B=0)\rangle + \langle\varphi_s(B\to\infty)\rangle)$ and the MFEs associated with characteristic points such as the low-field minimum, which resembles the LFE documented for the hyperfine mechanism in radical pairs (Timmel et al., 1998). These parameters are summarized in Figs. 3.8(b) and (c) as a function of k. For B_0 exceeding a few $d_{1,2}$, huge field effects χ in excess of 30 %, can be realized for intermediate k of the order of 0.2 $d_{1,2}$ (Fig. 3.8(c)). The magnitude of the low-field feature is approximately 12 % for small k-values. For context, at a distance of 17 Å, $d_{1,2}$ will be of the order of 10 MHz and $k = 0.01\ d_{1,2}$ would then correspond to a lifetime of $k^{-1} = 1.6\ \mu$s. Under these conditions, the low-field effect in dipolarly-coupled spin triads is expected to closely match what the hyperfine mechanism gives for radical pairs (*vide infra* for a substantial enhancement). Significant MFEs can also ensue for comparably short coherence times and, thus, quickly-relaxing radicals could be meaningfully considered in the triad model for small r.

Substantial MFEs can in fact be observed for a variety of geometries of the spin triad, a concept that is explored further in Chapter 5. Fig. 3.9 shows the dependence of the powder-averaged MFE and the relative anisotropy, i.e. the largest orientational spread of the singlet yield, relatively to the mean singlet yield, of general configurations for a magnetic field intensity of 50 μT (roughly the geomagnetic field). Assuming that spins 1 and 2 are located at $(0, a)$ and $(0, -a)$, respectively, with $a = 10$ Å, the maximum averaged MFE is ≈ 9 % at the location of the third spin $(\pm 1.58\ a,\ \pm a)$. The maximum anisotropy amounts to 21.5 % at $(\pm 3.18\ a,\ \pm 1.35\ a)$,

which corresponds to inter-radical distances as large as 40 Å. Thus sizeable MFEs are induced by the dipolar interaction even at relatively large distances, demonstrating that the effect is not predicated upon infrequent direct three-particle encounters, and suggesting that it may be practically applicable (Kattnig, 2017b).

The bond angle dependence for randomly oriented isosceles spin-triads is further discussed. For the geomagnetic field we observe the largest field effect for bond angles roughly corresponding to a pentagon's internal angle (144°) or slightly less than an equilateral triangle's (60°). For greater field intensities, large effects can be realized for all bond angles of practical relevance.

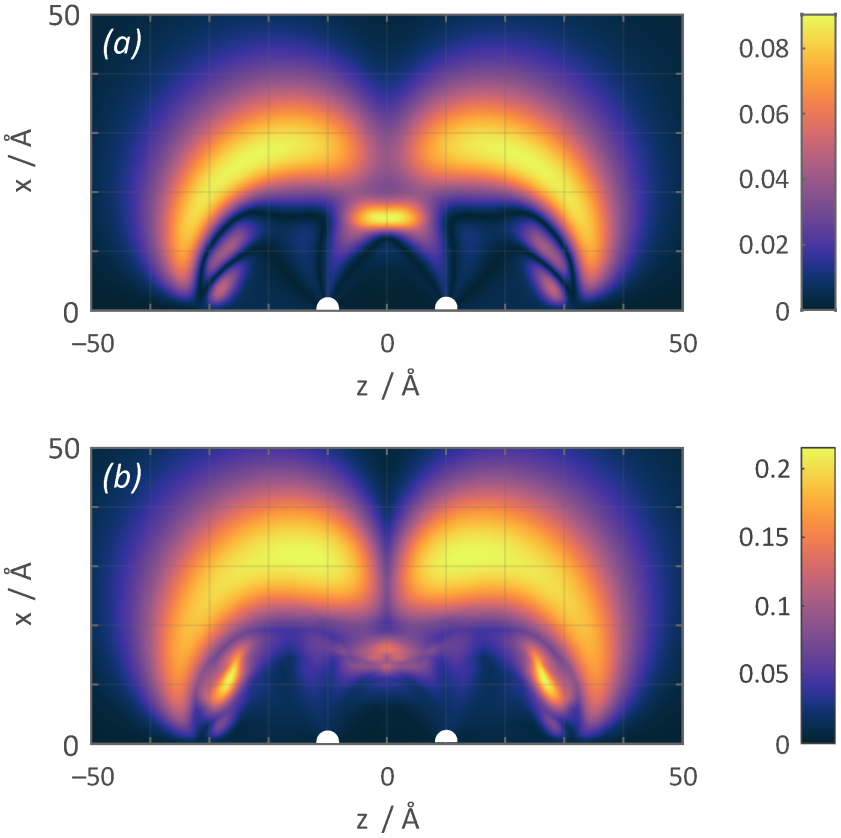

Figure 3.9: (a) Absolute value of the MFE. (b) Anisotropy relative to the mean singlet yield. Here $k = 0.0245\ d_{1,2}$ and $B_0 = 0.215\ d_{1,2}$ corresponding to a lifetime of 1 μs and the geomagnetic field (50 μT) for an inter-radical distance of 20 Å, and $J = 0$. Spins 1 and 2 are located at $(0, a)$ and $(0, -a)$, respectively with $a = 10$ Å, and the position of spin 3 is varied in the containing plane.

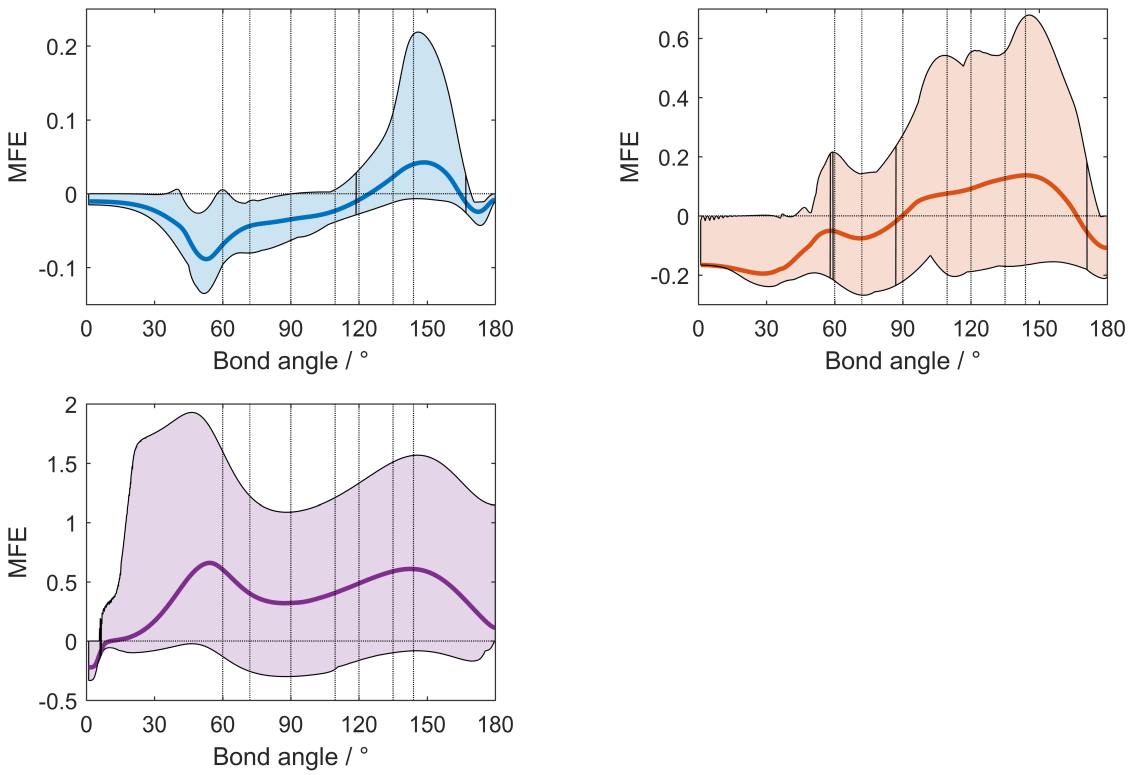

Figure 3.10: Bond angle dependence of the MFE for isosceles triangular spin triads with an adjacent radical distance of 20 Å and spin 2 at the centre for the Earth's magnetic field ($B_0 = 50\ \mu T$; top-left), $\gamma B_0 = d_{1,2}$ (right) and $\gamma B_0 = 1000\ d_{1,2}$ (bottom). The plots show the orientationally averaged of the MFE for an ensemble of randomly oriented spin triads and the orientational spread of the MFE. The latter is a measure of the directional anisotropy of the effect at the given field intensity. A lifetime of $k^{-1} = 1\ \mu s$ was assumed throughout.

3.5 D3M magnetic field effects in more general geometries

Fig. 3.10 illustrates the bond angle dependence of the MFE for isosceles triangular spin triads. Fig. 3.11 and Fig. 3.12 show the absolute value and anisotropy of the singlet yield, at fields of $B_0 = 50\ \mu$T and $B_0 = d_{1,2}$ respectively, for more general triad geometries together with the absolute value of the average MFE and its maximal absolute MFE value in a particular instance.

Unlike for the linear geometry, it is found that the MFEs of these systems typically do not decrease with increasing k^{-1}. For the isosceles triangular geometry, sizeable MFEs for k as large as 10 $d_{1,2}$ are predicted.

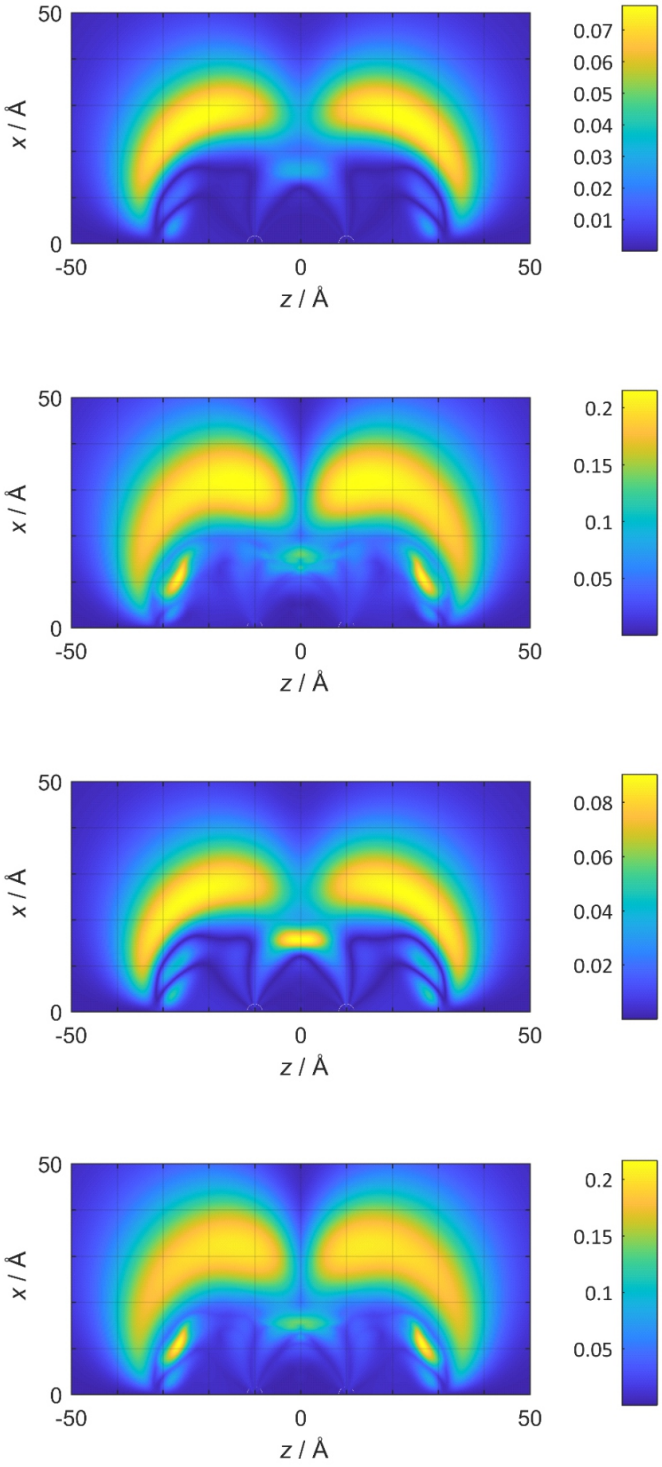

Figure 3.11: Three spins, various configurations. One spin is at $(0, -10)$ Å, one at $(0, 10)$ Å; the location of the third spin is varied in the (x,z)-plane; $B_0 = 50\ \mu T$, $k^{-1} = 1\ \mu s$. Top: Absolute value of the change in the orientationally averaged singlet yield, anisotropy of the singlet yield (i.e. the maximal absolute change divided by the mean effect), absolute value of the average MFE, and the maximal absolute value of the MFE realized for a particular orientation.

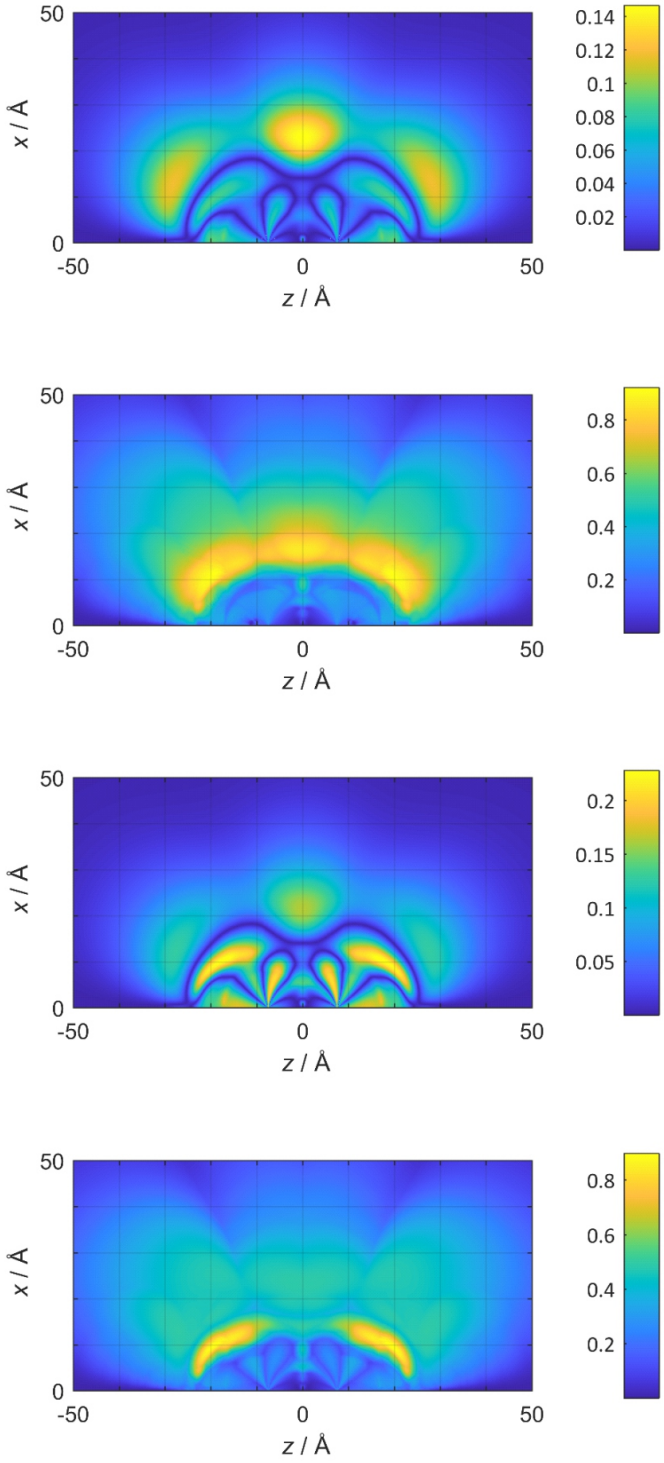

Figure 3.12: Three spins, various configurations. One spin is at $(0, -7.5)$ Å, one at $(0, 7.5)$ Å; the location of the third spin is varied in the (x,z)-plane; $B_0 = d_{1,2}$, $k^{-1} = 1\ \mu s$. Top: Absolute value of the change in the orientationally averaged singlet yield, anisotropy of the singlet yield (i.e. the maximal absolute change divided by the mean effect), absolute value of the average MFE, and the maximal absolute value of the MFE realized for a particular orientation.

3.5.1 MFEs in the equilateral triangular geometry

The MFEs in an equilateral triangular geometry are further investigated, choosing the position vectors of the spins as $\vec{\mathbf{r}}_1 = r(\frac{1}{2}, 0, 0)$, $\vec{\mathbf{r}}_2 = r(-\frac{1}{2}, 0, 0)$ and $\vec{\mathbf{r}}_3 = r((0, \sin(60°)), 0, 0)$. The corresponding dipolar tensors are of the form

$$D_{1,2} = \begin{pmatrix} -2 & 0 & 0 \\ 0 & 1 & 0 \\ 0 & 0 & 1 \end{pmatrix} d_{1,2} \tag{3.27}$$

$$D_{2,3} = \begin{pmatrix} \frac{1/4}{} & \frac{-3\sqrt{3}}{4} & 0 \\ \frac{-3\sqrt{3}}{4} & -\frac{5}{4} & 0 \\ 0 & 0 & 1 \end{pmatrix} d_{1,2} \tag{3.28}$$

$$D_{1,3} = \begin{pmatrix} \frac{1/4}{} & \frac{3\sqrt{3}}{4} & 0 \\ \frac{3\sqrt{3}}{4} & -\frac{5}{4} & 0 \\ 0 & 0 & 1 \end{pmatrix} d_{1,2} \tag{3.29}$$

For $B_0 = 0$, the singlet yield can be evaluated analytically. One obtains:

$$\begin{aligned} \varphi_S = \frac{5}{13} + \frac{3}{26} L\left(\frac{3\sqrt{13}}{4} d_{1,2}, k\right) + \frac{13+\sqrt{13}}{52} L\left(\frac{3}{8}\left(\sqrt{13}-1\right) d_{1,2}, k\right) \\ + \frac{13-\sqrt{13}}{52} L\left(\frac{3}{8}\left(\sqrt{13}+1\right) d_{1,2}, k\right) \end{aligned} \tag{3.30}$$

In addition, for the field along the z-direction, the following expression for the singlet yield can be derived

$$\begin{aligned} \varphi_S = \frac{1}{4}\left(4 - \frac{27}{117 + 16r^2 + 16b\,(4b-3)} - \frac{27}{117 + 16r^2 + 16b\,(4b+3)}\right) \\ -\frac{1}{4}\left(\frac{27\,(16r^2+27)}{729 + 16r^2\,(63 + 16r^2 + 16b\,(4b-3))} - \frac{27\,(16r^2+27)}{729 + 16r^2\,(63 + 16r^2 + 16b\,(4b+3))}\right). \end{aligned} \tag{3.31}$$

Here, $b = \frac{\gamma B_0}{d_{1,2}}$ and $r = \frac{k}{d_{1,2}}$. Note that φ_S approaches 1 as $B_0 \to \infty$.

These observations indicate that geometry indeed plays an important role (the precursor to the idea presented in chapter 5), and that the MFEs in certain

geometries may be less susceptible to variations in the lifetime. The system typically shows avoided crossings of energy levels, which nonetheless can give rise to spiky features (Hiscock et al., 2016; Sosnovsky et al., 2016).

3.5.2 Effects of the exchange interaction

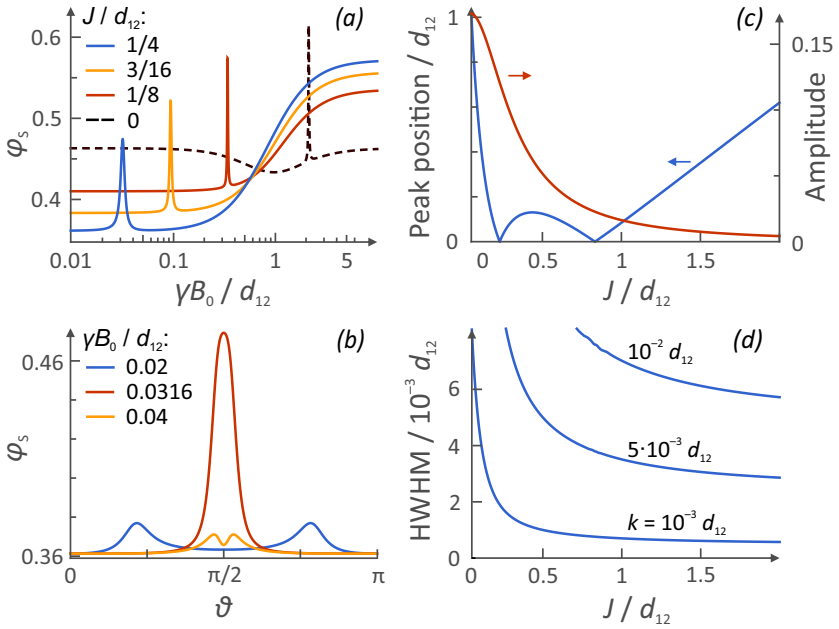

Figure 3.13: (a) Yield vs applied field for different exchange interaction strengths, $J/d_{1,2}$; here, $k/d_{1,2} = 0.001$ and $B_0||x$. (b) Yield as a function of orientation for different B_0; here $k/d_{1,2} = 0.001$. (c) The location and amplitude of a low-field peak's maximum, as a function of the exchange interaction strength with $k/d_{1,2} = 0.001$ and 0.01 (indistinguishable). (d) The half-width at half-maximum of a low-field peak as a function of $J/d_{1,2}$, for k as indicated in the figure.

Further, the effect of an additional exchange interaction on the MFEs is studied. As $\hat{H}_{ex}$ displays time-reversal symmetry, the eigenstates of the Hamiltonian are still double degenerate for $B_0 = 0$. Yet, remarkable effects at low field can emerge if the (anti-)crossings of energy levels are shifted to lower magnetic field intensities. An illustrative example of this phenomenon is provided by the linear spin-triad for $J = J_{1,2} = J_{2,3}$ and $J_{1,3} = 0$, i.e. for the symmetric coupling of adjacent spins, and with the magnetic field perpendicular to the triad axis. As shown in Fig. 3.13(a), the singlet yield of this system exhibits a sharp peak, which shifts to lower magnetic field intensities for exchange couplings approaching 0.25 $d_{1,2}$. Fig. 3.13(c) then shows how the amplitude and field-location of the peak vary as a function of the exchange coupling. For typical dipolar coupling strengths, this feature may occur at field values

smaller than the geomagnetic field. Formally, for these regions of maximal low-field sensitivity, the peak shifts from positive to negative magnetic field intensities. As shown in Figs. 3.13(c) and (d), the peak decreases in amplitude with increasing J and broadens as the recombination rate constant increases. It remains prominent for k up to 0.02 $d_{1,2}$ which, for typical parameters, equates to lifetimes of the order of microseconds (but could be less for smaller inter-radical distances). The figures below summarise the dependence of these characteristic parameters of the MFE as a function of k.

Figs. 3.14 to 3.16 show the powder averages of the singlet yield for dipolarly-coupled triads in the linear, equilateral triangular and isosceles geometries, respectively. They also depict, for each case, the field of half-saturation, locations of low-field minima and maxima, and absolute MFE values all as a function of the recombination rate constant k.

Importantly, the spike does appear in powder averages, suggesting that it could be relevant to MFEs in the randomly oriented samples implicated in biological radical reactions. Fig. 3.13(b) shows how a large directional anisotropy can occur in the low-field regime. Here, J has been fixed to $\frac{1}{4}$ $d_{1,2}$ and one can see that the spike results from an applied field $B_0 = 0.0316$ $d_{1,2}$, while comparatively little directional anisotropy can be seen for other low-field intensities. For negative J, and $J > 2$ $d_{1,2}$, the line shape does not exhibit a pronounced maximum; the main feature is a minimum at higher field.

It has been shown that remarkable MFEs can emerge in radical triads due to the dipolar interaction. This realization extends the current understanding of the magnetosensitivity of chemical reactions by providing an additional mechanistic pathway. Unlike the well-established RPM, this three-radical effect does not rely on hyperfine interactions or differing g-factors. Due to the slow decay of the dipolar interaction with distance, aspects of this mechanism could be unexpectedly relevant, e.g. in the context of magnetoreception, the adverse health effects putatively associated with electromagnetic field exposure, or for purposefully engineered sensing applications, coherent control, quantum information processing with spins in the solid state and

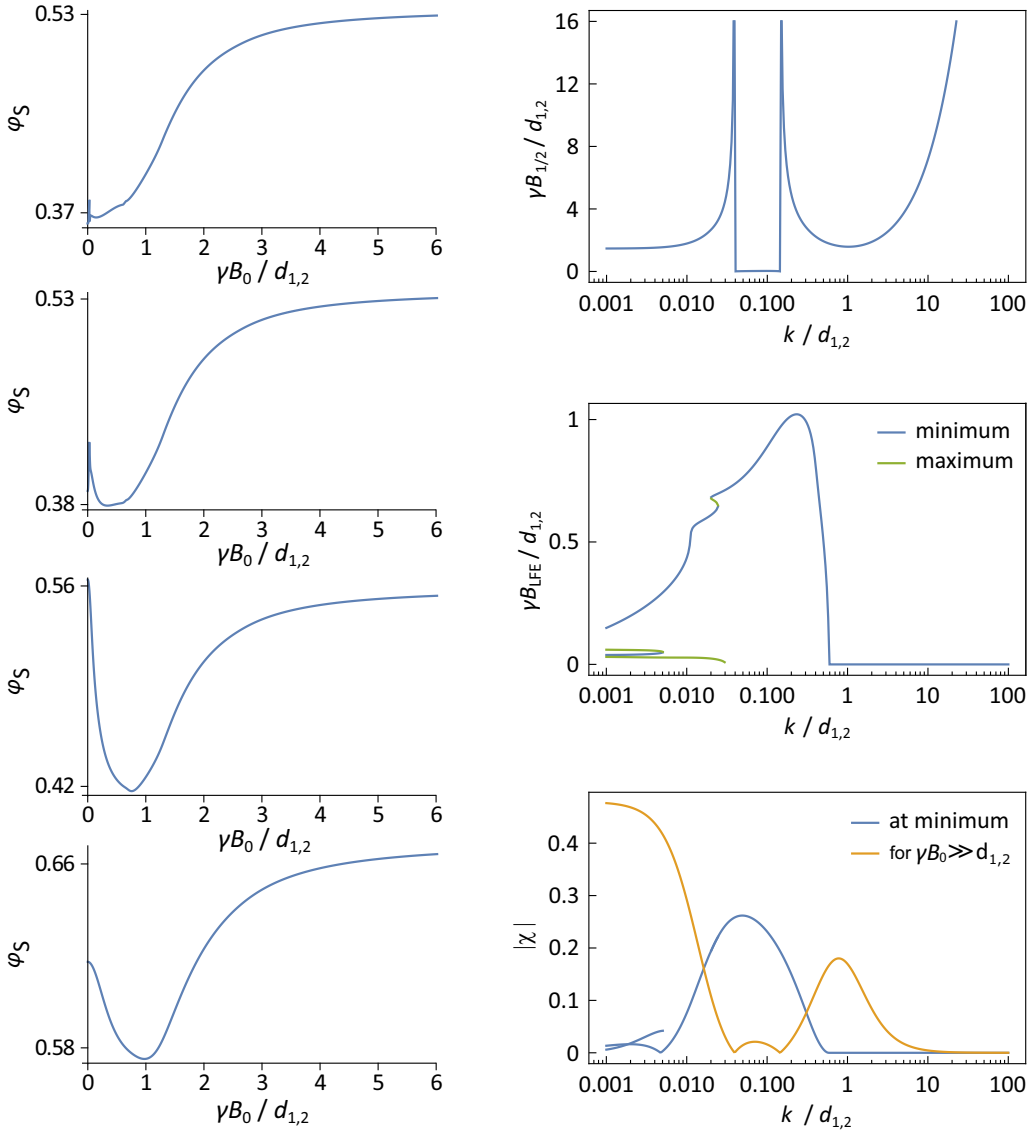

Figure 3.14: Powder averages of the singlet yield for a linear spin-triad, with all spins subject to electron-electron dipolar coupling and adjacent spins additionally subjected to exchange coupling: $J = J_{1,2} = J_{2,3} = 0.25\ d_{1,2}$. Left: Dependence of the singlet yield on the magnetic field intensity for different recombination rate constants $k = [0.001\ \text{(top)}, 0.00686, 0.0470, 0.322\ \text{(bottom)}]\ d_{1,2}$. Right: Field of half-saturation (top), location of (low-field) minima and maxima of the field-dependence of the singlet yield (centre) and absolute values of MFEs for a saturating magnetic field and at the characteristic minima (bottom), all represented as a function of the recombination rate constant k.

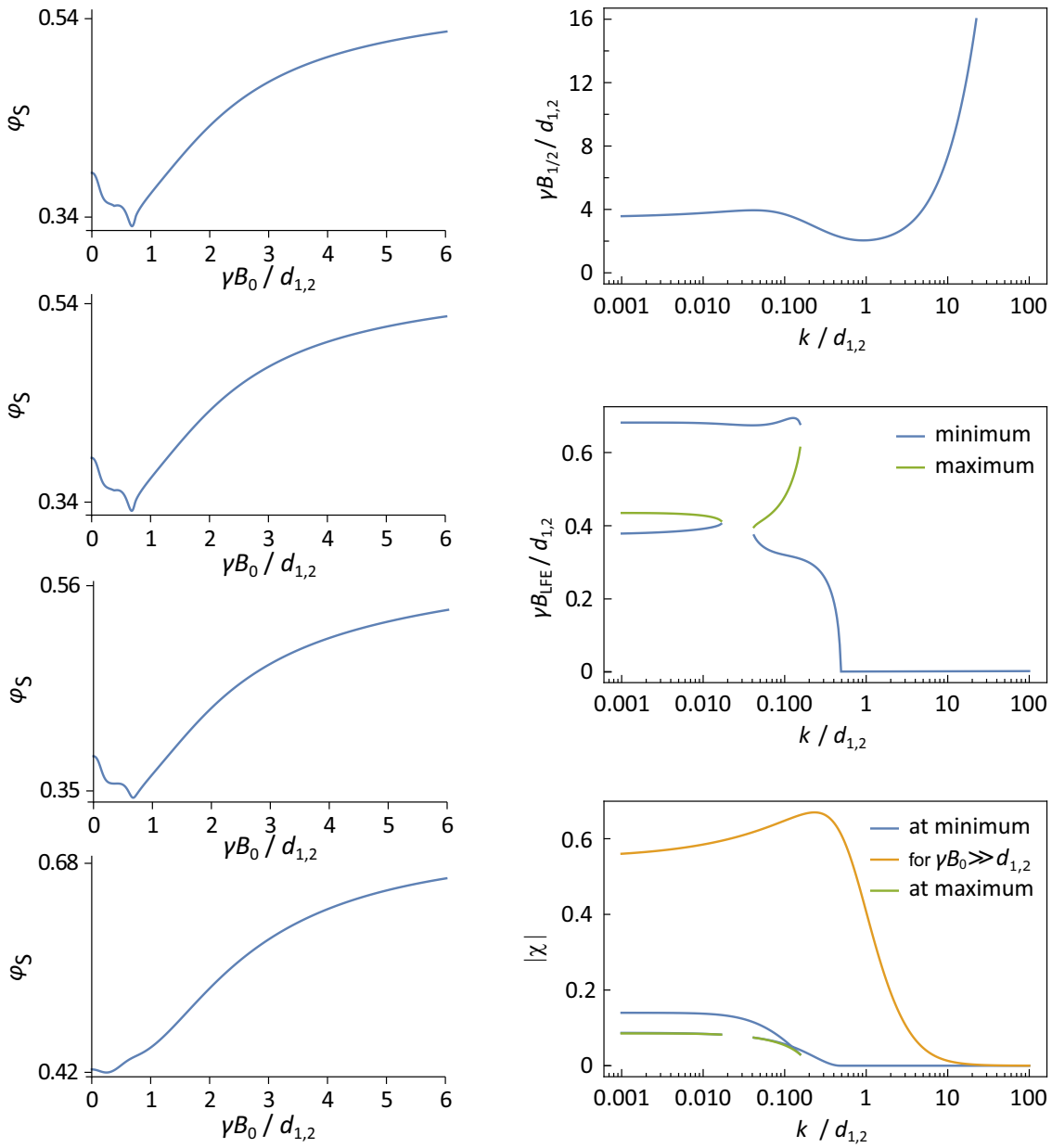

Figure 3.15: Powder averages of the singlet yield for a dipolarly coupled spin-triad in an equilateral triangular configuration. Left: Dependence of the singlet yield on the magnetic field intensity for different recombination rate constants $k = [0.001 \text{ (top)}, 0.00686, 0.0470, 0.322 \text{ (bottom)}]\ d_{1,2}$. Right: Field of half-saturation (top), location of (low-field) minima and maxima of the field-dependence of the singlet yield (centre), and absolute value of the MFEs for a saturating magnetic field and at the characteristic minima and maxima (bottom), all represented as a function of the recombination rate constant k.

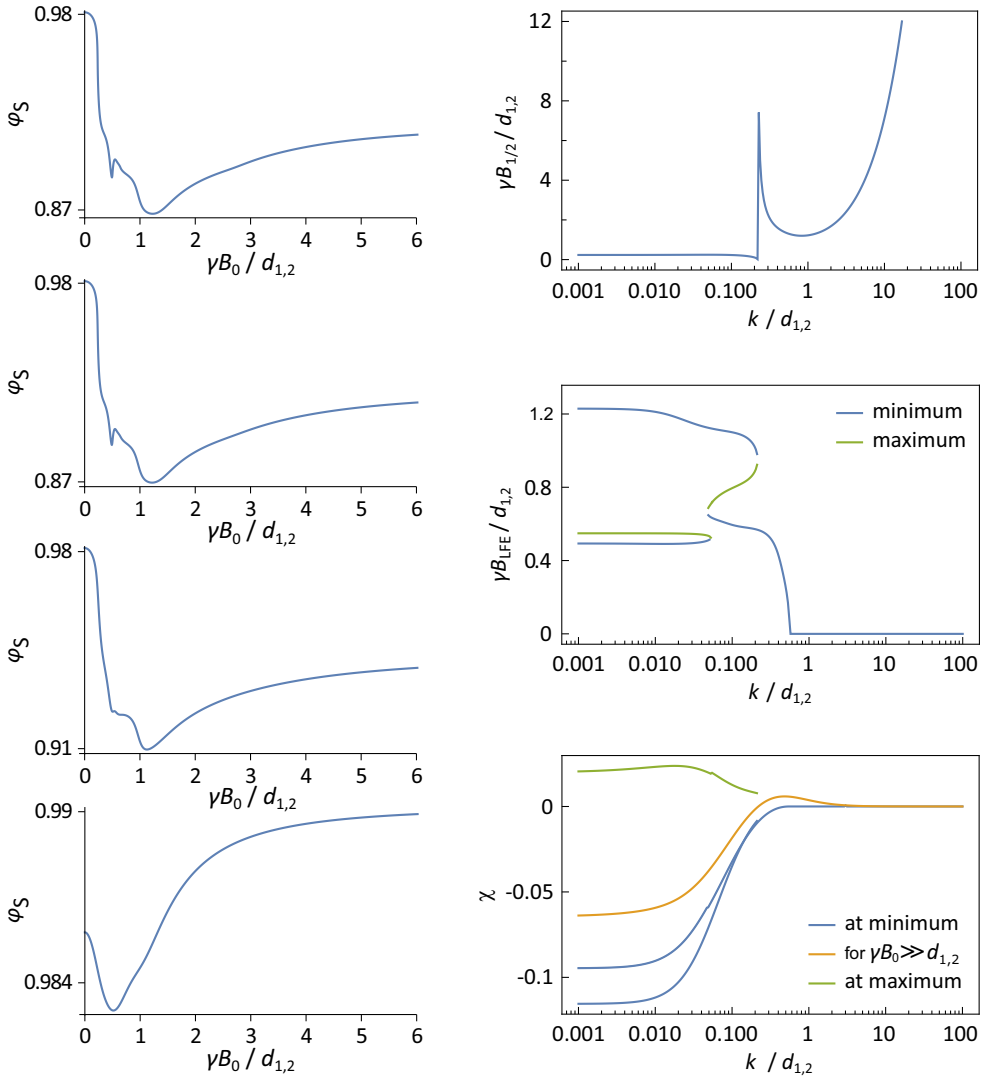

Figure 3.16: Powder averages of the singlet yield for a dipolarly coupled spin-triad in an isosceles triangular configuration, with the third radical at a distance of 2 $r_{1,2}$ from radicals 1 and 2. Left: Dependence of the singlet yield on the magnetic field intensity for different recombination rate constants $k = [0.001$ (top)$, 0.00686, 0.0470, 0.322$ (bottom)$]$ $d_{1,2}$. Right: Field of half-saturation (top), location of (low-field) minima and maxima of the field-dependence of the singlet yield (centre), and absolute value of the MFEs for a saturating magnetic field and at the characteristic minima and maxima (bottom), all represented as a function of the recombination rate constant k.

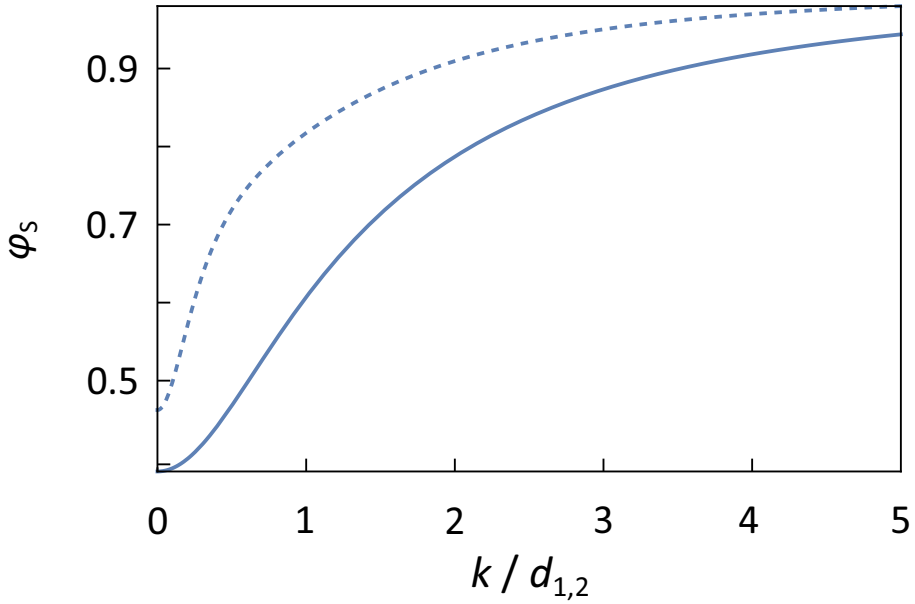

Figure 3.17: Singlet yield for $B_0 = 0$ for an equilateral triangular geometry (solid line) and the linear spin triad (dashed line) as a function of the recombination rate constant k.

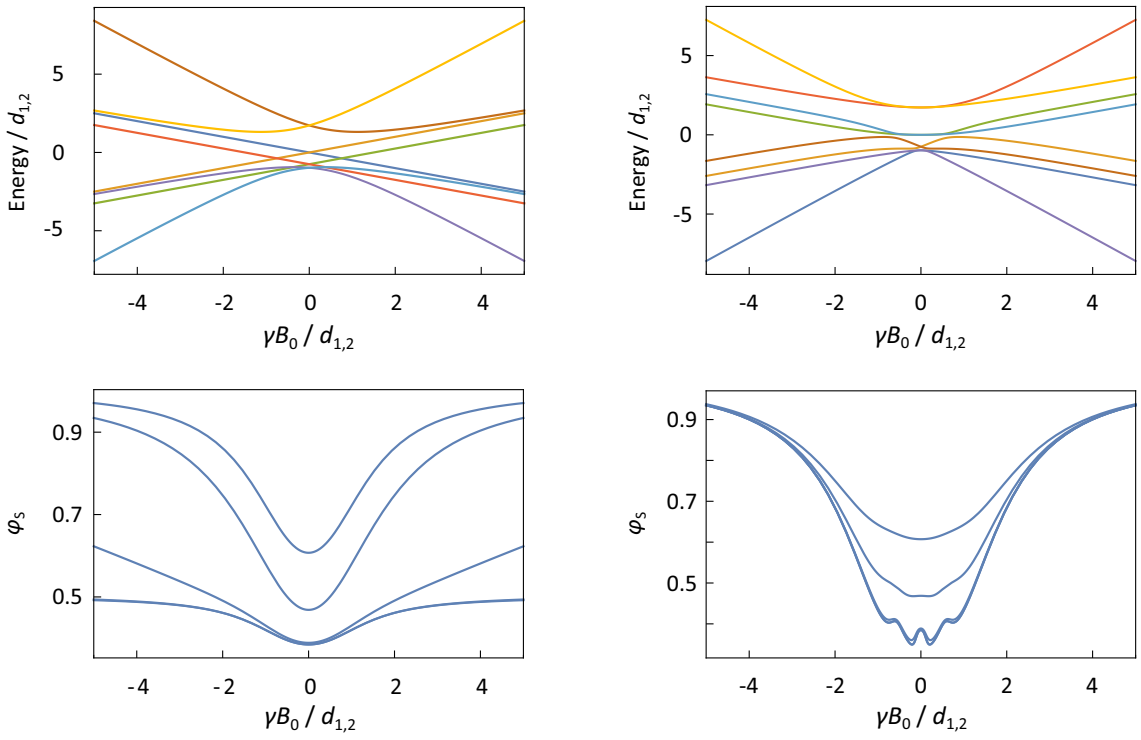

Figure 3.18: Energies of the eigenstates (top) and singlet yields (bottom) as a function of the magnetic field for a spin triad with an equilateral triangular geometry and the field oriented perpendicular to the ring plane (z-axis; left) or along the x- or y-axis (right). The singlet yields are plotted for $k = \{0.001, 0.01, 0.1, 0.5, 1\}\ d_{1,2}$, with the lowest k corresponding to the bottommost curve; the curves for $k = 0.001\ d_{1,2}$ and $k = 0.01\ d_{1,2}$ practically coincide.

potentially spintronics

The main results of this chapter are:

- Adding a third radical means the hyperfine interaction is no longer categorically required to see MFEs.

- The dipolar interaction can provide rich new features on its own, which can be further tuned by the exchange interaction.

- The results are quite different in different geometries.

These results may be tested experimentally using EPR spectroscopy (Orton, 1969; Drago, 1992). For example, one may be able to test for the presence of some of the new features presented in the figures in this chapter, which do not appear in standard RPM measurements from the cited literature, by cross-referencing where these features are forecast to appear with level crossing diagrams such as shown in the appendix (Fig. 9.10. As EPR spectroscopy is able to detect magnetic splittings, the spectrum obtained should show new peaks corresponding to the features introduced into these diagrams by the D3M mechanism that would not be present under the classical RPM. The tuning of the exchange interaction could also be tested in this way, by observing shifts in these new features corresponding to changes in the strength of the exchange.

4. Lipid Peroxidation

There is a vast amount of literature in existence surrounding the subject of lipid peroxidation reactions, their potential for deleterious influence on biological systems, and the possibility of their being influenced by external magnetic fields - including weak fields like that of the Earth. However, there also exists a fair amount of controversy in the literature, as not all publications are created equal. It is this controversy that will be addressed in this preliminary section, such that a critical eye may be cast.

First, reviews shall be addressed. A review paper ought to critically appraise the current state of knowledge regarding a given topic, however it is apparent that in some cases the authors have not in fact read the papers they purport to review, or, if they have, they are not being as critical in their appraisal as they claim. Ref (Ghodbane et al., 2013b), is one such example. The authors claim that they provide a critical review of the literature, yet they appear to report simply the abstracts of other papers. In one particular case, they fail to highlight some obvious deficiencies in a paper they are appraising, such as huge error bars and small sample sizes, and instead simply present their results at face value. When compared with reviews like those of (Valko et al., 2007; Kohen and Nyska, 2002), which highlight not only important results but also the experimental methodologies used, limitations therein, and ways in which future researchers should be careful to avoid falling into some of the common pitfalls of the delicate experiments they discuss, the schism between levels of quality becomes quite apparent.

The presence of reviews which fail to highlight limitations in experimental methodology and results is likely a significant factor in why the controversy surrounding lipid peroxidation still exists. One particular controversy surrounds effects

involving thiobarbituric reactive species (TBARS), which has arisen due to variable experimental quality in performing a related assay. TBARS are chemical species (usually aldehydes) that are produced in the final stage of a lipid peroxidation reaction, and are commonly used to assay for the presence of peroxidation (Kohen and Nyska, 2002). Ref. (Kabuto et al., 2001) claims to use precisely this assay, and observe that an external magnetic field has no statistically significant effect on iron-induced lipid peroxidation reactions, aside from within a small window of effectiveness between 2mT and 4mT. Contrasted with the well-written, well-documented (i.e. reproducible) study in Ref. (Lalo, Pankratov and Mykhaylyk, 1994) which claims to show that an external field in the millitesla regime can in fact accelerate lipid peroxidation reactions, one may quickly run into confusion. However, the former result should be considered dubious due to their small sample sizes used in their experiments, and also the staggeringly large error bars on graphs which claim to show a very slight decrease or no overall trend. It is such deficiencies that Ref. (Ghodbane et al., 2013b) failed to highlight, and may have inadvertently mislead other researchers.

Another more general area within which controversial results arise is in those papers which provide little, or no, detail about their methodology. This is a problem because it does not allow other experimentalists to reproduce, nor verify, the claimed results and as such conflicting *facts* can arise. (Pliss et al., 2017), for instance, presents a potentially interesting result, in that it claims to directly evidence two magnetosensitive steps in an oxidative chain reaction, but gives no real indication how the experiment could be replicated. This is a problem for both theoreticians and other experimentalists, as experimental results which verify a particular theory can entirely change the direction of a field of research if widely accepted. Avoiding such an outcome is why it is critical that experiments are reproducible, and that authors follow the example of, for example, (Lalo, Pankratov and Mykhaylyk, 1994; Kohen and Nyska, 2002; Valko et al., 2007) in critically appraising and appropriately documenting the protocols used.

The work comprising the remainder of this chapter is adapted from:

Sampson, C., Keens, R.H. and Kattnig, D.R., 2019. On the magnetosensitiv-

ity of lipid peroxidation: Two-versus three-radical dynamics. Physical Chemistry Chemical Physics, 21(25), pp.13526-13538, with permission from PCCP.

This chapter discusses lipid peroxidation reactions, and shows that the radical dynamics therein are indeed magnetosensitive. The standard Radical Pair Mechanism (RPM), and the newer D3M mechanism, are compared in the simulation of such reaction schemes and it is found that while the RPM can produce MFEs in peroxyl radical recombination, contrary to prior claims in the literature, D3M can give rise to larger effects. One crucial piece of information that the RPM has not been conclusively shown to elucidate is that the magnetosensitivity of lipid peroxidation is concentration-dependent - this fact is only apparent once one considers the dipolar interaction within the Hamiltonian. Further, it is shown that the inclusion of the hyperfine interaction within the D3M model (noting that in Chapter 3 the model was defined in the absence of hyperfine terms) does not lead to the abolition of effects predicted by D3M. In fact, this generalization shows that the D3M effects can be significant despite non-zero hyperfine interactions, i.e. in domains traditionally attributed to the RPM. A final interesting conclusion is that the dipolar contribution of the D3M model can actually to some degree immunize the MFEs predicted for lipid peroxidation reactions to the influence of a strong exchange interaction as expected to be present during, for example, the bond-forming recombination of lipid peroxyl radicals.

4.1 Modelling Lipid Peroxidation with D3M

The aim of this section is the assessment of the RPM and the D3M with respect to plausibility and relative importance. In particular, a toy model is provided, which aims to give a first understanding, while (necessarily) neglecting many of the intricacies of true reactive radical encounters in membranes. Attention is, in particular, given to the recombination of lipid peroxyl radicals (reaction V), because estimates based on established rate constants identify $RO_2^\bullet$ as the most abundant and long-lived (half-life of around 17s) radical species (Kohen and Nyska, 2002). Fig. 1.4B gives a schematic of the considered recombination process. The radicals

are assumed to encounter as F-pairs, i.e. with a random initial spin configuration. Recombination in the singlet state can allow the formation of diamagnetic products via an unstable tetroxide intermediate (Russell mechanism, reaction V in Fig. 1.4A) (Russell, 1957). The radicals can undergo singlet-triplet inter-conversion due to non-zero hyperfine interactions with magnetic nuclei (RPM) or the catalytic effect of a third radical interacting with the primary radical pair through the electron-electron dipolar interaction (D3M). If the inter-radical distance is small, this process will be influenced by the exchange interaction (Adrian, 1979; Keens, Bedkihal and Kattnig, 2018). These coherent processes potentially afford a magnetic field sensitivity to the recombination yield.

Due to the spin density of the peroxyl radicals being centred on the terminal oxygen, for which all magnetic isotopes have insignificant natural abundance (again, for ^{17}O I = 5/2 the natural abundance is only 0.037%), the RPM has been deemed insufficient for the process shown in Fig. 1.4B. Consquently, previous studies in this area have associated magnetosensitivity with reactions that do not involve the abundant peroxyl radicals (Kipriyanov Jr., Doktorov and Purtov, 2015; Pliss et al., 2017).

In more detail, the model is based on the following observations. Peroxyl radicals are considered as rigid cylindrical bodies. Based on the known membrane area per lipid of 0.7 nm^2 for 1-palmitoyl-2-oleoyl-sn-glycero-3-phospholipids (Hills Jr. and McGlinchey, 2016) and a presumed hexagonal densest packing of the cylindrical lipids in the membrane (packing density of circles on a hexagonal lattice: $\pi\sqrt{3}/6$), an effective lipid radius of $R = 4.5$ Å has been estimated. Assuming furthermore that the hydrophobic peroxyl groups aggregate at the membrane interior, the difference in vertical position of the radical functionalities across the membrane can be neglected. This yields an essentially two-dimensional model of circular "peroxyl radicals" on the membrane plane.

A simple Hamiltonian is employed to calculate the singlet yield based on multiple parameters, such as the hyperfine, dipolar, exchange and Zeeman interactions. This Hamiltonian takes the form:

$$\hat{H} = \hat{H}_{hfi} + \hat{H}_{ze} + \hat{H}_{dp} + \hat{H}_{ex}, \tag{4.1}$$

where $\hat{H}_{hfi}$ represents the hyperfine interaction, $\hat{H}_{ze}$ represents the Zeeman terms, $\hat{H}_{dp}$ represents the electron-electron dipolar interaction between radicals and finally $\hat{H}_{ex}$ is the Hamiltonian representing the exchange interaction. The interaction of the magnetic field with the nuclei is not included, as it is negligible relatively to any of the considered interactions. The functional form for the hyperfine interaction is:

$$\hat{H}_{hfi} = \sum_{i=1}^{N} \sum_{j}^{n_i} a_{ij} \hat{\mathbf{I}}_{ij} \cdot \hat{\mathbf{S}}_i, \tag{4.2}$$

where i labels a radical, $\hat{\mathbf{S}}_i$ is the spin vector operator for electron i, N is the total number of radicals in the system, n_i is the number of coupled nuclei in radical i and $\hat{\mathbf{I}}_{ij}$ is the nuclear spin vector operator of nucleus j in radical i. a_{ij} is the related hyperfine coupling constant (assumed isotropic). The Zeeman Hamiltonian describes the interaction of the electron spins with the magnetic field and has the following form (in angular frequency units):

$$\hat{H}_{zee} = \boldsymbol{\omega} \cdot \sum_{i=1}^{N} \hat{\mathbf{S}}_i, \tag{4.3}$$

where $\boldsymbol{\omega}$ is equal to $\frac{g\mu_B}{\hbar}\mathbf{B}_0$ with $\mathbf{B}_0$ denoting the applied magnetic field. Here, we have assumed identical radicals, each of which is associated with the same g-factor of $g \approx 2$. μ_B is the Bohr magneton and $\hbar$ is the reduced Planck's constant.

The dipolar interaction between electrons is calculated by the point-dipolar approximation:

$$\hat{H}_{dp} = \sum_{i<j}^{N} \hat{\mathbf{S}}_i \cdot \mathbf{D}_{ij} \cdot \hat{\mathbf{S}}_j \tag{4.4}$$

$$= d(|\mathbf{r}_{ij}|) \left[\hat{\mathbf{S}}_i \cdot \hat{\mathbf{S}}_j - 3 \left(\hat{\mathbf{S}}_i \cdot \mathbf{n}_{ij} \right) \left(\hat{\mathbf{S}}_j \cdot \mathbf{n}_{ij} \right) \right], \tag{4.5}$$

where,

$$d(r) = \frac{\mu_0 g^2 \mu_B^2}{4\pi\hbar r^3}, \tag{4.6}$$

$\mathbf{r}_{ij}$ is the vector connecting radicals i and j and $\mathbf{n}_{ij}$ is the unit vector parallel to $\mathbf{r}_{ij}$.

Finally, the exchange Hamiltonian used is as follows:

$$\hat{H}_{ex} = -\sum_{i<j}^{N} J(|\mathbf{r}_{ij}|)\left(\frac{1}{2} + 2\hat{\mathbf{S}}_i \cdot \hat{\mathbf{S}}_j\right), \tag{4.7}$$

where i and j label radicals, and $J(|\mathbf{r}_{ij}|)$ is the exchange coupling constant between the i^{th} and j^{th} radicals.

For the work presented here, it has been assumed that the system is generated in a random encounter, i.e. $\hat{\rho}(0) \propto \mathbb{1}$. To calculate the recombination yields, a process similar to that laid out in reference (Sosnovsky et al., 2016) has been followed, i.e. by solving the stochastic Liouville equation of the form:

$$\frac{d\hat{\rho}(t)}{dt} = -i[\hat{H}, \hat{\rho}(t)] - [\hat{K}, \hat{\rho}(t)]_+ - k_e\hat{\rho}(t), \tag{4.8}$$

where the spin-selective recombination is treated using the Haberkorn approach (Haberkorn, 1976; Fay, Lindoy and Manolopoulos, 2018). k_e is the escape rate constant, which accounts for the diffusive separation of the N-radical system into the bulk, scavenging and decay processes and all non-recombination processes in an effective manner; $[\cdot,\cdot]_+$ indicates the anti-commutator and $\hat{K}$ is given by

$$\hat{K} = \sum_{i,j} \frac{k_P(|\mathbf{r}_{ij}|)}{2} \hat{P}_{ij}^{(S)}, \tag{4.9}$$

where $k_P(|\mathbf{r}_{ij}|)$ represents the singlet recombination rate constant between radicals i and j (the left depopulation process at the bottom of in Fig. 1.4B). The projection operator onto the singlet state is:

$$\hat{P}_{ij}^{(S)} = \frac{1}{4}\mathbb{1} - \hat{\mathbf{S}}_i \cdot \hat{\mathbf{S}}_j. \tag{4.10}$$

In terms of the operator

$$\hat{A} = \hat{H} - i\hat{K} \tag{4.11}$$

the time-dependent density matrix is given by

$$\hat{\rho}(t) = \exp(-k_e t)\exp(-i\hat{A}t)\hat{\rho}(0)\exp(+i\hat{A}^{\dagger}t). \tag{4.12}$$

Eq. (4.12) can be evaluated by finding the eigenvalues and eigenvectors of $\hat{A}$. Denoting the latter by λ and $\mathbf{T}$, respectively, the time integral over $\hat{\rho}(t)$ is given by:

$$\int_0^{\infty} \hat{\rho}_{ij}(t)dt = \sum_{k,l,m,n} T_{i,k}(T^{-1})_{k,l}\hat{\rho(0)}_{l,m}\ (T^{-1})^*_{k,m}\ T^*_{j,n}\frac{1}{k_e + i(\lambda_k - \lambda_k^*)}. \tag{4.13}$$

From this, one can calculate the recombination yield according to:

$$\phi_P = 2Tr\left[\int_0^{\infty} \hat{\rho}(t)dt\hat{K}\right]. \tag{4.14}$$

In order to quantify the effect the magnetic field has on the recombination yield, one can define the MFE (χ_P), which is calculated by:

$$\chi_P(B_0) = \frac{\phi_P(B_0) - \phi_P(0)}{\phi_P(0)}, \tag{4.15}$$

where $\phi_P(B_0)$ is the recombination yield at a magnetic field B_0 and $\phi_P(0)$ is the recombination yield at zero field.

In general, the MFEs depend on the relative position of the radicals and the orientation of the magnetic field. This is as a result of the dependence of the electron-electron dipolar (EED) interaction on $\mathbf{r}_{i,j}$ as given in eq. (4.5) and the distance dependence of the exchange coupling constants and recombination rate constants. Here, an exponential distance dependence is assumed for the latter parameters:

$$k_P(r) = k_{P,0}\exp(-\beta(r - 2R)) \tag{4.16}$$

and similarly

$$J(r) = J_0 \exp(-\beta(r - 2R)), \tag{4.17}$$

with R denoting the lipid radius. A common decay length $\beta = 1.4$ Å^{-1} is employed for all exchange and rate terms.

The lateral diffusional displacement of lipids is estimated to be sufficiently small in a biological membrane, such that it can be neglected during the short time-span considered here (100 ns) in regard to the production of MFEs. Furthermore, it is estimated that the spin-rotational relaxation of the lipids considered as rigid bodies is slower than the characteristic time for the MFEs, as the rotational tumbling motion is sufficiently slow. An in-depth discussion of these simplifying assumptions can be found in the Appendix (section 9.2).

4.2 Results

4.2.1 Hyperfine coupling constants in lipid peroxyl radicals

In order to assess the possibility of hyperfine-mediated MFEs in the pairwise recombination of peroxyl radicals (reaction V in Fig. 1.4A), the hyperfine coupling constants of selected peroxyl radicals have been calculated using density functional theory. The basis set EPR-III and the exchange-correlation functional B3LYP have been used; details are summarised in the Appendix (Fig. 9.2).

This analysis was undertaken despite discouraging claims in the literature that the hyperfine-derived MFEs are impossible for $RO_2^\bullet$, as the spin density was exclusively concentrated on non-magnetic oxygen atoms (Kipriyanov Jr., Doktorov and Purtov, 2015; Pliss et al., 2017). Surprisingly, this study of two peroxyl radicals derived from the unsaturated fatty acid linoleic acid suggests that this is not the case. Marked hyperfine interactions of the order of 10 MHz have been found for the vicinal hydrogen atom, i.e. the hydrogen atom at the location of the peroxyl group. Two different locations for the peroxide group were tested: carbon 9 and 13, and the stereochemistry of the adjacent double bonds was chosen as e and z, and z and e, respectively (see Fig. 4.1). Herein, these lipids are referred to

as 9ez and 13ze. Based on product analyses, these radicals are expected to be central intermediates of the lipid autoxidation of linoleic acid and its derivative lipids (Spiteller, 1998). A systematic scan of the dihedral angle that the peroxide group makes with the backbone has been conducted. This analysis suggests that its rotation is significantly hindered, even at $T = 310$ K. The high energy configurations are 6.8 and 4.8 kJ/mol above the most stable rotamers of 9ez and 13ze, respectively. The Boltzmann weighted average hyperfine coupling parameters have been evaluated and are summarized in the Appendix (section 9.5).

For 9ez, the dominant hyperfine interaction at the vicinal hydrogen is characterised by a nearly axial tensor with an isotropic value of 13.5 MHz and anisotropy 14.8 MHz. For 13ze, the isotropic contribution and the anisotropy evaluate to 10.3 MHz and 14.6 MHz, respectively. In addition to the vicinal hydrogen atoms, a few of the hydrogen atoms in the neighbourhood of the peroxyl group exhibit small hyperfine interactions (see Fig. 4.1). The isotropic values of these additional interactions are smaller than 1 MHz in absolute value; the largest principal values approach 6 MHz (see Appendix Fig. 9.2).

Below, is considered the effect of the isotropic hyperfine coupling constant of the vicinal proton on the MFEs. For now the anisotropic components are disregarded for two reasons: Firstly, the anisotropies are expected to be reduced by the molecular motion. For example, fast rotation of 13ze about the axis of the carbon chain would reduce the anisotropy from 14.6 MHz to 4.4 MHz (details shown in the Appendix, Figs 9.3 and 9.4).

Secondly, considering anisotropic hyperfine interactions would unreasonably complicate the discussion, which here is focused on qualitative description rather than the quantitative reproduction of a particular MFE. In particular, all calculations would be dependent upon a multitude of parameters describing the relative orientation and their internal and rigid body dynamics. Even if this is desirable for a future study, these parameters cannot currently be described in sufficient detail to warrant this calculation.

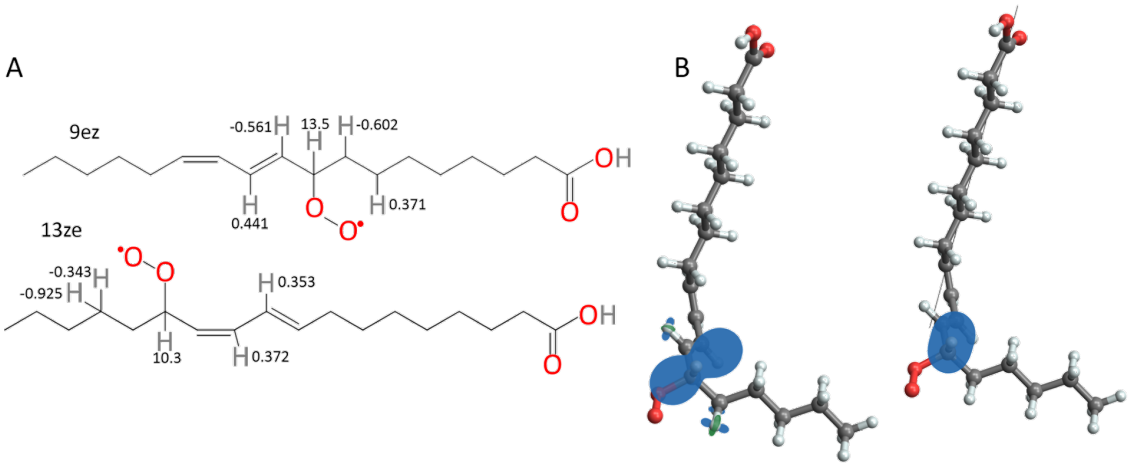

Figure 4.1: A: The structure of the isomers 9ez (top) and 13ze (bottom) of the linoleic acid peroxyl radical. Labels indicate the Boltzmann-weighted average isotropic hyperfine constant ($T = 310$ K) as the peroxyl group rotates. All coupling constants are shown in MHz. B: 3D model of the 13ze isomer with graphical representations of the hyperfine interactions. The left structure illustrates the hyperfine coupling constants at $T = 310$ K; the right structure shows the hyperfine interaction of the vicinal proton under the assumption that fast rotation about the carbon backbone (axis shown as black line) averages the hyperfine interaction (see Appendix Fig. 9.4).

4.2.2 MFEs in radical pairs (RPM)

In Fig. 4.2 are summarised the typical field-dependence of the recombination yield for the encounter of two or three $RO_2^{\bullet}$ radicals. The model calculations followed the general layout as discussed above. In the pair-wise reaction of identical radicals ($N = 2$), MFEs can only arise from the hyperfine-induced spin evolution. The electron-electron dipole (EED) interaction and the exchange interaction do not mix singlet and triplet states and no magnetosensitivity can arise from their action alone. However, the large hyperfine interaction from the vicinal proton does provide a magnetosensitive pathway that is unexpected in view of previous literature. This is evident from model calculations taking into account the isotropic components as derived in the previous section. In fact, if it were the only spin-coupling mechanism (Fig. 4.2, left, grey lines), large MFEs with equally large low-field effects (LFE) would be expected. The sign of the saturated MFE is negative, as expected for an F-pair with dominant recombination efficiency in the singlet configuration, i.e. the magnetosensitive spin dynamics resemble that of a triplet-born radical pair. The LFE results from altered S-T_0-mixing due to the alteration of conserved quantities in the presence and absence of magnetic fields (Timmel et al., 1998; Lewis et al.,

2018a; Lewis et al., 2018a). Its sizeable magnitude, as revealed by Fig. 4.2 (left), is in line with the simplicity of the spin system as derived above. More complex systems with many coupled nuclear spins typically yield smaller LFEs (Rodgers et al., 2007). For radical pairs in membranes, however, lateral diffusion is slow compared to the spin evolution, and it is happening in 2D so even fast motion would not average it to zero. Hence the EED is not averaged out by molecular motion and its effect of enlarging the singlet-triplet energy gap has a damping effect on the MFEs. For the magnetic field perpendicular to the membrane plane, in the presence of electron-electron dipolar coupling at the contact distance, the LFE is completely suppressed (Figure 4.2, left, blue lines). Conversely, for ensembles of randomly oriented two-radical systems, the LFE is preserved (Fig. 4.2, left, yellow lines), albeit shifted to larger field intensities. In any case, marked MFEs for $B_0 < 1$ mT appear possible. This is particularly true as our assumption of radicals at contact is expected to overestimate the effective electron-electron dipolar coupling. For a magnetic field comparable to the geomagnetic field (50 μT), MFEs of -3×10^{-5} are predicted by our model (compared to 0.011 without electron-electron dipolar coupling), when using 10.3 MHz for the hyperfine coupling constant. Effects of the exchange interaction are discussed below.

4.2.3 MFE caused or modulated by three-radical interactions

In three-spin systems, MFEs can ensue even in the absence of hyperfine coupling interactions from the electron-electron dipolar coupling. This effect has been shown to elicit remarkable low-field sensitivity and magnetic field dependencies that can differ from those inflicted by the RPM (Keens, Bedkihal and Kattnig, 2018). As in the recombination of $RO_2^{\bullet}$ radicals, the dipolar coupling is the dominant interaction, and we expected the D3M to strongly impact upon MFEs in lipid autoxidation. Hence, this possibility has been explored for a range of different scenarios.

In general, it has been assumed that the two radicals, henceforth referred to as A and B, are at contact and hence the effect of a third radical, radical C, has been

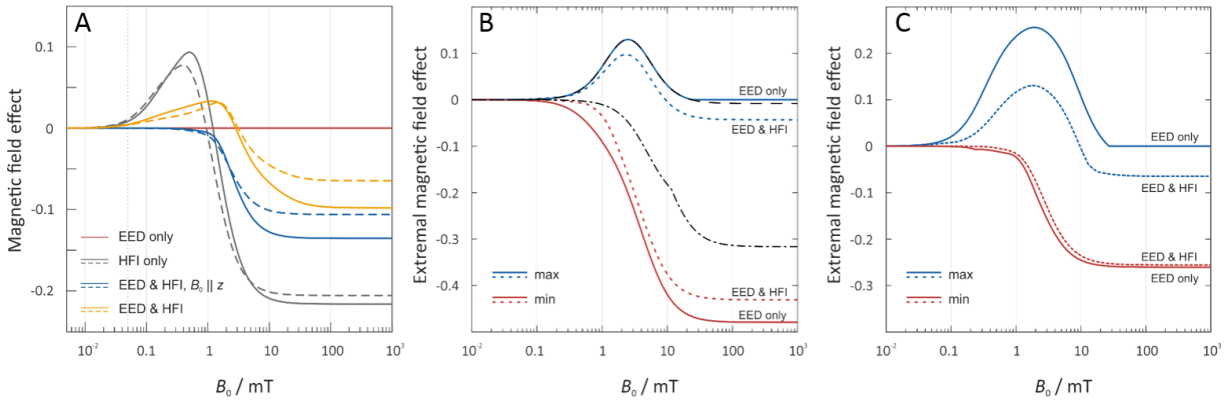

Figure 4.2: MFEs for two- and three-radical systems. Two radicals are always considered to be at contact, i.e. at a distance of 9 Å, and thus able to recombine. In the three-radical systems (panels B and C), the third radical position is scanned across the membrane plane with excluded volume effects taken into account. For the two-radical system (panel A), dashed lines indicate an isotropic hyperfine constant of 10.3 MHz for the vicinal proton; blue solid lines represent 13.5 MHz. Interactions within the Hamiltonian have been included according to the legend. In the three-radical system (panels B and C), the blue solid lines indicate the maximum MFE with the location of C varied. Similarly, the red solid lines indicate the minimum. Panel C applies to the MFE calculated from the mean recombination yields of systems randomly oriented with respect to the magnetic field. In each case, the exclusion of (solid lines) and inclusion of (dashed lines) the hyperfine coupling with a coupling constant of 10.3 MHz (right) was considered. For B, the black dashed and dashes-dotted lines indicate the maximal and minimal (most negative) MFEs resulting from the third spin in contact with the radical pair. $k_{P,0} = 0.2$ ns^{-1} and $k_e = 0.01$ ns^{-1}.

investigated in relation to its position. Fig. 4.3 shows the MFE on the recombination yield as a function of the location of C for the magnetic field oriented perpendicular to the membrane plane. Graphs are displayed for the field intensities 50 μT, 1 mT and 10 mT. Additional data for 100 mT are shown in the Appendix (Fig. 9.5); the MFEs at 100 mT are similar to those at 10 mT, however larger. Here, radical A has been placed at the coordinate $(R, 0)$ and radical B at $(-R, 0)$ of the membrane plane, with $R = 4.5$ Å denoting the particle radius. Results are shown for the first quadrant; the MFEs for the other quadrants are related by symmetry. The excluded region surrounding the origin is inaccessible to radical C (likewise of radius R) due to the finite size of the lipid radicals.

The left column of Fig. 4.3 highlights the effect of the dipolar coupling by equating the hyperfine terms to zero. Evidently, large MFEs are induced by the mere presence of the third radical. The effects are maximal for radical C positioned away from contact by approximately 3 Å. In particular, isosceles triangular arrangements

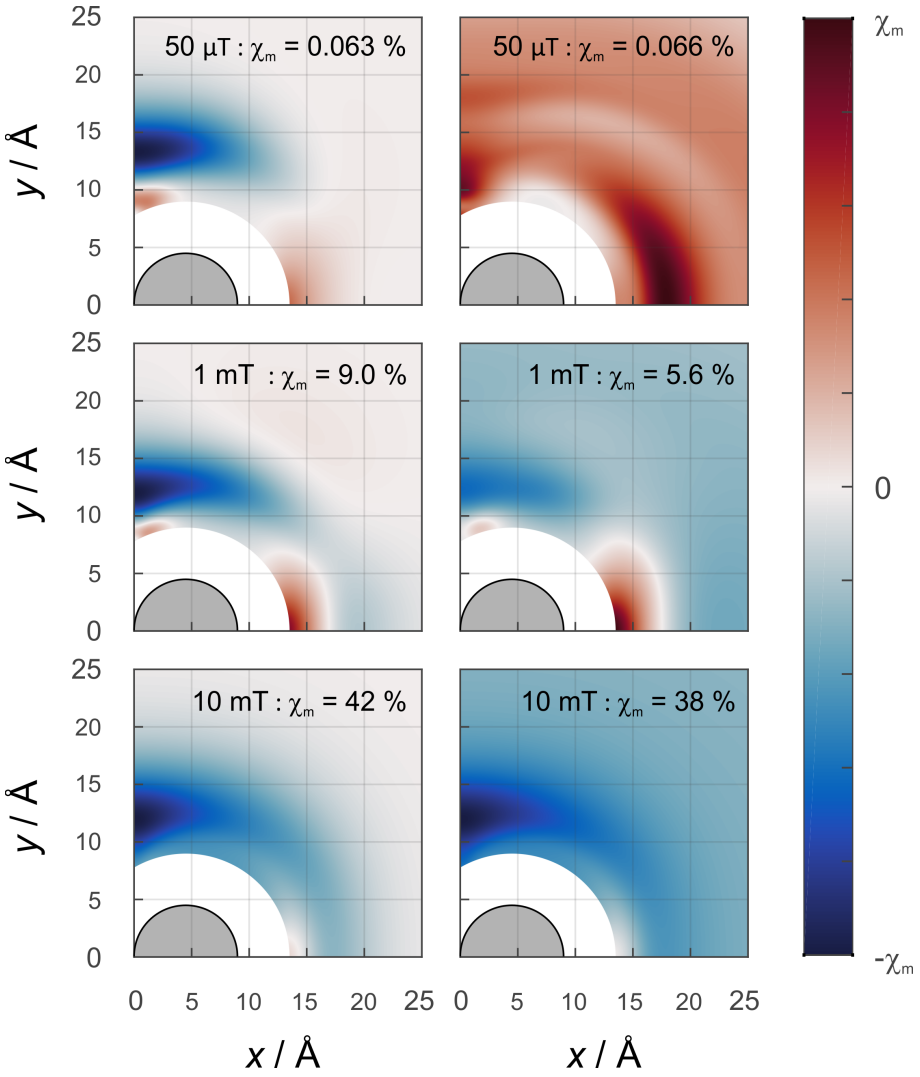

Figure 4.3: Dependence of the MFE χ_P in a three-radical system on the position of radical C. The vicinal, isotropic hyperfine interaction has been considered (right, $a = 10.3$ MHz) or disregarded (left). The magnetic field is perpendicular to the plane of the membrane and the field strengths are (from top to bottom) 50 μT, 1 mT and 10 mT. Simulation parameters: $k_{P,0} = 0.2$ ns^{-1} for all pairs of radicals, $k_e = 0.01$ ns^{-1} and $J = 0$. χ_m, the maximal absolute value of each MFE, is reported for each sub-panel. The colour bar extends from $-\chi_m$ to χ_m.

of the radicals with a triangle height of approximately 12 Å appear to yield large $|\chi_P|$. For selected positions of radical C, the MFEs are larger than those found for the radical pair model with hyperfine-induced spin mixing. The maximal MFEs amount to 0.063 %, 9.03 % and 41.9 % in absolute value for the three shown field intensities, 50 μT, 1 mT and 10 mT, respectively. While the figures bring to light the locations of the maximal MFEs, the large effects overwhelm the feature that significant MFEs can also ensue from rather remote C radicals. For example, for a magnetic field intensity of 10 mT, χ_P = -6.5 % results with C at (20 Å, 20 Å), a remarkable 25.3 Å (5.6R) away from the next closest radical. The inherent reactivity

of C is inconsequential everywhere but at the boundary of the excluded volume region. If C is assumed to be unreactive, the negative MFEs at this contact region are further enhanced (as is shown in Fig. 4.4). A minimal χ_R of -63.3 % at 100 mT is then achievable compared to -47.9 % for a reactive radical C. Fig. 4.4 shows the results, when a reactive C (left) or an unreactive C (right) is used. The results appear to be largely insensitive to the level of reactivity of the third radical, with only minor differences such as the magnitude of the MFE at contact when using $B_0 = 1$ mT. The location of the MFE, however, does not change in any significant way.

If the isotropic hyperfine interactions are re-engaged, the location dependence of the MFE reflects the simultaneous effects of the RPM and the D3M. With the noteworthy exception of the low-field region, the predominant effect of the RPM is the introduce a non-zero MFE when the radical C is moved great distances away from the radical pair (see Fig. 4.3, right column for $B_0 \geqslant 1$ mT). Other than that, the features of the D3M are still widely present for small C separations. While the MFEs here again exceed those predicted for the RPM alone, the presence of the hyperfine interactions slightly attenuates the MFEs compared to the D3M-only scenario. In particular, for $B_0 = 100$ mT an MFE of maximal absolute value of -43.0 % is found, instead of -47.9 % from above. This discussion applies to moderate to large field intensities ($B_0 \geqslant 1$ mT). At 50 μT the situation is more interesting: As is evident from Fig. 4.3 (top right panel), the dipolar coupling with radical C facilitates comparably large and positive MFEs even for large distances (maximal $|\chi_R| = 0.066$ %); this entails a sign inversion and more than 20-fold increase in magnitude with respect to the RPM-only MFE (-0.003 %). The large spatial extent of the dipolar coupling effect is revealed here in the sign change occurring at approximately 44 Å, above which the RPM-induced effect becomes dominant. Here, we have assumed a_i = 10.3 MHz as suggested for 13ze by our DFT calculations. Qualitatively agreeing conclusions can be drawn for a_{iso} = 13.5 MHz, i.e. 9ez (see Appendix Fig. 9.5).

In order to concisely characterize the field dependence of χ_P whilst withholding the complexity resulting from the position dependence of the D3M, the extremal

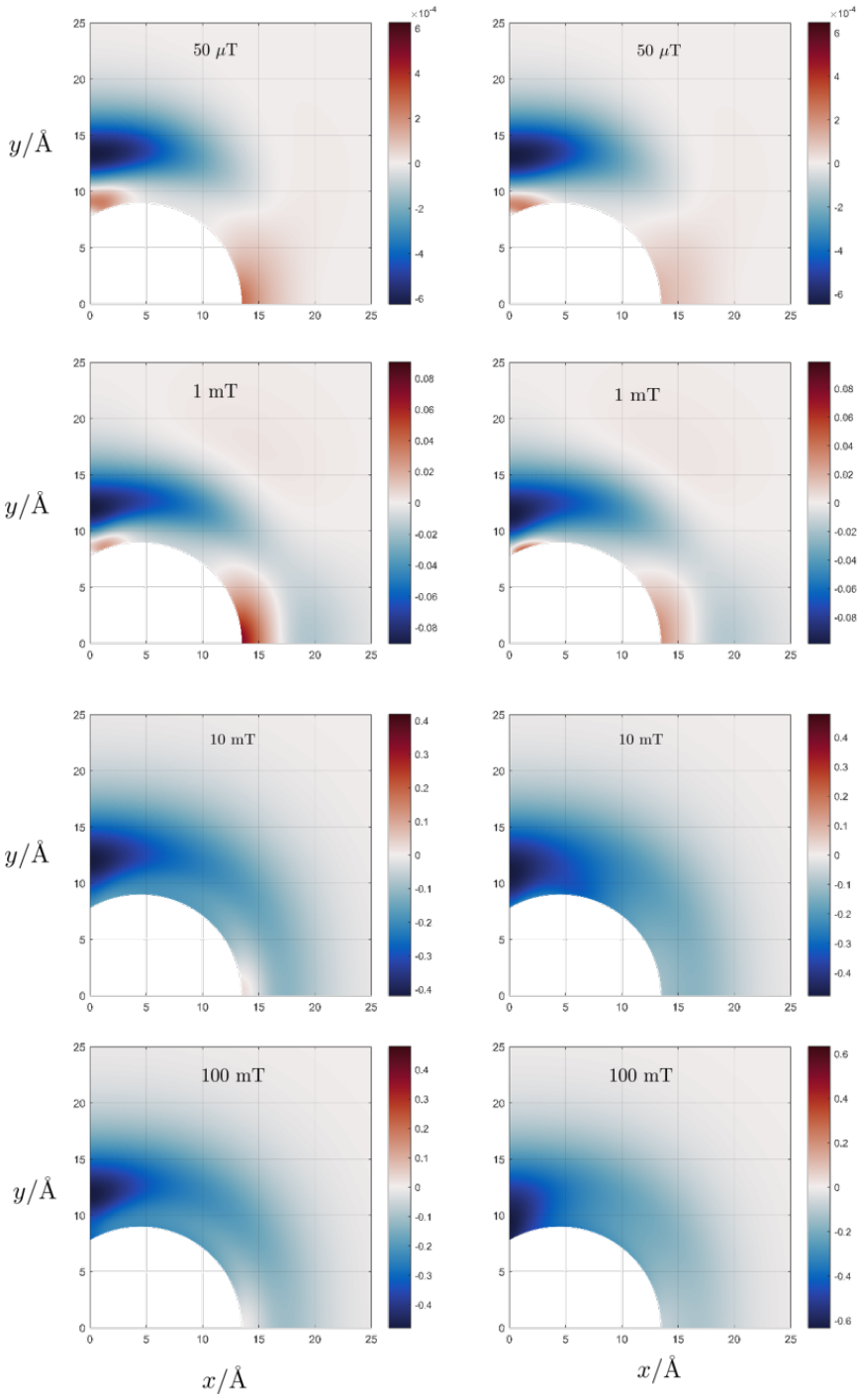

Figure 4.4: MFEs when the third radical (C) is reactive (left) and unreactive (right) for different magnetic field strengths. The magnetic field is perpendicular to the membrane plane. The parameters are as follows: $J = 0$, $k_{P,0} = 0.2$ ns^{-1}, $k_e = 0.01$ ns^{-1} and $a_{iso} = 10.3$ MHz.

(i.e. the largest positive and smallest negative) MFEs shall be focussed upon. Fig. 4.2 (middle and right) gives a representation of the supremal and infimal MFEs over all C locations as a function of the magnetic field intensity. Here two pertinent scenarios are focussed upon: D3M-only ($a = 0$) and the mixed scenario with both the hyperfine interaction (HFI) and EED included. The HFI-only situation is shown

in Fig. 4.5).

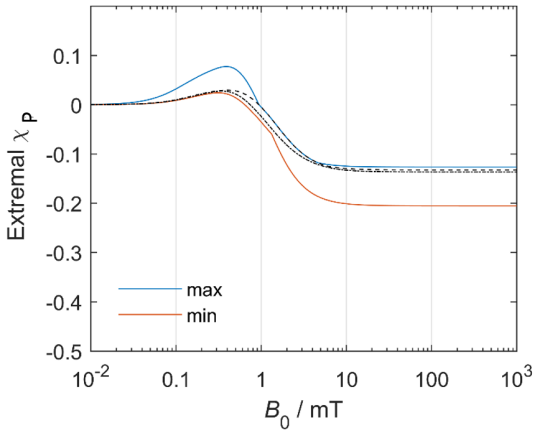

Figure 4.5: Magnetic field effects (χ_P) for a three-radical system when the HFI is included, but EED is excluded. Parameters: $a_{iso} = 10.3$ MHz, $J = 0$, $k_{P,0} = 0.2$ ns^{-1} and $k_e = 0.01$ ns^{-1}.

It merely serves to elaborate on the effect of the hyperfine interaction, but cannot be physically realised as the electron-electron dipolar coupling does not average to zero from molecular motion in membranes - at least not on the relevant time-scale. Comparing the D3M-only and the mixed-mechanism calculations, it becomes obvious that in the three-radical systems the electron-electron dipolar coupling is the dominant interaction. While the hyperfine interaction has a small damping effect on the D3M, it also moves the positive MFE-peak to a smaller magnetic field intensity of 1.87 mT. Surprisingly, the MFEs generated by the D3M (in the absence or presence of additional hyperfine interactions) can exceed those of the hypothetical HFI-only scenario (Fig. 4.5), or the effects predicted for isolated radical pairs (Fig. 4.2, left). In Fig. 4.2, the minimal and maximal MFE that results from the three radicals in (pairwise) contact (dashed black lines) have also been indicated. This analysis suggests that the extremal negative MFEs are generated by the D3M from configurations with radical C offset from the AB-radical pair. On the contrary, the maximal positive MFEs are typically generated with C in contact with one or both of the radicals. These findings are in line with the exemplary positional dependencies shown in Fig. 4.3.

As the orientational average of the electron-electron dipolar interaction is zero, the question arises to what extent the D3M can elicit MFEs for ensembles of

randomly oriented spin systems. The answer to this question is provided by Fig. 4.6, which shows the dependence of the orientationally averaged MFE on the position of radical C. The data clearly show that substantial MFEs arise from the D3M even for randomly configured spin systems. For certain relative positions of the radicals, MFEs of the order of -25 % at 10 mT are possible, both in the absence and in the presence of isotropic hyperfine interactions of $a = 10.3$ MHz. Again, the additional hyperfine interactions have a small damping effect on the MFEs for moderate field intensities. For the low field intensities, "large" effects ($\approx 4\%$ at 1 mT) appear to result from the equilateral triangular geometry. This is especially evident for the 50 μT magnetic field, but also visible at 1 mT - in particular for the D3M-only systems. For 50 μT, in D3M-systems, the MFEs are small for all but this particular configuration. On the contrary, if the hyperfine interaction is present as well, MFEs are observed for a wide range of distances. While in this particular case the MFE is predicted to be slightly larger in the isolated radical pair, in general the D3M-induced MFEs exceed those of the RPM in pairs of radicals. For example, for 10 mT, three-radical systems can elicit MFEs of -24.5 % (D3M-only) or -23.5 % (D3M and HFCs), while -4.5 % resulted from the isolated, randomly oriented radical pair. Fig. 4.7 provides more details on the orientational dependence of the MFE.

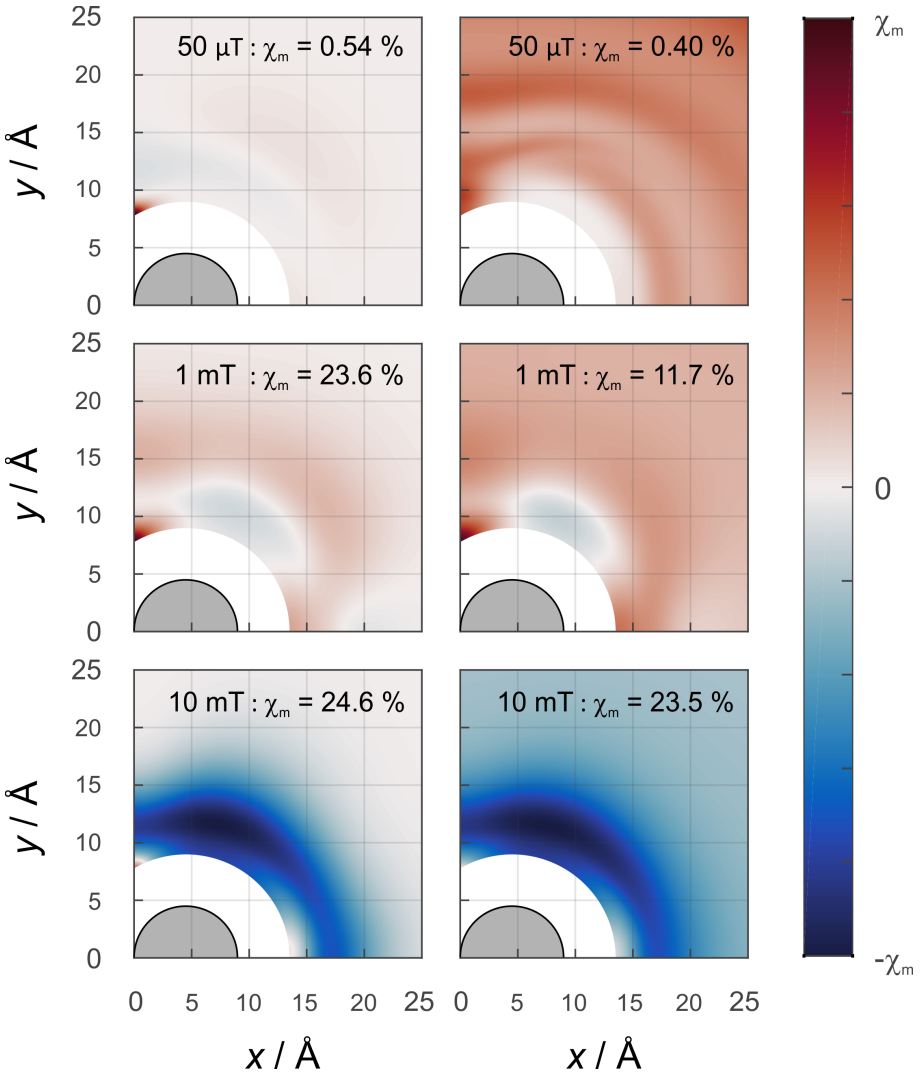

Figure 4.6: MFE of the average of the recombination yield when the magnetic field is oriented randomly with respect to the plane of the radicals. Details as for Fig. 4.3 apply. Without hyperfine (left) and with hyperfine (right, $a = 10.3$ MHz), field intensities from top to bottom: 50 μT, 1 mT and 10 mT.

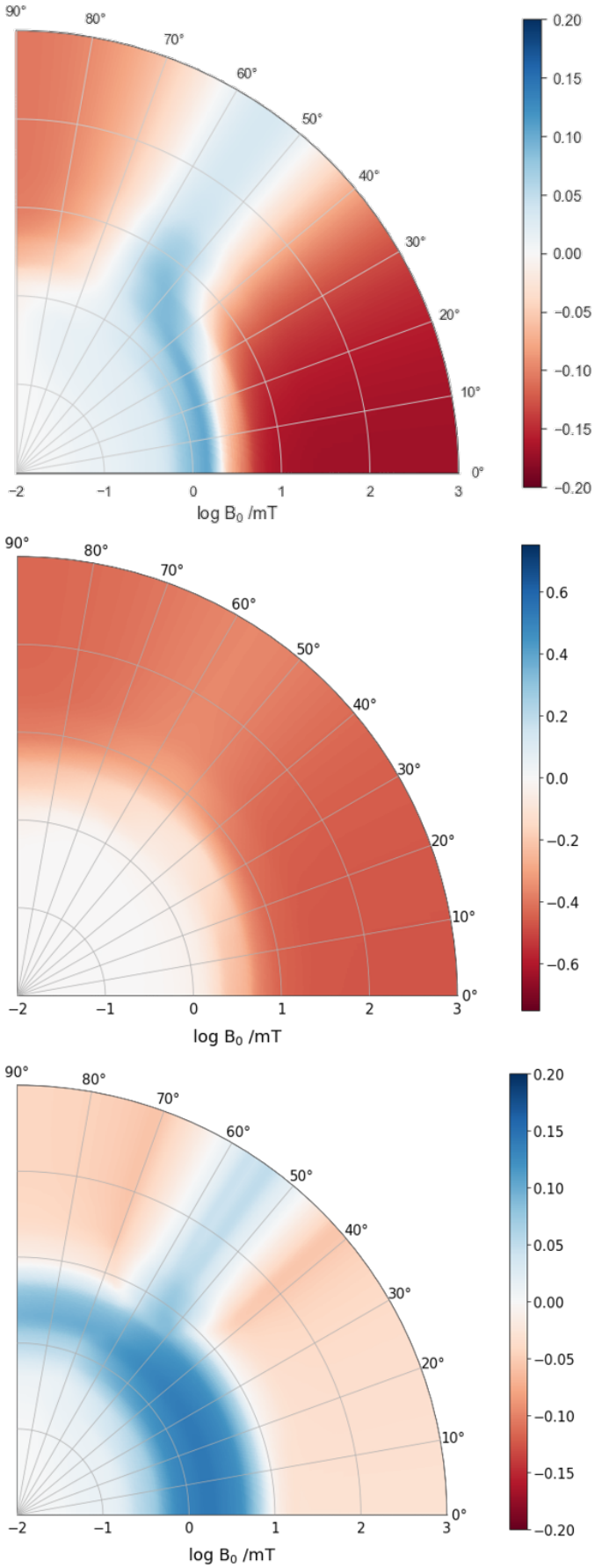

Figure 4.7: Dependence of the MFE on the orientation of the magnetic field. The field is rotated from parallel with z-axis to parallel with x-axis. Top: two-radical, middle and bottom: three-radical system. Dipolar and hyperfine interactions are included, the latter with a coupling constant of 10.3 MHz. Middle shows the minimum possible MFE and the bottom shows the maximum possible MFE for variable positions of the third radical.

4.2.4 Dependence on the orientation of the magnetic field

Here, it suffices to note that the anisotropy of the MFE, i.e. the maximal orientational change relative to the mean MFE, can be substantial in the three-radical systems (see Appendix Fig. 9.6). For the D3M-only systems, anisotropies of 21.5 % and 96.4 % for magnetic fields of 1 mT and 100 mT, respectively are found. Fig. 4.2 (right) illustrates the field dependence of the minimal and maximal MFEs of randomly oriented three-spin systems as a function of the magnetic field. It can be seen that the orientational average favours MFEs at low magnetic fields and the positive MFEs over those found for the B_0-field perpendicular to the membrane plane. In particular, in the rotationally averaged samples, the MFEs already arise at markedly smaller field intensities than for the perpendicular field direction, 0.03 vs. 0.3 mT (compare Fig. 4.2B and C). Fig. 4.7 shows the orientation dependence of the field-dependence of the MFE. The onset behaviour is not dissimilar to that observed for radical pairs (in the presence of the EED). However, the MFEs can be larger for the D3M by a factor of more than 3.

4.2.5 Effects of the Exchange Interaction

The exchange coupling is expected to impact upon the spin dynamics of adjacent radicals. In diradicals in solution, i.e. for averaged electron-electron dipolar interactions but relatively constant exchange interaction, characteristic MFEs can result from the S/$T_{\pm}$-crossing (Turro and Kraeutler, 1980; Steiner et al., 2018). For immobilized radical pairs, similar degeneracies of the electronic terms can ensue as a function of the dipolar coupling and the external magnetic field (Efimova and Hore, 2008). Here, the exchange coupling could compensate for the non-zero electron-electron dipolar interaction, thereby boosting MFEs and their anisotropies at low magnetic fields. Motivated by these findings, the dependence of our model of peroxyl radical recombination in membranes on the exchange coupling interaction has been analysed. Fig. 4.8 (A) shows the dependency of the MFE of the radical recombination yield for the RPM as a function of the magnetic field and the exchange interaction. The magnetic field was oriented perpendicular to the membrane, i.e. perpendicular to

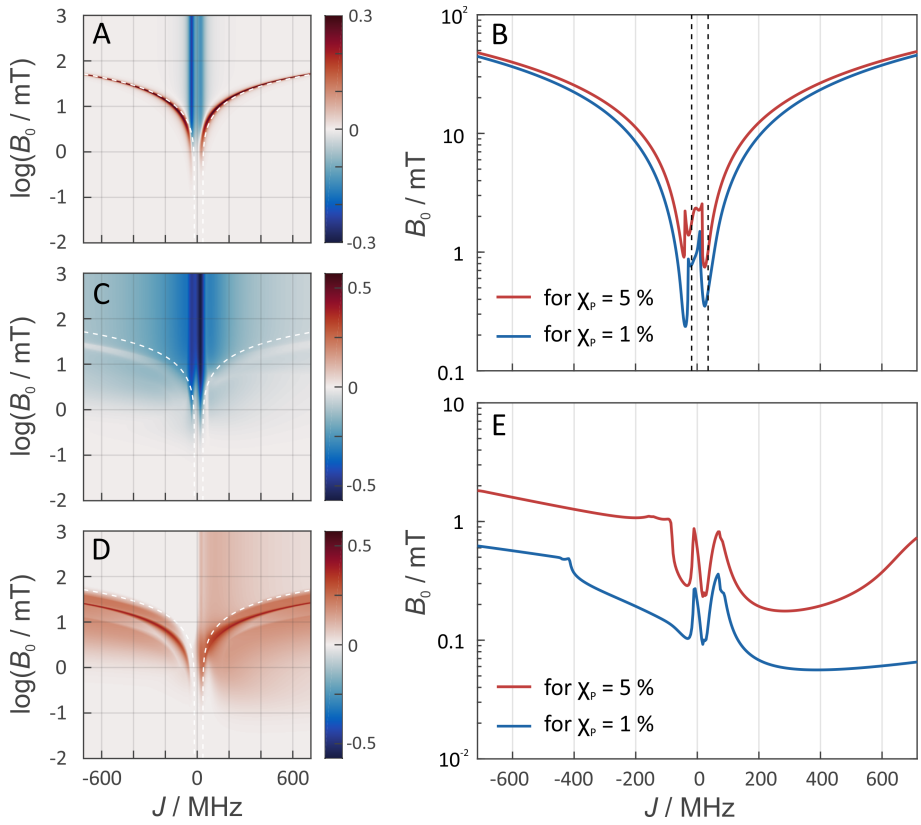

Figure 4.8: A: The MFE for the two-radical radical system when exchange is included. An isotropic hyperfine constant of 10.3 MHz was used and the dipolar interactions were included. B_0 is perpendicular to the radical axis. B: The magnetic field required for a MFE of 1% (red) and 5% (blue) for the same system as in panel A as a function of the exchange interaction. C and D: The minimal and maximal MFEs for the three-radical system when exchange is included. The hyperfine interaction is not included, but the dipolar interactions were taken into account. $\mathbf{B}_0$ is perpendicular to the plane made by the three-radicals. E: The field intensity for a MFE of 1% (red) and 5% (blue) for the three-radical system used in C/D.

the RP axis. For large $|J|$, the MFE is characterized by the crossing of the S state and a superposition state of T_+ and T_-. Disregarding the hyperfine interaction, the crossing field, B_c, can be calculated analytically. It is found that:

$$\frac{g\mu_B B_c}{\hbar} = \sqrt{4J^2 - dJ - \frac{1}{2}d^2} \tag{4.18}$$

with $J = J_{A,B}$ and $d = d_{A,B} > 0$ denoting the largest eigenvalue of the electron-electron dipolar coupling tensor. For $B_c = 0$, the crossings occur for $J = -\frac{1}{4}d$ and $J = \frac{1}{2}d$, in agreement with (Efimova and Hore, 2008), but using a different convention for the dipolar coupling parameter.

In Fig. 4.8A, B_c, as given by eq. 4.18, has been overlaid on the MFEs (dashed lines). It is apparent that the expression predicts the location of the positive MFEs

for larger, in absolute value, exchange coupling constants. For these regions, the involved superposition state of T_+ and T_-, approaches the pure states T_- and T_+, for positive and negative J, respectively, suggesting that the scenario is similar to that for $S/T_\pm$-crossing in the absence of electron-electron dipolar coupling. For smaller J, the hyperfine and the exchange coupling have to be treated equally and complex MFEs ensue. Fig. 4.8B gives the magnetic field intensities that are necessary to elicit MFEs of 1 % and 5 %, regardless of their sign. Two regions of high low-field sensitivity are evident around $J = -0.53d$ and $J = +0.35d$, for which a 1 % MFE can be induced by magnetic fields as small as 0.24 mT and 0.35 mT, respectively. For $J = 0$, a markedly higher field of 1 mT is necessary.

Fig. 4.8C to 4.8E addresses the J-dependence in the three-spin scenario. In order to highlight the effect due to the D3M mechanism, no hyperfine interactions have been considered here. The density plots in Fig. 4.8C and 4.8D give the maximal and minimal MFE realizable through the presence of the third radical. The plots show a positive peak of the MFE for large $|J|$, which resembles that found above for the radical pair scenario and is attributed to a level crossing of S and T_+/T_--states. However, here, it is shifted to weaker field intensities compared to B_c, eq. 4.18, for the radical pair at contact. Furthermore, the MFEs are found to be larger for the D3M-coupled three-radical system than for the radical pair. What is, however, even more remarkable is the fact that the MFEs in the low-field region do not vanish for large $|J|$. In particular, Fig. 4.8C and 4.8D shows marked MFEs in the $B_0 < 1$ mT region regardless of J, which are absent from the RPM model, Fig. 4.8B, except for the two peculiar Js identified above (i.e. $-0.53d$, $+0.35d$). This is even more prominent in Fig. 4.8E, which plots the field intensities that are necessary to elicit MFEs of 1% and 5% as a function of J. This plot reveals the following: Firstly, in general, lower magnetic field intensities are necessary to generate a 1% MFE for the D3M than for the RPM acting on radical pairs. Secondly, large $|J|$ values do not necessarily have a detrimental effect on the low-field sensitivity. E.g. a 1% effect results from Earth-like magnetic field intensities of 56 μT in the presence of a 385 MHz exchange coupling. Any exchange coupling in the range of 200 to 600

MHz gave rise to similar effects. For negative J, slightly larger field intensities are required, which, however, are still smaller than for the RPM. E.g., for -32 MHz, a field intensity of 0.1 mT was required for a one percent effect.

4.3 Discussion

D3M offers a pathway to unorthodox MFEs. For systems with non-zero hyperfine interactions, D3M can both boost and suppress MFEs relative to those expected from the classical RPM depending on the position of the third radical. For low fields, it can give rise to MFEs of flipped sign (such as those shown in Fig. 4.3 for $B_0 = 50$ μT). Unlike the RPM in radical pairs, D3M is applicable to radicals without hyperfine interactions and for $\Delta g = 0$. This is an important realisation, as it suggests MFEs for a large class of radical reactions that have not been assumed to be magnetosensitive. One system of this kind where this could be important is the recombination of two $RO_2^\bullet$ radicals. Here, magnetosensitivity was previously precluded, because of a presumed absence of hyperfine interactions that resulted from the electron density being concentrated on the oxygen atom (Kipriyanov Jr., Doktorov and Purtov, 2015; Pliss et al., 2017). This assumption is contrary to our investigation as summarised above, which does suggest significant non-zero hyperfine interactions of the vicinal protons. While this finding does suggest MFEs due to the conventional pairwise RPM, the D3M mechanism could nonetheless be relevant as it can produce stronger MFEs and explain a remarkable low-field sensitivity, which is robust in the presence of large exchange couplings.

As a consequence of the D3M, characteristics of the field dependence of the recombination yield (size of MFEs, width, LFE) will depend on radical concentration. We can estimate the required concentrations for the model of a circular "microreactor" containing a radical pair and an additional radical. We calculate the expectation value of the MFE if the radical and the radical pair are independently distributed over this microreactor while conforming to the excluded volume requirements resulting from the finite size of the radicals:

$$\begin{aligned}\overline{\chi}_r &= \frac{1}{V}\int_0^{\Omega-R} d_c \mathrm{d}d_c \int_0^{2\pi} \mathrm{d}\varphi_c \int_0^{\pi/2} \mathrm{d}\vartheta_{ab} \int_0^{\Omega-R} d_{ab}\mathrm{d}d_{ab} \\ & I(d_c,\varphi_c,d_{ab},\vartheta_{ab})\chi_r(\mathbf{r}_a(d_{ab},\vartheta_{ab}),\mathbf{r}_b(d_{ab},\vartheta_{ab}),\mathbf{r}_c(d_c,\varphi_c)),\end{aligned} \tag{4.19}$$

where the indicator function I is given by:

$$I(d_c,\varphi_c,d_{ab},\vartheta_{ab}) = \Theta(2R-r_{ac})\Theta(2R-r_{bc})\Theta(\Omega-R-r_a)\Theta(\Omega-R-r_b), \tag{4.20}$$

with Θ denoting the Heaviside theta function and the location of radical A and B in the membrane plane, i.e. xy-plane, given by

$$\mathbf{r}_{a,b}(d_{ab},\vartheta_{ab}) = \hat{x}(d_{ab} \pm R\cos\vartheta_{ab}) \pm \hat{y}R\sin\vartheta_{ab}. \tag{4.21}$$

Here, the upper sign refers to radical A and the lower to B. The Cartesian unit vectors have been represented by hatted quantities. The location of radical C is

$$\mathbf{r}_c(d_c,\varphi_c) = \hat{x}d_c\cos\varphi_c + \hat{y}d_c\sin\varphi_c. \tag{4.22}$$

The indicator function ensures that the radicals are always separated by at least $2R$ and that the radicals are confined within the microreactor of radius Ω. V is the phase space volume, i.e. the value of the integral over the indicator function.

Fig. 4.9 summarizes the dependence of the MFE on the size of the microreactor for Ω up to $10R$. For the scenario that the external magnetic field is perpendicular to the membrane plane and that the EED coupling is the only relevant interaction between the radicals (D3M-only), it is found that the MFE decreases to approximately -30% as the surface concentration increases to approximately 0.5 nm^{-2}. For the highest possible concentration, which corresponds to an equilateral arrangement of the three radicals in mutual contact within a microrector of radius $\Omega = (\frac{2}{\sqrt{3}+1})R$, the MFE amounts to -32%. However, in many respects the MFEs associated with the equilateral triangular configuration do not appear as a smooth progression of

the MFE at a lower surface concentration. It is furthermore noteworthy that the MFE increases faster at low concentrations, i.e. for surface concentrations below 0.15 nm^{-2}, than for higher concentrations. While large effects are obviously favoured by high concentrations, for $\Omega = 10R$, which corresponds to a surface concentration of merely 0.047 nm^{-2}, a respectable MFE of -5% ensues nonetheless. If both EED interactions and HFIs are considered, the MFEs at high surface concentrations resemble those for the D3M-only scenario. At low concentrations, on the other hand, the presence/relevance of the RPM is obvious, which leads to a levelling off of the MFE at -13% for small concentrations. The trend of the MFE vs. the microreactor size follows that of the case for the EED system, in that the MFE increases in absolute value as the surface concentration increases. A surface concentration of approximately 0.2 nm^{-1} leads to the doubling of the MFE over that characteristic for isolated radical pairs and the RPM. For both discussed scenarios the half-saturation widths, i.e. the magnetic field for which half the saturating MFE is achieved, increases with increasing surface concentration (see Appendix, Fig. 9.7), but it does so in a different way depending on whether hyperfine interactions are present or not. Furthermore, for both scenarios, no marked low-field feature is obvious. In the Appendix, are also presented data for confined three-radical systems subject to the HFI only. For this purely hypothetical scenario, a large low-field effect peaks at $B_0 \approx 0.36$ mT ensues. Its size, as well as that of the saturated MFE, decreases with increasing surface concentration (see Appendix, Fig. 9.9).

This analysis has also been extended to spin systems that are randomly oriented with respect to the external magnetic field (powder average). Remarkably, in this scenario, a feature resembling the LFE of the RPM is evident from the magnetic field dependence even in the absence of HFIs, as is shown in Fig. 4.9. While this peak of positive MFE resembles that of the hyperfine interaction-derived low-field effect, it here is the result of the EED-mediated process, which gives rise to spiky features at low fields, as anticipated from (Keens, Bedkihal and Kattnig, 2018). The low-field peak is located at approximately 0.8 mT and its amplitude increases with increasing surface concentration up to 0.2 nm^{-1}, beyond which it is approximately constant at

2%. At higher fields, the usual response and trends as described above apply. As the saturated MFE grows, in absolute value, faster than the low-field feature, its relative amplitude decreases as the microreactor radius is reduced. Fig. 9.8 in the Appendix summarises the characteristics observed for this new kind of LFE.

It is generally remarkable that the third radical can induce effects from a remote distance. The nature of this effect is position- and orientation-dependent, as shown in Fig. 4.3 and in the Appendix (Fig. 9.5).

Yet, the net effect does not disappear when the powder average of the system is taken; cf. Fig. 4.6. Although assumed in our calculations above, the third radical does not necessarily have to be of the same kind as those forming the reactive radical pair. In particular, more stable radicals such as those derived from radical scavengers could act as the third, i.e. "bystander", radical. Ultimately, this could mean that radical scavengers, while acting to reduce the effect of dangerous free radicals, could promote MFEs via the D3M as they give rise to long-lived radical species upon scavenging ROS, etc. (Lobo et al., 2010). These MFEs could enhance or counteract the accumulation of free radical damage depending on the relative position, the properties of the individual radicals and the magnetic field intensity, as outlined above.

An important property of the D3M is the immunisation to large exchange coupling, which is evident in Fig. 4.8 (C to E). This property is expected to be particularly relevant to radical reactions that involve bond formation (and thus positive J_{ex}), in systems of reduced mobility, for which no efficient pathways for radical separation and re-encounters are available. This evidently applies to many radical reactions in membranes or other biological environments. For these systems, the average exchange interaction of the reactive radical pair is expected to dominate over magnetic interactions. However, if a third radical were present, comparably large MFEs could be facilitated even for low fields as shown in Fig. 4.8. This might be one of the reasons why MFEs in biological systems are often found to be associated with conditions of oxidative stress. Such effects are, for example, detailed in the review by Valko *et al.*(Valko et al., 2007). The magnetosensitivity of such reactions could in

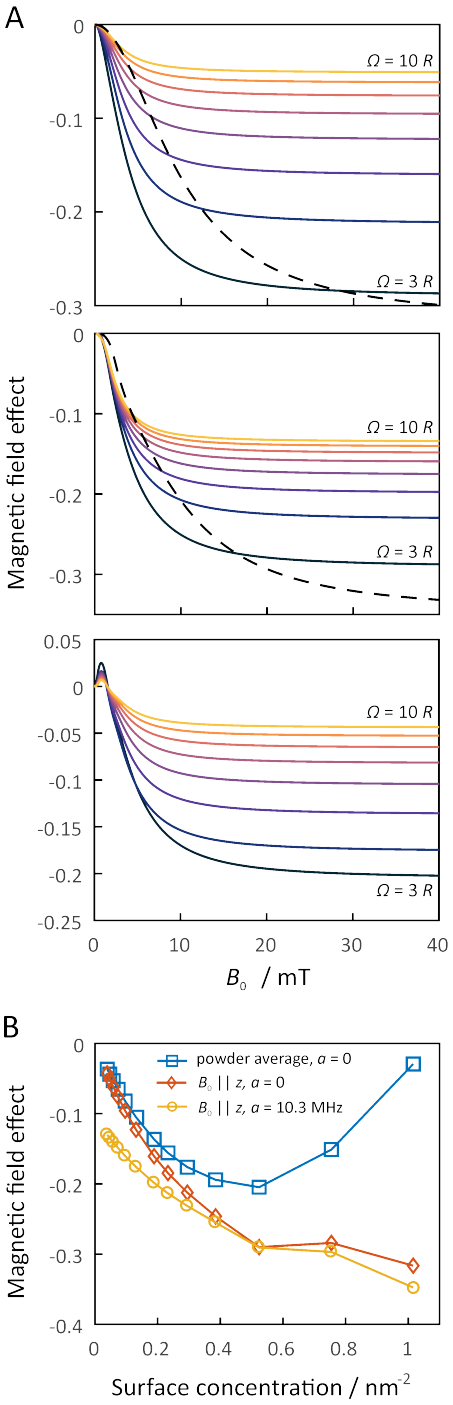

Figure 4.9: MFEs resulting from the D3M for circular microreactors. For panel A, the magnetic field of the top and middle rows are perpendicular to the membrane plane. The top row indicates a system without hyperfine interactions, the middle indicates the case when the hyperfine coupling constant in all 3 radicals is 10.3 MHz and the bottom row indicates the orientational average of the top row (dashed lines represent the unique case of the radicals in an equilateral triangle geometry). Panel A scans the magnetic field, and panel B shows the MFEs as a function of the surface concentration. All the other parameters are the same as for Fig. 4.2.

principle have a significant impact on the long-term risk assessment of magnetic field exposure, as oxidative stress has been linked to the pathogenesis of several human diseases including, notably, cancer (Barnes and Greenebaum, 2018). Clearly, many

more experimental and theoretical studies will be necessary to substantiate or refute this possible link. Here, only one more puzzle piece is provided to the understanding of which processes are to be considered in the first place.

As a consequence of the possible dependence of MFEs on concentration, as we propose here, it is suggested that study protocols, in particular in the biological context, ought to not only control the exposure conditions, but also regulate and document absolute radical concentrations. Only in this way can the reproducibility of the results be ensured, the underlying MFE be fully characterized and its mechanism unequivocally established. Conversely, it is not inconceivable that the irreproducibility haunting many exposure studies of biological systems resulted from concentration-dependent shifts in the MFE-generating mechanisms.

In principle, interesting MFEs could also result from the dipolar interaction between more than three radicals. While the mechanism only requires passing encounters of radicals, these encounters are obviously progressively less likely as the number of radicals increases. The exceptions to this are reactions in which radicals are generated with high local concentrations, e.g. such as in the context of ionising radiation interacting with biological tissue. In ion-beam therapy, huge local concentrations of hydroxyl radicals ensue in the surroundings of the so-called Bragg peak (Desouky and Zhou, 2016; Haume et al., 2018). While their short lifetime surely required high magnetic fields to induce MFEs, these radical clusters could be subject to MFEs due to a DnM with $n > 3$.

On the whole, these results show that, in theory, unusual MFEs are possible in the oxidative degradation of phospholipids. This could provide an explanation for the unorthodox MFEs observed in (Kabuto et al., 2001). Yet, we refrain at this stage from a direct comparison, as high-quality data of the field-dependence of the MFEs are currently lacking, both, for complex *in vivo* systems and *in vitro* models. However, our calculations do reproduce the conclusion that the rate of lipid peroxidation of 1,2-dioleoylphosphatidylcholine liposomes increases even with small fields (Lalo, Pankratov and Mykhaylyk, 1994).

4.4 Conclusions

Model calculations have been presented that demonstrate that the recombination of lipid peroxyl radicals is expected to be magnetosenstive. It has been shown that this magnetosensitvity is underpinned by the classical hyperfine mechanism, i.e. the RPM, as acting in radical encounter pairs, and, if the local radical concentration is sufficient, the dipolarly mediated spin dynamics in groups of three radicals (D3M). The suggestion of an RPM-based MFE of the symmetric recombination reaction of peroxyl radicals is in deviance with previous suggestions, which opposed this possibility with reference to the supposedly strong localisation of the spin density on the oxygen in the peroxyl groups, which precluded significant hyperfine interactions. Here, DFT calculations have been employed to show that this picture is ill-conceived, significant HFIs are observed for the vicinal proton and, to a lesser extent, a few other protons, and that RPM-derived MFEs are possible. These RPM-MFEs are, however, strongly impacted by the electron-electron dipolar coupling and the exchange interaction in the radical pair at contact, which suppresses marked effects to weak magnetic fields, i.e. the well known low-field effect.

It has been shown that the D3M model, previously introduced in (Keens, Bedkihal and Kattnig, 2018), is relevant to the considered scenario of peroxyl radical recombination if the local surface concentration is of the order of 0.1 nm^{-1}. This alternative mechanism has interesting properties: the third radical can induce effects even if it acts only as a remote "bystander", and is not involved in the actual recombination process by means other than its long-range electron-electron dipolar coupling interaction. A large variety of MFEs can result from this interaction, as shown above. The D3M could be particularly relevant for the low-field response of the recombination process. This is the consequence of two surprising effects. Firstly, in the presence of a third radical, the D3M-MFEs are to some degree immunised to the effect of strong exchange interactions, which are expected to reign in the recombination processes under bond-formation. Second, a feature resembling the low-field effect emerges from the D3M for randomly oriented samples. While this was anticipated based on a previous study (by the same authors) of idealised three-radical

systems (Keens, Bedkihal and Kattnig, 2018), it is remarkable that it generalises to the more realistic conditions (e.g. explicit consideration of recombination) used here and emerges despite the short lifetime of the three-radical system. This result demonstrates that, besides the RPM, the D3M is a second mechanism for a dedicated low-field response of radical reactions. An important conclusion of our study is that MFEs in lipid autoxidation, as well as more generally, could perhaps depend on the absolute radical concentrations as a consequence of its impact on the probability of three-radical encounters. This stipulates that studies of the effect of magnetic fields on biological systems should also report radical concentrations and procedures to ensure a constant radical background and antioxidant levels. Any parameter that impacts radical accumulation, e.g. light exposure, ought to be strictly controlled. In this context it is interesting to note that biological MFEs, i.e. MFEs on the level of cells or entire organisms, are often implicated with oxidative stress and/or radical promoting pre-exposures. Here has been established the plausibility of arguments of this form, and it is hoped that further experimental studies along these lines will be conducted, moving the field ever closer to a comprehensive understanding of the mysteries of MFEs in biology.

The main results for this chapter are:

- D3M effects are not abolished when hyperfine interactions are re-introduced.
- Unlike previous opinion in the literature, the concentration of radicals does in fact seem to affect the observed MFEs.
- Contrary to some of the controversy in the literature (previously addressed), lipid peroxidation reactions do indeed seem to have magnetosensitive reaction pathways.
- Following on from the geometric observation of chapter 3, optical isomerism has been shown to affect MFEs.

Experimentally, the next stage is to devise some tests that could be performed to examine these predictions, thus making a clearer link between these results and both the literature and physical reality. For example, it may be worth trying to

check that the magnitude of the LFE diminishes as the system gets more complex. This could be done for both more complex molecular structures, and higher radical concentrations. The effect of concentration could be taken from a physically relevant scenario like a radiotherapy protocol, in order to ground these predictions in physical relevance. There is an expected energy gap enlargement caused by the EED, even for planar membrane MFEs, so a similar EPR approach to that described at the end of chapter 3 could be taken here to find said splittings. It might also be interesting to deliberately use some species, e.g. superoxide, that are known to have no native hyperfine interactions to see if one can still measure the effects. If the sign of the MFE can be measured explicitly and reliably under these conditions, this could also be used as a way to show that the LFE manifests as predicted. Orientational effects could perhaps be tested by rotating static magnets.

5. How symmetry-breaking can amplify MFEs

This chapter is adapted from:

Keens, Robert H., Sampson, Chris and Kattnig, Daniel R. , How symmetry-breaking can amplify the magnetosensitivity of dipolarly coupled n-radical systems, The Journal of Chemical Physics 154(9), eprint: https://doi.org/10.1063/5.0041552,

with the permission of AIP Publishing.

In systems of more than two reactive radicals, the radical recombination probability can be magnetosensitive due to the mere effect of the inter-radical electron-electron dipolar coupling. Here, it is demonstrated that this principle, previously established for three-radical systems, generalizes to n-radical systems. The focus is on radical systems in the plane and the effects of symmetry are explored, in particular its absence, on the associated magnetic field effects (MFEs) of the recombination yield. It is shown, by considering regular configurations and slightly distorted geometries, that the breaking of geometric symmetry can lead to an enhancement of the magnetosensitivity of these structures. Further to this, it is demonstrated the presence of effects at low-field that are abolished in the highly-symmetric case. This could be important to the understanding of the behaviour of radicals in biological environments, in the presence of weak magnetic fields comparable to the Earth's, as well as the the construction of high-precision quantum sensing devices.

5.1 Introduction

In Chapter 3, D3M, which highlights the electron-electron dipolar (EED) coupling as a possible source of MFEs on radical recombination reactions in (partly) ordered, i.e. immobilized, systems of *three* radicals, was introduced as an alternative mechanism to offer a new perspective on biologically relevant chemical magnetosensitivity. The mechanism requires that more than two radicals simultaneously interact via the EED interaction, which can be the case even at low radical concentrations due to the slow decay of the dipolar interaction with distance (Keens, Bedkihal and Kattnig, 2018). D3M is distinct from other three-radical effects, such as the chemical Zeno effect, its use for quantum teleportation (Salikhov, Golbeck and Stehlik, 2007; Rugg et al., 2019), etc. as it realises an intrinsic magnetic field-sensitivity independent of hyperfine interactions. The effect has been suggested, as detailed in the previous chapter, to explain the putative magnetic field sensitivity of lipid autoxidation (Sampson, Keens and Kattnig, 2019), which is characterized by the recombination of radicals for which the hyperfine interaction is small compared to the EED coupling, and to enhance the cryptochrome compass sensitivity by an nonreactive "bystander" radical (Babcock and Kattnig, 2020). These findings are noteworthy insofar as in the RPM the effect of the EED interaction is well known to suppress MFEs in weak magnetic fields by energetically uncoupling the singlet and triplet manifolds, thereby suppressing their coherent interplay. On the other hand, the D3M effects appear to persist in the presence of both hyperfine and exchange interactions (Keens, Bedkihal and Kattnig, 2018; Sampson, Keens and Kattnig, 2019; Babcock and Kattnig, 2020).

In this chapter, D3M is generalised to treat larger systems of n spins, with $n \geq 3$, which shall be referred to as DnM. To the authors' knowledge, MFEs in systems of more than three radicals have not been studied at all in this context, and it is upon these systems that focus is primarily placed. Three-spin systems have been considered as a baseline for the DnM mechanism and built upon from there to observe new, surprising, and potentially biologically-relevant MFEs in these $n \geq 3$ systems.

This chapter is structured as follows: In Model and Computation the D3M

model is generalised to DnM, with $n \geq 3$, the pertinent parameters and assumptions of the model are summarised, and it is detailed how the Liovuille-von Neumann equation was solved for these systems. A qualitative model for DnM, based on an equipartitioning argument over accessible states for the case that one radical pair recombines, is also presented. In Results, characteristic features of DnM for selected systems are presented, whereby the focus is on planar systems, as inspired by (Sampson, Keens and Kattnig, 2019). The core theme is that systems with small geometric irregularities show stronger, more diverse MFEs, including new effects at low-field, when compared with their counterpart highly symmetric systems. Regular polygons are explored first, alongside their distorted counterparts, then move on to the special case of the linear chain.

With regard to the linear chains, the four-spin configuration forms the basis of the discussion but analogous results for three to six spins are further shown. Finally the results, their significance, and their potential applications to various areas of quantum biology are discussed in detail.

5.2 Model and Computation

Here, the premise of the *D3M* mechanism (Keens, Bedkihal and Kattnig, 2018), as shown in chapter 3, is used as the starting point, and extended to *DnM* with $n > 3$, where n is the number of interacting radicals. The effect of the oft-neglected electron-electron dipolar interaction is considered as the main contributor to MFEs. The DnM Hamiltonian (in angular frequency units) is thus:

$$\begin{aligned}\hat{H} &= \hat{H}_{dd} + \hat{H}_{ex} + \hat{H}_{Ze} \\ &= \sum_{i<j}^{N} \hat{\mathbf{S}}_i \cdot \mathbf{D}_{i,j} \cdot \hat{\mathbf{S}}_j - \sum_{i<j}^{N} J_{i,j} \left(\tfrac{1}{2} + 2\hat{\mathbf{S}}_i \cdot \hat{\mathbf{S}}_j \right) + \gamma \mathbf{B_0} \cdot \sum_{\mathbf{i}}^{\mathbf{N}} \hat{\mathbf{S}}_\mathbf{i},\end{aligned} \tag{5.1}$$

where the individual summands account for the electron-electron dipolar ($\hat{H}_{dd}$), exchange ($\hat{H}_{ex}$) and Zeeman interactions ($\hat{H}_{Ze}$). $\mathbf{B}$ denotes the applied magnetic field, B its intensity and $\gamma = \frac{g\mu_B}{\hbar}$ with g denoting the electron g-factor. The Larmor precession frequency is $\gamma B/2\pi$. Here, It has been assumed that the Zeeman

interaction is isotropic and identical for all radicals on account of the present focus on the MFEs of organic radicals in weak magnetic fields, i.e. $g \approx 2$; the anisotropies of g are negligible for moderate B.

The dipolar interaction Hamiltonian, calculated within the point-dipole approximation, is of the form:

$$\hat{\mathbf{S}}_i \cdot \mathbf{D}_{i,j} \cdot \hat{\mathbf{S}}_j = d_{i,j}(r_{i,j}) \left[\hat{\mathbf{S}}_i \cdot \hat{\mathbf{S}}_j - 3 \left(\hat{\mathbf{S}}_i \cdot \mathbf{e_{i,j}} \right) \left(\hat{\mathbf{S}}_j \cdot \mathbf{e_{i,j}} \right) \right], \quad (5.2)$$

where $\mathbf{e}_{i,j}$ is a unit vector in the direction of the vector connecting radical i and j at distance r_{ij} and:

$$d(r_{ij}) = \frac{\mu_0 g^2 \mu_B^2}{4\pi\hbar r_{ij}^3}. \quad (5.3)$$

Finally, the exchange Hamiltonian is:

$$\hat{H}_{ex} = -\sum_{i<j}^{N} J\left(|\mathbf{r}_{ij}|\right) \left(\frac{1}{2} + 2\hat{S}_i \cdot \hat{S}_j \right), \quad (5.4)$$

where $J\left(|\mathbf{r}_{ij}|\right)$ is the exchange coupling constant between the i^{th} and j^{th} radical.

Pairwise recombination was considered in this model. Making use of the Haberkorn approach (Haberkorn, 1976), this gives rise to a master equation of the form:

$$\frac{d\hat{\rho}}{dt} = -i\left[\hat{H}, \hat{\rho}\right] - \left[\hat{K}, \hat{\rho}\right]_+ - k_e\hat{\rho}, \quad (5.5)$$

where the bracket $[]_+$ denotes the anti-commutator and the recombination operator $\hat{K}$ is given by:

$$\hat{K} = \sum_{i<j} \frac{k_S\left(|\mathbf{r_{ij}}|\right)}{2} \hat{P}_{i,j}^{(S)}, \quad (5.6)$$

where $k_S\left(|\mathbf{r}|_{\mathbf{ij}}\right)$ represents the singlet recombination rate constant between radicals i and j. Here, $\hat{P}_{i,j}^{(S)}$ is the projection operator onto the singlet subspace of radicals i and j, which can be written in the form:

$$\hat{P}_{i,j}^{(S)} = \frac{1}{4}\hat{1} - \hat{S}_i \cdot \hat{S}_j. \quad (5.7)$$

.

Eq. 5.5 allows us to formulate the time-dependent density matrix as:

$$\hat{\rho}(t) = \exp(-k_e t)\exp(-i\hat{A}t)\hat{\rho}(0)\exp(i\hat{A}^{\dagger}t), \tag{5.8}$$

where k_e is the escape rate constant and $\hat{A}$ is a non-Hermitian effective Hamiltonian operator that accounts for coherent evolution and recombination:

$$\hat{A} = \hat{H} - i\hat{K}. \tag{5.9}$$

In eq. 5.8, an initial density matrix, $\hat{\rho(0)} = \hat{1}/2^n$, proportional to the identity matrix, was used to simulate a random initial spin configuration.

The reaction yields can be evaluated by finding the eigenvalues and eigenvectors of the effective Hamiltonian, denoted by λ and T respectively, and then computing the time-integrated density matrix from:

$$\begin{aligned} &\int_0^{\infty} \rho_{ij}(t) = \\ &\sum_{k,l,m,n} T_{i,k}T^{-1}_{k,l}\rho_{l,m}(0)(T^{-1})^{*}_{k,m}T^{*}_{j,n}\frac{1}{k_e + i(\lambda_k - \lambda_k^{*})}, \end{aligned} \tag{5.10}$$

where subscript indices denote matrix elements. Taking these quantities together, the singlet recombination yield can be calculated:

$$\varphi_S = 2Tr\left[\int \hat{\rho}(t)dt\hat{K}\right], \tag{5.11}$$

which was used to quantify the effect that the applied magnetic field has upon the recombination yield by defining the magnetic field effect (MFE) as:

$$\chi_S(B) = \frac{\varphi_S(B) - \varphi_S(0)}{\varphi_S(0)}, \tag{5.12}$$

where $\varphi_S(B)$ is the singlet yield at an applied field of intensity B, and $\varphi_S(0)$ is the same quantity at zero-field.

In general, the MFE depends on the geometry of the recombining radicals due to the distance-dependence of the EED interaction and of the parameters k_S and

J. For the latter parameters, both are assumed to have an exponential fall-off in keeping with the typical distance dependence of the electron coupling matrix element dictating electron transfer reactions. These take the form:

$$k_S(|\mathbf{r}_{ij}|) = k_{S,0} \exp(-\beta(|\mathbf{r}_{ij}| - 2R) \tag{5.13}$$

and

$$J(|\mathbf{r}_{ij}|) = J_0 \exp(-\beta(|\mathbf{r}_{ij}| - 2R). \tag{5.14}$$

In both of the above, the same decay rate, $\beta = 1.4$ Å^{-1} has been used. R is a reference distance, which can be interpreted as the radical radius; here it was fixed at 7.5 Å. For $r_{ij} = 2R$, $d_{1,2}$ thus was 15MHz. $k_{S,0}^{-1}$ was 200ns, and k_e^{-1} was 1 μs. B was varied between 0.001 and 1000 mT and it was perpendicular with respect to the plane of the reacting radicals. Solving eq. 5.5 in has been implemented in Python, whereby an MKL-based implementation was relied upon for solving the eigenvalue problem for non-Hermitian matrices. The computer code used is a generalisation of that described in ref. (Keens, Bedkihal and Kattnig, 2018) for more than three-radicals; this is included at the end of the Appendix. It covers an arbitrary number of radicals including all interactions named above, in addition to hyperfine interactions, if desirable. Being based on the eigenvalue decomposition of the effective Hamiltonian, it aims at systems of moderate size. Larger systems could in principle by treated by a Monte Carlo wavefunction approach (Keens and Kattnig, 2020), but are beyond this presentation.

5.3 A qualitative model of magnetosensitivity of a radical pair recombining in an environment of radicals

A qualitative model that accounts for the MFEs of the kind discussed here can also be offered. To this end, consider a pair of electron spins (radicals devoid of hyperfine interactions) poised to undergo a spin-selective recombination reaction

in the singlet state. Assume further that a reactive pair of spins interacts with an environment of radicals, which are assumed unreactive, e.g. due to being too distant to react or intrinsically unreactive. All $n = \ell + 2$ radicals are assumed to interact via EED interactions. Assuming that reactive radical pair is born in the singlet configuration, it can be asked with which probability it will still be in the singlet configuration at the moment of reaction. If the radical system is long-lived, the recombination reaction slow and decoherent channels are insignificant, one can assume that in first approximation the singlet probability upon recombination is obtained by equipartitioning the initial population over all accessible spin states. In weak magnetic fields for a random, i.e. asymmetric, geometric arrangement of spins with equally arbitrary magnetic field orientation, all spin states will be coupled by the EED interaction. Consequently, the long-time singlet probability will be $\frac{1}{4}$. This also applies to an arbitrary, i.e. non-special, spin configuration in a plane. While here the Hamiltonian can be decomposed into two blocks (assume that the plane is perpendicular to the z-direction; the EED direction then only couples states with a difference of total spin projection of $\Delta M = \pm 2$, giving rise to two blocks), the singlet probability still turns out as $\frac{1}{4}$. In high magnetic fields, on the other hand, the Zeeman interaction is dominant and states of different total spin projection $M = \sum_i m_i$ are energetically separated such that no spin mixing, i.e. singlet state redistributing, is possible between these states (while it remains intact within). The number of ways by which the additional spins (with index 3 to n) can produce a combined spin projection of $M_{3,\ldots,n} = \sum_{i=3}^{n} m_i$ is $\binom{\ell}{M_{3,\ldots,n}+\frac{\ell}{2}}$. A particular M can then be realized by combining the singlet state of the reactive radical pair with the $M_{3,\ldots,n} = M$ states of radical 3 to n, or combining the T_0 state of the reactive radical pair with the $M_{3,\ldots,n} = M$ states of radical 3 to n, or combining the T_+ state of the reactive radical pair with the $M_{3,\ldots,n} = M - 1$ states of radical 3 to n, or combining the T_- state of the reactive radical pair with the $M_{3,\ldots,n} = M + 1$ states of radical 3 to n. Thus, the number of states of projection M is

$$s(k) = \binom{\ell}{k-1} + 2\binom{\ell}{k} + \binom{\ell}{k+1}, \tag{5.15}$$

where $k = M_{3,\ldots,n} + \frac{\ell}{2}$. As the singlet configuration of spin 1 and 2 with projection specified by k is initially generated in $\binom{\ell}{k}$ ways, and the total number of initial singlet states is 2^ℓ and only the singlet pairs recombine, the singlet fraction in the equilibrated system is

$$\begin{aligned} p_{S\to S}(\text{high field}) &= \frac{1}{2^\ell}\sum_{k=0}^{\ell}\frac{1}{s(k)}\binom{\ell}{k}^2 \\ &= \frac{\ell^2+3\ell+4}{4(\ell^2+3\ell+2)} \\ &= \frac{1}{4}+\frac{1}{2n(n-1)}. \end{aligned} \tag{5.16}$$

Finally, the magnetic field effect is

$$\chi_{s\to S} = \frac{p_{S\to S}(\text{high field}) - p_{S\to S}(\text{low field})}{p_{S\to S}(\text{low field})}. \tag{5.17}$$

This suggests that the MFE ought to decrease with n, which is exactly what is found here for systems of related geometry. Practically, as can be seen below, in systems of diverse mutual reaction possibilities and a symmetric or broken symmetrical configuration, a rich variety of MFEs ensues, which cannot possibly be grasped by the argument presented here. Yet, this discussion provides at least a qualitative description of the origin of the MFEs (in a particular scenario). An analogous analysis can be carried out for a radical pair born in the triplet configuration and recombining as a singlet state. As $p_{T\to S} = \frac{1}{3}(1 - p_{S\to S})$, the singlet probability in low fields is $\frac{1}{4}$ and in high fields

$$p_{T\to S}(\text{high field}) = \frac{1}{4} - \frac{1}{n(n-1)}. \tag{5.18}$$

The naïvely predicted MFE is

$$\chi_{T\to S} = -\frac{2}{3n(n-1)}. \tag{5.19}$$

5.4 Results

Here, planar systems of up to six radicals have been considered with the magnetic field applied perpendicular to the plane of the radicals. While it may seem most natural to consider regular polygons, simplices or an evenly-spaced linear arrangement (spin chain) when generalizing D3M to more than three radicals, it was found that the MFE profiles of such systems can be markedly changed, and often enhanced, with respect to the weak-field sensitivity by the introduction of a small imperfection.

Specifically, regular polygons of up to six spins (point group D_{nh}), and linear spin chains of three to six spins have been considered within the present study. Schematics of the considered geometries and small imperfections introduced into the regular structures can be seen in Figs. 5.1 (polygons) and 5.2 (linear chains). The distortions used were small, and enacted upon one spin at a time. An example pertinent to the distortions in regular polygons is the square systems presented in Fig. 5.1, which differ geometrically only in the position of one spin. The cases of both a small tangential distortion (by 0.75 Å or 1.5 Å) and a radial distortion (1.5 Å) have been explored. The quantity $d = 2R$ is representative of the distance between radicals, and was fixed to 15 Å for all but displaced neighbouring spins. Similar small distortions were applied to the other polygons studied. The coordinates of all geometries are reported in the appendix 9.9.

With regard to the linear chains, two generic cases were considered: that of a distortion occurring at the end of the chain ($L_{n,n}$ in Fig. 5.2) and that of a shift in the chain originating at a location within it ($L_{n,m}$ ($m \neq n$) in Fig. 5.2). For the latter case, for in-axis displacements, all spins following the displaced radical were likewise rearranged to preserve the inter-spin distances between all but one pair of spins in the chain (in the same way as moving the end spin would affect only one pair, i.e. the terminal spin and its only neighbour). For all distortions, the minimal distance of radicals was $2R$. Within these two generic cases, distortions in each axial direction were considered independently of each other, that is, a distortion along either x, y, or z, the latter of which agrees with the direction of the applied magnetic field.

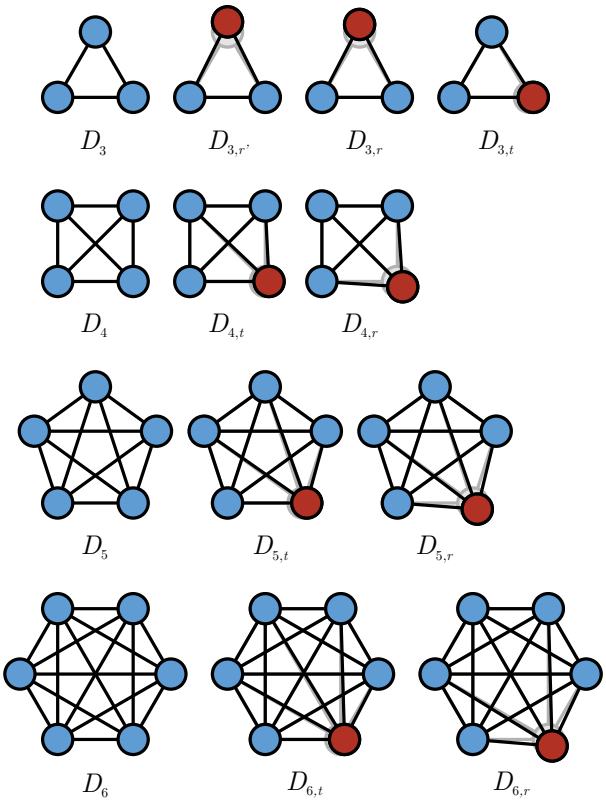

Figure 5.1: Schematics of the distortions introduced into the regular polygon geometries. The spins highlighted in red show the areas a which a distortion was applied. The shadowy regions denote the undistorted geometries. The distorted geometries are shown next to the regular geometries (labelled D_n) to illustrate how minor the applied distortions are in comparison with the regular structure, with guiding lines between spin pairs included to highlight subtle changes in the overall symmetry of the shape and thus the interaction parameters in the spin Hamiltonian. In essence, radial and tangential displacements of one spin are considered, indicated by the subscript labels "r" and "t", respectively. Here, a displacement of 0.05 and 0.1 parts of the inter-spin distance ($2R$) were assumed for the "t" and "r"-variants, respectively. For the triangular geometry both a smaller ($0.1 \times 2R$; $D_{3,r}$) and a larger radial displacement ($0.133 \times 2R$; $D'_{3,r}$) have been considered.

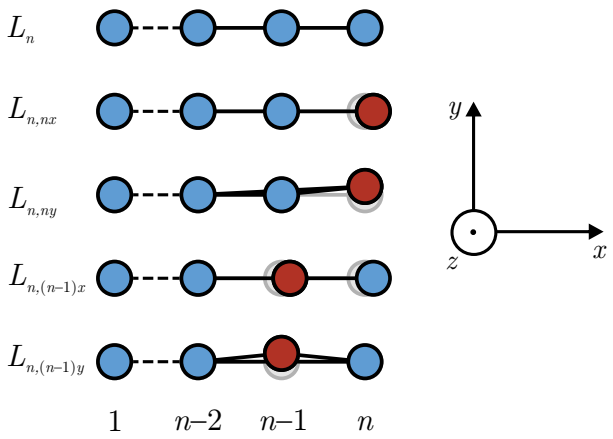

Figure 5.2: Schematics of the distortions introduced into the linear chain geometries. The L_n case at the top shows the generic labelling convention for a linear chain of n spins, and the spins highlighted in red show the areas a which a distortion was applied. The shadowy regions highlight the difference between the regular and distorted geometries. Distortions for which the red spin is displaced perpendicular (labelled as "y" and "z", which are perpendicular and parallel to the applied magnetic field direction) or parallel ("x") to the spin chain axis have been considered. For the x-displacements of the ith spin, all spins following the ith were also displaced in order to maintain the same inter-spin distance of $2R$ for all but the $(i-1,i)$-pair.

Analysis is commenced by considering the MFEs predicted for the polygonal structures. For the square-geometries of four spins, Fig. 5.3 shows the MFE on the recombination yield in the singlet state, $\chi_S(B)$, as a function of the applied magnetic field, B, and the exchange interaction J_0. The MFE here is reproduced for the regular square geometry (D_4) and the radial ($D_{4,r}$) and tangential ($D_{n,t}$) distortions. In addition, Fig. 5.4 provides MFE data for the regular and radially distorted pentagon. It was found that all structures considered exhibit a rich variety of MFEs, whereby the recombination yield is attenuated in high fields. This is in line with the predictions of the naive, qualitative model introduced above, provided that (within this model) the initial state is assumed to be the triplet state of the recombining pair. While the detailed simulations assumed a random initial spin configuration, fast recombination in the singlet state is indeed expected to give rise to spin dynamics resembling that of a triplet-born pair. The detailed calculations also reproduce the naive prediction insofar as the high-field MFEs are decreasing with increasing number of interacting spins, n. Indeed, MFEs of up to -0.28, -0.17, -0.11 and -0.06 were found for the regular polygons with n ranging from 3 to 6. What is unexpected though is the behaviour upon minor geometrical distortions, as described

next.

With reference to Fig. 5.3 and 5.4 (see Fig. 5.5 for the full version of the pentagonal case - zoomed in here for ease and closeness of comparison with Fig. 5.3), it is apparent that for the undistorted geometries, e.g. D_4 and D_5, the strongest MFEs are confined to regions of weak exchange, and that there are very few regions, if any, of low-field sensitivity. However, applying minor geometrical distortions, such as $D_{4,r}$, $D_{4,t}$ or $D_{5,r}$ in Figs. 5.3 and 5.4, the emergence of new regions of strong sensitivity to moderate-to-high field intensities at moderate exchange, and new regions of weak-field sensitivity, can be seen. In particular, it is remarkable that the distortions often span new low-field effects below 1 mT and, in part, at field intensities comparable to the Earth's magnetic field and lower, that were completely abolished in the high-symmetry case. What is particularly noteworthy here is that these low-field effects can emerge for comparably strong exchange coupling constants. For the distorted D_5-geometries, e.g., the low-field effects clearly extend beyond the considered window of $|J_0| < 3d_{1,2}$ (see Fig. 5.4). In higher fields, it is likewise found that the primary peak of sensitivity is split to yield several regions of strong moderate-to-high field sensitivity extending to larger, in absolute value, exchange coupling. Taken together, these observations suggest that the distortion grants resilience to the suppressive effects that the exchange interaction usually exerts by energetically decoupling singlet and triplet states. Of further interest is the fact that the effects produced by $D_{n,r}$, $D_{n,t}$, are very different. This suggests that it not only matters *that* axes of symmetry are broken, but *how* this symmetry-breaking occurs. As for the magnitude of the maximal effects, it is found that in the majority of cases studied, the maximal $|\chi_S(B)|$ are comparable for distorted and regular geometries.

5.5 Linear Chains

The analysis continues with a discussion of the linear spin chains. Figs. 5.6 - 5.9 shows, for linear systems of between three and six spins (inclusive and respective), the recombination yield in the singlet state as a function of the applied magnetic field and the exchange interaction J_0 between pairs of spins in both perfect (evenly-spaced)

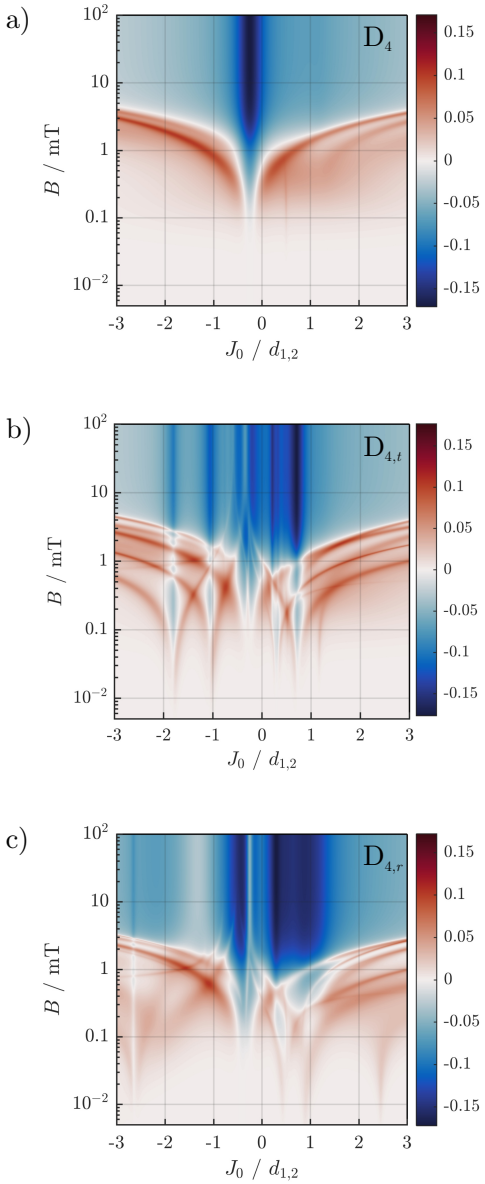

Figure 5.3: Heatplots showing the MFE, $\chi_S(B)$ of the square geometries as a function of the exchange coupling parameter J_0 and the magnetic field flux density, B. Panel a) shows the profile obtained for the perfect square geometry D_4, b) from distortion $\mathrm{D}_{4,t}$ and c) from $\mathrm{D}_{4,r}$. It can be seen that the two distorted geometries show numerous new regions of sensitivity across all magnetic field strengths and exchange interactions studied.

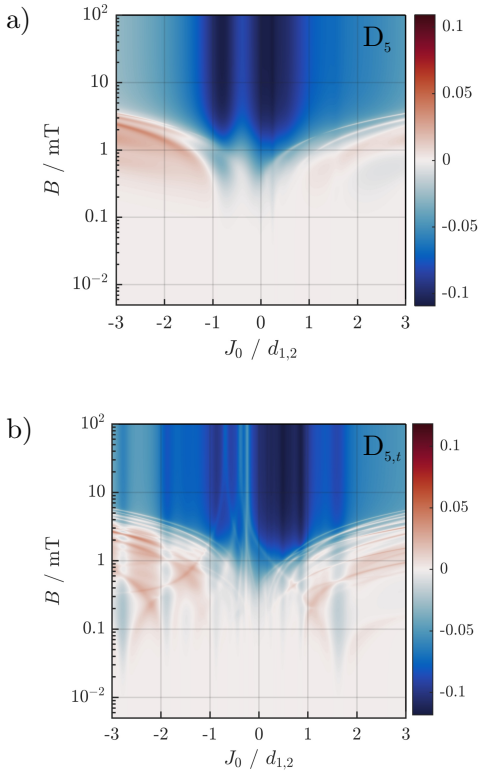

Figure 5.4: Heatplots showing the MFE, $\chi_S(B)$ of two pentagonal geometries as a function of the exchange coupling parameter J_0 and the magnetic field flux density, B pentagonal geometries. Panel a) shows the profile obtained from the perfect pentagonal geometry D_5 and panel b) that from $D_{5,t}$. It can be seen that the distorted geometry shows numerous new regions of sensitivity not available in the highly-symmetric case.

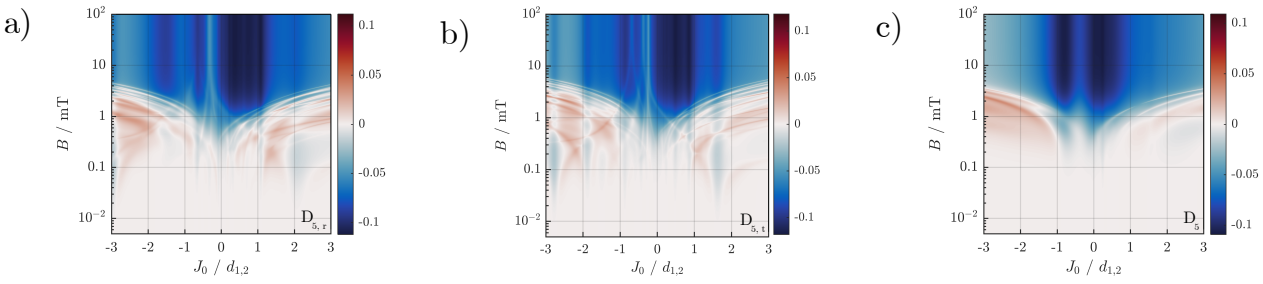

Figure 5.5: MFE profiles for the pentagonal geometries. a) shows the profile obtained by a radial distortion of one spin by 1.5Å, b) shows that for a tangential displacement of one spin by 1.5Å, and c) shows the control case of the regular pentagon.

and imperfect variations; cf. Fig. 5.2 for illustrations of the nature of the distortions. The three-spin system has attracted particular interest in the perfect case due to the emergence of a sharp spike (as discussed in chapter 3) of the singlet yield resulting from a level crossing in low magnetic fields (Keens, Bedkihal and Kattnig, 2018). Such spikes in MFE profiles are indicative of a region of high magnetic sensitivity, as could potentially be realized in an optimized quantum navigational device design.

The linear chains share common features that are evident for all n studied. In the symmetric case (exemplified by L_4 in Fig. 5.7, panel a), the MFE is characterized by a sharp feature of positive χ_S for negative J_0, which extends to low field intensities, and a broad plateau of negative χ_S for positive J_0 and large B. With increasing n, the maximal absolute value of the MFE is reduced (in agreement with the qualitative model from above), the sharp low-field feature of positive χ_S is split into an increasing number of components extending over an increasingly larger range of J_0, and the high-field plateau of negative χ_S broadens. Again, distortions, even if only minor (by less than 10 % of the inter-spin distance), can have marked effects on the MFE. For example, $L_{4,3x}$ (Fig. 5.7, panel d) shows an overall amplification of the MFEs relative to the symmetric case, as well as a new region of weak-field sensitivity not accessible for the latter. $L_{4,4x}$ (panel e) also shows new (but different) areas of weak-field sensitivity, again showing that the particulars of the distortion are actually important to the alterations in the MFE profile. The y-distortions, e.g. $L_{4,4y}$ (see Fig. 5.7, panel c) on the other hand are overall attenuating the MFE, but do still produce a new region of sensitivity to moderate-to-high field intensities at strong exchange, thus providing exchange resilience not afforded by the symmetric case. Finally, z-distortions, e.g. $L_{4,3z}$ (Fig. 5.7 panel f), show more subtle effects, the most significant deviation from the symmetric case consisting in the emergence of moderate-intensity weak-field effects at strong exchange. Other linear chains show effects in a similar pattern to that described for L_4. For example, for $n = 5$ too, the most notable amplifications is provided by the x-distortions, $L_{5,4x}$ and $L_{5,5x}$ (see Fig. 5.8). In general, considering the combined data, one can see three effects of small-scale distortions: a) The onset of MFEs is more pronounced and occurs at

more diverse exchange interactions for distorted geometries. b) Distorted geometries produce new MFEs at high fields. c) Distorted geometries are more resilient to strong exchange interactions. As for the mechanistic underpinning of the effect, one can observe that weak-field MFEs are strongly impacted by quantum level (anti-)crossings as a function of the applied magnetic field. Distorting the geometry these interactions become more diverse and in some cases true crossings become avoided crossings (Keens, Bedkihal and Kattnig, 2018). Such points are the regions of highest sensitivity, and are represented as the sharpest regions in the MFE profile of a system. For a qualitative illustration of how level crossings are influenced, see Fig. 9.10 in the appendix.

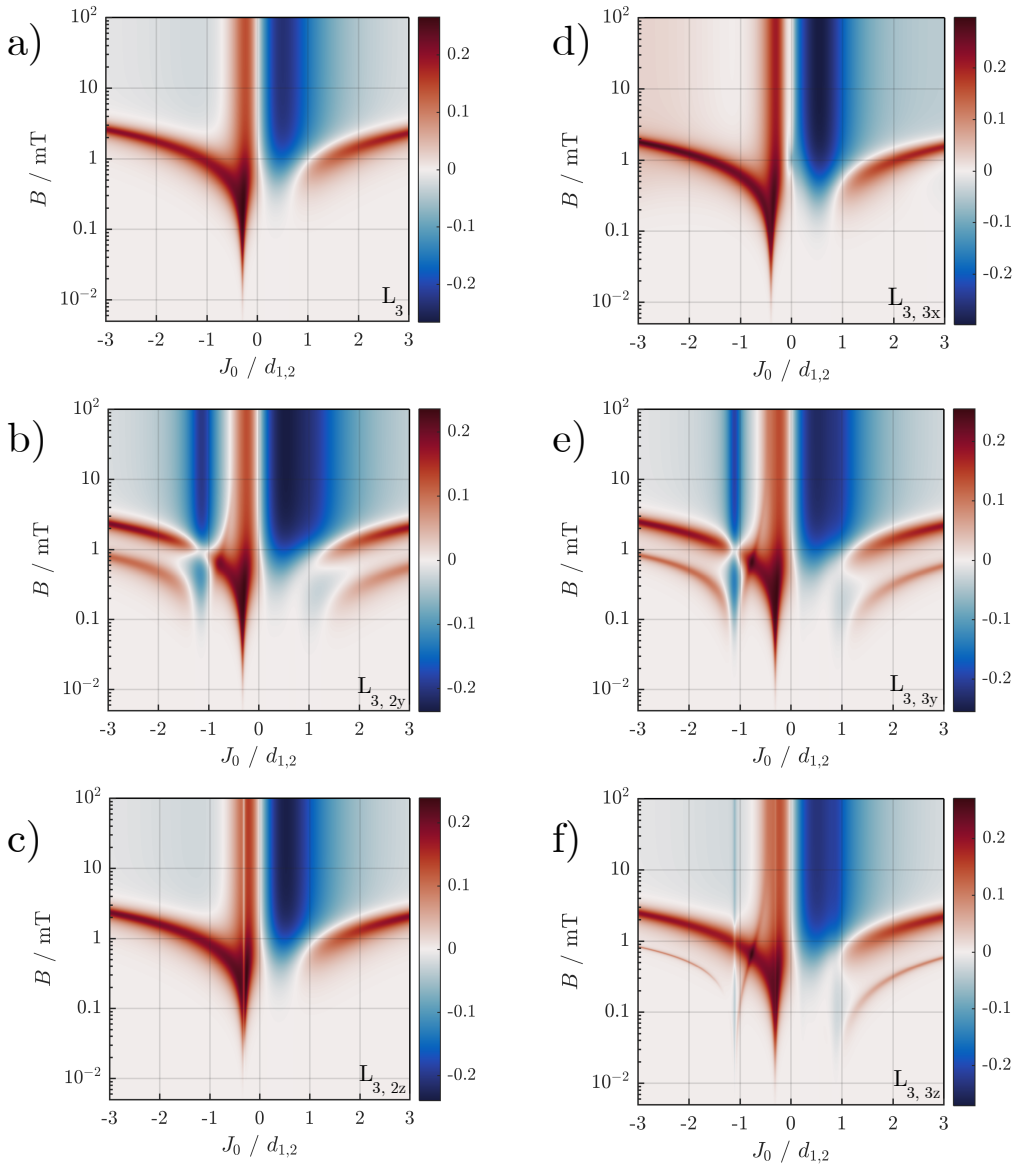

Figure 5.6: MFE profiles for the linear 3-spin geometries. a) shows the control case of the evenly-spaced chain. b) shows the profile obtained from a 1.5 Å displacement of spin 2 in the y-direction, c) shows the profile obtained from a 1.5 Å displacement of spin 2 in the z-direction, and d) - e) show the profiles obtained from a 1.5 Å displacement of spin 3 in the x-, y- and z-directions respectively.

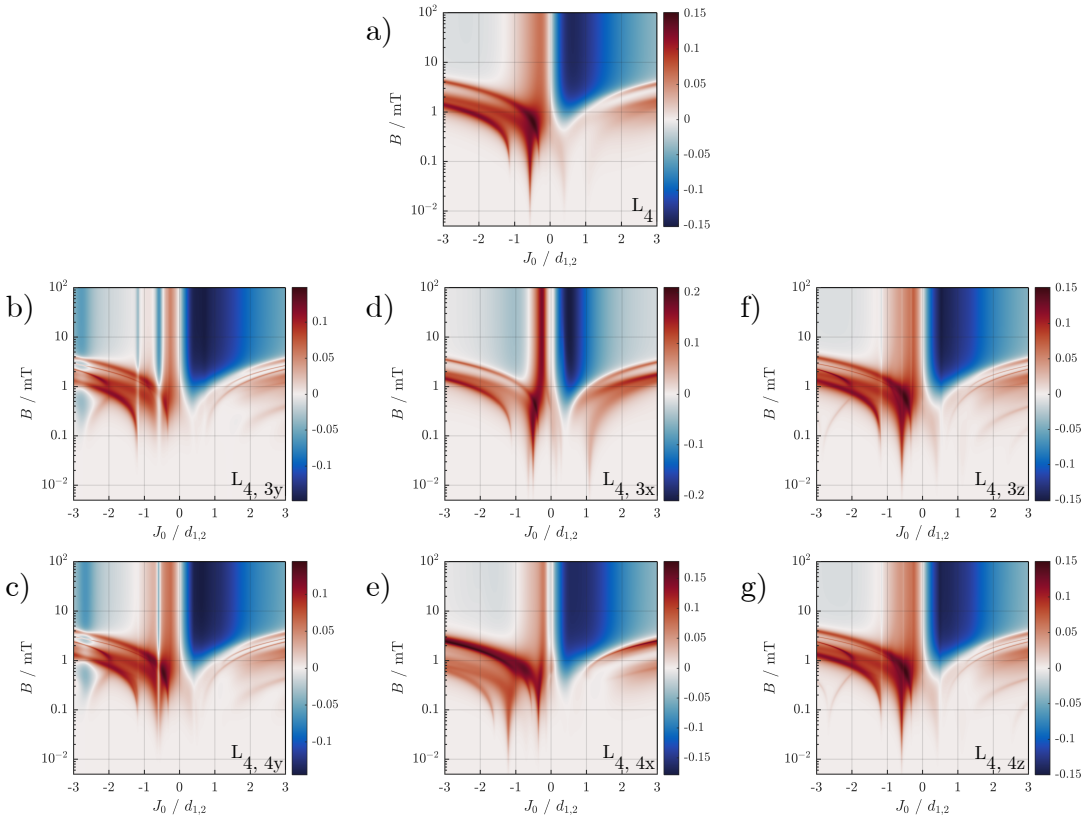

Figure 5.7: MFE profiles for the linear 4-spin geometries. a) shows the control case of the evenly-spaced chain. b) and c) show the profiles obtained from a 1.5 Å displacement of spin 3 and 4, respectively, in the y-direction, d) and e) show the profile obtained from a 1.5 Å displacement of spin 3 and 4, respectively, in the x-direction, and f) and g) show the profiles obtained from a 1.5 Å displacement of spin 3 and 4, respectively, in the z-direction.

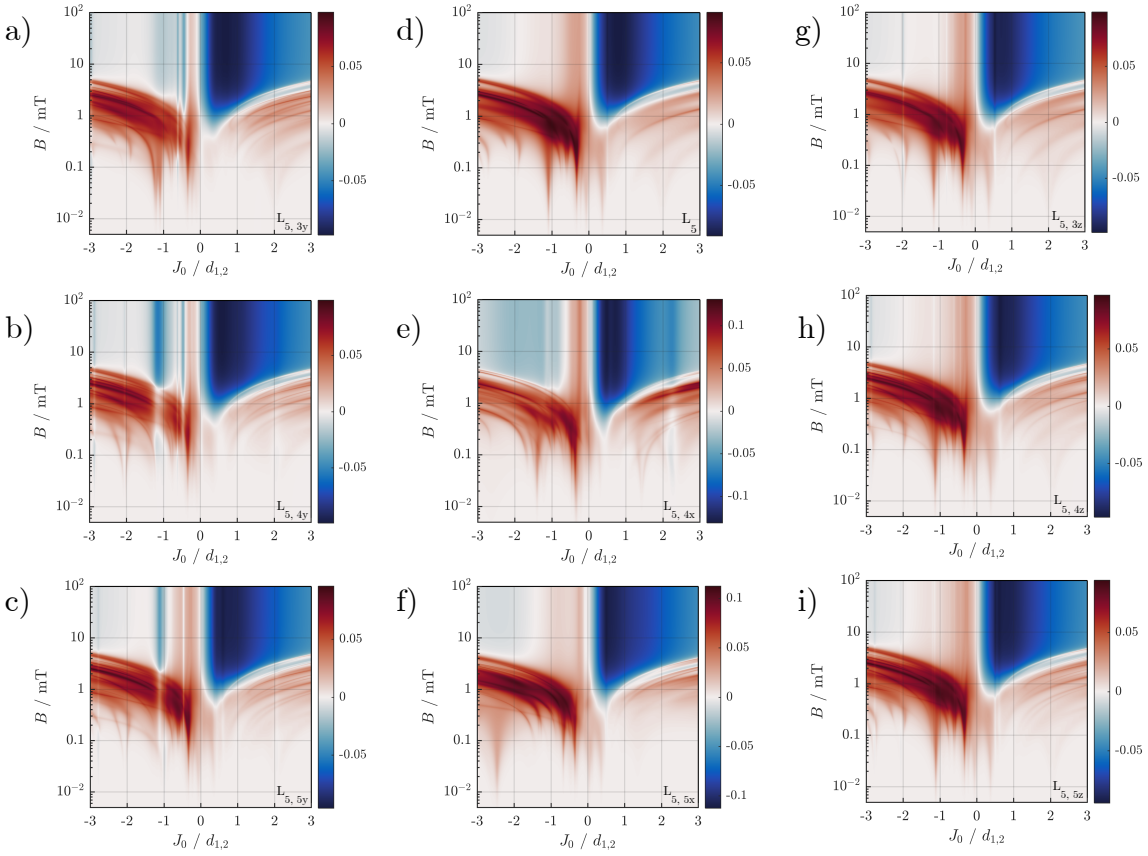

Figure 5.8: MFE profiles obtained from distorting the five-spin linear geometry. Panel d) shows the control case of the evenly-spaced chain, L_5. Panels a) - c) show the distortions in the y-direction: $L_{5,3y}$ and $L_{5,4y}$, and $L_{5,5y}$ respectively. Panels e) and f) show the distortions in the x-direction: $L_{5,4x}$ and $L_{5,5x}$, respectively. Panels g) - i) show the distortions in the z-direction: $L_{5,3z}$ and $L_{5,4z}$, and $L_{5,5z}$ respectively.

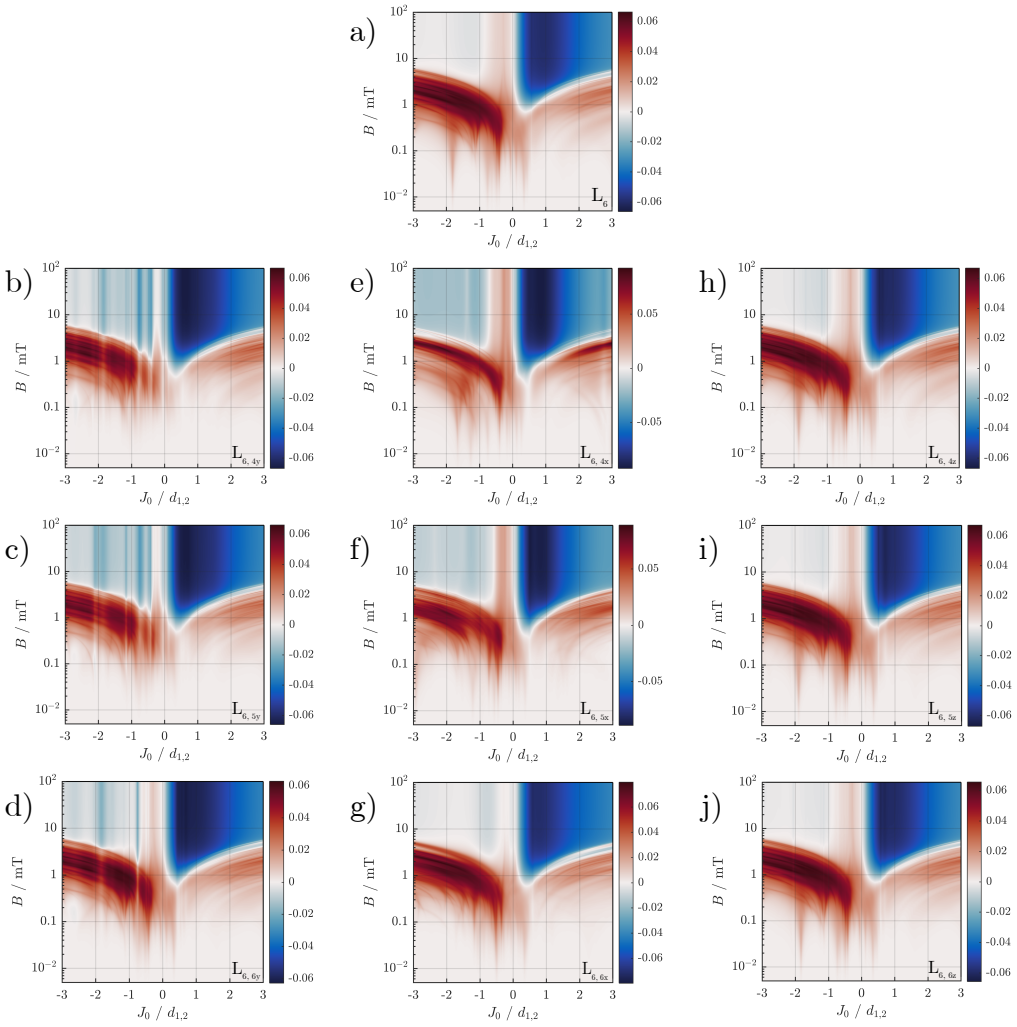

Figure 5.9: MFE profiles for the linear 6-spin geometries. a) shows the control case of the evenly-spaced chain. b) - d) show the profiles obtained from a 1.5 Å displacement in the y-direction of spins 4, 5, and 6 respectively. e) - g) show the profiles obtained from a 1.5 Å displacement, in the x-direction, of spins 4, 5, and 6 respectively and h) - j) show the profiles obtained from a 1.5 Å displacement, in the z-direction of spins 4, 5, and 6 respectively.

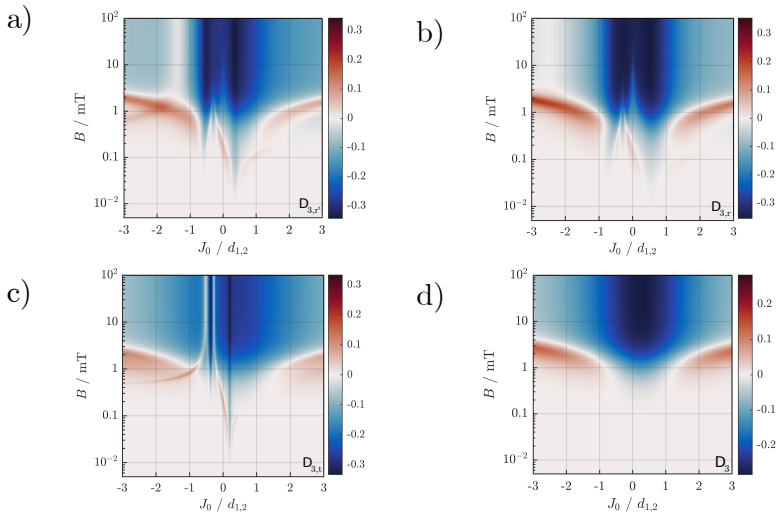

Figure 5.10: MFE profiles for the triangular geometries. a) and b) show the profiles obtained for radial distortions of the apical spin, by 1.5 Å and 2.01 Å respectively. c) The tangential displacement of one spin by 1.5Å. d) The control case of the perfect equilateral triangle.

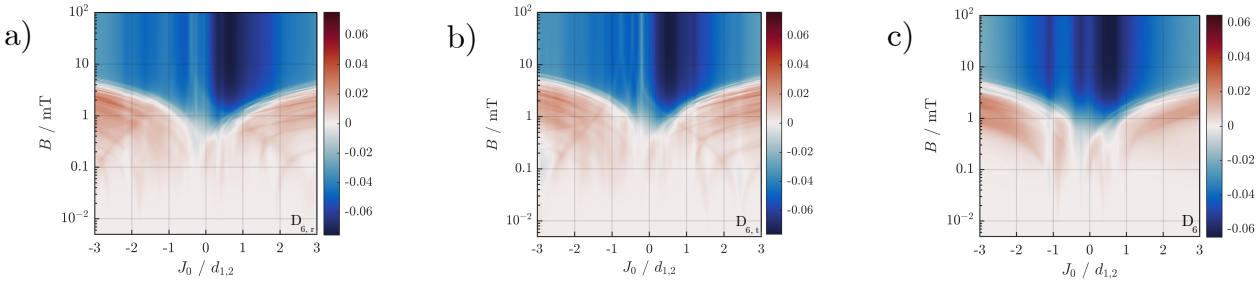

Figure 5.11: MFE profiles for the hexagonal geometries. a) shows the profile obtained by a radial distortion of one spin by 1.5Å, b) shows that for a tangential displacement of one spin by 1.5Å, and c) shows the control case of the perfect hexagon.

5.5.1 Even smaller distortions produce the same effects

In many cases, even minor distortions can somewhat enhance the effect (e.g. for $D_{3,r}$ the maximal absolute MFEs increases from 0.28 to 0.34 employing only a minor radial displacement of 5% of the inter-radical distance; similar effects are seen for the central x-displacements of linear chains; see below).

Similar conclusions can be drawn for the triangular geometry, and larger polygons, in that applying a small distortion and thus breaking some of the axes of symmetry again amplifies the effects at low-field and produces sensitivity to fields of geomagnetic field strength and even lower, at more diverse values of the exchange parameter. See Figs. 5.10 and 5.11 for figures analogous to the discussed pentagonal and square cases. See also Figs. 5.12 - 5.14 for an illustration that even a radial

distortion as small as 0.75 Å is sufficient to produce the effects shown here for 0.75 Å displacements.

5.6 MFE measure

In order to quantitatively capture the observations qualitatively summarised above, a new measure $M(B)$, is introduced defined by:

$$M(B) = \frac{1}{\Delta J} \int |\chi_S(B,J)|_{\text{dist}} - |\chi_S(B,J)|_{\text{per}} dJ, \tag{5.20}$$

where $|\chi_S(B,J)|_{\text{dist}}$ is the absolute value of the MFE at a particular value of field B of the distorted geometry, and $|\chi_S(B,J)|_{\text{per}}$ is the same quantity for the perfect geometry. ΔJ is the range of exchange values that the integral is evaluated for; the same exchange region was used as in the density plots above, i.e. J_0 ranging from $-3d_{1,2}$ to $3d_{1,2}$ and, thus, $\Delta J = 6d_{1,2}$. A positive value of $M(B)$ indicates that, at the magnetic field B, on the average the MFE is enhanced by the distortion for the considered range of exchange interactions.

$M(B)$ has been evaluated for the analysed geometries (using Simpson quadrature). The results are shown in Figs. 5.15 and 5.16. In these figures one can see that $M(B)$ is almost always positive for weak to moderate magnetic fields. The dose dependence shown in these figures represents a significant deviation from the theoretical curves predicted by the conventional RPM (cf. Hayashi and Nagakura, 1984, Fig. 6.2). One can see from the referenced figure that the canonical RPM predicts a clearly biphasic dose-response, where the two distinct curves were proposed to allow one to infer the spin of the precursor (i.e. by comparing the experimental dose-response measurements to these curves, and matching the shape to either the S- or T- response). The figures in this chapter, however, show a much richer, more diverse, profile than the simple biphasic response previously predicted, and it is hoped that these results will allow new ways for experimentalists to interpret their biological data. It has been shown in previous chapters that the D3M mechanism is capable of recreating the effects predicted by the conventional RPM. However, here

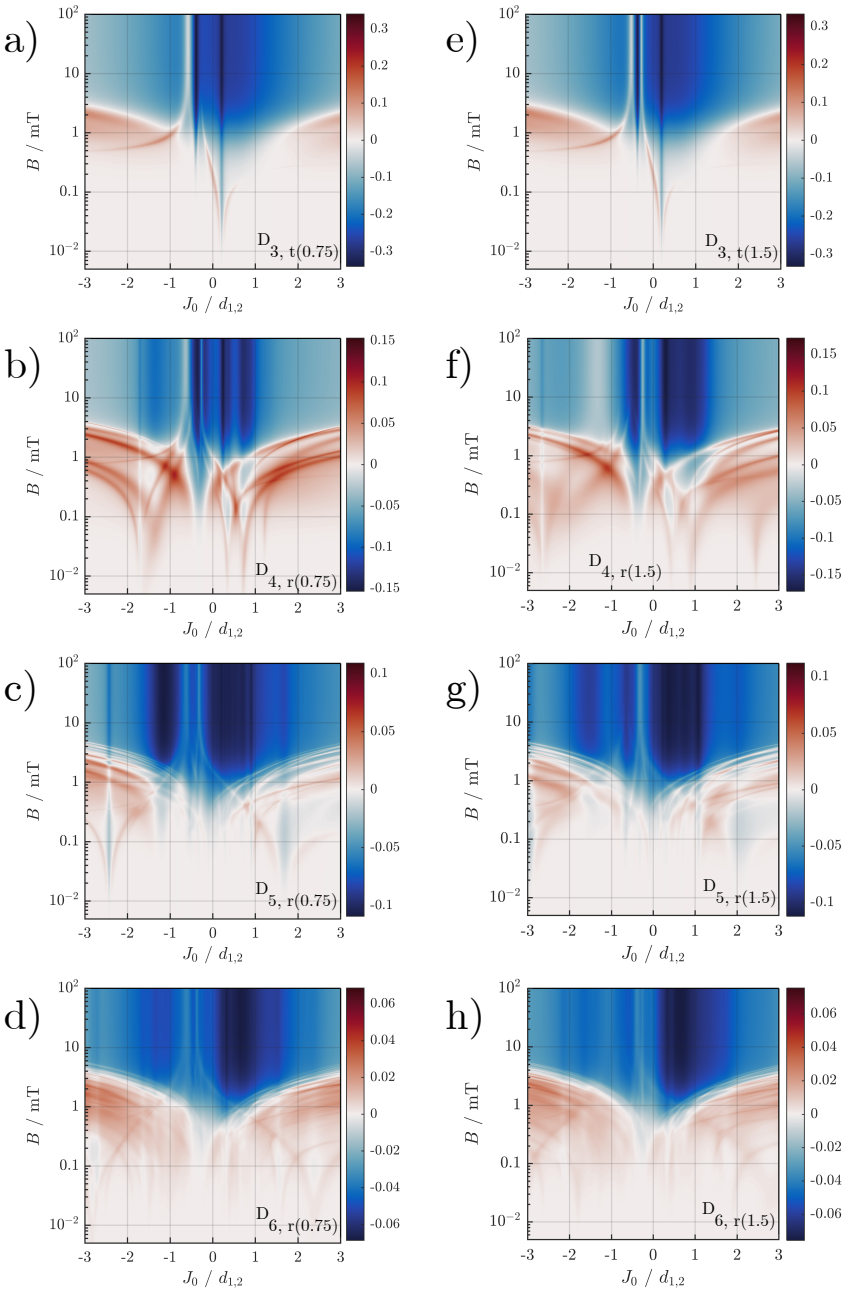

Figure 5.12: A comparison showing that, in fact, 0.75 Å is sufficient to realise the observed effects in the planar geometries studied. The left-hand side of the figure shows the systems distorted by 0.75 Å, and the right-hand side shows the counterpart to each distorted instead by 1.5 Å. From top to bottom, the rows contrast the triangular case (tangentially distorted), the square case (radially distorted), the pentagonal case (radially distorted) and the hexagonal case (radially distorted).

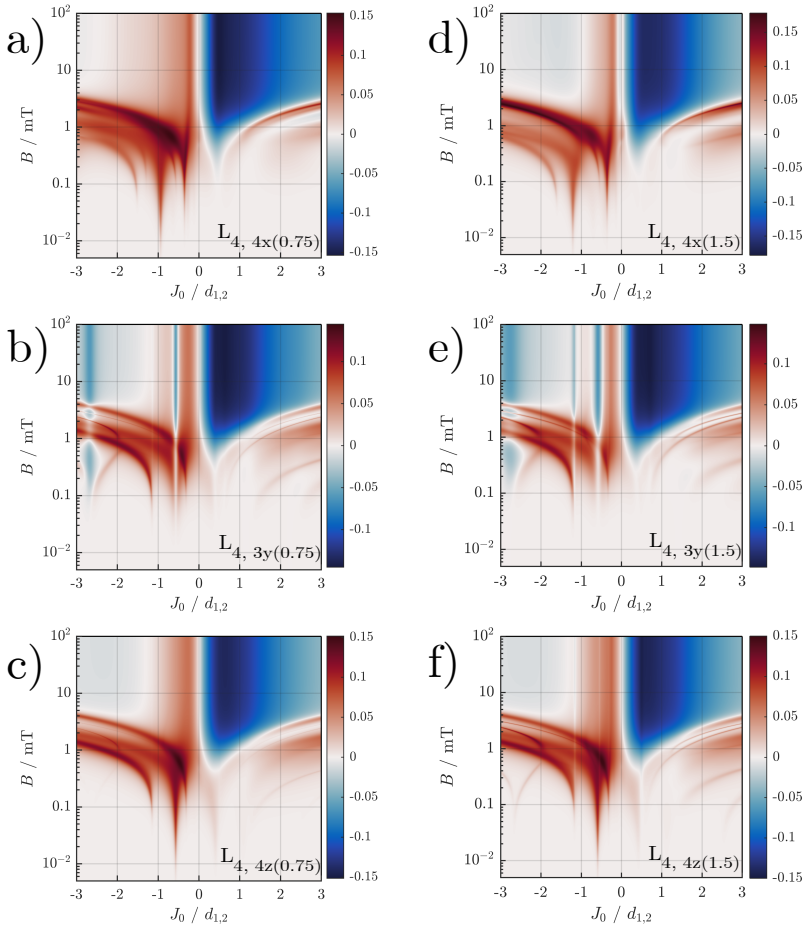

Figure 5.13: A comparison showing that, in fact, 0.75 Å is sufficient to realise the observed effects in the 4-spin linear geometries studied. The left-hand side of the figure shows the systems distorted by 0.75 Å, and the right-hand side shows the counterpart to each distorted instead by 1.5 Å. From top to bottom, the rows contrast displacements of spin 4 in the x-direction, spin 3 in the y-direction, and spin 4 in the z-direction, respectively.

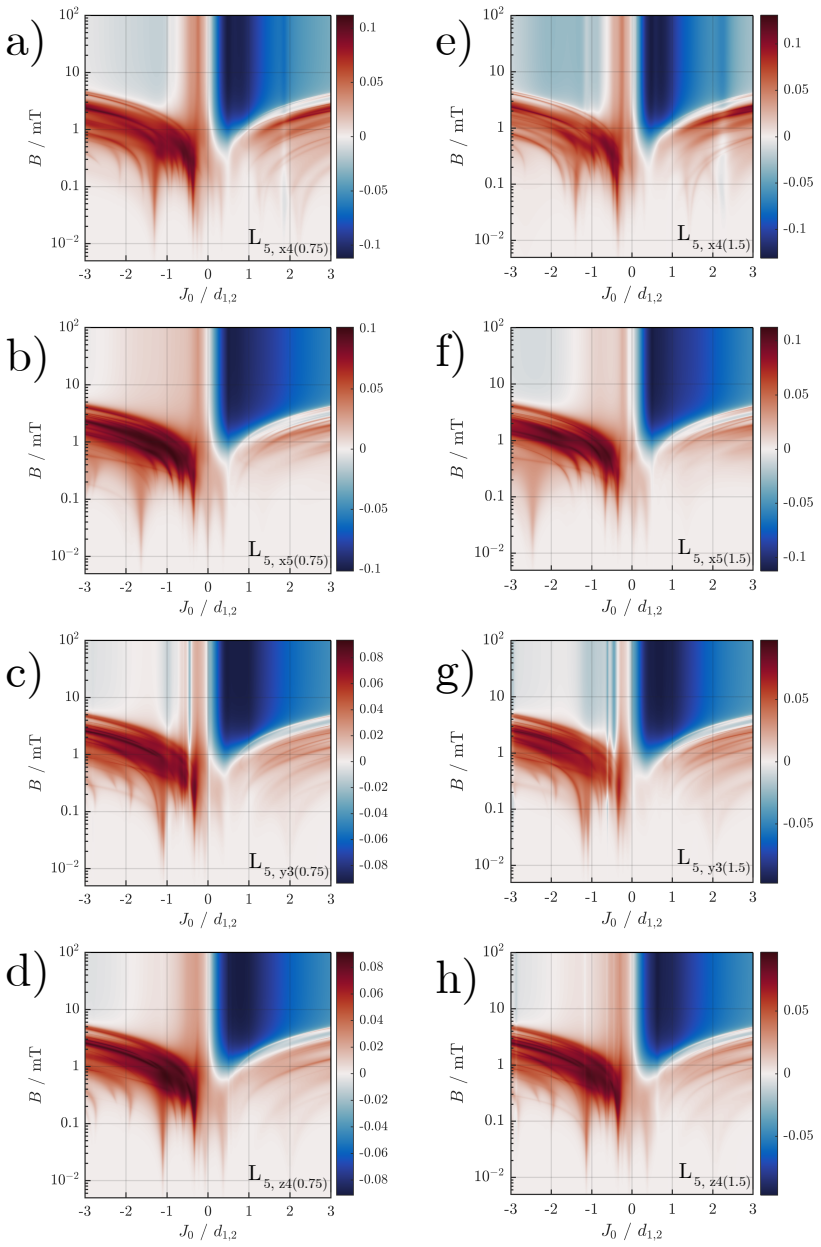

Figure 5.14: A comparison showing that, in fact, 0.75 Å is sufficient to realise the observed effects in the 5-spin linear geometries studied. The left-hand side of the figure shows the systems distorted by 0.75 Å, and the right-hand side shows the counterpart to each distorted instead by 1.5 Å. From top to bottom, the rows contrast displacements of spin 4 in the x-direction, spin 5 in the x-direction, spin 3 in the y-direction, and spin 4 in the z-direction, respectively.

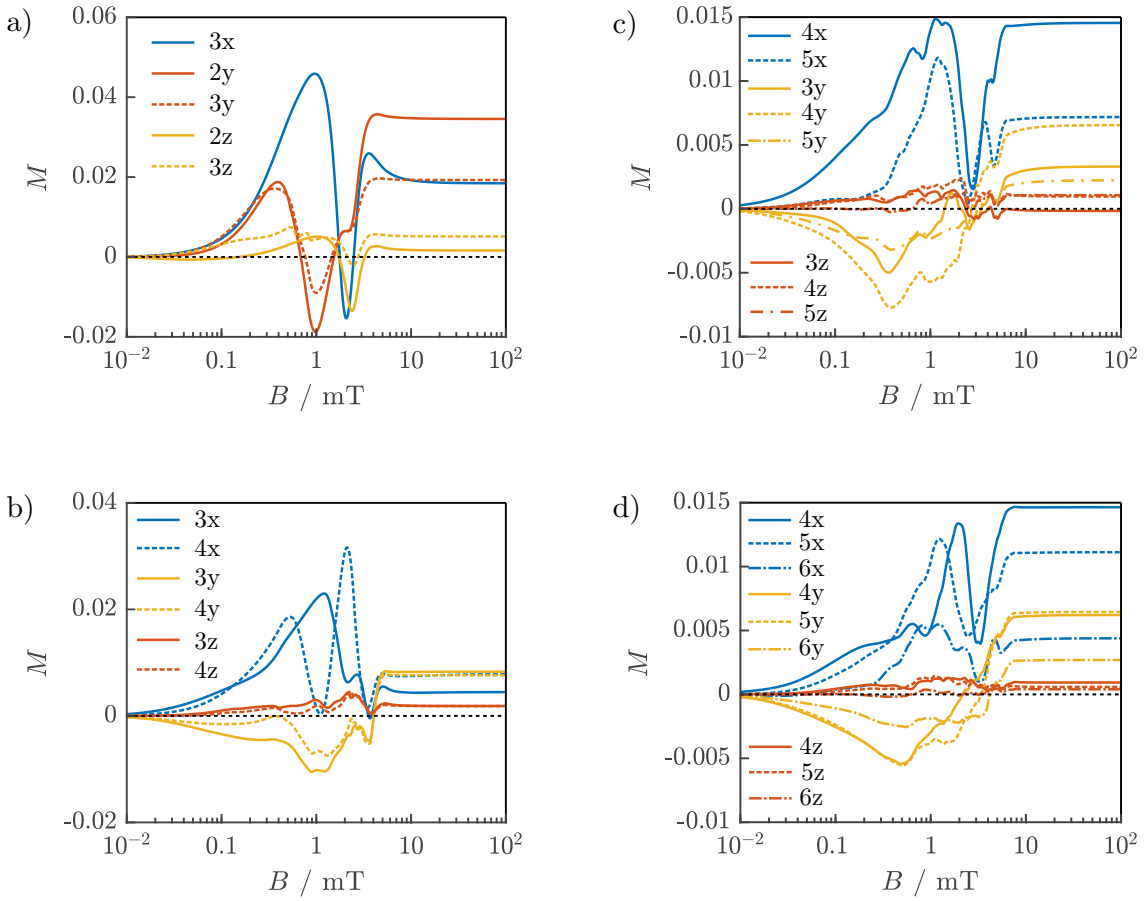

Figure 5.15: MFE enhancement measures $M(B)$, calculated using the perfect geometry as the reference value, shown for the distorted linear chain systems from 3 (a) to 6 (d) spins in length. Blue, red and orange curves represent displacements in the x-, y- and z-direction, respectively. Each sub-figure has been averaged over the exchange parameter for J_0 in the range from $-3d_{1,2}$ to $3d_{1,2}$.

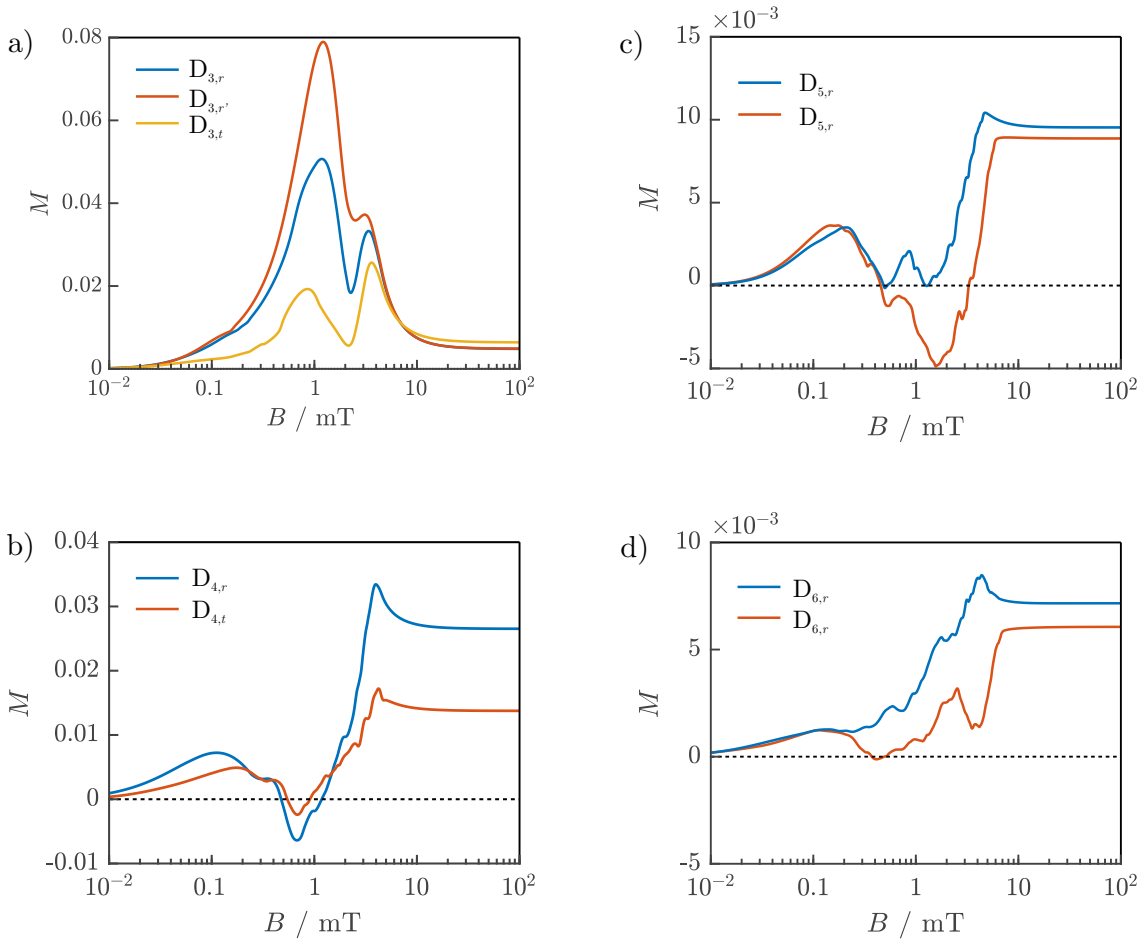

Figure 5.16: MFE enhancement measures, calculated using the perfect geometry as the reference value, for distorted n-gon system for n between 3 (a) and 6 (d), inclusive. Each sub-figure has been averaged over the exchange parameter for J_0 in the range from $-3d_{1,2}$ to $3d_{1,2}$

is shown a unique signature (in the much richer response profiles referenced above) that could be tested with experimental data to verify the presence of D3M effects in biological systems.

For weak fields - in particular around the Earth's magnetic field intensity - the distorted geometry almost always outperforms the perfect geometry. The one exception to this pattern is the distortion in the y-direction for the special case of the linear geometry, which is overall detrimental to the weak-field MFEs. In general for the linear geometries, one can see that $M(B)$ is strongly positive for distortions in the x-direction, and slightly positive for those in the z-direction across all field intensities. For the regular polygons, weak field and high-field results are generally positive, showing the distorted geometry outperforming the perfect geometry. Results are mixed for moderate field intensities, being the triangular geometry's most impressive region of amplification, but an area where the square and pentagonal measures are negative before returning to positivity at high field; the hexagonal measure is positive everywhere. The fact that the measures for the different distortions of the same individual geometries are so varied is further evidence that it is not only the breaking of the symmetry that matters to the magnetosensitivity of a spin system, but also *how* the symmetry is broken. Note furthermore that extending the integral to a larger J_0-range would give a larger $M(B)$ for many of the cases studied.

With this new measure, it is noted that the distorted triangle is a particularly impressive case, with the distortion reducing the minimum field required to see a strong effect by a factor of ten (see the Appendix, Tables 9.4 and 9.5) and producing an Earth-strength MFE where previously this was forbidden by the symmetry.

5.7 Discussion

Though symmetry can be a powerful tool, the breaking of symmetry can produce new and often interesting results. *Spontaneous* symmetry-breaking is a widely known phenomenon, observed e.g. in the Ginzburg-Landau theory of phase transitions, systems described by the so-called 'Mexican Hat' potential, the Jahn–Teller effect and indeed present even in many everyday situations (Shaver et al., 2007; Rosenstein

and Li, 2010; Frost, Pienta and Coffey, 2018). Examples of semiconductor quantum devices (Portnoi et al., 2009), show how technological applications, e.g. in sensing, can be revolutionized by deliberately breaking symmetries, and the work reported here suggests that similar principles might apply for magnetic "sensing" as it e.g. pertains to biological MFEs or more generally to spin chemical phenomena (Kattnig, Solov'yov and Hore, 2016; Kattnig, 2017b). In particular, it is argued that a natural symmetry absence may go some way to explaining the remarkable sensitivity of these systems to weak magnetic fields, and also how such effects can be sustained under realistic scenarios involving e.g. large exchange coupling.

It has been shown in the previous chapter that the re-introduction of hyperfine interactions does not significantly dampen DnM magnetic field effects if the dipolar interaction is the dominant term of the spin Hamiltonian (which, as also shown in the previous chapter, it is in the regime of inter-radical separations covered here), and so one can be confident that the effects shown in this chapter would persist in the presence of coupled nuclei (Sampson, Keens and Kattnig, 2019).

While highly symmetric structures of n radicals are at this stage of study a logical extension of the previously explored model it is surprising to realise that virtue in fact lies in imperfection. One would expect that the geometries from random encounters of radicals, as well as the average biological structure, are much more likely to be distorted than perfectly regular - suggesting that the present finding adds an important piece to the puzzle of understanding biological magnetosensitivity, where imperfect geometries are statistically far more likely to arise than perfect order.

It is clear that the simulations detailed in this chapter describe scenarios that are difficult to realize in practice. Obviously, aligning six spins in a perfect hexagonal arrangement to then undergo mutually reactive quantum spin dynamics might be difficult to actualise. However, considering one pair of radicals to be in an initial singlet state (between which $d_{1,2}$ would be defined) in the presence of other radicals acting as an external 'bath' is not unrealistic. One way to realise this chemically would be to generate radical pairs in the presence of more stable radicals. As soon as

the constraint upon perfection (symmetry) is removed, the practicality of realisation increases significantly, and indeed may even occur naturally or at random. Though this particular scenario is not considered in the present work, it would be a way to build up the kind of configurations explored in this chapter. The author hopes this motivates more experimental research into this idea.

It is interesting to note that the MFEs in radical pairs and dipolarly coupled n-spin systems can also be viewed a result of the absence of symmetry in their own right. The missing symmetry here is a permutation symmetry of two electron spins poised to recombine to form a diamagnetic state(Keens, Bedkihal and Kattnig, 2018). In the conventional Radical Pair Mechanism, this symmetry is broken by hyperfine interactions with magnetic nuclei. In D3M this asymmetry is provided by the electron-electron dipolar interaction in systems of more than two radicals. In this sense, for both scenarios remarkable MFEs can result from this natural symmetry absence.

Practically, the amplifications observed here could also be used to make quantum devices more sensitive, easier to make, and easier to control. Quantum devices made using the principles of this mechanism would not be subject to a precise positional confinement of the reacting radicals, and so small distortions would work to the advantage of the engineer. Such devices would be more sensitive due to the extra features available in the MFE profiles that, as has been illustrated in this work, appear when a system's geometric equilibrium is removed. The effects could furthermore be optimized by tuning the exchange interaction, moving the anti-crossings responsible for the MFE spikes to lower field values thereby realizing optimal sensitivity at the projected field intensity.

5.8 Conclusion

DnM treats the oft-neglected electron-electron dipolar interaction as the main contributor to MFEs rather than the conventionally-used hyperfine interaction. This mechanism thus applies to radicals without dominant hyperfine interactions, but can impact the spin dynamics in classical radical pair systems with non-negligible hyper-

fine and/or exchange interactions, as recently demonstrated for lipid peroxidation and the avian compass. This interaction pattern of three radicals thus provides a robust additional mechanism for radical systems at concentrations for which three-radical correlations cannot be neglected. Here, the possibility of this mechanism has been explored for systems comprising more than the previously considered three radicals. It has been demonstrated that a rich variety of magnetosensitivity can in principle ensue for n-radical systems coupled by the long-range electron-electron dipolar interaction. These effects have been further explored in configurations that are more statistically likely to occur in nature, by comparing the perfect theoretical systems of regular geometries with slightly distorted geometries that break various rotation and reflection symmetries. In the vast majority of cases considered, such imperfections have enhanced the magneto-sensitivity.

In many respects, symmetry appears as a fundamental principle in nature. In organisms and structures where minimal inter-site distance, maximal packing density, or aesthetic appeal, is required, perfectly regular geometry is widespread. Symmetry is also the first port of call in many theoretical treatments. However, it has here been shown that the absence of symmetry can be just as effective as its imposition. It has been found that not only do the distorted geometries provide new regions of sensitivity for weak magnetic fields to alter the reaction yields, but distorted geometries appear to often surpass regular geometries in terms of the strength of onset for the MFEs, and the overall magnitude thereof. In particular, increasing sensitivity to weak magnetic fields has been observed for selected values of the exchange parameter and an increase the number and range of exchange parameters for which low-field sensitivity manifests.

These findings are important because they further suggest that the D3M model and its generalisation discussed here, DnM, can provide enhanced magnetosensitivity in a variety of circumstances. The prediction of new MFEs in such systems allows for the consideration of processes and conditions that had previously been thought impossible due to the constraints of the RPM, and further inspire experimental endeavours into the study of magnetic field effects in ordered systems and at high

radical concentrations or the production of devices that utilize n-spin processes as a measuring tool. Here, many questions about realisability remain open. However, it is not the aim of this work to guide future experiments yet, but rather to instigate the principal possibility to observe magnetic field effects in radical recombination reactions due primarily to the electron-electron dipolar interactions of three or more radicals and to highlight that imposing perfect geometries might reduce the sensitivity towards weak magnetic fields.

The main results of this chapter are:

- Geometry can affect the manifestation of MFEs, as established in chapter 3, but the effect also generalises to larger systems.

- The breaking of geometric symmetries also allows for richer, and stronger, effects than in the regular configuration. MFEs can be enhanced, through these effects.

- It matters not just *that* geometric symmetries are broken, but *how* they are broken is also important.

These observations represent a significant deviation from anything previously published in the literature, so the next necessary step is for some experimental observations to be made such that the predictions made here can become grounded in physical reality. Some ways that the predictions made in this chapter could be experimentally tested, are as follows: The new, richer, MFE profiles could be tested in the same way as in previous chapters, with EPR spectroscopy being used in conjunction with energy level diagrams in an effort to isolate new features predicted and demonstrated in the figures in this chapter. In order simulate the regular geometries studied here, artificially immobilised structures would probably need to be used, which could then be distorted slightly to emulate the perturbations proposed here. Such an experimental setup could also then be used to introduce entirely random motion on all axes as a form of control. Linear chains could perhaps be tested in a similar manner, or by using setups from spintronics. One other way suggested in this chapter, to actualise the results, is to use a pair of radicals in

an initial singlet state in the presence of other radicals acting as a sort of 'bath', i.e. generation of a radical pair in the presence of more stable radicals, and then track the MFE profile as the reaction naturally evolves. This may form part of an experimental setup designed to test the predictions made here.

6. Noise in biological systems, and how it is not always deleterious

In this chapter the idea that environmental noise, the conventional nemesis of quantum technology, plays a significant role in shaping the magnetosensitive response is discussed. Considering singlet-triplet dephasing, introduced upon geometrically regular structures, one finds that noise can *enhance* MFEs on its own. The case of completely uncorrelated noise affecting the entire system has also been considered, which abolishes the enhancements that could be seen in the case of singlet-triplet dephasing. Thus it is shown that singlet-triplet dephasing, can actually serve constructively alongside the effects already predicted by the DnM model, rather than destructively as previously may have been expected.

Finally, taking noise effects together with the slight geometric distortion in the structure discussed in the previous chapter is shown to lead to unexpectedly large magnetosensitivity. This could be utilised in the construction of quantum navigational and sensing devices, and possibly moves us ever closer to understanding the hitherto elusive avian compass and the sensitivity of biological systems to magnetic field of intensities comparable to the geomagnetic field.

6.1 Introduction

Noise is a very natural phenomenon, and widely recognised as an integral part of the 'hot, noisy biological environment' inherent to living systems. However, noise is generally considered to be an enemy of quantum mechanical effects, with dissipators such as singlet-triplet dephasing, as well as uncorrelated noise between spins, being

considered the primary loss mechanism for information and decoherence in quantum systems. Thus, noise is often minimised, either by force or by assumption. While it can be true that noise damps the system, and mutes any effects one might have been watching, there are less intuitive scenarios where the presence of noise can actually be *beneficial* to the system. A model suggesting the inclusion of more S-T dephasing (due to reaction processes) has been proposed as an alternative to the standard Haberkorn model of dissipative dynamics (Haberkorn, 1976; Jones and Hore, 2010a), but the authors themselves admit that their model would be difficult to experimentally distinguish from the Haberkorn approach and so a detailed discussion thereof shall not be undertaken here. However, it is shown in this chapter that the presence of noise can have significant effects upon entangled systems of radicals that are undergoing inter-conversionary dynamical interactions as described by the Radical Pair Mechanism (RPM). In particular, it is shown that noise can *enhance*, not damp as one might have expected, the strength of the magnetic field effect (MFE) observed in such systems where there are more than two radicals coupled by the electron-electron dipolar interaction. In the absence of hyperfine interactions or differences in g-factors, the insistence on more than two radicals is important for symmetry reasons, as was explained in chapter 3, and can enhance MFEs as seen in both the perfect and distorted geometric systems elucidated in chapter 5.

6.2 Noise in DnM

The DnM Hamiltonian and model has been thoroughly explained in Chapter 5, and shall not be re-stated here. What follows is a discussion of the new consideration: noise.

A common dismissal of the quantum effects in biology is that noise, for example that caused by the finite temperatures of living systems, would likely damp any such effect and possibly render it negligible. This is especially true when the geomagnetic field is considered, as its low intensity mandates long coherent lifetimes to detect an effect. Noise is often excluded from *in silico* simulations for simplicity. However, some studies have shown that the singlet yield, and hence the resultant MFE,

of a magnetosensitive reaction is indeed impacted by the level of systemic noise (Gauger et al., 2011; Poonia, Saha and Ganguly, 2015; Tiersch and Briegel, 2012; Kattnig, Solov'yov and Hore, 2016; Kattnig, 2017b). By inclusion of the Lindblad super-operator in the present calculations, noise can be included into the, previously introduced, *DnM* model (Kryszewski and Czechowska-Kryszk, 2008; Sampson, Keens and Kattnig, 2019).

The general form of noise operators considered here is given by the Lindblad superoperator:

$$\hat{\hat{L}} = \Gamma \sum_{i=0}^{N} \hat{S} \otimes \hat{S}^{*} - \frac{1}{2}\left(\hat{S}^{\dagger}\hat{S} \otimes \mathbb{1} + \mathbb{1} \otimes (\hat{S}^{\dagger}\hat{S})^{T}\right), \tag{6.1}$$

where $\hat{S}$ defines the interaction between the system of interest and an external 'bath', (Kryszewski and Czechowska-Kryszk, 2008). Such a form arises when an open system can be described as a quantum dynamical semi-group (Hornberger, 2009), which allows a rigorous formulation of the Markov assumption of quantum theory - namely that the system and the bath are uncorrelated at all times, i.e.:

$$\rho_{SB} = \rho_{S} \otimes \rho_{B}, \tag{6.2}$$

where the three density operators here represent that of the combined open system, the system itself, and the external bath, respectively.

In order to select realistic interactions between the system and an external theoretical bath, two different noise operators were explored. One is labelled xyz uncorrelated (xyz_{uc}) and the other singlet/triplet dephasing (P_{uc}). There exist both correlated and uncorrelated forms of noise operators, but uncorrelated noise is the most physically relevant and experimentally realisable so that is what has been considered in both cases.

The form of motion noise operator used consists of a sum over each dissipator acting on the density matrix of the system, individually and distributively. Labelled as xyz_{uc}, this operator takes the form $\sum_{\alpha,n}^{N} \hat{\hat{L}}_{\alpha}^{(n)}$, where N is the number of radicals in the system, $\alpha \in \{x, y, z\}$ and $n \in \{1, 2, ..., N\}$.

The other noise operator used, for singlet-triplet dephasing, is:

$$P_{uc} = \sum_{\alpha,n}^{N} P^{\alpha}_{n,n+1}, \tag{6.3}$$

where P is a projector, $\alpha \in \{S, T\}$, denoting singlet and triplet respectively, and i labels the radicals. Note that the seemingly non-existent term arising when $i = N$ is indicative of the ring-like topology in the planar geometries; for the linear chain, this final term is set to zero (i.e. the sum ranges to $N - 1$). The lifetimes were scaled within the confines of the standard exponential model for recombination rate fall-off.

6.3 Results

For ease of comparison between cases, the enhanced MFE shall be calculated using the same approach as in the previous chapter (cf. Eq. 5.20), except in this case instead of contrasting a distorted geometry and a perfect one, the comparison this time is between the no-noise system and the system in the presence of noise. For consistency, it has also been ensured that the parameters used in the studies of Chapter 5 were kept the same for the respective studies in this chapter. The reader is directed to Chapter 5 for the discussion of rate constants, field direction etc.

The maximum such effects are shown here, with the baseline (i.e. zero) being no improvement upon the no-noise case. For each case studied, two figures are presented. The first is the distribution of enhanced MFEs, and the second is the distribution of values of the noise parameter that produced the maximum effect for each value of exchange tested. An extensive study has been conducted, producing around a hundred separate graphs detailing individual results. It would be impractical to try and show each one of these, so a sample has been included in the chapter proper and additional results will be shown in the appendix, sections 9.11 and 9.12.

Low and moderate field effects found will be of particular interest to the field of quantum biology. Such effects can be seen, for example, in the weak-exchange region of Fig. 6.1, where ten percent enhancements to the noiseless MFE occur at

sub-mT field strengths.

6.3.1 Linear Chains

Initially, linear spin chains are considered. Across this study, chains of between three and five spins have been considered. The results for the three-spin case will be presented in the chapter proper, with the larger cases shown analogously in the appendix (Section 9.11).

6.3.2 Planar Geometries

Regular n-gons from three to five spins in size have been studied. The triangular case will be presented in the chapter proper, and the larger systems, as well as some extra geometries, are shown in the appendix (section 9.11). As with the linear chains shown in the preceding subsection, one can see enhancements that follow the MFEs of the noiseless case, which is encouraging as it both shows that the effects of noise enhancement to MFEs does not come at the cost of established MFEs, and also that the linear chain is not a special case of this effect.

6.4 Combined Enhancement

It has been shown in Chapter 5 that geometric imperfections introduced into a spin system can enhance the MFEs observed. Imagining such a structural distortion (away from the perfection of a regular shape) as geometric noise, these two types of noise have been used simultaneously in order to elucidate any synergy between them. It was found that these two additions to the dynamics complement each other, rather than acting destructively, and synergistically enhance the MFEs of the systems as shown in the preceding subsections. In this section are presented the three-spin linear chain, triangle, and square systems, again, but with small geometric distortions introduced into the structures as done in Chapter 5. Further results, which would be impractical to show in the chapter proper, are found in the appendix, section 9.12. The resulting geometries were $L_{3,3x}$ and, $D_{3,r}$ and $D_{4,t}$ (as introduced

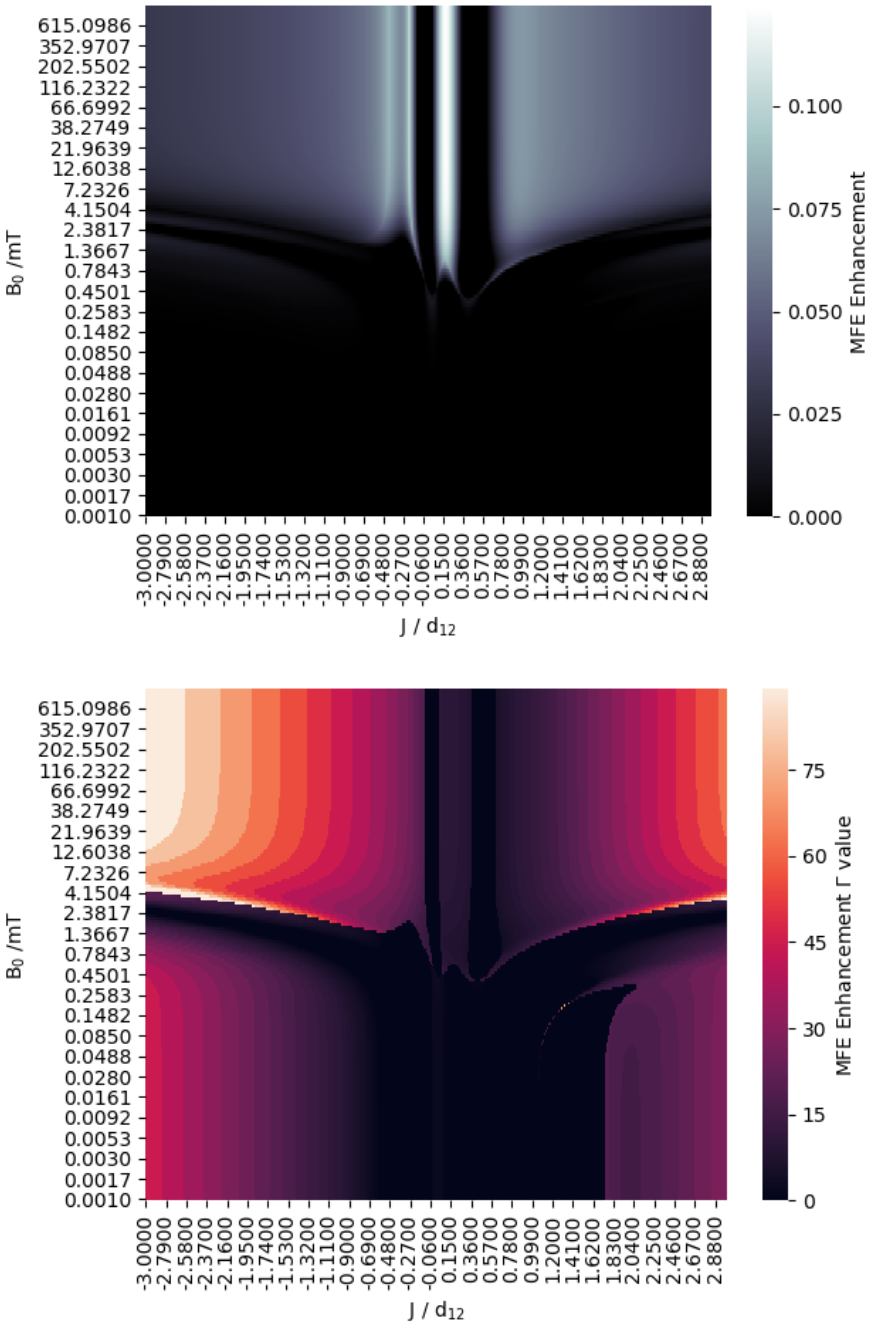

Figure 6.1: Three-spin linear system (L_3), under the DnM formalism and in the presence of exchange and S-T dephasing. The top panel shows regions where the presence of noise can gives an enhanced MFE relatively to the no-noise system. The bottom panel shows the value of the noise parameter, Γ (in MHz), that produced the corresponding enhanced MFE in the upper panel. In both cases, the x-axis denotes the exchange parameter J given in units of $d_{1,2}$.

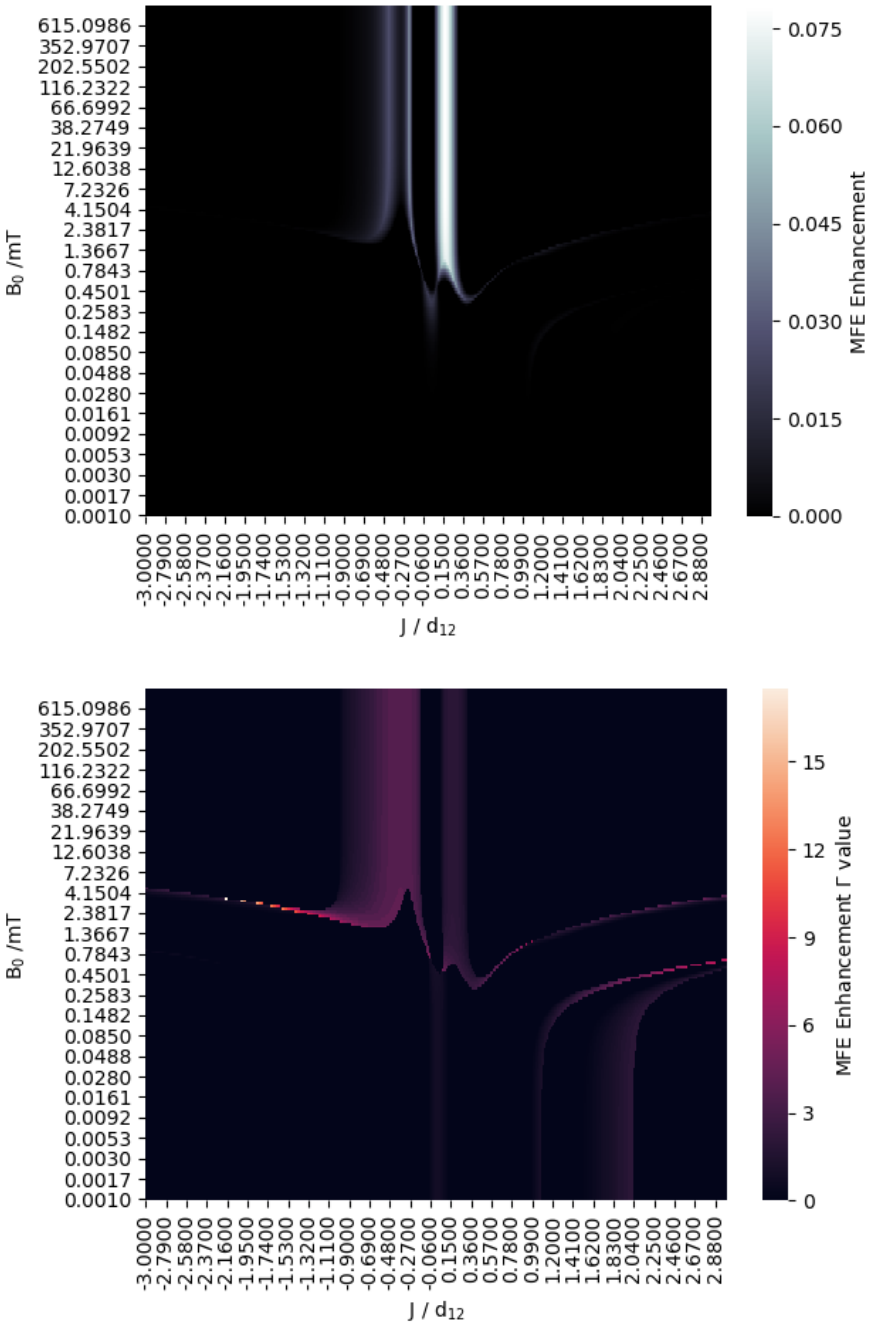

Figure 6.2: Three-spin linear system (L_3), under the DnM formalism and in the presence of exchange and xyz uncorrelated noise. The top panel shows regions where the presence of noise can gives an enhanced MFE relatively to the no-noise system. The bottom panel shows the value of the noise parameter, Γ (in MHz), that produced the corresponding enhanced MFE in the upper panel. Note the abolition of most of the enhancements shown by S-T dephasing. In both cases, the x-axis denotes the exchange parameter J given in units of $d_{1,2}$.

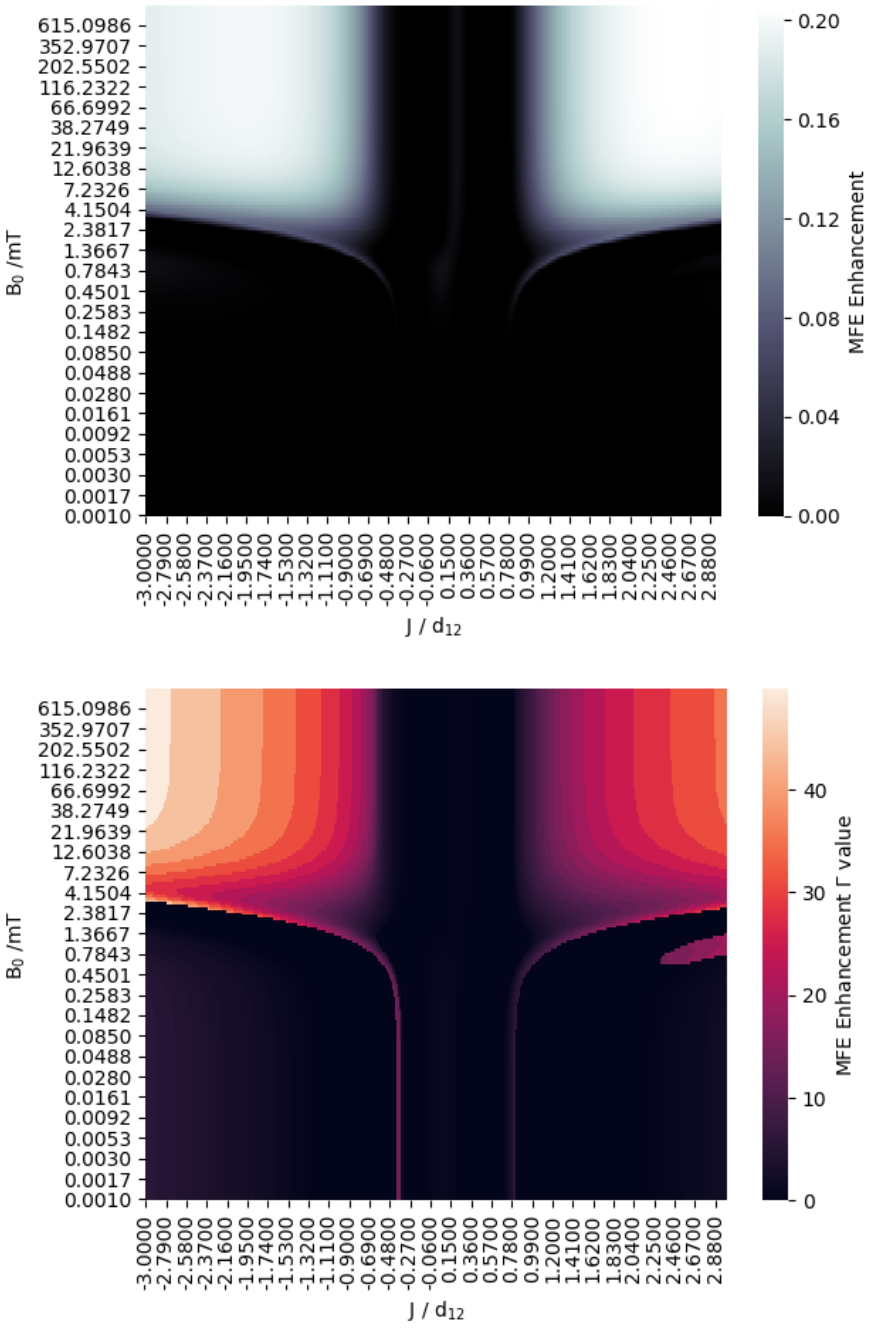

Figure 6.3: Equilateral triangle system (D_3), under the DnM formalism and in the presence of exchange and S-T dephasing. The top panel shows regions where the presence of noise can gives an enhanced MFE relatively to the no-noise system. The bottom panel shows the value of the noise parameter, Γ (in MHz), that produced the corresponding enhanced MFE in the upper panel. In both cases, the x-axis denotes the exchange parameter J given in units of $d_{1,2}$.

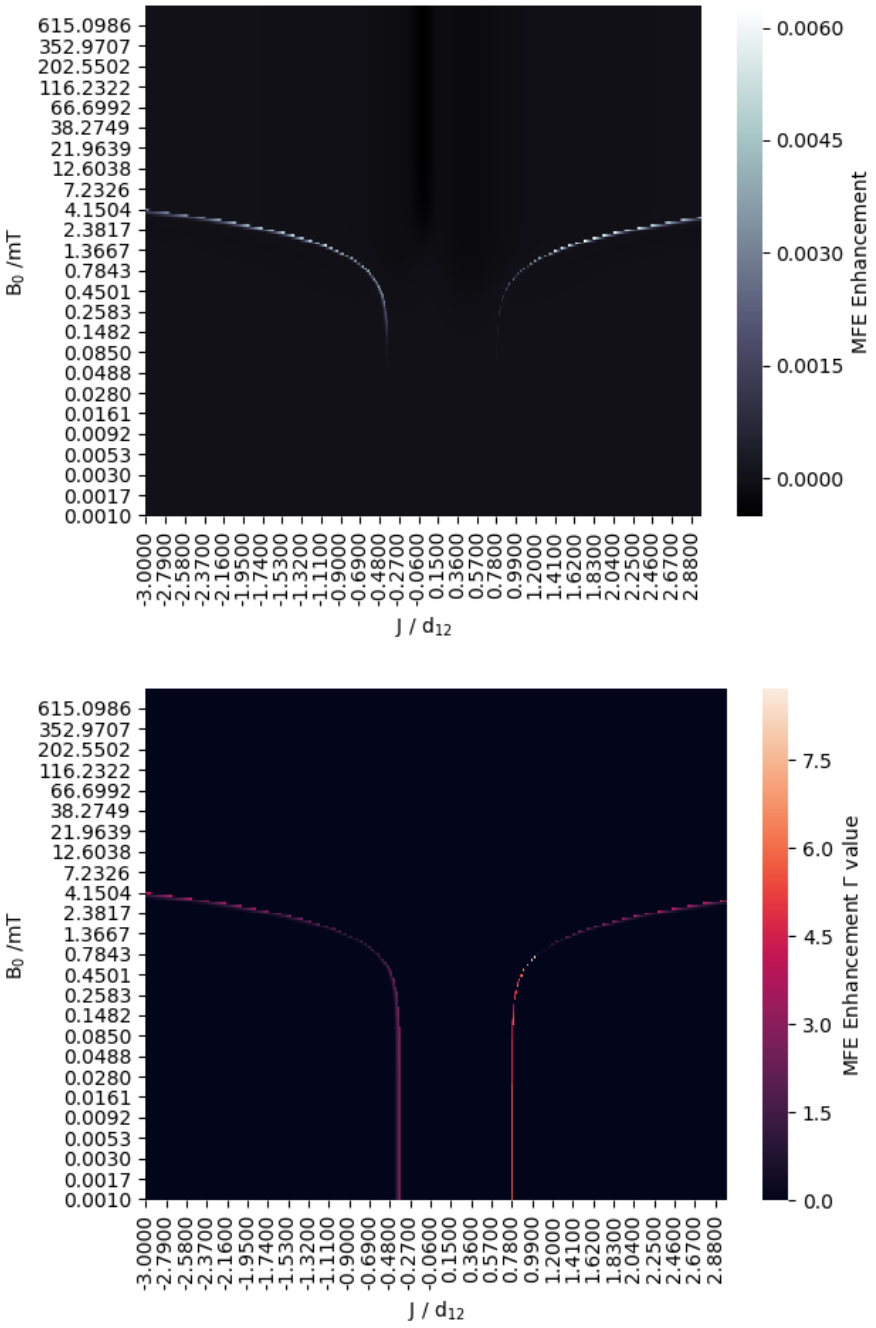

Figure 6.4: Equilateral triangle system (D_3), under the DnM formalism and in the presence of exchange and xyz uncorrelated noise. The top panel shows regions where the presence of noise can gives an enhanced MFE relatively to the no-noise system. The bottom panel shows the value of the noise parameter, Γ (in MHz), that produced the corresponding enhanced MFE in the upper panel. Note the abolition of most of the enhancements shown by S-T dephasing. In both cases, the x-axis denotes the exchange parameter J given in units of $d_{1,2}$.

in Figs. 5.1 and 5.2), and were treated in conjunction with the introduction of noise as in their respective previous sections.

6.5 Discussion

For linear chains, by comparing the figures in this subsection, it can be seen that singlet-triplet dephasing can act to enhance MFEs even at strong values of the noise parameter, whereas xyz uncorrelated noise tends to abolish these effects. This is seen most clearly by comparing the panels of Fig. 6.1 and contrasting these with Fig. 6.2. In the former pair of figures (singlet-triplet dephasing), enhancements are seen especially prominently at moderate to high field that are abolished in the latter pair of figures (xyz uncorrelated). Thus, for linear chains, it is encouraging to see that the most physically relevant noise considered is also the one which shows the strongest enhancements. It should also be noted that the central region (where $J/d_{1,2} \approx 0.15$) displays a strong feature in both cases, but that this feature is present with and without these sources of noise, and therefore should be considered an artefact, rather than a causal feature.

It can be seen in Fig. 6.3 that singlet-triplet dephasing produces significant MFE enhancements in the planar geometries, consistent with the case of the linear chain. It can also, again consistently, be noted that xyz uncorrelated noise (Fig. 6.4) produces no such significant enhancement.

The two frustrations (geometric distortion and S-T dephasing) presented in the previous chapter, and Figs. 6.1 and 6.3, respectively, have been combined, and it has been found that, taken together, these two individually nice effects actually seem to *enhance* each other synergistically. That is, one can see up to twenty percent enhancement in the overall MFE. The combined results are shown in Figs. 6.5, 6.7 and 6.9, with the counterpart xyz-uncorrelated cases (the purpose of which are, again, to verify that noise which should abolish the new MFEs shown does in fact do so) shown in Figs. 6.6, 6.8, and 6.10.

It is interesting to see that the isosceles triangular system shows its significant enhancements at moderate to high field, with little improvement in the low-field

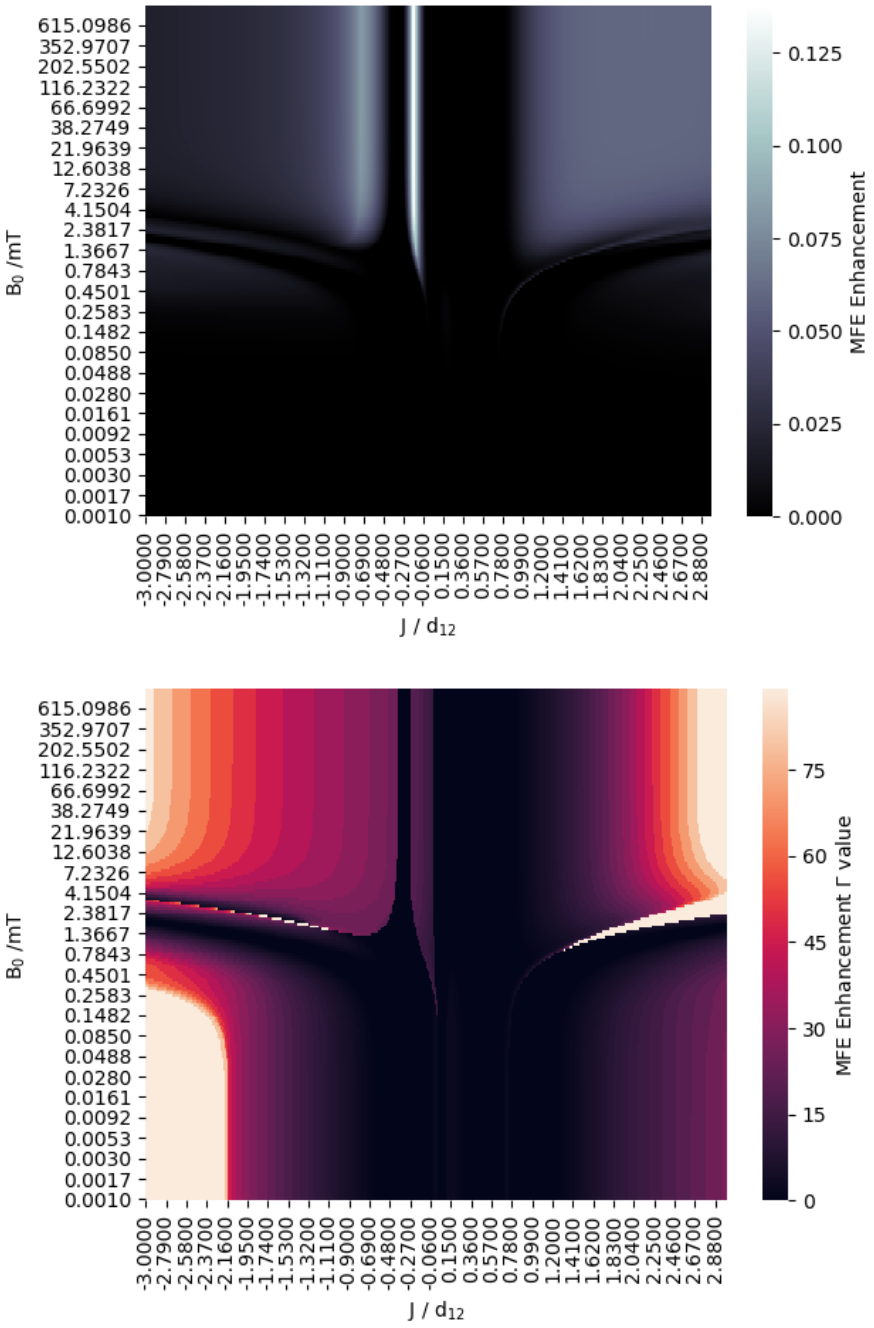

Figure 6.5: Three-spin distorted linear system ($L_{3,3x}$), under the DnM formalism and in the presence of exchange and S-T dephasing. The top panel shows regions where the presence of noise can gives an enhanced MFE relatively to the no-noise system. The bottom panel shows the value of the noise parameter, Γ (in MHz), that produced the corresponding enhanced MFE in the upper panel. In both cases, the x-axis denotes the exchange parameter J given in units of $d_{1,2}$.

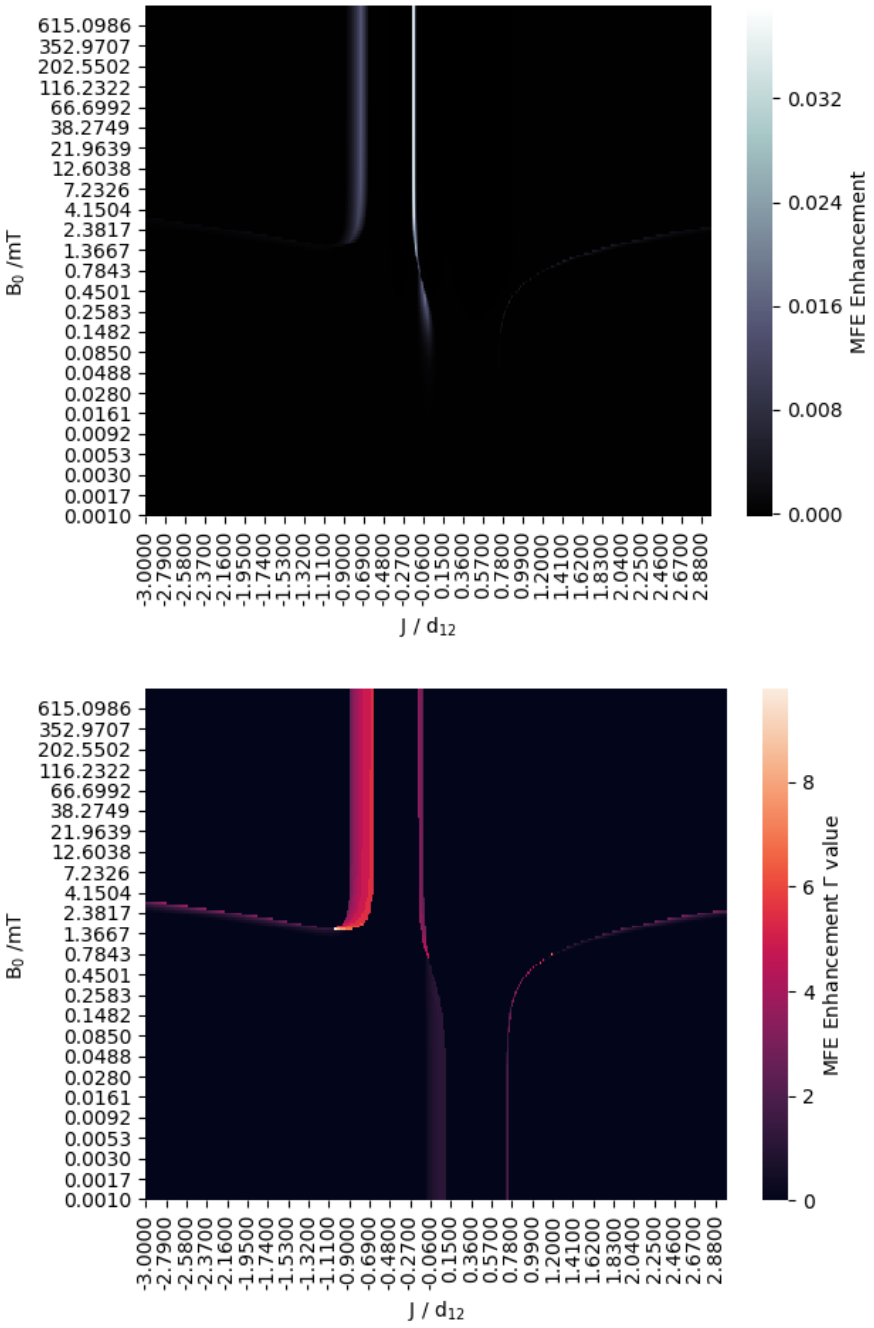

Figure 6.6: Three-spin distorted linear system ($L_{3,3x}$), under the DnM formalism and in the presence of exchange and xyz uncorrelated noise. The top panel shows regions where the presence of noise can gives an enhanced MFE relatively to the no-noise system. The bottom panel shows the value of the noise parameter, Γ (in MHz), that produced the corresponding enhanced MFE in the upper panel. Note the abolition of most of the enhancements shown by S-T dephasing. In both cases, the x-axis denotes the exchange parameter J given in units of $d_{1,2}$.

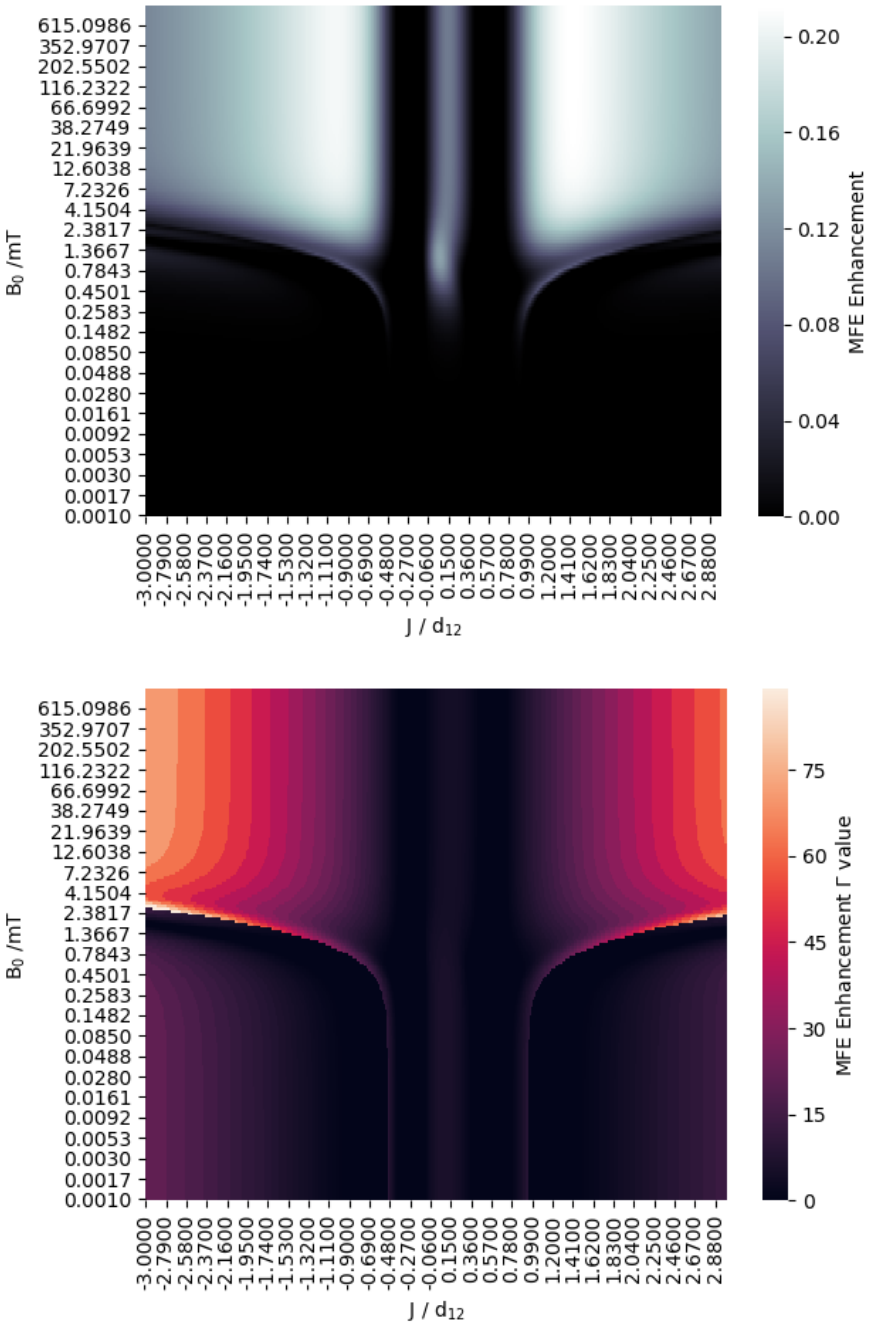

Figure 6.7: Isosceles triangle system ($D_{3,r}$), under the DnM formalism and in the presence of exchange and S-T dephasing. The top panel shows regions where the presence of noise can gives an enhanced MFE relatively to the no-noise system. The bottom panel shows the value of the noise parameter, Γ (in MHz), that produced the corresponding enhanced MFE in the upper panel. In both cases, the x-axis denotes the exchange parameter J given in units of $d_{1,2}$.

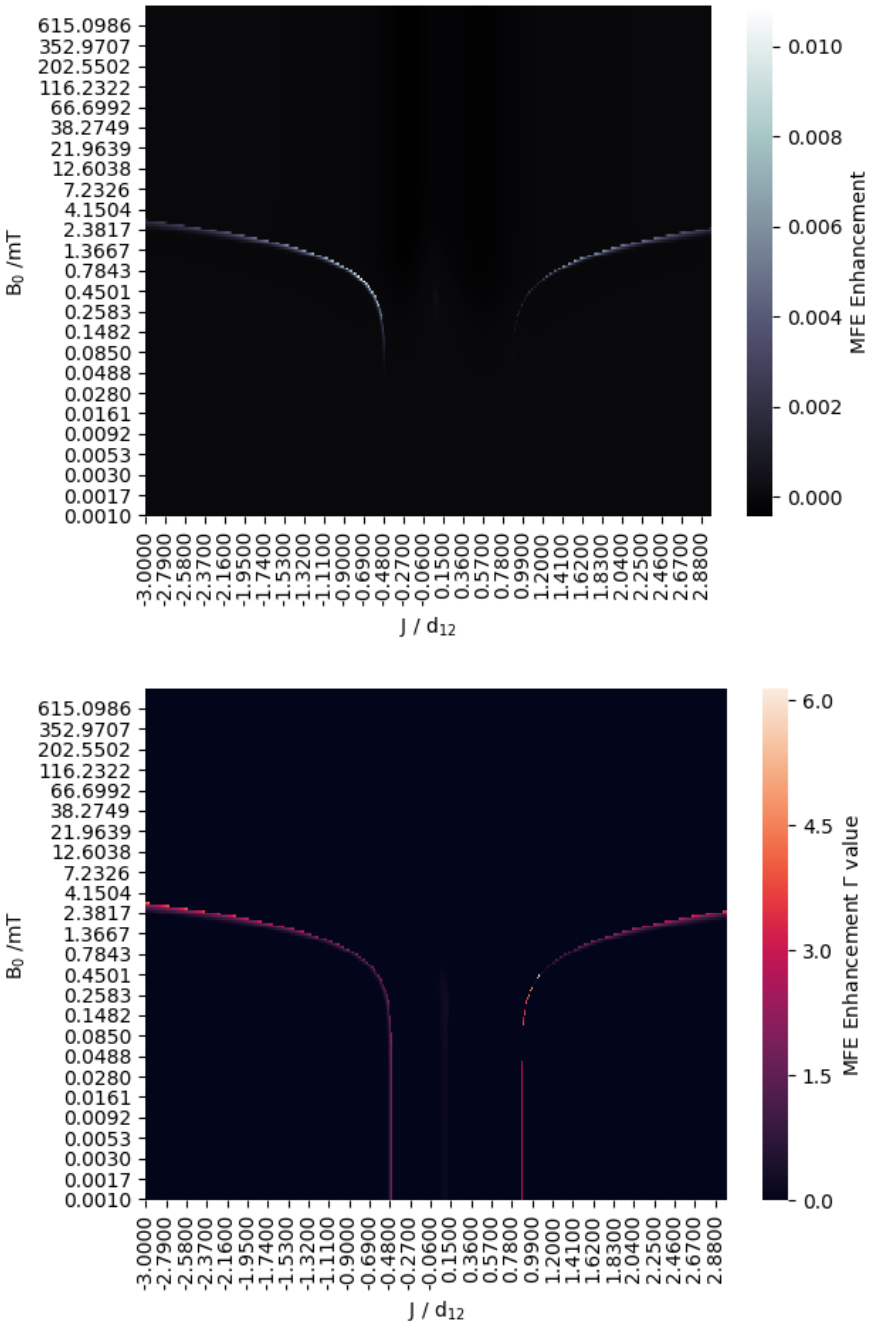

Figure 6.8: Isosceles triangle system ($D_{3,r}$), under the DnM formalism and in the presence of exchange and xyz uncorrelated noise. The top panel shows regions where the presence of noise can gives an enhanced MFE relatively to the no-noise system. The bottom panel shows the value of the noise parameter, Γ (in MHz), that produced the corresponding enhanced MFE in the upper panel. Note the abolition of most of the enhancements given by S-T dephasing. In both cases, the x-axis denotes the exchange parameter J given in units of $d_{1,2}$.

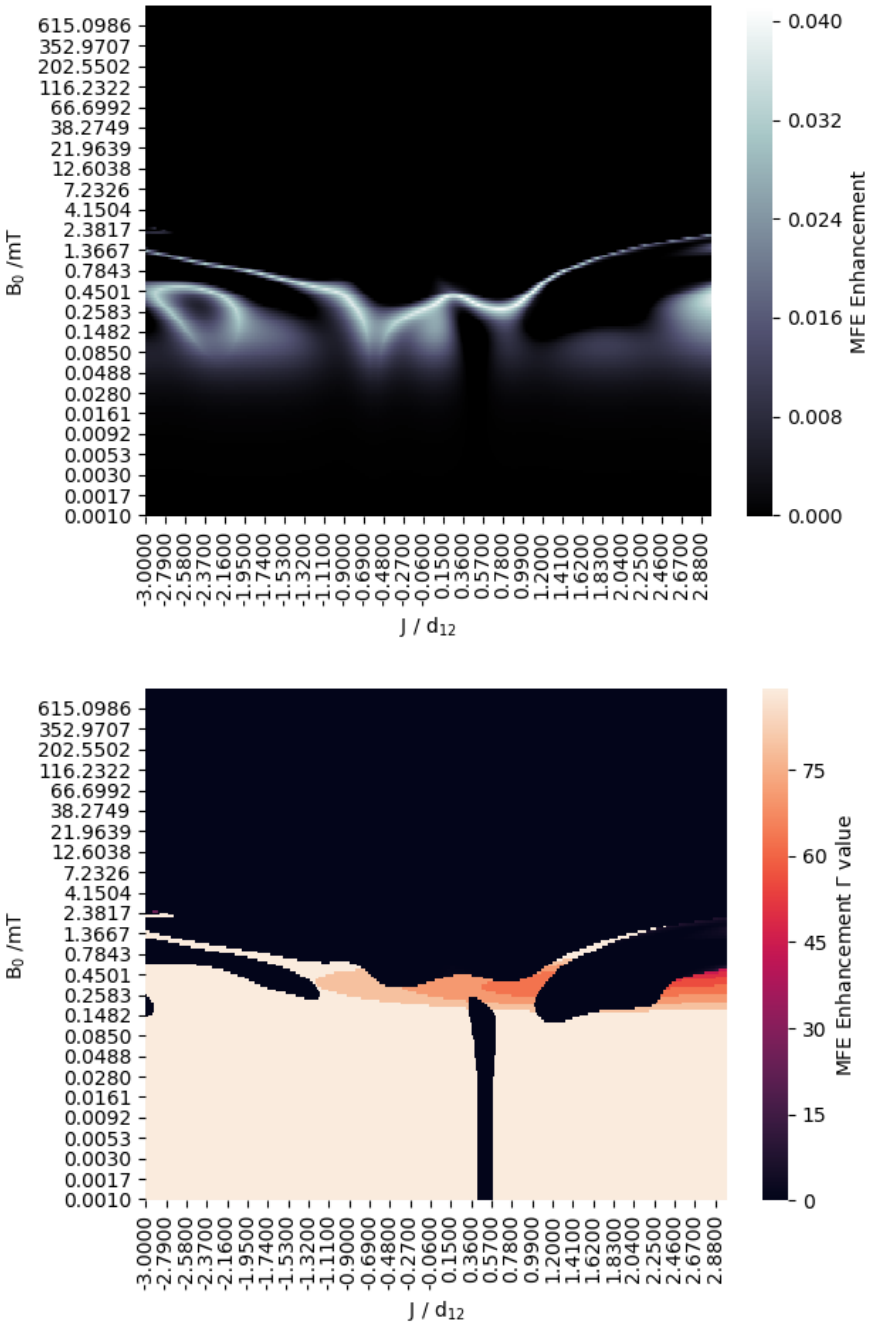

Figure 6.9: Distorted square system ($D_{4,t}$), under the DnM formalism and in the presence of exchange and S-T dephasing. The top panel shows regions where the presence of noise can gives an enhanced MFE relatively to the no-noise system. The bottom panel shows the value of the noise parameter, Γ (in MHz), that produced the corresponding enhanced MFE in the upper panel. In both cases, the x-axis denotes the exchange parameter J given in units of $d_{1,2}$.

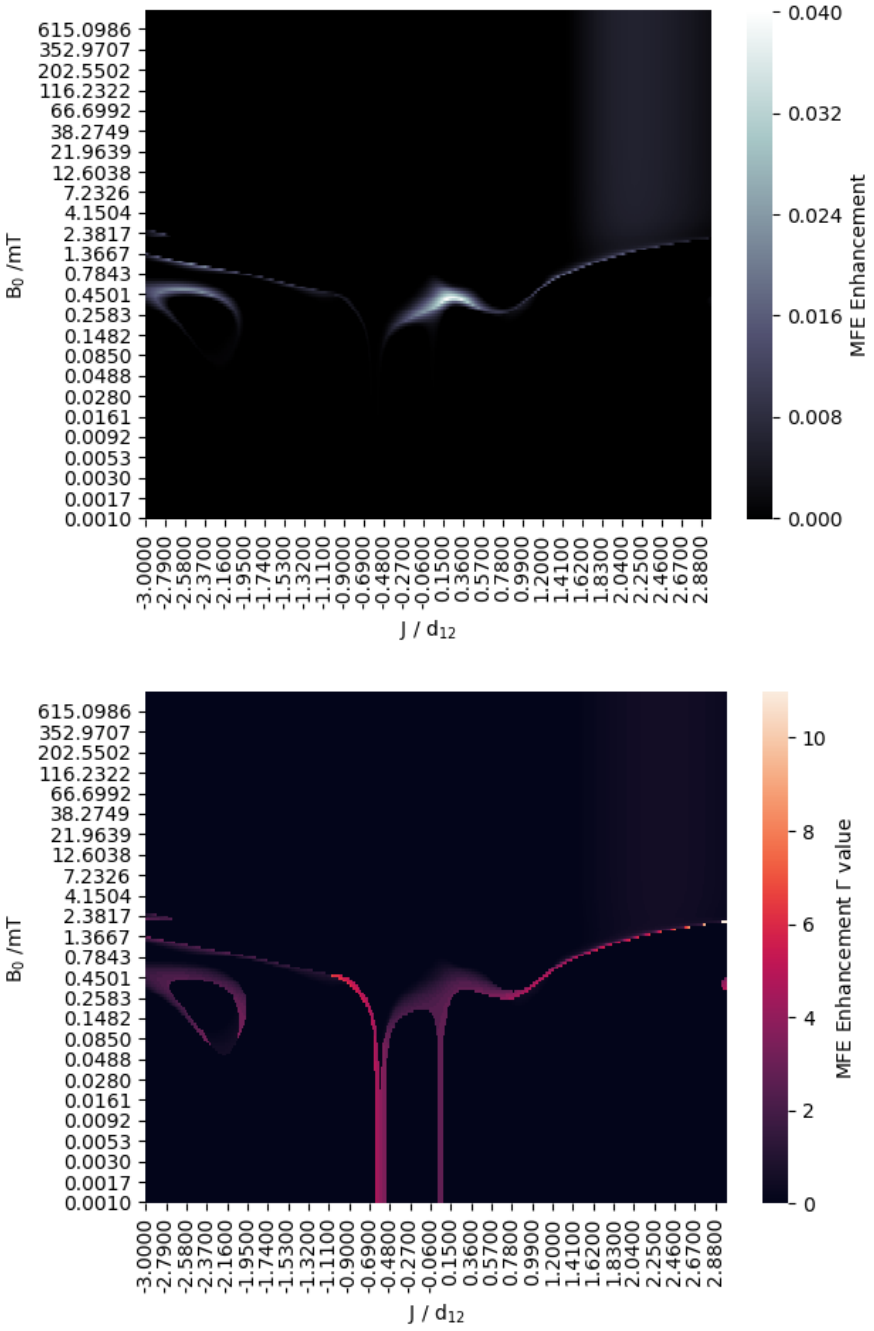

Figure 6.10: Distorted square system ($D_{4,t}$), under the DnM formalism and in the presence of exchange and xyz uncorrelated noise. The top panel shows regions where the presence of noise can gives an enhanced MFE relatively to the no-noise system. The bottom panel shows the value of the noise parameter, Γ (in MHz), that produced the corresponding enhanced MFE in the upper panel. Note the abolition of most of the enhancements given by S-T dephasing. In both cases, the x-axis denotes the exchange parameter J given in units of $d_{1,2}$.

region, but the distorted square system shows interesting behaviour only in this low-field region (cf. Figs. 6.7 and 6.9). Motivated by this disparity, though while noting that such an investigation is currently computationally prohibitive, it would be interesting in the future to see if there exists any similarities between a set of systems with an even number of spins and those with an odd number of spins.

In particular, it is noted that the distortion-dephasing effect moves the peak enhancement away from the region of zero exchange in both directions each time. This broadening of the ranges where one can observe the maximum enhancement provides more configurations which could be experimentally explored and exploited.

These results show that S-T dephasing is a type of systemic noise that can serve to enhance MFEs in the system. This is particularly relevant for quantum biological spin systems, where quantum coherence between spins is required for MFEs to occur within both the conventional RPM model and more recent D3M models.

6.6 Conclusion

In this chapter it has been shown that the strongest noise-enhanced effects broadly follow the lines of the strongest effects in the absence of noise, which is encouraging as it has been shown that noise does not simply abolish the pre-existing strong MFEs - especially at low field and weak exchange, which one may expect to be the most vulnerable to interference. It is noted that in some cases rather strong values of the noise parameter produce the maximum enhancements, even at low field. This is not the case for xyz uncorrelated noise, where the noise seems to provide no significant enhancement or diversification, but can be seen convincingly for singlet-triplet dephasing. In the latter case, one can see that at both high and low field values moderate to strong noise can enhance the MFEs of the system. Thus it has been shown that the DnM model is not just resilient to systemic noise, but symbiotically works with it.

The main results of this chapter are:

- Noise can actually be an MFE enhancer rather than purely deleterious.

- Coupled with geometric distortions, there is a certain synergy that may be exploited, with singlet-triplet dephasing showing the most promise (and physical relevance) for this distortion-dephasing effect to be exploited.

The predictions made in this chapter are unlike almost anything proposed thus far in the literature. The one exception, perhaps, is the Jones-Hore model which showed that the addition of extra noise into the Haberkorn model of recombination can still give sensible physical predictions Jones and Hore, 2010a. In order to test the predictions made in this chapter, and thus ground them more in physical reality, one could search for the strong peaks and new effects (i.e. new areas of magnetic sensitivity shown in the MFE profiles given in this chapter) not predicted in the absence of noise and/or distortion. This could be done by using EPR to (once again) detect the energy gaps that are predicted to exist in the presence of that level of exchange (by comparison with energy level profiles), to confirm the value of J for a given measurement, and then compare the measured MFE with what is expected based on the geometry used. It would probably also be instructive to search for some peaks in the spectrum which are not predicted, and to test the addition of entirely random noise as a control (i.e. to verify that xyz-uncorrelated noise does indeed abolish the observed effects). Another methodology that may be implementable is to perform some ultrafast-style experiments, that is, to try to make some measurements on a timescale where the noise has yet to be effective (i.e. substantially faster than the expected coherence lifetime for the system in question), and compare these to longer-timescale measurements where noise has had sufficient time to act.

7. The Monte-Carlo Wavefunction Approach for non-Lindbladian Master Equations

This chapter is adapted from the work presented in: Keens, R.H. and Kattnig, D.R., 2020. Monte-Carlo wavefunction approach for the spin dynamics of recombining radicals. New Journal of Physics, 22(8), p.083064., with permission from the New Journal of Physics.

The Monte-Carlo wavefunction (MCWF) approach is adapted to treat the open-system spin dynamics of radical pairs subject to spin-selective recombination reactions. For such systems, non-Lindbladian master equations are frequently employed, which account for recombination via the non trace-preserving Haberkorn superoperator alongside the reaction-dependent exchange and singlet-triplet dephasing terms. This chapter shows that this type of master equation can be accommodated in the MCWF approach, by introducing a second type of quantum jump, which accounts for the reaction simply by appropriately terminating the propagation. In this way, one can evaluate approximate solutions to the time-dependent radical pair survival probability for systems that have been considered untreatable with the master equation approach until now. This chapter explicates the suggested approach with calculations for radical pair reactions that have been suggested to be relevant for the quantum compass of birds and related phenomena.

7.1 Introduction

The general challenge, should one wish to model spin dynamics, is that the size of Hilbert space grows exponentially with the number of considered spins; this makes full noise calculations like in the previous chapter incredibly computationally demanding. It is a particularly stringent constraint for the dynamics of open quantum systems which do not preserve pure states and thus mandate a formulation in Liouville space, which scales quadratically in Hilbert space dimension (Breuer and Petruccione, 2002). This often leaves theoreticians with the choice between modelling small, but often biologically irrelevant, processes or systems of moderate size that are simplified to an extent that they are unrealistic. In this chapter, a more efficient approach to modelling systems of the kind encountered in quantum biology will be developed and explored.

For typical open quantum systems, i.e. master equations of the standard Lindblad form, a significant step toward solving (more) realistic problems came with the introduction of the Monte Carlo Wave Function (MCWF) approach (Mølmer, Castin and Dalibard, 1993; Kornyik and Vukics, 2019; Plenio and Knight, 1998). The MCWF method, which is otherwise known as the quantum jump method, replaces the evolution of the density matrix with an ensemble average over individual quantum trajectories of wave functions evolved under a pseudo-Hamiltonian and subject to quantum jumps, i.e. discontinuous modifications of the wavefunction, which together account for the openness of the system. Unfortunately, the spin dynamics of radical pairs does not conform to standard Lindblad form if asymmetric (i.e. different in the singlet and triplet configurations) reactivity is included by the Haberkorn approach and its recent additions (Haberkorn, 1976; Jones and Hore, 2010b; Jones, Maeda and Hore, 2011; Fay, Lindoy and Manolopoulos, 2018). This means that the MCWF approach cannot be robustly applied to solve large spin dynamics problems.

Spin-selective recombination processes are an integral part of the spin dynamics of radical systems.(Steiner and Ulrich, 1989; Brocklehurst, 2002; Salikhov et al., 1984; McLauchlan and Steiner, 1991) Various ways to include this aspect in the master equations have been discussed in the recent literature (Jones and Hore,

2010b; Jones, Maeda and Hore, 2011; Fay, Lindoy and Manolopoulos, 2018; Kominis, 2009; Kominis, 2015). The traditional approach, due to Haberkorn (Haberkorn, 1976), suggests that singlet (rate constant k_S) and triplet (k_T) recombination can be accounted for by the superoperator

$$\hat{\hat{K}}\rho = -\frac{k_S}{2}\left\{P_S, \rho\right\} - \frac{k_T}{2}\left\{P_T, \rho\right\}, \tag{7.1}$$

where $P_{S,T}$ are the singlet and triplet projection operators, respectively. This gives rise to a non-trace preserving equation of motion of the (concentration-weighted) density operator, for which the trace of ρ gives the survival probability of the radical (pair) systems. The form of eq. 7.1 has been hotly debated (Purtov, 2010; Kominis, 2009; Jones, Maeda and Hore, 2011; Jones and Hore, 2010b; Kominis, 2015; Tsampourakis and Kominis, 2015; Kominis, 2016; Jeschke, 2016) and confirmed (Tiersch et al., 2012; Jones et al., 2011b; Ivanov et al., 2010). Recently, Fay et al. have suggested a series of quantum master equations to describe the recombining radical pair, which they derive from a microscopic description of the electron transfer reaction using the Nakajima–Zwanzig projector approach (Fay, Lindoy and Manolopoulos, 2018). To second order in the electronic coupling of radical pair and product states (i.e. in the nonadiabatic limit), the authors recover the Haberkorn master equation augmented with an additional reactive exchange coupling term (which was also discussed in (Kattnig, Rosspeintner and Grampp, 2011)). To the fourth order in the coupling (i.e. for more adiabatic reactions) an additional singlet-triplet dephasing (S/T-dephasing) term (Shushin, 1991) of the form

$$\hat{\hat{K}}'\rho = -k_{ST}\left(P_S\rho P_T + P_T\rho P_S\right) \tag{7.2}$$

appears, the rate k_{ST} of which depends on the specific configuration of the system. The quantum measurement approach to radical pair recombination by Jones and Hore can also be understood as a result of the synergistic effect of $\hat{\hat{K}}$ and $\hat{\hat{K}}'$, in this case with the particular choice of $k_{ST} = (k_S + k_T)/2$ (Jones and Hore, 2010b; Jones, Maeda and Hore, 2011). This suggests a central role of the Haberkorn approach

augmented by some additional S/T dephasing for the spin dynamics of radical systems, which is in fact reflected in the widespread use of this combination for modelling experimental data (Hoang et al., 2018; Shushin, 1991).

If $\hat{\hat{K}}$ from eq. 7.1 is the only non-coherent term in the master equation, the spin dynamics of the system can still be evaluated relatively cheaply, as ρ(t) can be constructed from an approach based on the propagation of wavefunctions under a non-Hermitian, effective Hamiltonian (of the form given by eq. 7.9 below) (Lewis, Fay and Manolopoulos, 2016). Thus the simulation process can be handled entirely in the comparably small Hilbert space. Singlet-triplet dephasing as given by $\hat{\hat{K}}'$ in eq. 7.2, does not allow for this quasi-pure state evolution approach. Using $P_S = 1 - P_T$, one can however rewrite eq. 7.2 in many equivalent ways, one of which is

$$\hat{\hat{K}}'\rho = 2k_{ST}\left(P_S\rho P_S - \frac{1}{2}\left\{P_S^\dagger P_S, \rho\right\}\right). \tag{7.3}$$

As eq. 7.3 is in the form of a Lindblad dissipator, the dynamics it induces can in principle be considered within the MCWF approach (Mølmer, Castin and Dalibard, 1993; Kornyik and Vukics, 2019; Plenio and Knight, 1998). However, for this to provide a feasible approach to the spin dynamics of radical systems, one requires a means to extend the MCWF approach to also include the non-unitary contributions associated with the asymmetric recombination of radical pairs as described by eq. 7.1. This is the aim of this contribution.

Quantum trajectories have previously been suggested for the modelling of radical pair dynamics (Kritsotakis and Kominis, 2014). However, it has been argued that Haberkorn's theory cannot be cast in terms of quantum trajectories (Tsampourakis and Kominis, 2015). The presented extension to the MCWF approach allows it to be applied to non-Lindbladian master equations resulting from terms of the form of eq. 7.1. This broadens the applicability of MCWF to the spin dynamics of radical systems subject to spin-selective reactivity. The approach accommodates singlet-triplet dephasing, and thus applies to the description of chemical radical pair reactivity beyond the conventional Haberkorn approach. It is also applicable to models that apply the Haberkorn reaction operator (or extensions thereof) to

the dynamics of open quantum systems with a Lindblad form, e.g. random field relaxation or Redfield type relaxation superoperators of arbitrary genesis (Kattnig, 2017c; Worster, Kattnig and Hore, 2016; Kattnig et al., 2016a; Kattnig, Solov'yov and Hore, 2016). In the limit of infinite samples, the MCWF model agrees exactly with the direct integration of the master equation. It is shown that the approach allows one to obtain estimates of the magnetic field effects of large spin systems, which are considered (currently) intractable using the direct integration method.

This chapter is structured as follows: first, a derivation of the extended MCWF approach is presented and the unique steps taken to make it applicable to the non-Lindbladian recombination term, as shown in eq. 7.1, are explained. Then, some results obtained with this approach are presented, and their equivalence to those obtained with the direct integration of the master equation demonstrated, showing also the comparison between the efficiency and numerical error of both methods. Finally, applications for the approach, and ways to further increase its capability, are suggested.

7.2 Derivation

The MCWF method aims to reconstruct the equation of motion of the (spin) density operator from the ensemble average of stochastic quantum trajectories of state vectors (Mølmer, Castin and Dalibard, 1993; Kornyik and Vukics, 2019; Plenio and Knight, 1998). The approach predominantly provides a computational tool, the efficiency of which rests on the reduction in dimensionality (associated with treatment of Hilbert space state vectors instead of density operators) and the fact that often a relatively small (relative to the Hilbert space dimension) number of samples is sufficient to adequately reconstruct the observables of interest. While individual MCWF trajectories do not necessarily convey reality, they have occasionally been interpreted to do just that, i.e. to reflect the behaviour of single realisations of

quantum systems. First, consider the master equation:

$$\begin{aligned}\frac{d\rho}{dt} &= -i[H,\rho] + \hat{\hat{D}}\rho + \hat{\hat{K}}\rho \\ &= -i[H,\rho] + \sum_m^M \left(J_m \rho J_m^\dagger - \frac{1}{2}\{J_m^\dagger J_m, \rho\} \right) - \frac{1}{2}\sum_n^N \{K_n, \rho\}\end{aligned} \tag{7.4}$$

Here, square (curly) brackets denote the (anti-) commutator. The first term accounts for the coherent evolution under Hamiltonian H (in angular frequency units). The second term, $\hat{\hat{D}}\rho$, is in so-called Lindblad-form and describes decoherence processes in the Born-Markov approximation (Breuer and Petruccione, 2002). The sum extends over M quantum jump or collapse operators, J_m, the maximal number of which is one smaller than the square of the Hilbert space dimension (Huang, Sun and Yi, 2008). The third term, $\hat{\hat{K}}\rho$, here assumed in Haberkorn form, is unique to the treatment of the spin dynamics of radical systems. It describes chemical transformations of the radicals, i.e. their spin-selective recombination to form various reaction products. Typically, the K_n relate to the singlet or triplet projection operators of the reactive pair (i,j) of radicals:

$$K_n = k_{S,T}^{(i,j)} P_{S,T}^{(i,j)}, \tag{7.5}$$

with

$$P_S^{(i,j)} = \frac{1}{4} - \mathbf{S_i} \cdot \mathbf{S_j}, \tag{7.6}$$

and

$$P_T^{(i,j)} = 1 - P_S^{(i,j)}, \tag{7.7}$$

where S_i denotes the spin vector operator (in multiples of $\hbar$) of spin i. For recombination terms K_n of the form of eq. 7.5, $K_n = K_n^\dagger K_n$ applies and the recombination operator assumes a form that, except for one term missing, is reminiscent of the Lindbladian. However, as a consequence of the presence of $\hat{\hat{K}}\rho$ the dynamics do not preserve the trace of the ρ, i.e. ρ is actually the density operator weighted by the probability that the radical system has not yet recombined. In principle, this peculiarity can be avoided by introducing shelfing states, which allows one to recover

the classical Lindblad form throughout (Gauger et al., 2011). However, this comes at the cost of enlarging the Hilbert space by product states, the spin degrees of freedom of which are assumed unobserved. Also note that by absorbing the singlet-triplet dephasing in the J_ms, eq. 7.4 applies to various approaches to treat reactive radical systems, including the Jones-Hore model and the quantum master equation approach (Fay, Lindoy and Manolopoulos, 2018; Jones and Hore, 2010b; Jones, Maeda and Hore, 2011). The equation of motion can be re-expressed in the form:

$$\frac{d\rho}{dt} = -i\left(H_{\text{eff}}\rho - \rho H_{\text{eff}}^{\dagger}\right) + \sum_{m}^{M} J_m \rho J_m^{\dagger}, \tag{7.8}$$

with H_{eff} denoting the effective Hamiltonian:

$$H_{\text{eff}} = H - \frac{i}{2}\sum_{n}^{N} K_n - \frac{i}{2}\sum_{m}^{M} J_m^{\dagger} J_m, \tag{7.9}$$

which marks the starting point of the MCWF approach. As H_{eff} is non-Hermitioan, it induces a non-structure-preserving map in the Hilbert space of the system. The algorithm starts out from an ensemble of state-vectors, $\{|\phi(0)\rangle\}$, that appropriately sample the initial density operator $\rho(0)$. The state vectors are assumed to evolve under the effective Hamiltonian H_{eff} according to

$$\frac{d}{dt}|\phi(t)\rangle = -iH_{\text{eff}}|\phi(t)\rangle \tag{7.10}$$

and undergo occasional quantum jumps (to be described below). Closely following the exposition of (Mølmer, Castin and Dalibard, 1993), the evolution of $|\phi(t)\rangle$ to $|\phi(t+\delta t)\rangle$ shall be considered, where the time increment δt is arbitrary, but sufficiently small such that terms including δt of order 2 and higher can be neglected. Under this assumption, the non-unitary evolution produces the state:

$$\left|\phi^{(1)}(t+\delta t)\right\rangle \approx (1 - iH_{\text{eff}}\delta t)\,|\phi(t)\rangle\,. \tag{7.11}$$

The square of the l^2 norm of the state decreases during this evolution from its value at t, $\langle\phi(t)|\,\phi(t)\rangle = l^2$, to:

$$\left\langle \phi^{(1)}(t+\delta t)\right|\,\phi^{(1)}(t+\delta t)\rangle = (1-\delta p)\,l^2, \tag{7.12}$$

where to first order in δt:

$$\begin{aligned}\delta p &= \frac{i\delta t}{l^2}\,\langle\phi(t)|\,H_{\text{eff}} - H_{\text{eff}}^{\dagger}\,|\phi(t)\rangle \\ &\equiv \sum_{m}^{M}\delta p_m + \sum_{n}^{N}\delta p'_n.\end{aligned} \tag{7.13}$$

It is later shown that the squared norm l^2 cancels, so this is no significant divergence from the original approach, which assumes $l^2 = 1$. Yet, the more general assumption of $l^2 \neq 1$ was impelled here by the intrinsic non-trace preserving formulation of the dynamics in the presence of spin-selective recombination processes as described by eq. 7.4. δp is interpreted as the probability that a quantum jump occurs within time interval δt. The probability that this jump involves the m^{th} Lindblad term and the n^{th} reaction term is given by δp_m and $\delta p'_n$, respectively:

$$\delta p_m = \frac{\delta t}{l^2}\,\langle\phi(t)|\,J_m^{\dagger}J_m\,|\phi(t)\rangle$$

$$\begin{aligned}\delta p'_n &= \frac{\delta t}{2l^2}\,\langle\phi(t)|\,K_n^{\dagger} + K_n\,|\phi(t)\rangle \\ &= \frac{\delta t}{l^2}\,\langle\phi(t)|\,K_n\,|\phi(t)\rangle\,,\end{aligned} \tag{7.14}$$

where the last equality in the expression of $\delta p'_n$ applies for Hermitian K_n (e.g. reaction terms composed from singlet and triplet projection operators). It is implied here that $\delta p << 1$ (as δt is small), which guarantees that the probability of two jumps occurring within one timestep δt is negligible. Quantum jumps are introduced into the time evolution of the state vectors as a stochastic element, thereby mimicking the physically expected, uncertainty of quantum processes. To this end, a quasi-random number u between zero and one is drawn from the continuous uniform distribution.

If, as in the vast majority of cases by construction, $\delta p < u$, no jump has occurred and the state vector is renormalized and propagated on. If, however, $\delta p \geq u$, a quantum jump is executed. The actual jump process is again selected at random from the M Lindblad and N kinetic terms, whereby the relative probability is $\delta p_m/\delta p$ and $\delta p'_n/\delta p$, respectively. This leaves us with three distinct events to consider in the time-evolution of the state vector: no jump, Lindbladian jump, and recombination/reaction. In the event of no jump, which occurs with probability $1 - \delta p$, the re-normalized state vector at $t + \delta t$, $|\phi(t + \delta t)\rangle$, can be chosen as

$$|\phi(t+\delta t)\rangle \Big|_{\text{no jump}} = l \frac{\left|\phi^{(1)}(t+\delta t)\right\rangle}{|| \, |\phi^{(1)}(t+\delta t)\rangle \, ||}. \tag{7.15}$$

Alternatively, in the event of a jump associated with J_m (occurring with probability δp_m), the re-normalized wavefunction is obtained from

$$|\phi(t+\delta t)\rangle \Big|_{\text{jump}} = l \frac{J_m \, |\phi(t)\rangle}{||J_m \, |\phi(t)\rangle \, ||}. \tag{7.16}$$

So far, this entirely equals the established MCWF approaches. The new case that has been introduced is that of reaction/termination, which occurs with probability $\delta p'_n$. As the associated superoperator is not of Lindblad form, this event requires an approach that differs from MCWF algorithm as traditionally implemented. it can physically reasoned that a termination reaction should eliminate the trajectory upon which it occurs, rather than propagating it. Thus is chosen, for the termination state, the new state vector to be the zero function:

$$|\phi(t+\delta t)\rangle \Big|_{\text{reaction}} = 0 \tag{7.17}$$

for $t + \delta t$ and all subsequent times. This is equivalent to stating that all expectation values following the reaction event are equated to zero, i.e. the quantum state is whence absent from the population weighted ensemble.

Herein is demonstrated the equivalence between this extended MCWF approach and the master equation approach by showing that the master equation, eq. 7.4, can be recovered from the ensemble average of MCWF trajectories. One can begin by

considering a pure state with density operator $\sigma(t) = |\phi(t)\rangle \langle\phi(t)|$. It is found that this quantity at the later time $t + \delta t$ by averaging over many MCWF trajectories. This will give rise to the time averaged $\sigma(t + \delta t)$, here denoted $\bar{\sigma}(t + \delta t)$, as a linear combination of the state-vector diads from above, each weighted by the associated probability:

$$\bar{\sigma}(t+\delta t) = l^2(1-\delta p')\frac{\left|\phi^{(1)}(t+\delta t)\right\rangle \left\langle\phi^{(1)}(t+\delta t)\right|}{||\,|\phi^{(1)}(t+\delta t)\rangle\,||^2}$$

$$+\sum_m l^2\delta p_m \frac{J_m\,|\phi(t)\rangle\,\langle\phi(t)|\,J_m^\dagger}{||J_m\,|\phi(t)\rangle\,||^2} \tag{7.18}$$

$$+\sum_n^N \delta p'_n\, 0.$$

$\delta p'_n$, multiplied by its zero generator, has been deliberately included to make clear the distinction between this method and the previous MCWF implementation. Using eqs. 7.11 and 7.17, this simplifies to:

$$\begin{aligned}\bar{\sigma}(t+\delta t) = &\left|\phi^{(1)}(t+\delta t)\right\rangle \left\langle\phi^{(1)}(t+\delta t)\right| \\ &+ \delta t\sum_m^M J_m\,|\phi(t)\rangle\,\langle\phi(t)|\,J_m^\dagger,\end{aligned} \tag{7.19}$$

which can be written to first order in δt as:

$$\bar{\sigma}(t+\delta t) =$$

$$(1 - iH_{\text{eff}}\delta t)\,\sigma(t)\left(1 + iH_{\text{eff}}^\dagger\delta t\right) + \delta t\sum_m^M J_m\sigma(t)J_m^\dagger \tag{7.20}$$

$$= \sigma(t) - i\delta t\left(H_{\text{eff}}\bar{\sigma}(t) - \bar{\sigma}(t)H_{\text{eff}}^\dagger\right) + \delta t\sum_m^M J_m\sigma(t)J_m^\dagger.$$

Finally, in the limit $\delta t \to 0$ one recovers eq. 7.8 for the pure initial state. The approach also holds for any convex combination of initial states, if the initial state is sampled from these states and is thus general. This completes the proof.

In summary, by imposing that a reaction event terminates the trajectory that is being propagated it has been demonstrated the equivalence between an adapted version of the MCWF approach and the master equation that governs radical pair dynamics, or more generally, radical system dynamics, with recombination terms of non-Lindbladian form.

7.3 Implementation

Actually evaluating the MC evolution as a succession of many tiny steps δt, each of which treated to first-order in time as done above, is tedious. Instead, the following algorithm was used to simulate a single realization of a quantum system (Plenio and Knight, 1998). Observe that based on the description from above, the probability of no-jump after n steps is

$$\begin{aligned} P_{no}(t = n\delta t) &= \Pi_{j=0}^{n-1} \left\| (1 - iH_{\text{eff}}\delta t) \left| \phi(j\delta t) \right\rangle \right\|^2 \\ &= \left\| (1 - iH_{\text{eff}}\delta t)^n \left| \phi(0) \right\rangle \right\|^2 . \end{aligned} \tag{7.21}$$

In the limit $\delta t \to 0$, while $n\delta t = \tau$, this expression reduces to:

$$P_{no}(\tau) = \left\| \exp(-iH_{\text{eff}}\tau) \left| \phi(0) \right\rangle \right\|^2 , \tag{7.22}$$

and the jump probability is:

$$P(\tau) = 1 - P_{no}(\tau) = 1 - \left\| \exp(-iH_{\text{eff}}\tau) \left| \phi(0) \right\rangle \right\|^2 . \tag{7.23}$$

This can be interpreted as the cumulative distribution function of the waiting time τ until the next jump. Thus, instead of painstakingly accumulating many δt-steps, samples are drawn from the waiting time distribution. Practically, this can be implemented by drawing a uniform random number $u \in [0, 1)$ and performing the non-unitary deterministic time evolution generated by H_{eff} until the squared norm of the state vector falls below u. At the moment where this happens, a quantum jump

is executed. The collapse/kinetic operator for the jump can be from the $N + M$ possibilities at random, where the relative probability of choosing J_m and K_n is proportional to δp_m and $\delta p'_n$, respectively. This approach increases the efficiency of solving the problem by allowing one to rely on higher order ordinary differential equation (ODE) solvers (as opposed to the inefficient Euler method used in the derivation above), which utilize markedly larger and, possibly, adaptive time steps. Since the approach is derived from the $\delta t \to 0$ limit, it also evades the issue of quantum jumps taking a finite amount of time (see the discussion in (Kornyik and Vukics, 2019)). The downside is that exact time point of the quantum jump must be identified. Using state-of-the-art ODE solvers that provide dense outputs, i.e. representations of the solution as interpolation function in t, this can be realized efficiently by retracing the solution to the point where the jump condition is met (Rackauckas and Nie, 2017). It is found that the problems considered here are efficiently integrated by 5/4 Runge-Kutta methods, such as Dormand-Prince's and Tsitouras' approach (Dormand and Prince, 1986; Tsitouras, 2011), both of which provide free 4^{th} order interpolants to be used in backtracking and interpolating the solution on a user-provided time grid (a point every nanosecond was used here). The performance of the Runge-Kutta methods could even be exceeded by using adaptive multi-step methods. In particular, the 5^{th} order Adams-Moulton method (using the 4^{th} order Runge-Kutta approach to calculate starting values) has proved highly efficient (Schwarz and Köckler, 2013).

Radical pairs that are generated in the singlet electronic state are considered. The initial state is, hence, an incoherent mixture of singlet states whereby all nuclear spin configurations are equally probable, since the states are quasi-degenerate and the temperature is comparably high:

$$\rho(0) = \frac{1}{Z} P_s \otimes_i 1_i \tag{7.24}$$

Here, Z is the total number of nuclear spin states and the direct product comprises all nuclei via the index n. Consequently, the MCWF approach requires one to sample different nuclear spin states in a way that converges, for every nuclear Hilbert space,

to the required scaled unity density 1_i. This could clearly be realized by iterating over all Z nuclear spin states e.g. in the canonical basis (i.e. the eigenstates of I_i^2 and $I_{i,z}$). However, the exponential scaling of Z with the number of nuclear spin renders this approach impractical for large spin systems, i.e. those that the MCWF approach aims to cover, since the computational time complexity is not one that can be practically used for any but the smallest of systems. This exponential scaling can be avoided by, once again, performing a Monte Carlo sampling over randomly chosen initial states (Weiße et al., 2006). A study by the Manolopoulos group suggests that, in the context of the wavefunction-based approach to solving eq. 7.4 without using Lindblad dissipators, this limitation can be overcome by stochastically sampling the nuclear spin wave functions in the form of spin coherent states (Lewis, Fay and Manolopoulos, 2016). This approach promises rapid convergence of expectation values with the number of sampled states and, importantly, the number of required states not scaling (or even decreasing) with the size of the Hilbert space (Weiße et al., 2006). The over-complete set of spin coherent states, parametrised by θ and ϕ, can formally be obtained by rotating the $I_{i,z}$ eigenstate with highest projection, $|I_i, I_i\rangle$, to point in the direction $\hat{n} = \hat{n}(\theta, \phi)$ of polar angle θ and azimuthal angle ϕ, e.g. by rotating by angle θ around the axis parallel to $\hat{n} \times \hat{z}$ (the hat on classical vectors is intended to mean normalisation) (Lieb, 1973; Radcliffe, 1971):

$$\begin{aligned} |\Omega_i\rangle &= |\theta_i, \phi_i\rangle \\ &= \exp\left(i\theta\widehat{\hat{n} \times \hat{z}} \cdot \vec{I_i}\right) |I_i, I_i\rangle \\ &= cos\left(\frac{\theta_i}{2}\right)^{2I_i} \exp\left(tan\left(\frac{\theta_i}{2}\right) e^{i\phi} I_{i,-}\right) |I_i, I_i\rangle \,. \end{aligned} \tag{7.25}$$

As the states satisfy the completeness relation

$$1_i = \int_0^{\pi} sin(\theta_i) d\theta_i \int_0^{2\pi} d\phi_i \, |\Omega_i\rangle \langle\Omega_i| \,, \tag{7.26}$$

the MCWF approach can be realized by randomly sampling the orientation $\hat{n}$ for each of the nuclear spins from the unit sphere. As the MCWF is stochastic as such, the additional spin coherent states sampling is seamlessly integrated.

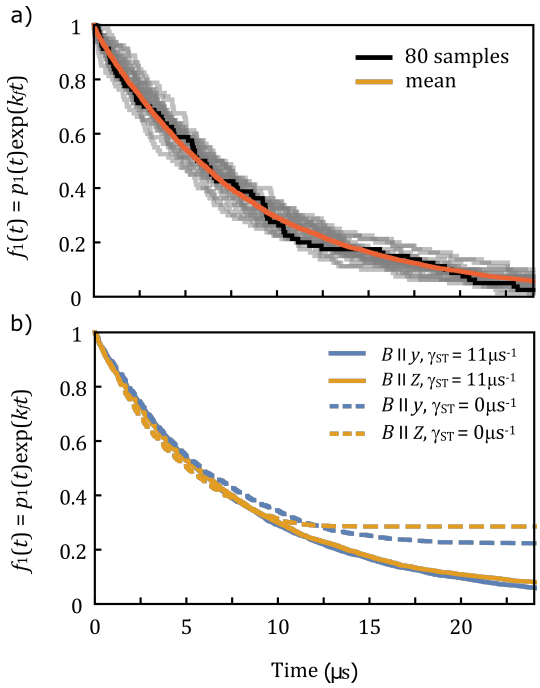

Figure 7.1: Transformed survival probability, $f_1(1) = p_1(t)\exp(k_f t)$, as a function of time for the [FAD$^{\bullet-}$ W$^{\bullet+}$] system with 8 + 8 nuclear spins, subject to S/T-dephasing at the rate $\gamma_{ST} = 11$ μs^{-1} and a magnetic field of $B = 1$ mT. A recombination rate of $k_b = 0.5$ μs^{-1} was assumed. (a) shows the reconstruction of the time-dependence of $f_1(t)$ for many trajectories using the MCWF approach. The solid red line shows the eventually converged mean; every gray curve, a single of which has been highlighted in black, corresponds to 80 samples. Here, $B = 1$ mT is aligned with the $\hat{z}$-axis of FAD. (b) summarizes the converged results for or different field directions in the absence and presence of S/T-dephasing. Note that S/T-dephasing strongly attenuates the anisotropy of the response to magnetic field.

7.4 Results

The author and group members have implemented the MCWF approach for spin dynamic calculations on radical pairs as outlined above. Here is presented an assessment of its performance established in terms of two prototypical radical pair systems with putative relevance to magnetoreception (Lee et al., 2014; Hiscock et al., 2016; Maeda et al., 2012). These radical pairs comprise a semi-reduced flavin adenine dinucleotide, FAD, non-covalently bound in the protein cryptochrome, i.e. FAD$^{\bullet-}$, and a partner radical. *In vitro*, the combination of FAD$^{\bullet-}$ and an oxidized tryptophan radical, W$^{\bullet+}$, is known to convey magnetosensitivity (Maeda et al., 2012; Kattnig et al., 2016b). *In vivo*, the identity of the second radical is less clear and currently fiercely debated (Kattnig, 2017c). In model calculations, systems of so called reference-probe character have been found to elicit large anisotropic magnetic field effects (Lee et al., 2014; Procopio and Ritz, 2020). The prototypical

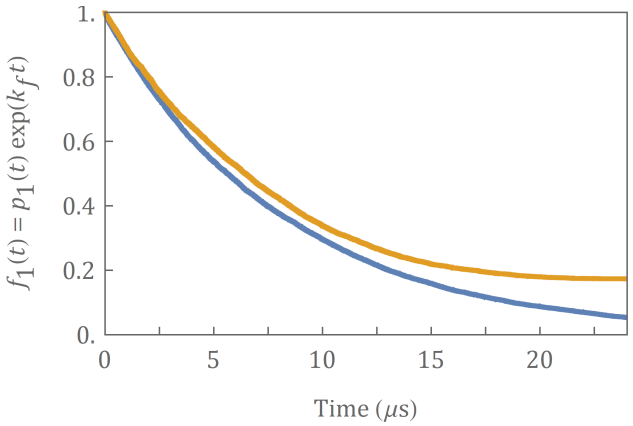

Figure 7.2: $f_1(t) = p_1 \exp(k_f t)$ for the [FAD$^{\bullet-}$ W$^{\bullet+}$] radical pair with 8 + 8 nuclear spins, $k_b = 0.5$ µs^{-1} and $B = 0$, with (blue) and without (orange) S/T-dephasing at a rate of $\gamma_{ST} = 11$ µs^{-1}.

system of this type is [FAD$^{\bullet-}$ Z$^{\bullet}$], where the flavin is combined with a radical devoid of hyperfine interactions, Z$^{\bullet}$. A radical of this kind could possibly result from a reoxidation reaction of the fully reduced FAD cofactor with molecular oxygen (Hammad et al., 2020; Pooam et al., 2019; Wiltschko et al., 2016). Note that many details of cryptochrome magnetoreception are as yet unknown and no concrete picture has yet emerged from the combined literature. However, this is not an issue here, where the purpose is to discuss MCWF approach for recombining radical pairs as treated within the Haberkorn, respectively quantum master equation, framework. Radical pair magnetic field effects are attributed to a delicate interplay of the coherent evolution, predominantly due to hyperfine and the Zeeman interaction, and spin selective recombination. For oriented systems, the typical Hamiltonian is of the form

$$H = H_1 + H_2, \tag{7.27}$$

where

$$H_k = \frac{\mu_B g_j}{\hbar} \vec{B} \cdot \vec{S}_k + \sum_i \vec{S}_k \cdot A_{ki} \cdot \vec{I}_{k,i}. \tag{7.28}$$

Here, $\vec{B}$ is the applied magnetic field, g_k the g-factor (g-anisotropy is neglected here, because the focus is on organic radicals in comparably weak magnetic fields), A_{ki} is the hyperfine tensor and $\vec{S}_k$ and $\vec{I}_{k,i}$ are the individual electron and nuclear spin operators, respectively. In addition, the exchange and electron-electron dipolar interaction should be taken into account. These interactions are sometimes the source

of unexpected effects, but often are found to attenuate MFEs in weak magnetic fields (Babcock and Kattnig, 2020; Efimova and Hore, 2008). As is commonly done, these extra terms shall be neglected here for simplicity. Note nonetheless that their inclusion would not pose an additional difficulty as the effective Hamiltonian, H_{eff}, as resulting from eq. 7.28 does not in general allow for a factorisation anyway. The radical pair systems considered here can either recombine in the singlet configuration (with rate k_b) or proceed in a non-spin selective process to form a reaction product (rate k_f), which in the context of magnetoreception is thought to involve a protein structure rearrangement, whence innervating a signalling cascade (Kattnig, Nielsen and Solov'yov, 2018). The kinetic superoperator $\hat{\hat{K}}$ is thus of the form

$$\hat{\hat{K}}\rho = -\frac{k_b}{2}\left\{P_S, \rho\right\} - k_f\rho, \tag{7.29}$$

which is tantamount to setting $k_S = k_f + k_b$ and $k_T = k_f$ in eq. 7.1. Here it is assumed that the radical pairs are subject to S/T-dephasing (see eq. 7.2 above; dissipation rate $k_{ST} = \gamma_{ST}$) as a result of the reactive encounter process and/or the modulation of the exchange and electron-electron dipolar interaction terms by molecular motion. In addition, random field relaxation is assumed, and accounted for by a Lindblad dissipator with uncorrelated noise associated with the Cartesian spin operators of the two radicals $J_m \in \{S_{k,x}, S_{k,y}, S_{k,z}\}$ (Kattnig, Solov'yov and Hore, 2016; Kattnig, 2017c). Assuming that the dissipation rates for all directions are equal to $\gamma_{RF,k}$, this gives rise to the combined term for radical k of the form

$$\hat{\hat{R}}_k\rho = \gamma_{RF,k}\left[\sum_{\alpha\in\{x,y,z\}} S_{k,\alpha}\rho S_{k,\alpha} - \frac{3}{4}\rho\right]. \tag{7.30}$$

Furthermore, it is assumed that the radical pair is generated in the singlet state, e.g. by a swift, spin-conserving electron transfer reaction of diamagnetic precursors, and, thus, $\rho(0) = P_S/Tr[P_S]$.

The singlet probability, $p_S(t) = Tr[P_S\rho(t)]$ or the survival probability is the tracked quantity, $p_1(t) = Tr[\rho(t)]$ of the radical pair over time, whence the yields of

the recombination, Y_S and escape/signalling product, Y_1 can be calculated from

$$Y_S = k_b \int_0^\infty p_s(t)dt, \tag{7.31}$$

and

$$Y_1 = k_f \int_0^\infty p_1(t)dt, \tag{7.32}$$

respectively. Evaluating $p_1(t)$ from the MCWF approach is particularly straight forward, as it is derived from sampling the recombination time only. In particular, no evaluation of expectation values on a regular time grid (in addition to the usual following of the trace of ρ for the purpose of identifying the moments of quantum jumps) is necessary. This allows for a particularly efficient implementation.

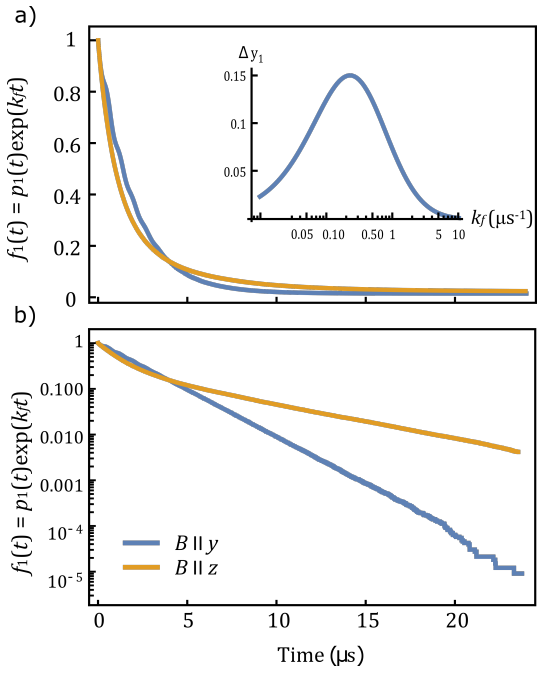

Figure 7.3: (a) The test case used here was the [FAD$^{\bullet-}$ Z$^{\bullet}$] system, with 14 spins under random field relaxation with rate $\gamma_{RF} = 0.2$ µs^{-1} and $k_b = 2$ µs^{-1}. Here, it has been assumed $B = 50$ µT, which is of the order of the geomagnetic field at mid-latitude. The insert shows the dependence of the magnetic anisotropy for this system, evaluated as the difference of Y_1 when the field is in the $\hat{y}$ and $\hat{z}$-direction, respectively, on the forward rate constant k_f. (b) shows $f_1(t)$ on a logarithmic scale. $t_{\max} = 24$ µs and $N = 476,800$ Monte Carlo samples have been collected.

Here are reported some attempts of applying the MCWF approach to the two radical pair systems [FAD$^{\bullet-}$ W$^{\bullet+}$] and [FAD$^{\bullet-}$ Z$^{\bullet}$] subject to the outlined scenario, whereby a variable number of hyperfine-coupled nuclei was taken into account. The relevant hyperfine parameters, up to 12 for FAD$^{\bullet-}$ (including two nitrogens with

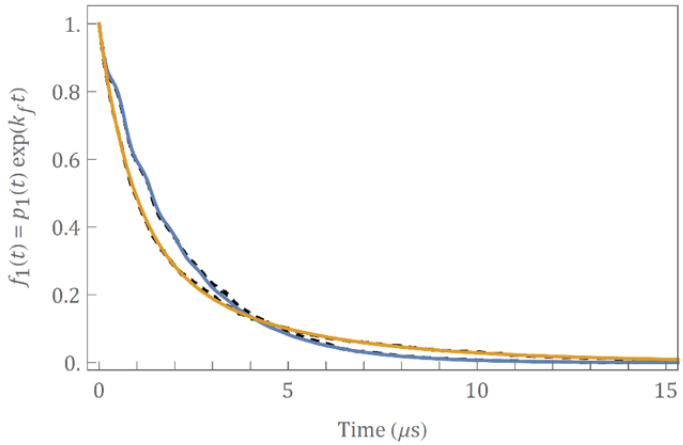

Figure 7.4: $f_1(t)$ of the [FAD$^{\bullet-}$ Z$^{\bullet}$] systems with parameters as specified for Fig. 7.3. Solid lines: calculated using the MCWF approach with $N = 3200$ samples only. The general shape of the transformed survival probability is hardly discernible from the converged result (dashed lines).

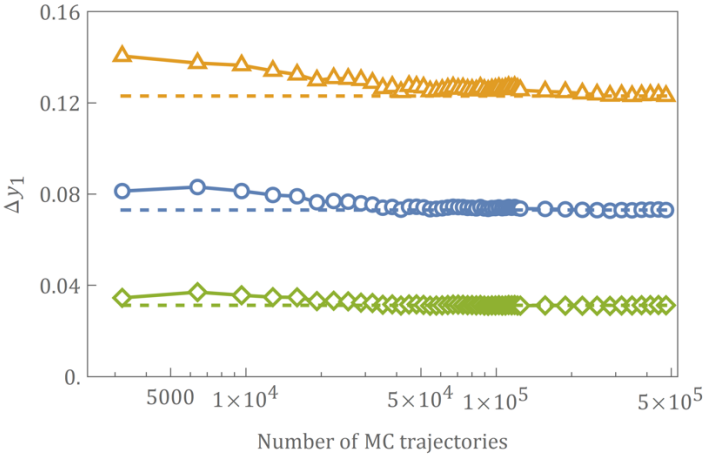

Figure 7.5: ΔY_1 for the [FAD$^{\bullet-}$ Z$^{\bullet}$] described in Fig. 7.3 at $B = 50$ µT with random field relaxation as a function of the number N of averaged MC trajectories. The orange, blue and green data apply to $k_f = 0.5$ µs^{-1}, 1 µs^{-1} and 2 µs^{-1}, respectively.

$I = 1$) and up to 8 (one nitrogen) for W$^{\bullet+}$, are summarized in the appendix, sections 9.13.1 and 9.13.2. For the simulations with a variable number of hyperfine-coupled nuclear spins reported here, the hyperfine interactions in FAD$^{\bullet-}$ were added in the order N5, N10, H6, 3 x H8, Hβ1, Hβ2, H9, and 3 x H7. For W$^{\bullet+}$ the order was N1, H1, Hβ2, H4, H2, H6, Hβ1, H7 and H5. Figure 7.1 shows exemplary results for [FAD$^{\bullet-}$ W$^{\bullet+}$] subject to S/T-dephasing at the rate $\gamma_{ST} = 11$ µs^{-1} and a magnetic field of $B = 1$ mT. Analogous data for $B = 0$ mT are shown in Fig. 7.2.

A recombination rate of $k_b = 0.5$ µs^{-1} was assumed, which is typical for this kind of system. Here is shown the transformed survival probability $f_1(t) = p_1(t)\exp(+k_f t)$ as a function of time, which is independent of k_f as by the form of $\hat{\hat{K}}$, eq. 7.29, the

forward reaction induces a simple exponential decay of the density matrix. Typical values of k_f would be of the order of 1 μs^{-1}. Figure 7.1(a) shows how the MCWF approach reconstructs the time-dependence of an observable from many trajectories; 80 individual runs are combined into one grey line; the eventually converged average is shown as a red solid line. Figure 7.1(b) shows converged results for different orientations of the magnetic field with and in the absence of S/T-dephasing. Note that without S/T-dephasing the dynamics populate states which are part of the kernel of the Liouvillian and thus do not decay. S/T-dephasing breaks the longevity of the associated radical pair population. Figure 7.3 features the [$FAD^{\bullet -}$ $Z^{\bullet}$] spin system with 14 spins under random field relaxation (cf. eq. 7.30) with rate $\gamma_{RF} = 0.2$ μs^{-1}. Here, it has been assumed $B = 50$ µT, which is of the order of the geomagnetic field at mid-latitude. Figure 7.3(a) shows $f_1(t)$ for different orientations of the magnetic field and the dependence of the magnetic anisotropy, assessed in terms of the difference of the escape yield for the magnetic field aligned with the $\hat{z}$ and $\hat{y}$-direction, on the rate k_f. To this end, the yield was obtained by numerically integrating $p_1(t)$ up to a cut-off time of $t_{max} = 24$ µs. $f_1(t)$ for a smaller number of samples and the convergence behaviour of ΔY_1 for this system are shown in Figs. 7.4 and 7.5. Of particular note here is that the general shape of the transformed survival probability can be seen to be hardly distinguishable from the converged result, which attests to the robustness of the methodology used in the present work, and the validity of the results obtained therefrom.

For smaller spin systems, the accuracy of the method has been compared to the result obtained from direct integration of the master equation using Tsitouras' Runge–Kutta pairs of order 5(4) with adaptive time stepping to ascertain a relative and absolute error of 10^{-8}. For the [$FAD^{\bullet -}$ $Z^{\bullet}$] problem with random field relaxation ($\gamma_{RS} = 0.2$ μs^{-1}) and 10 coupled nuclei (including two nitrogen atoms), Figure 7.6 illustrates the deviation of the direct integration and the MCWF approach when $160,000$ Monte Carlo samples are drawn. The maximal deviations are of the order of 10^{-3} – invisible to the eye when comparing $f_1(t) = p_1(t)\exp(k_b t)$ in the range from 0 to 1. Figure 7.7 shows similar data for [$FAD^{\bullet -}$ $W^{\bullet +}$] with 4 hyperfine-coupled

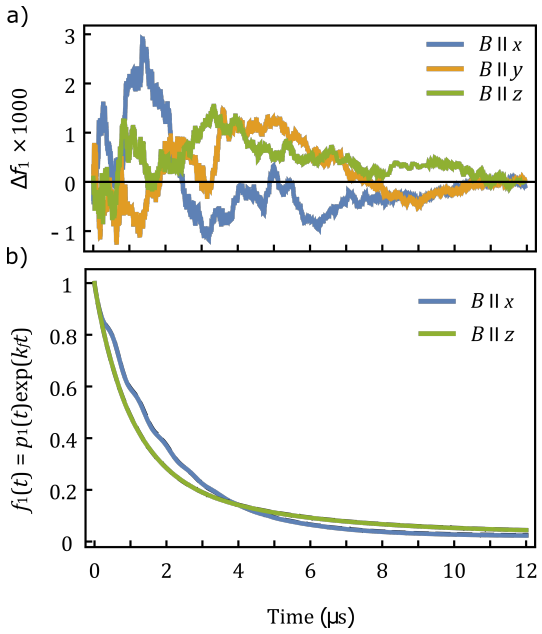

Figure 7.6: (a) Deviation of the direct ME integration and MCWF approach with 160,000 samples drawn, for the [FAD$^{\bullet-}$ Z$^{\bullet}$] problem with random field relaxation ($\gamma_{RS} = 0.2$ µs^{-1}), $k_b = 2$ µs^{-1} and 10 coupled nuclei (including two nitrogen atoms) for different orientations of the magnetic field ($B = 50$ µT) as indicated. (b) The transformed survival probability of this system as a function of time. The ME and MCWF approaches are indistinguishable on the image scale.

nuclear spin in every radical when 16,000, ten times fewer, samples are averaged in the MCWF approach. Analogous data for S/T-dephasing are provided in Fig. 7.8. These data show that the two approaches provide congruent results. Naturally, the accuracy of the MCWF method depends on the number of accumulated trajectories. Figure 7.9 shows the root-mean-square error

$$E_i = \sqrt{\frac{1}{t_{max}} \int_0^{t_{max}} \left(f_{i,MCWF} - f_{i,ME}\right)^2 dt} \tag{7.33}$$

of $f_i(t) = p_i(t)\exp(k_f t)$ as a function of the number of MC samples. ME stands for the direct, i.e. naïve, integration of the master equation. t_{max} was set to 24 µs. The error bars indicate twice the standard deviation of the mean of E_i evaluated from 4 to 94 independent repeats (depending on the sample number) of the error calculation. Both f_1 and f_S decrease approximately with $N^{-1/2}$, as is expected for the standard error of Monte Carlo estimators. Importantly, for the studied systems, no systematic difference between the MCWF and master equation method became apparent, which is expected for an implementation based on eq. 7.22 provided that the error tolerances

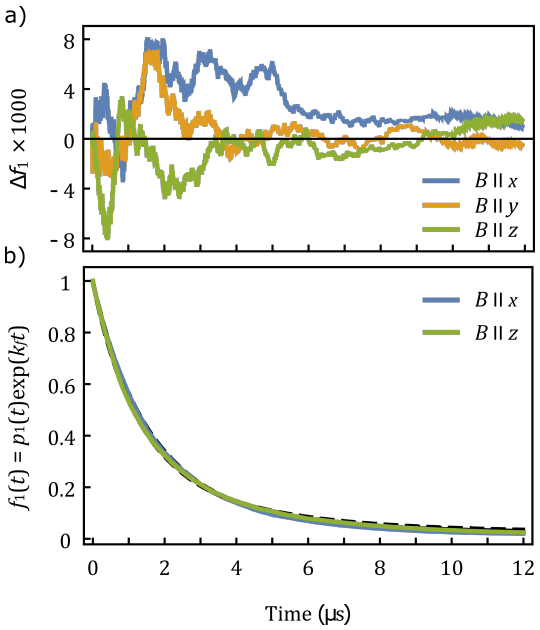

Figure 7.7: (a) Deviation of the direct ME integration and MCWF approach with 16,000 samples drawn, for the [FAD$^{\bullet-}$ W$^{\bullet+}$] with 4 hyperfine-coupled nuclear spin in every radical, random field relaxation ($\gamma_{RS} = 0.2\ \mu s^{-1}$), $B = 1$ mT and $k_b = 2\ \mu s^{-1}$. (b) The transformed survival probability of this system as a function of time.

associated with the numerical integration and quantum jump time localisation are chosen to be sufficiently low. Different approaches of sampling the initial nuclear spin wavefunction have also been compared. In addition to the spin coherent state sampling described above, nuclear spin wave functions were randomly picked in the $\{I_i^2, I_{i,z}\}$-basis and used a complete set of basis functions, i.e. all $\{I_i^2, I_{i,z}\}$-basis states were sampled in succession. It was not possible to discern a significant difference in the error of $f_1(t)$, i.e. the standard deviation associated with the sampling process (which is larger than the indicated standard deviations of the mean of the sampled error) exceeded the differences of the approaches. This indifference is reassuring, as it suggests that the error introduced by stochastically sampling the nuclear spin functions does not lead to undue error compared with complete sampling, where it is possible. The approach based on spin coherent states is valuable as for large spin systems drawing less than Z samples is often unavoidable or, in fact, desirable, which is where this method is expected to offer good convergence (Lewis, Fay and Manolopoulos, 2016). Based on the results here, however, the question of whether spin coherent state sampling is superior to the random picking of the finite set of states cannot be answered. For f_S the analogous conclusions apply. It is interesting

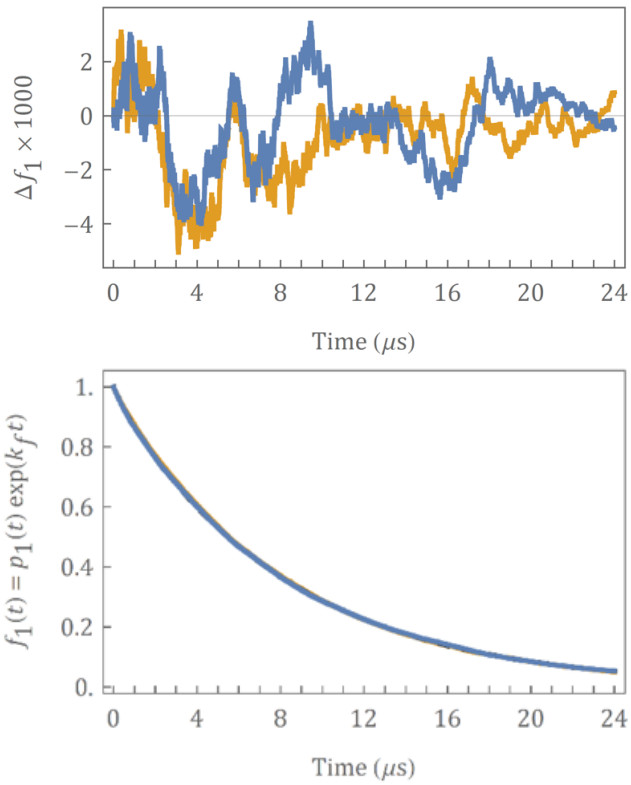

Figure 7.8: Error of the MCWF approach relative to the ME method for a small [FAD$^{\bullet-}$ W$^{\bullet+}$] spin system with 4 + 4 coupled nuclear spins subject to S/T-dephasing. $N = 16,000$, $k_b = 0.5$ µs^{-1}, $gamma_{ST} = 11$ µs^{-1}, $B = 1$ mT. Considered nuclei: N5, N10, H6, H8 in FAD$^{\bullet-}$ and N1, H1, Hβ2, H4 in W$^{\bullet+}$. The magnetic anisotropy is tiny under the simulation conditions. For $k_f = 1$ µs^{-1}, Y_1 differs by only 0.0051 for the y (blue) and z-direction (orange); the yield for the z direction is $Y_1 = 0.88$.

to note that for the system analysed here the ratio of the errors E_S/E_1 appears to be systematically smaller for the spin coherent state sampling than the other implemented approaches (whilst the differences are again smaller than the standard deviations). This might indicate a small inherent advantage of the spin coherent state when singlet yields are observed. This observation will require more detailed studies to become conclusive.

The MCWF approach strength lies in its applicability to comparably large spin system for which the master equation approach cannot realistically be applied. This advantage becomes obvious when comparing the CPU times to generate a solution for the two approaches as a function of the number of coupled spins, as it is summarised in Figure 7.10, with a further result for the S/T-dephasing scenario shown in Fig. 7.11. Here, the starting point was a basic [FAD$^{\bullet-}$ Z$^{\bullet}$] or [FAD$^{\bullet-}$ W$^{\bullet+}$] system that comprised all nitrogen spins. Adding one proton spin at a time, the runtime

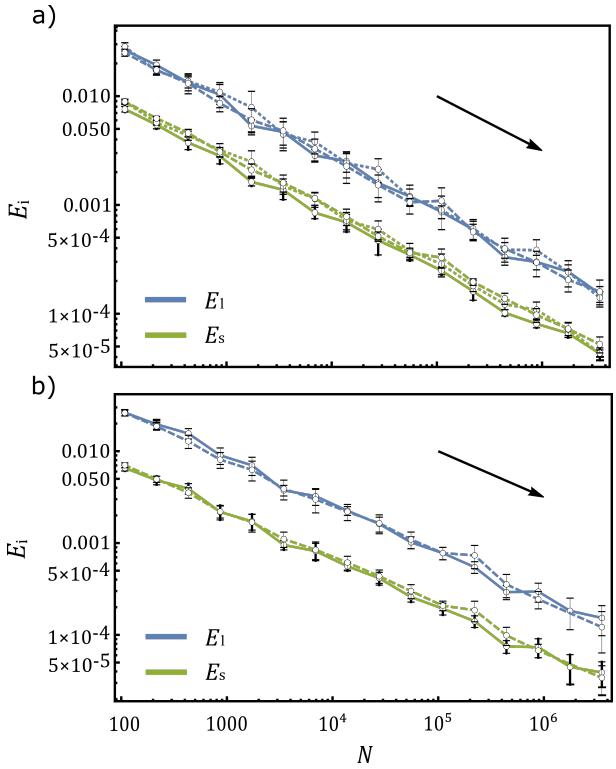

Figure 7.9: RMS error of the transformed singlet and survival probability within the implementation of the MCWF approach compared to the numerical implementation of the direct integration of the master equation as a function of the number of Monte Carlo samples N. (a) applies to the 5 spin system FAD$^{\bullet-}$ W$^{\bullet+}$] system; (b) collects data for an 8 spin system of the same type. The errors E_S and E_1 are shown in green and blue, respectively. Different sampling strategies of the initial nuclear spin configurations are encoded by line styles: solid lines: spin coherent state sampling; dashed lines: random sampling of nuclear spin states in the Zeeman basis; and dotted lines: complete sampling. The arrow indicates the slope of the expected $N^{-1/2}$-dependence. Linear fits to the data are in agreement with this expectation within statistical error. The error bars indicate two standard deviations of the mean error E_i evaluated from 94 to 4 independent repeats for a given sample size N. All additional parameters are as for Fig.
7.6.

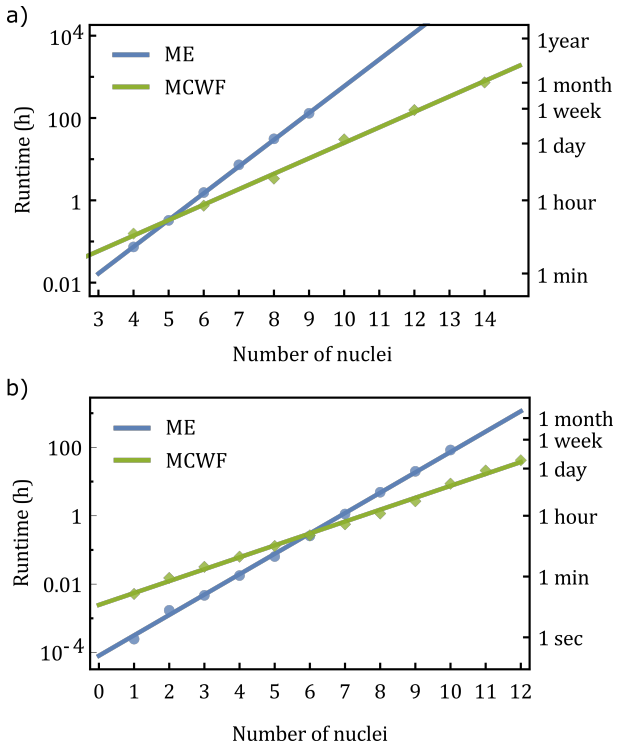

Figure 7.10: Comparison of the CPU time required to generate a solution for both the integration of the ME and the implementation of the MCWF approach, as a function of the number of coupled spins in the system. Panel (a) shows a [FAD$^{\bullet-}$ W$^{\bullet+}$] system that comprised all nitrogen spins and a variable number of proton spins, and panel (b) shows a basic [FAD$^{\bullet-}$ Z$^{\bullet}$] system. Simulation parameters are as given in Fig.
1 and 2 for the respective systems. 2^{16} samples have been drawn for the MCWF approach and $t_{max} = 12$ µs. The MCWF method used the Dormand-Prince 5/4 Runge-Kutta method with an absolute error tolerance of 10^{-8} and a relative error tolerance of 10^{-6}.

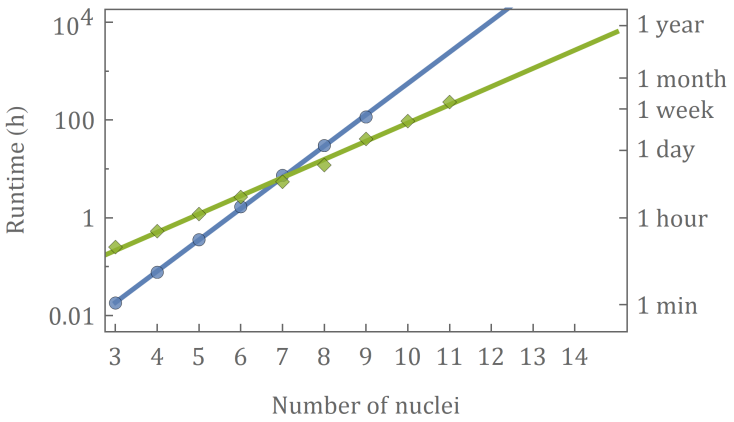

Figure 7.11: Runtime scaling for the [FAD$^{\bullet-}$ W$^{\bullet+}$] simulations with fast S/T-depahsing for the ME (blue) and MCWF (green) approach. Parameters: $B = 1$ mT, $k_b = 0.5$ µs^{-1}, $\gamma_{ST} = 11$ µs^{-1}, $t_{\max} = 24$ µs. Nuclear spins have been added in alternation to FAD$^{\bullet-}$ and W$^{\bullet+}$. Simulation parameters as described for Fig. 7.1 apply.

dependence as given in the figure is obtained. For the ME approach, the elapsed time scales according to $\mathcal{O}(4^n)$ to $\mathcal{O}(4.5^n)$, where n is the number of considered nuclear spins, while for the MCWF approach scales as $\mathcal{O}(2.4^n)$. Overall, the $\mathcal{O}(4^n)$ scaling of the master equation method quickly renders the calculation formidable. E.g. for only $4 + 4$ nuclear spins, the integration of the [FAD$^{\bullet-}$ W$^{\bullet+}$] system up to 12 µs already requires 31 hours. The direct integration of the systems shown in Fig. 7.1 and 7.3 can be considered intractable by the current means as it would require 48 days for the smaller [FAD$^{\bullet-}$ Z$^{\bullet}$] system or even 453 years for the [FAD$^{\bullet-}$ W$^{\bullet+}$] system (provided the memory requirements could be met). On the other hand, the weaker $\mathcal{O}(2.4^n)$ of the MCWF approach found here allows much larger spins systems, realistically up to 20 spins, to be integrated. Here, the key question is not only the Hilbert space dimension but in addition the required accuracy of the solution. If significant accuracy is required, the MCWF method can become arbitrarily expensive as the $\mathcal{O}(N^{1/2})$ scaling of the error of the averaged quantities mandates potentially huge sample sizes. As such, for small systems the direct integration is preferred.

7.5 Discussion

The primary advantage of the Monte Carlo wavefunction method for obtaining time-dependent quantum expectation values is that systems of greater complexity are amenable to this treatment than can be tackled using the direct integration of

the master equation. This advantage stems from the fact that the method rests on the propagation of wavefunctions. For a Hilbert space dimension $d = 4Z$, the number of wave function components is equal to $4Z$ while the number of density matrix components is equal to $d^2 = 16Z^2$. In the worst case, i.e. for dense operators, the propagation would scale quadratically in the number of components. Practically, the sparsity of H_{eff} caters for a more favourable scaling (for both approaches). In particular, one may expect an ideal scaling of $\mathcal{O}(dlnd)$ for the propagating of a state vector, as a) the bilinear combination of spin operators of the form $S_{k,\alpha}I_{ki,\beta}$ (with $\{\alpha, \beta\} \in x, y, z$) directly couple at most five states and that b) there are $\mathcal{O}(lnd)$ such terms. Regardless of the actual scaling, the MCWF propagation will turn out to be exceedingly more efficient than directly integrating the master equation, as the latter requires $\mathcal{O}(d)$ applications of H_{eff} and therefore $\mathcal{O}(d^2lnd)$ operations. Practically, a scaling of $\mathcal{O}(d^{1.26})$ was found for the MCWF method applied to the [$FAD^{\bullet-}$ $W^{\bullet+}$] radical pair and $\mathcal{O}(d^{2.2})$ for the direct integration.

The primary disadvantage of the MCWF method is that the calculated quantities contain a statistical uncertainty, which needs to be reduced to an application-specific limit. The uncertainty results from the variability of the initial nuclear spin configuration and the stochasticity of the quantum jumps. It has to be contained by sampling, which however, comes at a significant cost of computation time, as the statistical error decreases as $N^{-1/2}$ with increasing number of samples N. Fortunately, the method inherits a remarkable scaling behaviour from wavefunction-based approaches to spin dynamics for closed quantum system, which suggest that for large spin systems significantly fewer than Z samples of the initial nuclear spin configuration are often sufficient to arrive at adequately converged observable trajectories (Lewis, Manolopoulos and Hore, 2014). Practically, a constant number of samples, independent of problem dimension, proves to work well, suggesting that the scaling behaviour as suggested above still applies to the MCWF approach on the whole. For more than approximately 10 spins, the MCWF method quickly becomes the only feasible approach to integrate eq. 7.4. For small systems, on the other hand, the added overhead of averaging a large number of stochastic trajectories to obtain

the open system dynamics, outweighs the benefit of a moderate memory saving. Master equation methods are therefore generally more efficient when Hilbert space dimensions are on the order of a couple of hundred states or smaller.

Alternative approaches to simulate the dynamics of relaxing systems could in principle be built on the closed-system dynamics of spin systems. To this end, one would have to engineer a time-dependent stochastic process such that the coherent dynamics sampled over this process will give rise to the dynamics as predicted by the master equation 7.4 (Lewis, Fay and Manolopoulos, 2016). Up to second order, this could e.g. be realised in the framework of the Redfield approach (Breuer and Petruccione, 2002). However, this strategy does not overcome the difficulty that many trajectories have to be sampled and comes at the conceptual disadvantage that a particular, mostly arbitrary, realisation of the stochastic process modulating the spin Hamiltonian will have to be conjured up. E.g. in order to realise S/T-dephasing, one could assume a stochastically modulated exchange or electron-electron dipolar interaction, but the modulation process, interaction strength, etc. would have to be chosen subjectively (Kattnig et al., 2016a). While the result will, to second order in the perturbation, only depend on the second moment of the interaction strength and the correlation time, higher order contributions will be difficult to rule out in general, which renders the process idiosyncratic. In particular, for systems for which the microscopic details are unclear, this introduces an unnecessary (and possibly misleading, if contributions of order higher than 2 should become necessary) arbitrariness, where a description in terms of effective parameters, as contained in the Lindblad master equation might be preferred. One will furthermore have to ensure that the chosen process does not induce other processes, e.g. T/T-dephasing, if this is not desirable at the stage of the calculation. The advantage of this closed-system approach lays in the fact that well-established approaches for propagating closed radical pair systems subject to Haberkorn recombination can be utilised, either on the quantum level, or, if very large spin systems are to be addressed, on the semiclassical level (Schulten and Wolynes, 1978; Lewis, Manolopoulos and Hore, 2014; Manolopoulos and Hore, 2013). In fact, the quantum propagation of the closed

systems is expected to be more efficient than the MCWF approach, as it does not require the event detection of quantum jumps. Thus, the integration methodology can be optimised to the sampling of the relevant observables on a regular time grid instead, which has e.g. been realized efficiently by using exponential integrators based on the Arnoldi method (Sidje, 1998).

Despite the advents of the MCWF method, the integration of open spin system is a time-consuming process for all but simplistic systems of only a few spins. The fact that a large number of trajectories has to be accumulated is, however, offset by the prospect that these calculations can be carried out in parallel. In fact, as only a few state-vectors need to be stored, the individual resource requirements are modest and a massively parallel implementation on high-performance clusters is easily realised. Furthermore, when the evaluation of time-dependent observables, e.g. $p_1(t)$ or $p_S(t)$, is required for the purpose of comparing with experiments, an integration accuracy of 10^{-2} to 10^{-3} might be sufficient (to realise results that are converged when plotted on the full scale of the calculation/experiment), which can often be realised with as few as 1000 samples. While this is encouraging, the calculation of reaction yields, e.g. Y_1 and Y_S, does typically require more samples for convergence to the required (experimental) precision. In particular, the MCWF method cannot provide a simple answer to some of the challenges posed by the spin dynamics thought to underpin magnetoreception. For such systems, long-lived coherences have been postulated, which in many cases nonetheless only give rise to small anisotropies of the reaction yields. This is particularly problematic for the prototypical [$FAD^{\bullet -}$ $W^{\bullet +}$] systems, which for realistic descriptions of the nuclear spin degrees of freedom (for the closed system dynamics; open system dynamics have hardly been addressed), give rise to only tiny relative anisotropies of often markedly less than 1% (Hiscock et al., 2016; Atkins et al., 2019). In combination with the long lifetimes, this requires a substantial investment in computing time to resolve these tiny directional effects. Note, however, that much larger effects can result from the [$FAD^{\bullet -}$ $Z^{\bullet}$] or some recently introduced radical triad systems (Kattnig and Hore, 2017c; Kattnig, 2017c; Lee et al., 2014).

It should also be noted that the scaling behaviour of the MCWF approach,

while growing weaker than that of the master equation approach, is still exponential in the number of coupled spins. While algorithms for simulating spin dynamics that scale polynomially in the number of spins have become popular in the field of theoretical magnetic resonance spectroscopy, these methods do not usually provide sufficiently accurate solutions for the modelling of radical pair dynamics in weak magnetic fields. Here, it is expected that the MCWF approach can fill the gap that exists for open quantum system dynamics between the toy systems that are straightforwardly treated by the master equation approach and the realm of semiclassical approaches (possibly with direct inclusion of the bath degrees of freedom) (Hogben et al., 2011; Hogben, Hore and Kuprov, 2010; Kuprov, Wagner-Rundell and Hore, 2007).

The disadvantage of having to sample a large number of trajectories can sometimes emerge to be a virtue. This can be the case if, e.g., the effects of random stochastic dependent interactions are to be addressed or if a random motion modulates the spin Hamiltonian, such as is the case if the radical pair undergoes mutual diffusive motion (Evans et al., 2016). Including these otherwise difficult to accommodate aspects in the description is straight forward in the MCWF approach, e.g. by combining the integration of the wavefunction with a stochastic differential equations solver to accounting for these random processes. This is clearly a field where one can expect to see much interest in the near future.

For systems where the effective Hamiltonian factors due to the existence of invariants, e.g. as is the case for isotropic spin systems, large savings of CPU time can be realised by utilizing the block structure of operators. Likewise, marked improvements of the time complexity and its scaling are to be expected for problems for which the effective Hamiltonian can still be diagonalised, but a description of the open state dynamics is aimed for (e.g. to include the effect of S/T-dephasing). In these cases, an efficient approach could be realised by implementing the main propagation step in between quantum jumps in the eigenbasis of the effective Hamiltonian. This is expected to provide a significant boost to the speed for the large class of systems of intermediate size, i.e. systems that are non-trivial in terms of the open system

dynamics but too small to be well-described by semiclassical approaches. While this idea has not been explored further here, it is expected that future application focused on actual applications will profit from this or similar tactics. In fact, the symmetry decomposition of the Hilbert space that could have been realised has not been considered here, but the three protons in the methyl groups at C7 and C8 of the flavin radical anion are completely equivalent and could thus be treated in a coupled spin basis. In this sense, the presented results are representative of the worst case scenario, where the structure of the effective Hamiltonian cannot be utilised in any particular way. Actual application might profit from additional efficiency boosts within the outlined MCWF approach and exceed the current application.

Eventually, while the aim here is not for new insights into the radical pair dynamics putatively underpinning magnetoreception, but rather for a more efficient methodology that may be useful for studying them, a novel observation should be pointed out. As illustrated in Fig. 7.1, S/T-dephasing appears to strongly attenuate the anisotropy of the magnetic field effect, i.e. in the presence of this relaxation process with $\gamma_{ST} = 11\ \mu s^{-1}$ the orientational differences in $f_1(t)$ are essentially washed out. While obviously more detailed studies of this effect are required, this once again highlights the importance of focusing on the study of open system dynamics to unravel the true nature of biological magnetic field effect. Indeed, hitherto no credible demonstration of magnetic anisotropy has been realised for the [$FAD^{\bullet-}$ $W^{\bullet+}$] radical pair.

7.6 Conclusions

It has been shown that the quantum Monte Carlo wavefunction (MCWF) approach can be extended to the non-Lindbladian master equations relevant to the spin dynamics of radical systems. This was achieved by stipulating that when radicals recombine they are no longer active in the interactions of the system, and thus the path describing them should be terminated upon a recombination occurring which was added into the MCWF framework by the introduction of an additional "quantum jump" to describe the termination step. This new approach has been

tested against the benchmark of direct integration of the master equation with a Runge-Kutta approach, and find that the asymptotic time-complexity of the MCWF approach is $\mathcal{O}(2.4^n)$ compared to the master equation scaling of $\mathcal{O}(4.5^n)$, where n is the number of protons in the system. This speed-boost allows large spin systems of up to twenty fully-interacting spins to be integrated, where previously this was computationally intractable. Small spin systems, on the other hand, are better treated using the traditional, direct integration of the master equation. It is expected that the MCWF method will become a useful asset in the study of magnetoreception and other biological magnetic field effects that are discussed in the context of the emerging discipline of quantum biology. In this context, the complexity of the radical systems of biological relevance in terms of the large number of hyperfine coupled nuclear spins has so far precluded the study of open system dynamics for realistic scenarios. Here, it is expected that the delineated approach to significantly broaden the range of problems that can be routinely analysed.

8. Conclusion

The work presented hitherto can be summarised as follows: Chapter 1 provided an introduction to the field of quantum biology, indicating some of the key questions of the field, as well as pertinent hypotheses and experimental findings. Chapter 2 supplied the theory to these concepts by presenting the RPM Hamiltonian, the Haberkorn formalism of recombination, the consequent master equation and some known hypotheses and methodologies to solve it. This chapter concluded with the motivation of a new theory - an extension to the RPM. Chapter 3 introduced the D3M model, and demonstrates that neglecting the dipolar and exchange interactions from the Hamiltonian leads to the loss of many subtle and interesting effects. Chapter 4 presented a case study of this model in action: the magnetosensitivity of lipid peroxidation reactions. Chapter 5 generalised the idea of D3M to n spins and shows that the biological MFEs predicted by DnM can be significantly amplified by the relaxation of the constraint of symmetry. Chapter 6, introduced noise into the systems studied in chapter 5 and shows that one can further enhance the effects found from geometric distortion alone by considering singlet-triplet dephasing. Finally, chapter 7 introduced a method to make the use of DnM more computationally practical by extending the Monte-Carlo Wavefunction approach to non-Lindbladian master equations.

Specific key details, insights, and ideas for future work are now given:

This thesis has challenged the conventional wisdom of spin dynamics in biological systems by exploring notable shortcomings in the hitherto widely accepted Radical Pair Mechanism. In particular, the categorical requirement that hyperfine interactions must be present in order to see magnetic field effects in radical spin dynamics has been shown to be false for systems with three or more radicals. That is,

the conventional Radical Pair Mechanism is far from a generalised explanation but in fact a very special case - it holds precisely for *pairs* of radicals. Furthermore, for such systems with more than two radicals, the assumption that the dipolar interaction can be simply neglected from the Hamiltonian has been shown to be a faulty assumption. As with the previous instance of hyperfine interactions, this conventional assumption holds precisely for pairs of radicals (i.e. $n = 2$) due to symmetry but breaks the moment a third radical is introduced. Given that completely isolated pairs of radicals are highly unlikely to arise in a realistic biological system, a new mechanism for the description of biological radical dynamics is necessitated.

D3M is this mechanism. Chapter 3 introduced the D3M model, and demonstrated that neglecting the dipolar and exchange interactions from the Hamiltonian leads to the loss of many subtle and interesting effects. D3M has been applied to radical systems of three or more radicals, initially in the absence of hyperfine interactions to show their superfluity regarding the realisation of MFEs. New effects have been demonstrated by this mechanism, including the remarkable emergence of directional sensitivity to fields weaker than the geomagnetic field - something that the RPM cannot predict. This work could be progressed further by introducing some experimental work to test the predictions made and afford a full grounding in reality. The first of such predictions it would make sense to test is the presence of a new, richer, MFE profile with the addition of a third radical, and subsequently the effect of the exchange at tuning this. This could be done by the use of EPR spectroscopy to locate the energy splittings expected from the inclusion of the dipolar interaction (which would not be expected to be present under the canonical RPM).

Chapter 4 presented a case study of this model in action: the magnetosensitivity of lipid peroxidation reactions. The main results of this chapter were that D3M effects are not abolished by the presence of hyperfine interactions, and that (contrary to conventional wisdom) radical concentration can affect the magnetosensitive reaction dynamics. This is important for the study of certain therapeutic treatments, such as used for the destruction of tumours, because it suggests that the negative impact could be reduced non-invasively by the application of an appropriate magnetic field.

This work could be extended by introducing some experimental work to test how far and to what extent radical concentration really has the predicted effect, which would also be the first and foremost prediction to test due to its immediate relevance to real systems: namely, radiotherapy. This is an important real application, because if the precise physical impact of radical concentration on the magnetodynamics of lipid peroxidation could be established then one could imagine that physicians could introduce controlled doses from an external magnetic field as an addition to the standard therapeutic procedure, with the aim of lessening the well-known deleterious side effects of such treatments.

Chapter 5 presented a generalisation of D3M to larger systems (i.e. DnM) and continued the exploration of the importance of symmetry to biological MFEs. The most surprising finding of this study was that breaking geometric symmetries can have a significant effect upon the MFE profile of a system. Specifically, it was found that the biological MFEs predicted by DnM can be significantly amplified by the relaxation of the constraint of symmetry. In particular, those systems that were only slightly geometrically different from the high-symmetry case showed MFEs (some at sub-geomagnetic field) that were abolished by the imposition of geometric symmetry upon the system. This suggests that, while symmetry may be mathematically convenient for the study of radical dynamics, its imposition can also lead to the loss of vital information about the system under consideration. This idea is also biologically motivated, as the notion that a high-symmetry system would persist for a meaningful amount of time (between a millisecond and a microsecond for the conventional RPM to have effect) in the high-energy, so-called 'hot, noisy' biological environment is questionable. The main results of this chapter were that D3M effects are not a special case of three-spin systems, but can actually also be observed in larger, more complex, systems. Also, the effects of geometry were shown to be significant in the magnetic response of the system. The work in this chapter could be extended by running some larger simulations, on some much more powerful hardware, to see if there exists an even-odd disparity in the number of spins and the MFE profiles of the resultant geometries. It appears as though this may be the case, from

the results in this chapters, but there are not enough data points to draw a conclusive pattern from.

Chapter 6 then went on to explore the second of the adjectives: 'noisy'. Noise was introduced into the DnM model, and the systems considered in the geometric study were once again probed. This chapter presented the result that noise in the system is not necessarily disadvantageous to the quantum dynamics or magnetosensitivity thereof, and further that the combination of natural noise, such as singlet-triple dephasing, and the geometric distortions introduced in chapter 5, can actually display a certain synergy in that they can (taken together) enhance the overall MFE observed. The noise types considered were the widely remarked-upon singlet-triplet dephasing and uncorrelated noise in all operators as a control. Unsurprisingly, the control abolished the MFEs observed in chapter 5. However, singlet-triplet dephasing (arguably the most biologically relevant type of noise to quantum radical dynamics) showed the much more interesting result of not just preserving the MFEs produced by the geometric considerations of chapter 5 but in some cases *enhancing* them. This further bolsters the idea that DnM can provide a more realistic description of biological radical dynamics than the conventional radical pair mechanism.

This work could be extended by considering other physically-relevant types of noise, and perhaps the effects of direct consideration of temperature upon the quantum magnetodynamics of the system. This would be of direct relevance to real systems, because biological systems are well-known to operate within a "hot, noisy" regime, within which many critics of the field have argued that quantum effects would be washed out due to their energies being lower than k_BT. Since it has been shown that noise is not always the destructive force that one may expect, the direct incorporation of physiological temperature into the system would be a very interesting extension. This would also aid experimentalists in attempting to measure the effects of noise, because they are unable to simply "turn off" temperature in living systems in the way theoreticians conducting proof-of-concept simulations can.

Finally, in chapter 7, the more practical concern of computability was addressed.

Specifically, a more efficient way of implementing DnM for systems where n goes beyond the six-spin systems explored as proof of concept which were until recently considered totally intractable through direct integration of the master equation. By adapting a method known as the Monte Carlo Wavefunction approach to be applicable to non-Lindbladian Hamiltonians (such as those discussed in preceding chapters), it was shown that not only could larger spin dynamics calculations be done faster than by direct integration but that the numerical error associated with the results gained was no worse in spite of this speed boost. This approach could likely benefit from implementation on a GPU, or other similar high-performance hardware, and this is the next suggested investigation along these lines.

9. Appendix

This appendix contains supporting details for the various studies carried out during the preparation of each preceding chapter. Items found herein were not included in the relevant chapter proper either because they were produced independently by group members, or it would have been impractical in terms of coherence and readability to include them.

Section by section, this appendix consists of:

- Pertaining to Chapter 3, a derivation of the dipolar coupling tensors is presented.
- Pertaining to Chapter 4:
  - A discussion of lateral diffusion in lipid peroxidation reactions.
  - A discussion of the effects of spin-relaxation on lipid peroxidation.
  - The g-tensor and hyperfine tensor calculations used.
  - A discussion of MFE anisotropies and microreactors.
- Pertaining to Chapter 5:
  - A schematic of how energy level crossings are influenced by geometric distortion.
  - The coordinates of spins in the geometries discussed.
  - Tables of values showing the minimum field required to see one and five percent MFEs in the geometries studies, alongside the corresponding exchange value.
  - A collection of results from larger geometries discussed, but not shown, in the chapter proper.

- Pertaining to Chapter 6:

  - A collation of many additional results from all geometries studied. The results are analogous to the sample shown in the main chapter, and broadly support the main results thereof.

- Pertaining to Chapter 7:

  - The hyperfine couplings for the FAD and W radicals used in the simulations detailed in the chapter proper.

  - The computational resources used.

- Finally, the code developed over the course of this project for running the simulations and producing the results, both shown and published, is included for completeness.

9.1 Dipolar tensor derivation

The following matrices were presented in chapter 3:

$$D_{1,2} = \begin{pmatrix} 1 & 0 & 0 \\ 0 & 1 & 0 \\ 0 & 0 & -2 \end{pmatrix} \tag{9.1}$$

$$D_{2,3} = \frac{1}{r^3} \begin{pmatrix} \frac{[3\cos(2\theta)-1]}{2} & 0 & -3\cos(\theta)\sin(\theta) \\ 0 & 1 & 0 \\ -3\cos(\theta)\sin(\theta) & 0 & -\frac{[1+3\cos(2\theta)]}{2} \end{pmatrix} \tag{9.2}$$

and

$$D_{1,3} = \frac{1}{f(r,\theta)^3} \begin{pmatrix} 1 - G_1(r,\theta) & 0 & G_2(r,\theta) \\ 0 & 1 & 0 \\ G_2(r,\theta) & 0 & G_1(r,\theta) \end{pmatrix} \tag{9.3}$$

These matrices are given relative to the dipole-dipole interaction in pair $(1,2)$, and r here is relative to $r_{1,2}$. Herein follows a derivation of their matrix elements.

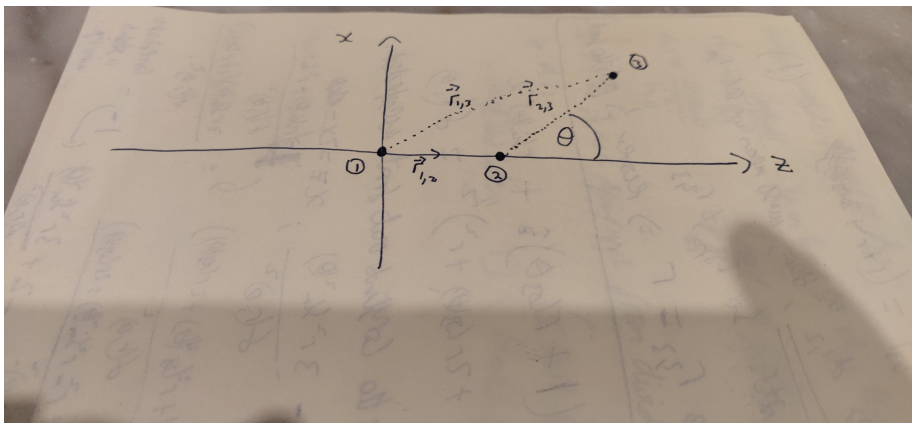

Figure 9.1: A particular case for how the general geometry considered in this derivation could look.

The starting point for the derivation is eq. 3.2, which will be re-stated here for convenience, with all quantities as defined in the chapter proper:

$$\hat{\mathbf{S}}_i \cdot \mathbf{D}_{i,j} \cdot \hat{\mathbf{S}}_j = d_{i,j}(r_{i,j}) \left[\hat{\mathbf{S}}_i \cdot \hat{\mathbf{S}}_j - 3 \left(\hat{\mathbf{S}}_i \cdot \vec{\mathbf{e}}_{i,j} \right) \left(\hat{\mathbf{S}}_j \cdot \vec{\mathbf{e}}_{i,j} \right) \right]. \tag{9.4}$$

Recall that the geometry assumed (without loss of generality) was spins 1 and 2 positioned along the z-axis, with spin 3 located somewhere in the xz-plane, displaced at an angle θ from the z-axis. A particular example of how this geometry may look is shown in Fig. 9.1.

9.1.1 Derivation of $D_{1,2}$

$$\vec{\mathbf{e}}_{1,2} = \frac{\vec{\mathbf{r}}_{1,2}}{|\vec{\mathbf{r}}_{1,2}|} \tag{9.5}$$

The matrices in question were all presented in units of $d_{1,2}$ which, having divided through by all of the fundamental constants presented in the chapter proper, amounts to considering $|\vec{\mathbf{r}}_{1,2}|$ equal to unity in this unit system. As such, $\vec{\mathbf{e}}_{1,2}$ is simply $\hat{z}$.

This simplifies eq. 3.2 to:

$\hat{S}_{1,x}\hat{S}_{2,x} + \hat{S}_{1,y}\hat{S}_{2,y} + \hat{S}_{1,z}\hat{S}_{2,z} - 3\hat{S}_{1,z}\hat{S}_{2,z}$

after having evaluated the scalar products. By orthogonality, this is then just

$$\hat{S}_{1,x}\hat{S}_{2,x} + \hat{S}_{1,y}\hat{S}_{2,y} + -2\hat{S}_{1,z}\hat{S}_{2,z}. \tag{9.6}$$

Comparing this with the LHS of eq. 3.2, one can then see that the matrix elements of $D_{1,2}$ are the coefficients of the operators in the above matrix representation by factoring operators in spin 1 out to the left and operators in spin 2 out to the right. This can be done due to the commutativity of scalar multiplication. The same logic applies to $D_{2,3}$ and $D_{1,3}$, so only the calculation of the relevant elements will be presented, rather than their respective matrix representations, for brevity.

9.1.2 Derivation of $D_{2,3}$

$$\vec{\mathbf{e}}_{2,3} = \frac{\vec{\mathbf{r}}_{2,3}}{|\vec{\mathbf{r}}_{2,3}|} \tag{9.7}$$

Let $|\vec{\mathbf{r}}_{2,3}|$ be denoted as r. $\vec{\mathbf{r}}_{2,3}$ can then be written as (considering Fig. 9.1 by way of illustration) $rcos(\theta)\hat{z} + rsin(\theta)\hat{x}$, and hence:

$$\vec{\mathbf{e}}_{2,3} = cos(\theta)\hat{z} + sin(\theta)\hat{x} \tag{9.8}$$

.

Consequently:

$$\hat{\mathbf{S}}_2 \cdot \vec{\mathbf{e}}_{2,3} = \hat{S}_{2,z}cos(\theta) + \hat{S}_{2,x}sin(\theta), \tag{9.9}$$

and similarly for $\hat{\mathbf{S}}_{\mathbf{3}}$.

The matrix elements one should expect to see then will come from:

$$\hat{S}_{1,x}\hat{S}_{2,x} + \hat{S}_{1,y}\hat{S}_{2,y} + \hat{S}_{1,z}\hat{S}_{2,z} - 3\left(\hat{S}_{2,z}cos(\theta) + \hat{S}_{2,x}sin(\theta)\right)\left(\hat{S}_{3,z}cos(\theta) + \hat{S}_{3,x}sin(\theta)\right). \tag{9.10}$$

This leads to the following system of equations, each of which corresponds to the labelled matrix element with xx, for example, corresponding to the $\hat{S}_{2,x}\hat{S}_{3,x}$ coefficient; the operators will be omitted for brevity, since the logic has already been established in the previous subsection:

$$
\begin{aligned}
xx &= 1 - 3sin^2(\theta) \\
yy &= 1 \\
zz &= 1 - 3cos^2(\theta) \\
xz &= -3cos(\theta)sin(\theta) \\
zx &= -3cos(\theta)sin(\theta)
\end{aligned}
\tag{9.11}
$$

All that remains to recover the required matrix elements is standard trigonometric manipulations, using the double-angle formulae, in the xx and zz elements.

As a final note, the factor of $\frac{1}{r^3}$ that appears as a multiplier to the matrix $D_{2,3}$ as presented is simply a product of the scaling of $d_{2,3}$ by $d_{1,2}$ (as mentioned for the units used here).

9.1.3 Derivation of $D_{1,3}$

The logic here, again, is identical to the previous two subsections, so only the new information for this element will be shown here. The unique step in this subsection is the calculation of the unit vector $\vec{\mathbf{e}}_{1,3}$.

Referring to Fig. 9.1 by way of example, one can see that the three position vectors form a triangle. Thus, $\vec{\mathbf{r}}_{1,3} = \vec{\mathbf{r}}_{1,2} + \vec{\mathbf{r}}_{2,3}$.

As such, again emphasising the units being used here to avoid confusion, one can see that this is given by $\vec{\mathbf{r}}_{1,3} = (1 + rcos(\theta))\hat{z} + rsin\theta\hat{x}$. Hence:

$$
\vec{\mathbf{e}}_{1,3} = \frac{(1 + rcos(\theta))\hat{z} + rsin\theta\hat{x}}{(1 + 2rcos(\theta) + r^2)^{\frac{1}{2}}} \tag{9.12}
$$

With this information, the exact procedure from the previous subsection can be followed (albeit with significantly more tedious algebra) to reproduce the matrix elements, and this will not be repeated here.

9.2 Assessment of lateral diffusive motion

To the author's knowledge, no data exist regarding the diffusion of lipid radical peroxides in membranes. However, it has been shown that the diffusion coefficients for stable radical molecules are similar to those of the non-radical molecules, whereas unstable radical molecules have been shown to diffuse slower than their non-radical counterparts (Donkers and Leaist, 1997; Terazima, Okamoto and Hirota, 1993). In a review by Macháň *et al.*Macháň and Hof, 2010, diffusion coefficients for lipids in giant unilamellar vesicles are reported to range from 1.4 $\mu m^2 s^{-1}$ to 7 $\mu m^2 s^{-1}$. However, they are expected to be significantly smaller in actual biological environments. As lipid peroxides are relatively stable radicalsGaschler and Stockwell, 2017 that are a similar in size to lipids, it is approximated that the radical species would diffuse at a rate comparable to that of its non-radical precursor. Based on these facts, it is estimated that lipid peroxides will undergo a diffusive displacement of significantly less than the free Brownian diffusion length $L_D = \sqrt{4Dt}$ calculated with the above diffusion coefficients. A characteristic time t can be estimated based on a typical spin relaxation time of an organic radical, because all MFE have to manifest within the lifetime of the pertinent spin coherences (*vide infra*). Assuming a coherent lifetime of 100 ns, it is thus estimated a lateral displacement of less than 1.7 to 0.7 nm. Therefore, in good approximation, diffusion shall be neglected during the time-spans that give rise to the formation of the MFE in a biological membrane.

9.3 Assessment of spin relaxation

MFEs are expected if the spin and reaction dynamics occur on time-scales that are faster or comparable to spin relaxation times. Thermalized spin systems cannot convey magnetosensitivity to weak magnetic fields, because the Zeeman interaction energy is small compared to the thermal energy, $k_B T$, and, thus, equilibrium properties are negligibly affected. Alkyl peroxyl radicals in free solution are subject to fast spin relaxation as a consequence of large g-anisotropies, which facilitates efficient spin rotational relaxationW. Atkins and Kivelson, 1966. Consequently,

EPR spectra of alkyl peroxyl radicals in liquid solution at room temperature are typically broadForbes et al., 2007; Symons, 1969. Yet, an order of magnitude estimate suggests that spin rotation will likely not impact the MFEs of lipid peroxyl reactions in membranes for short-lived, i.e. reactive, encounters, because the deviations of the g-tensor principal values from the g-factor of the free electron are sufficiently small and the motional correlation time is sufficiently long. This argument is based on the rotational diffusion rates from Klauda et al., 2008 ($D_{\parallel} = 1{\times}10^7$ s^{-1} and $D_{\perp} = 1{\times}10^8$ s^{-1}) to estimate a typical motional correlation time of the lipid (using $\tau_c = 1/(4D_{\perp} + 2D_{\parallel}) \sim 2$ ns) and

$$T_1^{-1} = T_2^{-1} = \frac{1}{9\tau_c} \sum_{a\in\{x,y,z\}} (g_{aa} - g_e)^2 \tag{9.13}$$

to evaluate the order of magnitude of the spin rotational relaxation rates. Here, the g_{aa}s are the principal values of the g-tensor. With g-parameters calculated using DFT, the presented estimates suggests spin relaxation times exceeding 10 μs. While this estimate is based on a simplified view of molecular dynamics that neglects internal degrees of freedom, it shows that even motions that are faster by two orders of magnitude will not suppress the MFEs discussed here (for an assumed maximal encounter time of 100 ns). Unfortunately, at the time of writing the author was not aware of a detailed motional model that would have allowed the estimation of internal motion at the current stage. In order to put this in context, note that, for the same τ_c, the superoxide radical anion is expected to relax faster by a factor of 33. It is important to realize that our assessment applies to the scenario that all radicals are lipid bound. The cage reaction suggested in Kipriyanov Jr., Doktorov and Purtov, 2015 involved a free hydroxyl radical, the fast relaxation of which almost certainly abolishes MFEs due to the RPM for moderate field intensities (estimated relaxation time: 1 nsVerma and Fessenden, 1976, which is consistent with the EPR line width in Becker, La Vere and Sevilla, 1994).

9.4 Calculation of the g-tensor

The g-tensor was calculated for the most stable conformer of the radical isomer 9ez using the Gaussian16 software. The unrestricted B3LYP exchange-correlation functional was used with a Def2TZVP basis set and a tight convergence criterion for the SCF iterations. This approach yielded the following shifts relative to the free electron g-factor:

XX	YY	ZZ
-304.2	5961.6	27887.8

Table 9.1: g-tensor shifts relative to the free electron (ppm)

9.5 Calculating the Hyperfine Interactions

The hyperfine coupling constants of two isomers of linoleic acid peroxyl radical, 13ze and 9ez, as described in the main text, were calculated by DFT using NWChem 6.8.1. The dihedral angle that the peroxyl group makes with the backbone chain was scanned from -180 to 180°with 38 points. At each dihedral angle a geometry optimisation was performed while holding the selected dihedral angle constant. Each simulation used the def2-tzvp basis set with the exchange-correlation functional B3LYP, an SCF threshhold of 1×10^{-8} and the xfine grid. Using the resultant optimised structures, the hyperfine values were calculated using the same exchange-correlation functional with the EPR-III basis. The largest hyperfine coupling constant was found for the hydrogen vicinal to the peroxide group.

Fig. 9.2A shows the dependence of the isotropic hyperfine constants on the peroxyl dihedral angle for several hydrogen atoms of interest in the 9ez and 13ze isomers. There is evidently a large range of values a_{iso} can take depending on the orientation of the dihedral angle. To calculate the average interaction, a Boltzmann average was calculated. The potential energy surface for this rotation is shown in Fig. 9.2B. With these data, the Boltzmann-weighted average hyperfine coupling tensor $\langle \mathbf{A} \rangle$ can be calculated from

$$\langle \mathbf{A} \rangle = \sum_i z_i \mathbf{A}_i, \tag{9.14}$$

$$z_i = \frac{e^{-\Delta E_i/(k_B T)}}{\sum_j e^{-\Delta E_j/(k_B T)}}, \tag{9.15}$$

where $\mathbf{A}_i$ is the hyperfine tensor of conformation i after alignment of the backbone (carbons 1 to 8) to the minimal energy configuration. E_i is the potential energy of the i^{th} orientation associated with the dihedral angle, k_B is the Boltzmann constant and T is the temperature. Here, was used a temperature of 310 K to be in line with temperatures within biological systems. By following this method, a_{iso} associated with 13ze was calculated to be 10.3 MHz. An equivalent process was followed for 9ez to produce an a_{iso} of 13.5 MHz.

Tables 9.2 and 9.3 show the largest anisotropic hyperfine coupling constants when the Boltzmann-weighted average is calculated. In both isomers the isotropic constants are all below 1 MHz with the exception of the hydrogen bonded to the same carbon as the peroxide group, where the hyperfine coupling constants increase substantially to over 10 MHz.

The anisotropic hyperfine constants were not considered in the main section of the article. However, their magnitudes and signs are shown in Fig. 9.3. When the rotation of the lipid about its backbone is considered, the anisotropy is strongly reduced. This is shown in Fig. 9.4. As the as the anisotropy fades with molecular motion, the isotropic model is an appropriate approximation to make for this system.

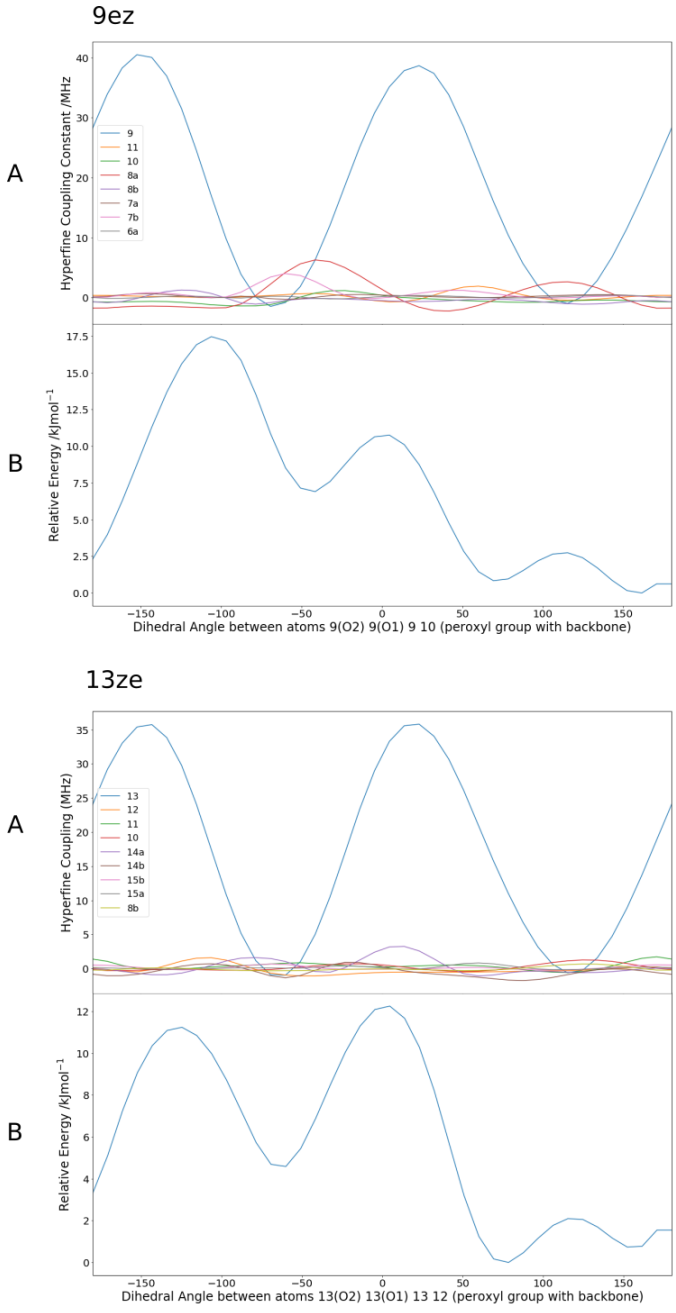

Figure 9.2: A: Isotropic hyperfine coupling constants as the peroxide group rotates around the dihedral angle made with the backbone of the lipid. Each atom label corresponds to a hydrogen within each lipid peroxide radical where the number represents the carbon number on the backbone. B: Potential energy surface as the peroxide group rotates around the dihedral angle made with the backbone of the lipid.

Atom Number	a_{iso} (MHz)	anisotropy (MHz)	asymmetry
6a	0.155	1.52	0.00805
5b	-0.008	2.11	0.0327
7a	0.225	3.93	0.0286
7b	0.371	8.03	0.0493
8b	-0.602	8.65	0.188
8a	0.103	4.39	0.105
10	-0.561	9.44	0.135
11	0.441	2.44	0.0878
12	0.008	1.67	0.0482
9	13.488	14.9	0.0465

Table 9.2: 9ez hyperfine coupling constants. Each atom label corresponds to a hydrogen within each lipid peroxide radical where the number represents the carbon number on the backbone.

Atom Number	a_{iso} (MHz)	anisotropy (MHz)	asymmetry
8a	-0.005	1.70	0.0234
15a	0.223	2.29	0.0537
15b	0.137	2.78	0.0747
16a	-0.024	1.61	0.0608
14b	-0.925	10.1	0.166
14a	-0.343	6.49	0.0951
10	0.353	1.21	0.0488
11	0.372	2.98	0.0567
12	-0.238	8.01	0.158
13	10.317	14.6	0.0385

Table 9.3: 13ze hyperfine coupling constants. Each atom label corresponds to a hydrogen within each lipid peroxide radical where the number represents the carbon number on the backbone.

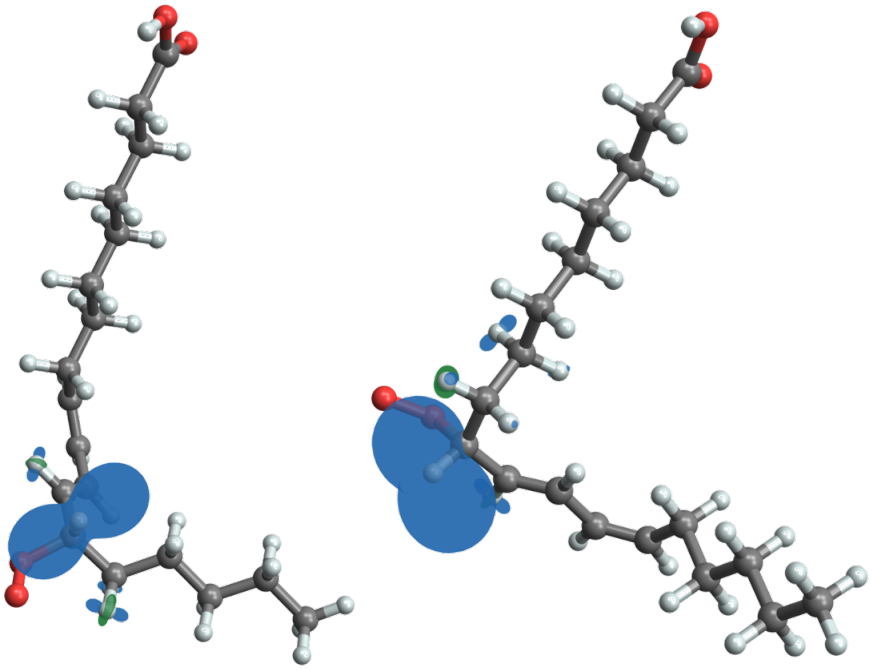

Figure 9.3: Average hyperfine coupling tensors when the dihedral angle describing the orientation of the peroxyl group fluctuates in the potential given by Fig. 9.2 for 13ze (left) and 9ez (right). Blue indicates positive and green negative hyperfine components in the respective direction.

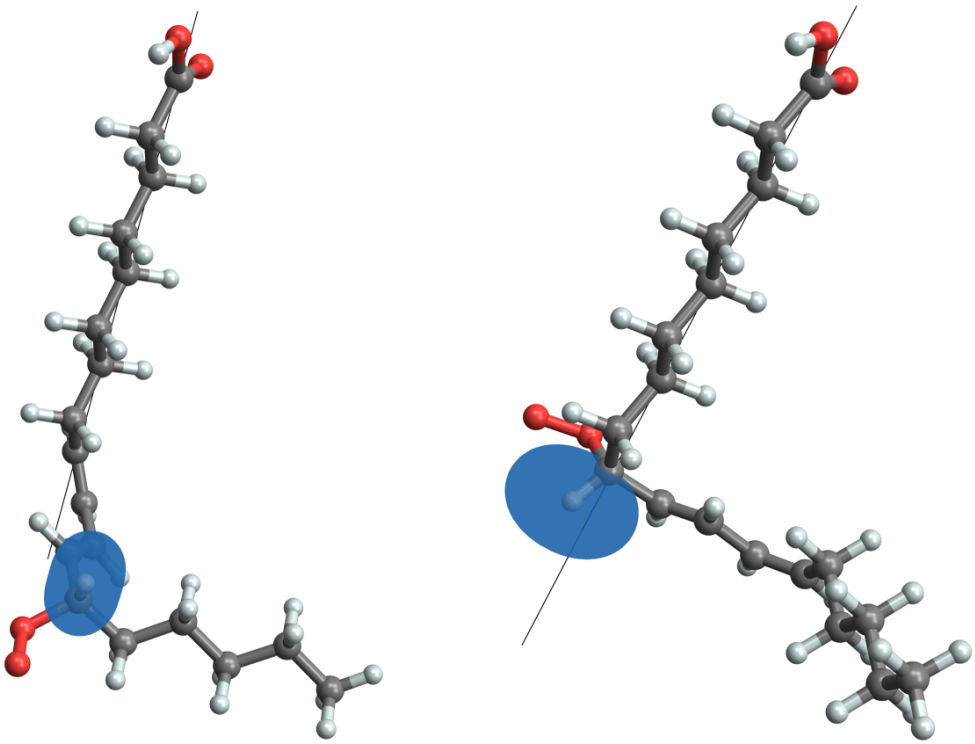

Figure 9.4: 13ze (left) and 9ez (right) shown with the average hyperfine interaction on the vicinal hydrogen when it is averaged by fast rotation about the carbon backbone (axis of rotation indicated by the black line) in addition to the fluctuations of the orientation of the peroxyl group.

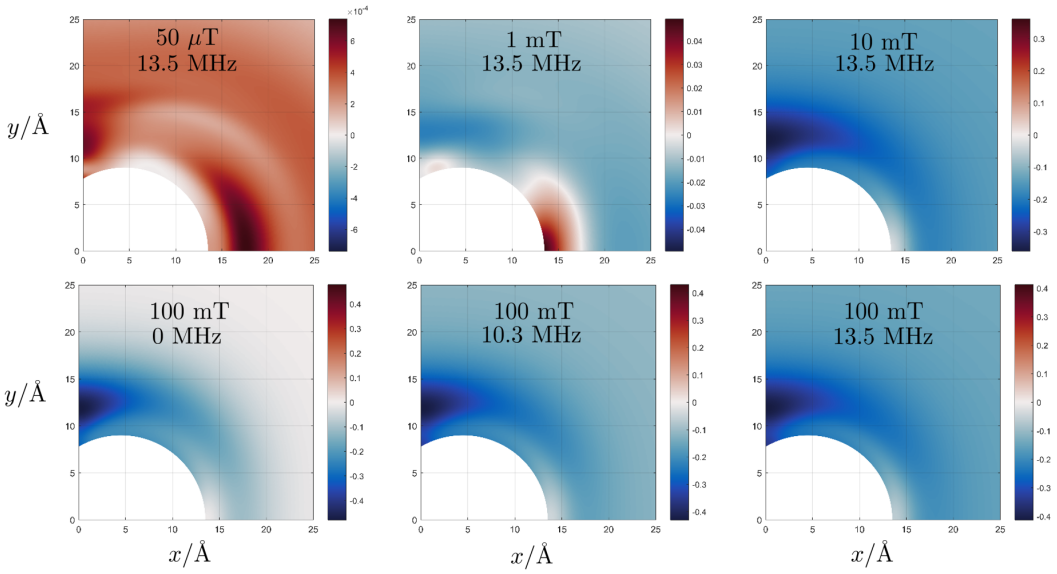

Figure 9.5: Magnetic field effects (χ_P) for three-radical systems when the magnetic field is perpendicular to the plane of the membrane. The strength of the magnetic field and the value of the hyperfine coupling constant used is shown in each graph. For all calculations $J = 0$, $k_{P,0} = 0.2$ ns^{-1} and $k_e = 0.01$ ns^{-1}.

9.6 Anisotropies of the MFE

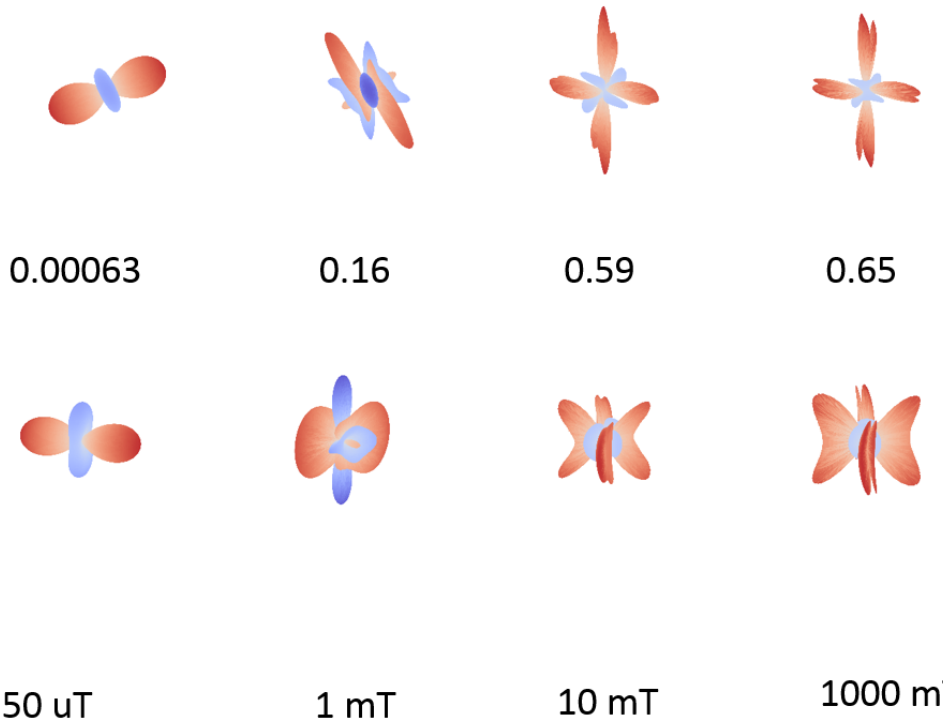

Figure 9.6: Plots of the anisotropies of the MFEs of a three-radical system for 50 μT (left), 1 mT (middle-left), 10 mT (middle-right), 1000 mT (right). The top and bottom show the same image from different angles and the numbers indicate the anistropies (%). Parameters are as follows: $k_{P,0} = 0.2$ ns^{-1}, $k_e = 0.01$ ns^{-1}, $J = 0$, $a_{iso} = 0$, $|\mathbf{r}_{1,3}| = 13.7$ Å, $|\mathbf{r}_{2,3}| = 15.5$ Å.

9.7 Microreactors

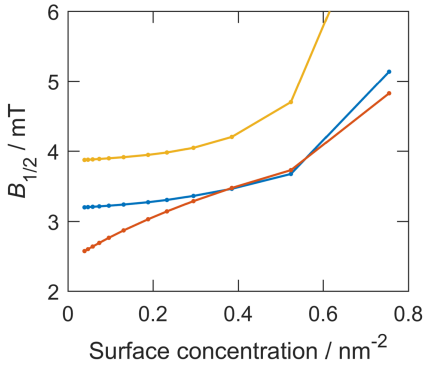

Figure 9.7: The magnetic field at which the MFE reaches half saturation plotted against the surface concentration of the lipids. The blue and red lines represent the cases with $a = 0$ and $a = 10.3$ MHz, respectively, both with the magnetic field oriented perpendicular to the membrane plan. The yellow line shows the rotational average when $a = 0$.

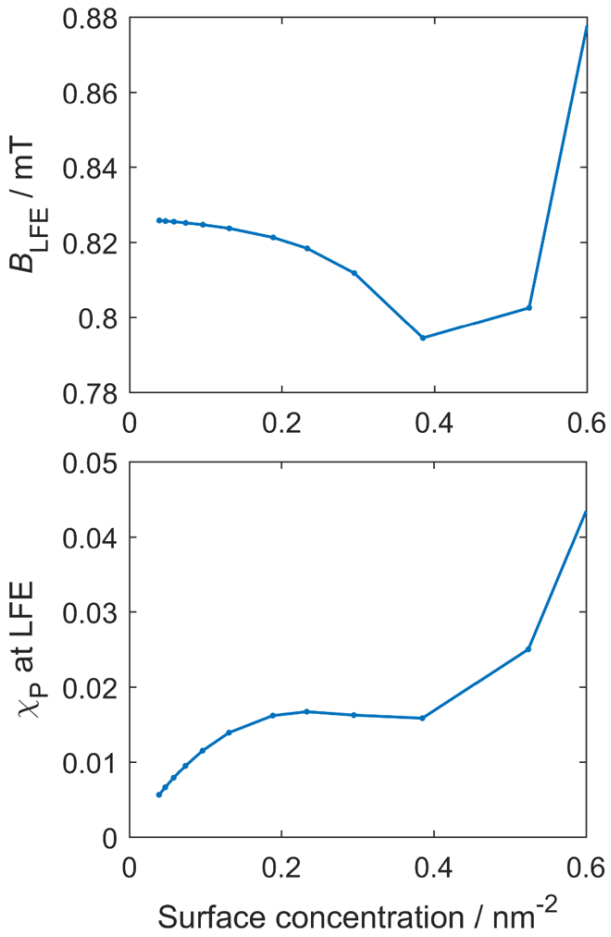

Figure 9.8: Characteristics of the low-field effect for orientationally averaged samples of circular microreactors containing three radicals at variable concentrations. Top: the magnetic field at which the low field effect occurs as a function of the surface concentration of the lipid radicals. Bottom: Magnetic field effect at the peak of the low-field feature. Parameters: $k_{P,0} = 0.2$ ns^{-1} and $k_e = 0.01$ ns^{-1}, $J = 0$.

9.8 Level-crossing diagrams for chapter 5

As an illustration, here are included level crossing diagrams for the simplest system studied. Although the crossings and anti-crossing responsible for a rich variety of MFEs are similarly present in the larger systems, the three-spin triangular geometry was chosen to illustrate, as the diagrams for the larger systems quickly become incomprehensible.

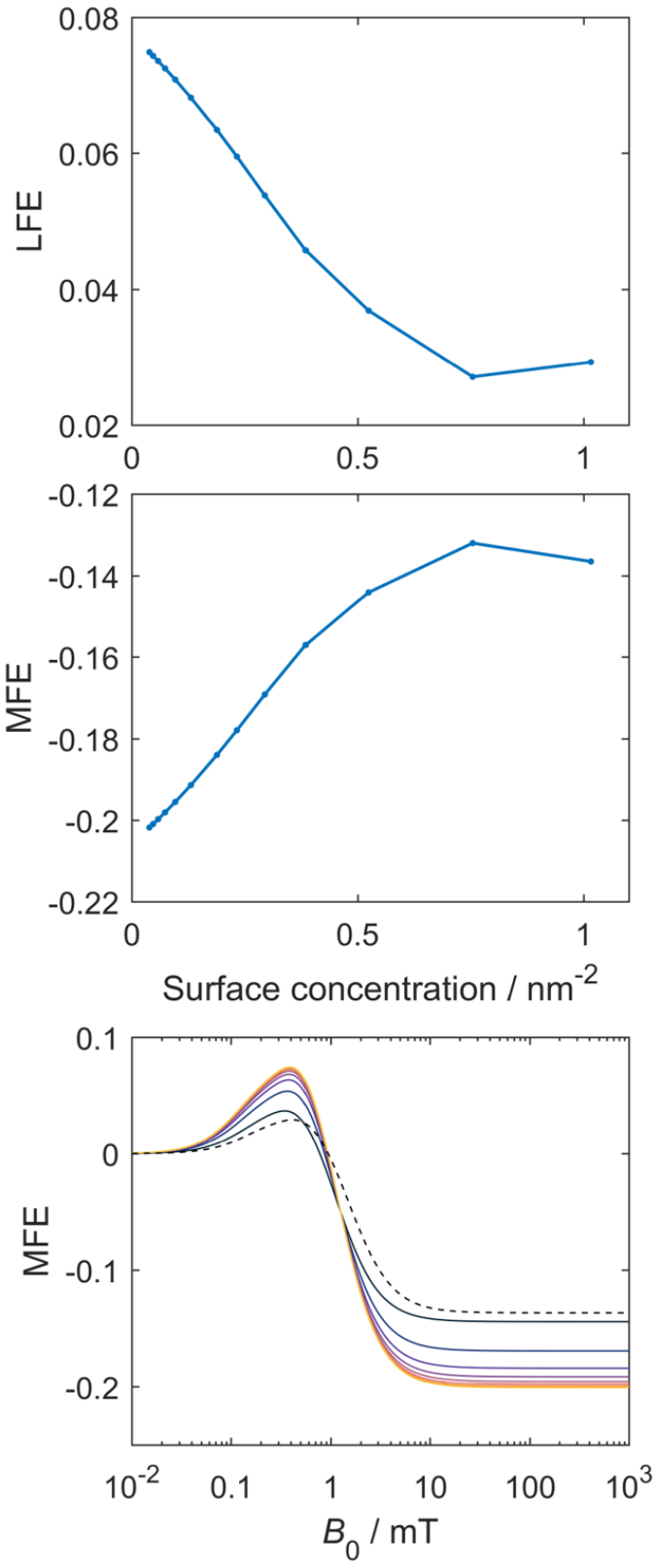

Figure 9.9: Characteristics of the magnetic field effect for circular microreactors containing three radicals at variable concentrations under the hypothetical scenario that the electron-electron dipolar interaction is absent. Top: the low field effect as a function of the surface concentration. Middle: the saturated magnetic field effect as a function of surface concentration. Bottom: the magnetic field effect as a function of the magnetic field. Parameters: $k_{P,0} = 0.2$ ns^{-1}, $k_e = 0.01$ ns^{-1}, $J = 0$ and $a = 10.3$ MHz.

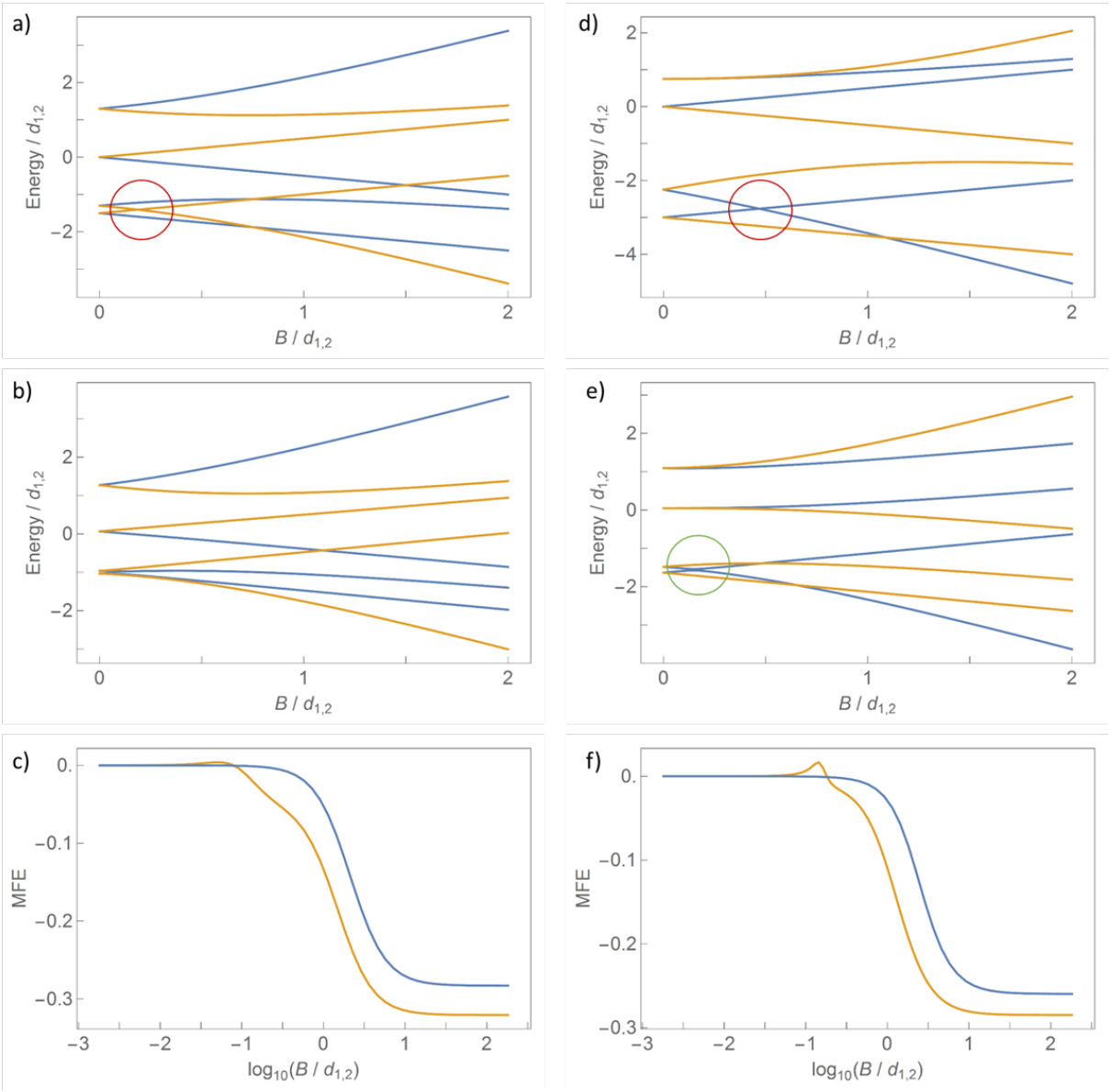

Figure 9.10: a) to d) Energy level diagrams, i.e. energy eigenvalues as a function of the applied magnetic field, for the equilateral triangle (a and d) and the radially distorted triangle $D_{3,r}$ (b and d) for $J_0 = 0.25d_{1,2}$ (left, a, b) and $J_0 = 0.75d_{1,2}$ (*right*, d, e). c and f) Magnetic field effects as a function of the magnetic field B for the equilateral (blue lines) and distorted triangle (solid lines) for $J_0 = 0.25d_{1,2}$ (*left*, c) and $J_0 = 0.75d_{1,2}$ (*right*, f). In the level diagrams, states associated with the two blocks of the Hamiltonian in the Zeeman basis are drawn as blue and orange lines respectively. For the symmetric triangles in a) and d), true level crossings of states of the same block are indicated by red circles. No such level-crossings exist for the distorted geometry (b and e). The circled "crossing" in e) is in fact an anti-crossing, which gives rise to the peak in the MFE profile at low fields.

9.9 Coordinates of geometries from chapter 5

All coordinates here are given in Angstroms. For the non-linear geometries, floating-point approximations to the displacement have been given for readability, but we note that the exact geometric values were input into the code. For example, for the radial distortion of the square we kept the common displacement of 1.5 Å radially, which is $\frac{3\sqrt{2}}{4}$ Å in both x and y of the Cartesian plane. This has been given as an additional 1.06 Å, below, for readability only.

- Three-spin linear chain
  - L_3: [[0, 0, 0], [15, 0, 0], [30, 0, 0]]
  - $L_{3,3x}$: [[0, 0, 0], [15, 0, 0], [31.5, 0, 0]]
  - $L_{3,3y}$: [[0, 0, 0], [15, 0, 0], [30, 1.5, 0]]
  - $L_{3,3z}$: [[0, 0, 0], [15, 0, 0], [30, 0, 1.5]]
  - $L_{3,2y}$: [[0, 0, 0], [15, 1.5, 0], [30, 0, 0]]
  - $L_{3,2z}$: [[0, 0, 0], [15, 0, 1.5], [30, 0, 0]]
- Four-spin linear chain
  - L_4: [[0, 0, 0], [15, 0, 0], [30, 0, 0], [45, 0, 0]]
  - $L_{4,3x}$: [[0, 0, 0], [15, 0, 0], [31.5, 0, 0], [46.5, 0, 0]]
  - $L_{4,3y}$: [[0, 0, 0], [15, 0, 0], [30, 1.5, 0], [45, 0, 0]]
  - $L_{4,3z}$: [[0, 0, 0], [15, 0, 0], [30, 0, 1.5], [45, 0, 0]]
  - $L_{4,4x}$: [[0, 0, 0], [15, 1.5, 0], [30, 0, 0], [46.5, 0, 0]]
  - $L_{4,4y}$: [[0, 0, 0], [15, 0, 0], [30, 0, 0], [45, 1.5, 0]]
  - $L_{4,4z}$: [[0, 0, 0], [15, 0, 0], [30, 0, 0], [45, 0, 1.5]]
- Five-spin linear chain
  - L_5: [[0, 0, 0], [15, 0, 0], [30, 0, 0], [45, 0, 0], [60, 0, 0]]
  - $L_{5,3y}$: [[0, 0, 0], [15, 0, 0], [30, 1.5, 0], [45, 0, 0], [60, 0, 0]]

- $L_{5,3z}$: [[0, 0, 0], [15, 0, 0], [30, 0, 1.5], [45, 0, 0], [60, 0, 0]]
- $L_{5,4x}$: [[0, 0, 0], [15, 0, 0], [31.5, 0, 0], [46.5, 0, 0], [61.5, 0, 0]]
- $L_{5,4y}$: [[0, 0, 0], [15, 0, 0], [30, 0, 0], [45, 1.5, 0], [60, 0, 0]]
- $L_{5,4z}$: [[0, 0, 0], [15, 0, 0], [30, 0, 0], [45, 0, 1.5], [60, 0, 0]]
- $L_{5,5x}$: [[0, 0, 0], [15, 0, 0], [30, 0, 0], [45, 0, 0], [61.5, 0, 0]]
- $L_{5,5y}$: [[0, 0, 0], [15, 0, 0], [30, 0, 0], [45, 0, 0], [60, 1.5, 0]]
- $L_{5,5z}$: [[0, 0, 0], [15, 0, 0], [30, 0, 0], [45, 0, 0], [60, 0, 1.5]]

- Six-spin linear chain
  - L_6: [[0, 0, 0], [15, 0, 0], [30, 0, 0], [45, 0, 0], [60, 0, 0], [75, 0, 0]]
  - $L_{6,4x}$: [[0, 0, 0], [15, 0, 0], [30, 0, 0], [46.5, 0, 0], [61.5, 0, 0], [76.5, 0, 0]]
  - $L_{6,4y}$: [[0, 0, 0], [15, 0, 0], [30, 0, 0], [45, 1.5, 0], [60, 0, 0], [75, 0, 0]]
  - $L_{6,4z}$: [[0, 0, 0], [15, 0, 0], [30, 0, 0], [45, 0, 1.5], [60, 0, 0], [75, 0, 0]]
  - $L_{6,5x}$: [[0, 0, 0], [15, 0, 0], [31.5, 0, 0], [46.5, 0, 0], [61.5, 0, 0], [76.5, 0, 0]]
  - $L_{6,5y}$: [[0, 0, 0], [15, 0, 0], [30, 0, 0], [45, 0, 0], [60, 1.5, 0], [75, 0, 0]]
  - $L_{6,5z}$: [[0, 0, 0], [15, 0, 0], [30, 0, 0], [45, 0, 0], [60, 0, 1.5], [75, 0, 0]]
  - $L_{6,6x}$: [[0, 0, 0], [15, 0, 0], [30, 0, 0], [45, 0, 0], [60, 0, 0], [76.5, 0, 0]]
  - $L_{6,6y}$: [[0, 0, 0], [15, 0, 0], [30, 0, 0], [45, 0, 0], [60, 0, 0], [75, 1.5, 0]]
  - $L_{6,6z}$: [[0, 0, 0], [15, 0, 0], [30, 0, 0], [45, 0, 0], [60, 0, 0], [75, 0, 1.5]]

- Triangular geometry
  - D_3: [[0, 0, 0], [15, 0, 0], [7.5, 12.99, 0]]
  - $D_{3,r}$: [[0, 0, 0], [15, 0, 0], [7.5, 14.49, 0]]
  - $D_{3,r'}$: [[0, 0, 0], [15, 0, 0], [7.5, 14.985, 0]
  - $D_{3,t}$: [[0, 0, 0], [15.75, 0, 0], [7.5, 12.99, 0]]

- Square geometry
  - D_4: [[0, 0, 0], [15, 0, 0], [0, 15, 0], [15, 15, 0]]

- $D_{4,t}$: [[0, 0, 0], [15, 0, 0], [0, 15, 0], [15.75, 15, 0]]
- $D_{4,r}$: [[0, 0, 0], [15, 0, 0], [0, 15, 0], [16.06, 16.06, 0]]

- Pentagonal geometry
  - D_5: [[0, 0, 0], [15, 0, 0], [19.64, 14.27, 0], [7.5, 20.65, 0], [-4.64, 14.27, 0]]
  - $D_{5,t}$: [[0, 0, 0], [15.75, 0, 0], [19.64, 14.27, 0], [7.5, 20.65, 0], [-4.64, 14.27, 0]]
  - $D_{5,r}$: [[0, 0, 0], [16.06, -1.06, 0], [21.14, 14.27, 0], [7.5, 20.65, 0], [-4.64, 14.27, 0]]

- Hexagonal geometry
  - D_6: [[0, 0, 0], [15, 0, 0], [22.5, 12.99, 0], [15, 25.98, 0], [0, 25.98, 0], [-7.5, 12.99, 0]]
  - $D_{6,t}$: [[0, 0, 0], [15.75, 0, 0], [22.5, 12.99, 0], [15, 25.98, 0], [0, 25.98, 0], [-7.5, 12.99, 0]]
  - $D_{6,r}$: [[0, 0, 0], [16.06, -1.06, 0], [22.5, 12.99, 0], [15, 25.98, 0], [0, 25.98, 0], [-7.5, 12.99, 0]]

9.10 Tables of values for exchange parameters showing a prescribed MFE intensity

Table 9.4: The minimum fields required to see a five percent MFE in the listed geometries and their distorted counterparts. The values are listed alongside the value of the exchange parameter where it was measured.

Geometry	Field (mT)	Exchange ($d_{1,2}$)
G_3	0.539	0.250
$G_{3,r}$	0.050	0.370
$G_{3,r'}$	0.127	0.540
$G_{3,t}$	0.025	0.200
G_4	0.243	0.080
$G_{4,r}$	0.276	1.719
$G_{4,t}$	0.119	0.520
G_5	0.692	0
$G_{5,t}$	0.708	0.010
$G_{5,r}$	0.697	0
G_6	1.902	0.390
$G_{6,t}$	1.347	0.480
$G_{6,r}$	1.256	0.610
L_3	0.014	−0.290
$L_{3,x3}$	0.013	−0.400
L_4	0.021	−0.560
$L_{4,x3}$	0.021	−0.510
$L_{4,x4}$	0.023	−1.209
L_5	0.066	−0.330
$L_{5,x4}$	0.033	−0.370
$L_{5,x5}$	0.067	−0.350
L_6	0.228	−0.410
$L_{6,x4}$	0.114	−0.390
$L_{6,x5}$	0.121	−0.460
$L_{6,x6}$	0.161	−0.510
$G_{3,r,0.75}$	0.024	0.210
$G_{4,r,0.75}$	0.094	0.530
$G_{5,r,0.75}$	0.664	−0.010
$G_{6,r,0.75}$	1.522	0.330
$L_{3,x3,0.75}$	0.013	−0.380
$L_{4,x3,0.75}$	0.0211	−0.530
$L_{5,x4,0.75}$	0.021	−0.939
$L_{5,x4,0.75}$	0.044	−0.360
$L_{5,x5,0.75}$	0.069	−0.350
$L_{6,x4,0.75}$	0.159	−0.400
$L_{6,x5,0.75}$	0.162	−0.520
$L_{6,x6,0.75}$	0.193	−0.570

Table 9.5: The minimum fields required to see a one percent MFE in the listed geometries and their distorted counterparts. The values are listed alongside the value of the exchange parameter where it was measured.

Geometry	Field (mT)	Exchange ($d_{1,2}$)
G_3	0.223	0.250
$G_{3,r}$	0.015	0.360
$G_{3,r'}$	0.026	0.540
$G_{3,t}$	0.008	0.200
G_4	0.067	0.500
$G_{4,r}$	0.010	0.909
$G_{4,t}$	0.015	−1.759
G_5	0.240	−0.720
$G_{5,t}$	0.043	−2.778
$G_{5,r}$	0.037	−2.958
G_6	0.213	−0.839
$G_{6,t}$	0.158	−2.369
$G_{6,r}$	0.118	−2.818
L3	0.006	−0.290
$L_{3,x3}$	0.005	−0.400
L_4	0.008	−0.560
$L_{4,x3}$	0.007	1.089
$L_{4,x4}$	0.008	−1.209
L_5	0.012	−1.089
$L_{5,x4}$	0.009	−0.340
$L_{5,x5}$	0.013	−2.458
L_6	0.024	−1.809
$L_{6,x4}$	0.022	−1.659
$L_{6,x5}$	0.022	−0.460
$L_{6,x6}$	0.020	−0.510
$G3, r, 0.75$	0.008	0.210
$G_{4,r,0.75}$	0.006	0.720
$G_{5,r,0.75}$	0.021	−2.438
$G_{6,r,0.75}$	0.175	−2.259
$L_{3,x3,0.75}$	0.005	−0.380
$L_{4,x3,0.75}$	0.008	−0.530
$L_{4,x4,0.75}$	0.007	−0.939
$L_{5,x4,0.75}$	0.011	−1.309
$L_{5,x5,0.75}$	0.012	−1.629
$L_{6,x4,0.75}$	0.019	−0.979
$L_{6,x5,0.75}$	0.020	−0.450
$L_{6,x6,0.75}$	0.022	−0.580

9.11 Additional results pertaining to chapter 6

This section contains additional results from chapter 6. First, the longer linear chains discussed in chapter 6 proper are shown, followed by the square

9.11.1 Linear Chains

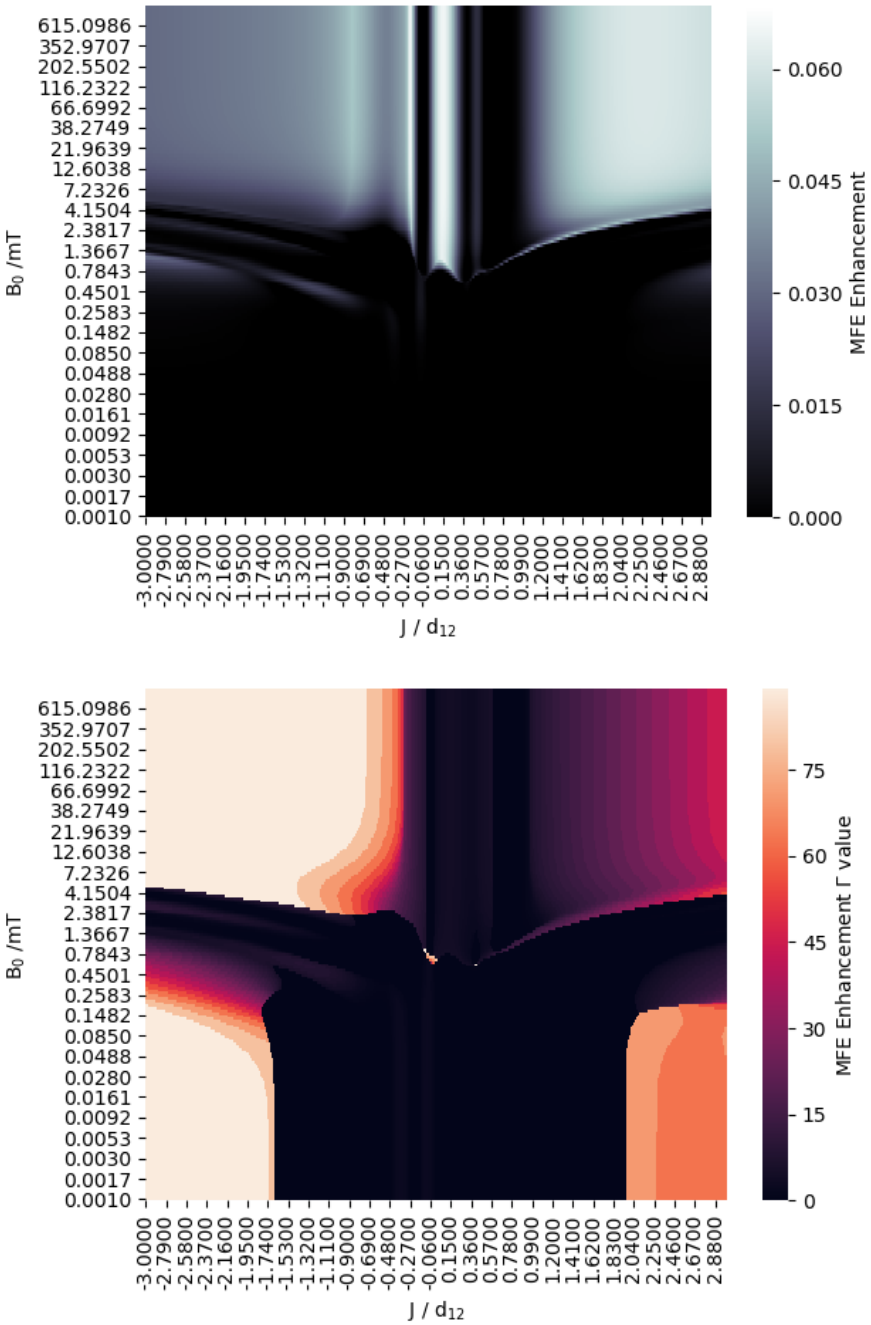

Figure 9.11: Four-spin linear system (L_4), under the DnM formalism and in the presence of exchange and S-T dephasing. The top panel shows regions where the presence of noise can gives an enhanced MFE relatively to the no-noise system. The bottom panel shows the value of the noise parameter, Γ (in MHz), that produced the corresponding enhanced MFE in the upper panel.

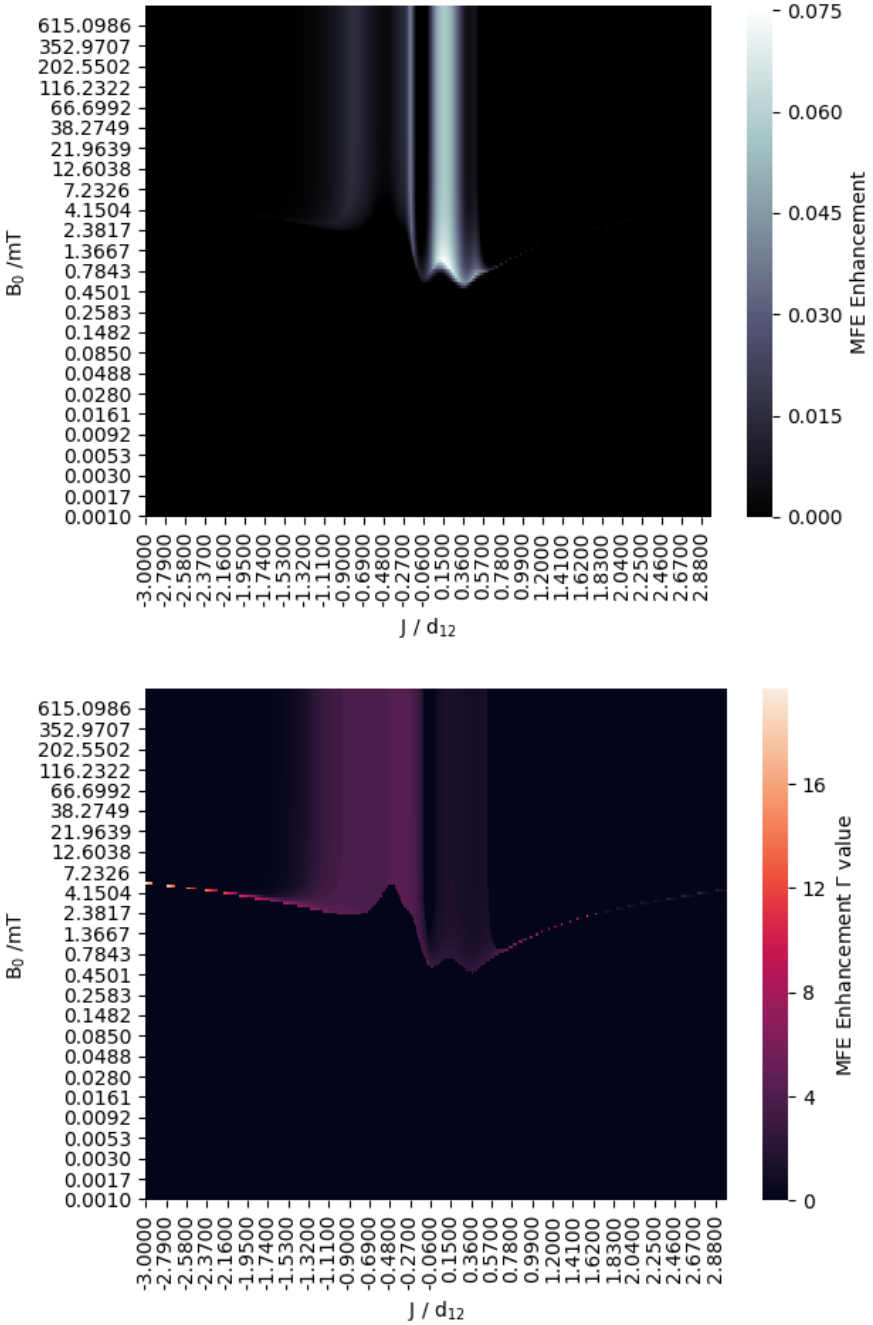

Figure 9.12: Four-spin linear system (L_4), under the DnM formalism and in the presence of exchange and xyz-uncorrelated noise. The top panel shows regions where the presence of noise can gives an enhanced MFE relatively to the no-noise system. The bottom panel shows the value of the noise parameter, Γ (in MHz), that produced the corresponding enhanced MFE in the upper panel.

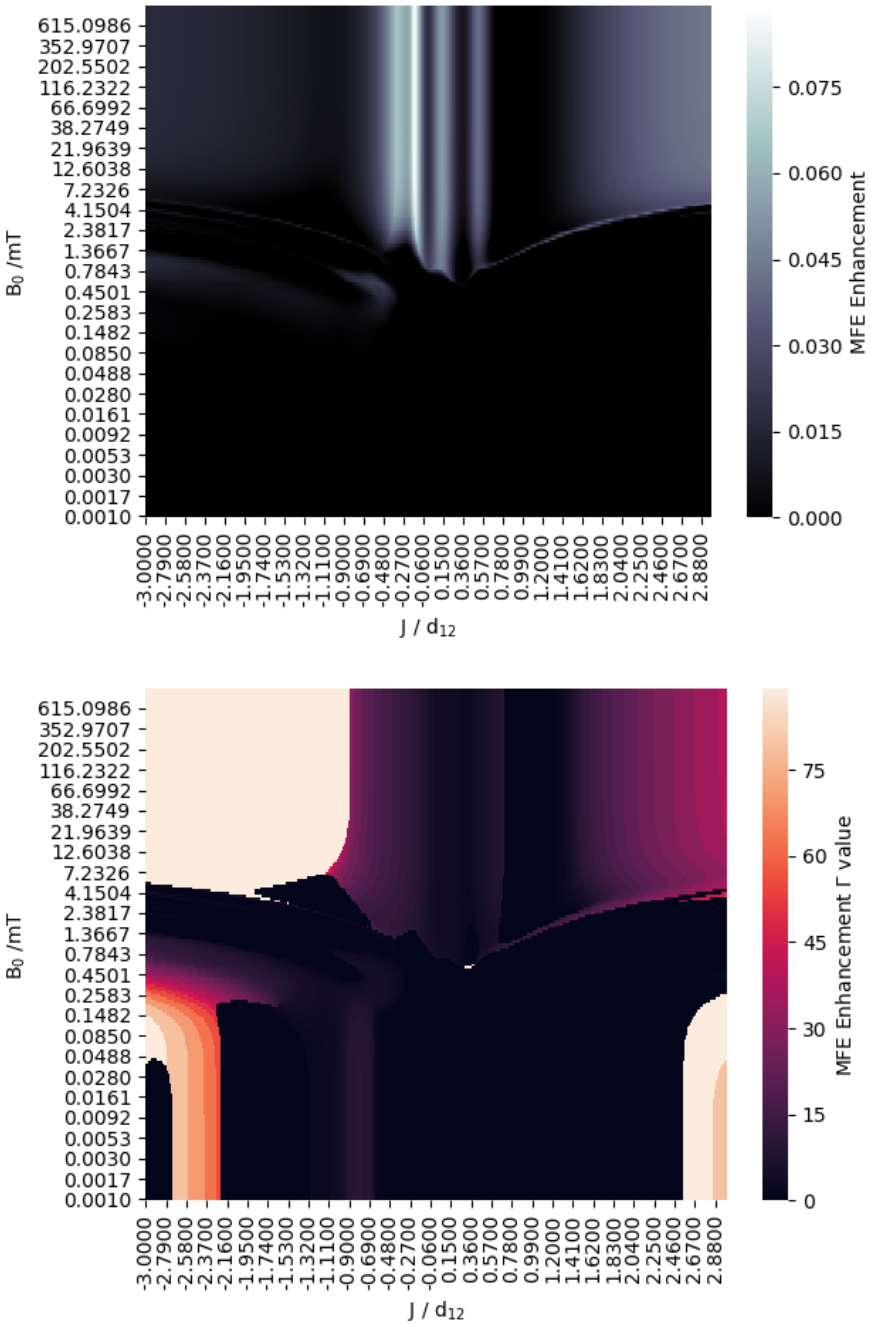

Figure 9.13: Five-spin linear system (L_5), under the DnM formalism and in the presence of exchange and S-T dephasing. The top panel shows regions where the presence of noise can gives an enhanced MFE relatively to the no-noise system. The bottom panel shows the value of the noise parameter, Γ (in MHz), that produced the corresponding enhanced MFE in the upper panel.

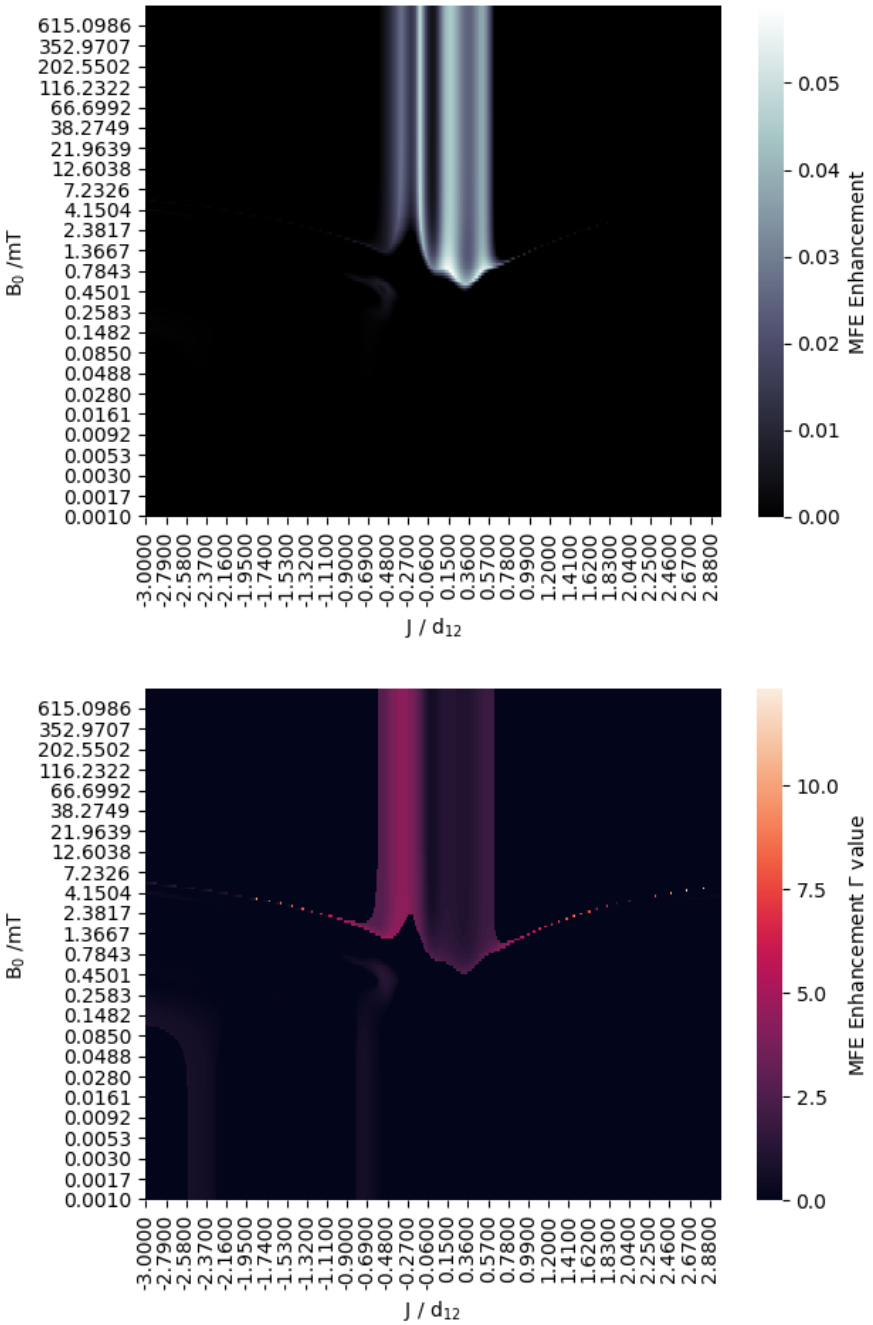

Figure 9.14: Five-spin linear system (L_5), under the DnM formalism and in the presence of exchange and xyz-uncorrelated noise. The top panel shows regions where the presence of noise can gives an enhanced MFE relatively to the no-noise system. The bottom panel shows the value of the noise parameter, Γ (in MHz), that produced the corresponding enhanced MFE in the upper panel.

9.11.2 Square, Pentagon, and additional geometries

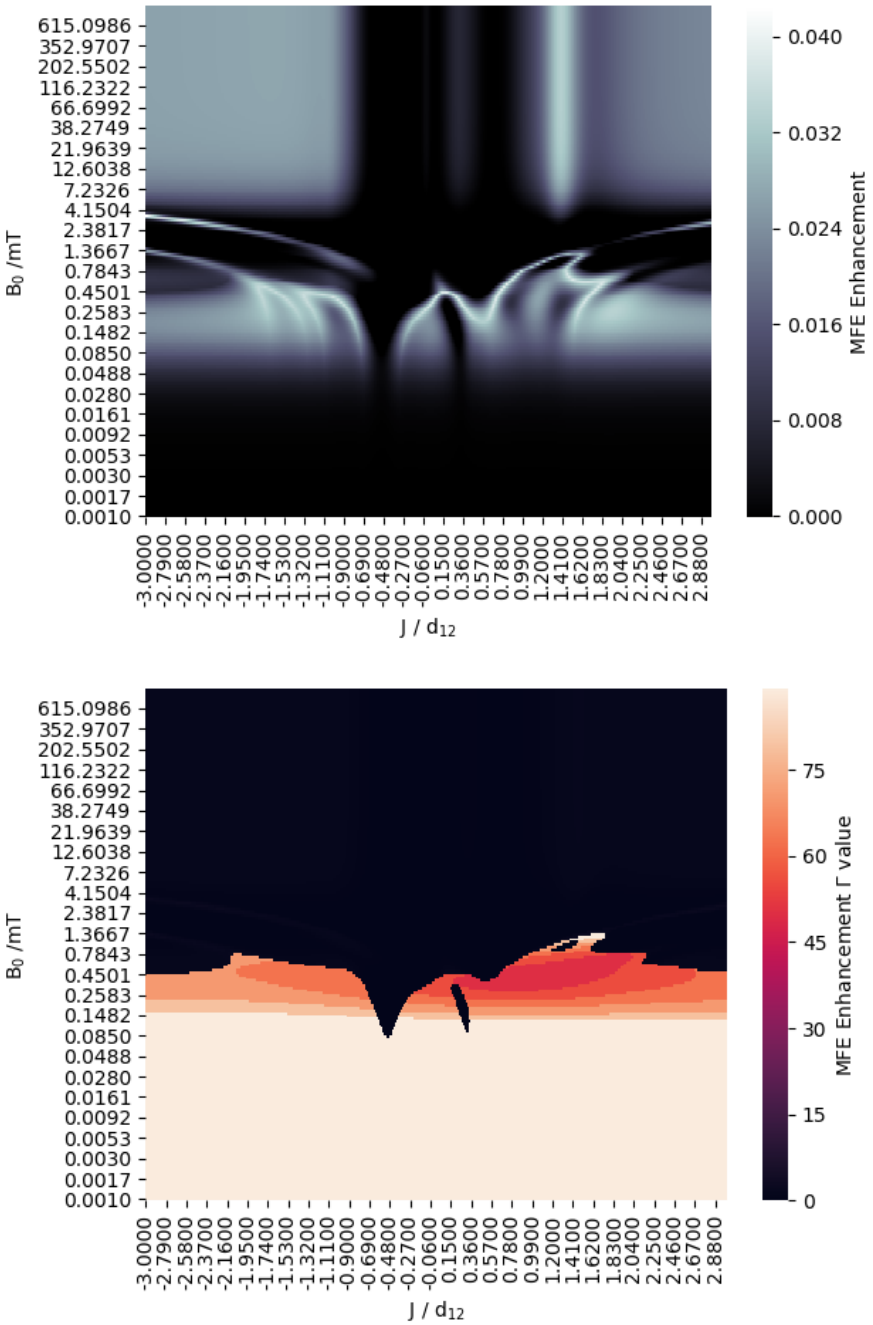

Figure 9.15: Square system (D_4), under the DnM formalism and in the presence of exchange and S-T dephasing. The top panel shows regions where the presence of noise can gives an enhanced MFE relatively to the no-noise system. The bottom panel shows the value of the noise parameter, Γ (in MHz), that produced the corresponding enhanced MFE in the upper panel.

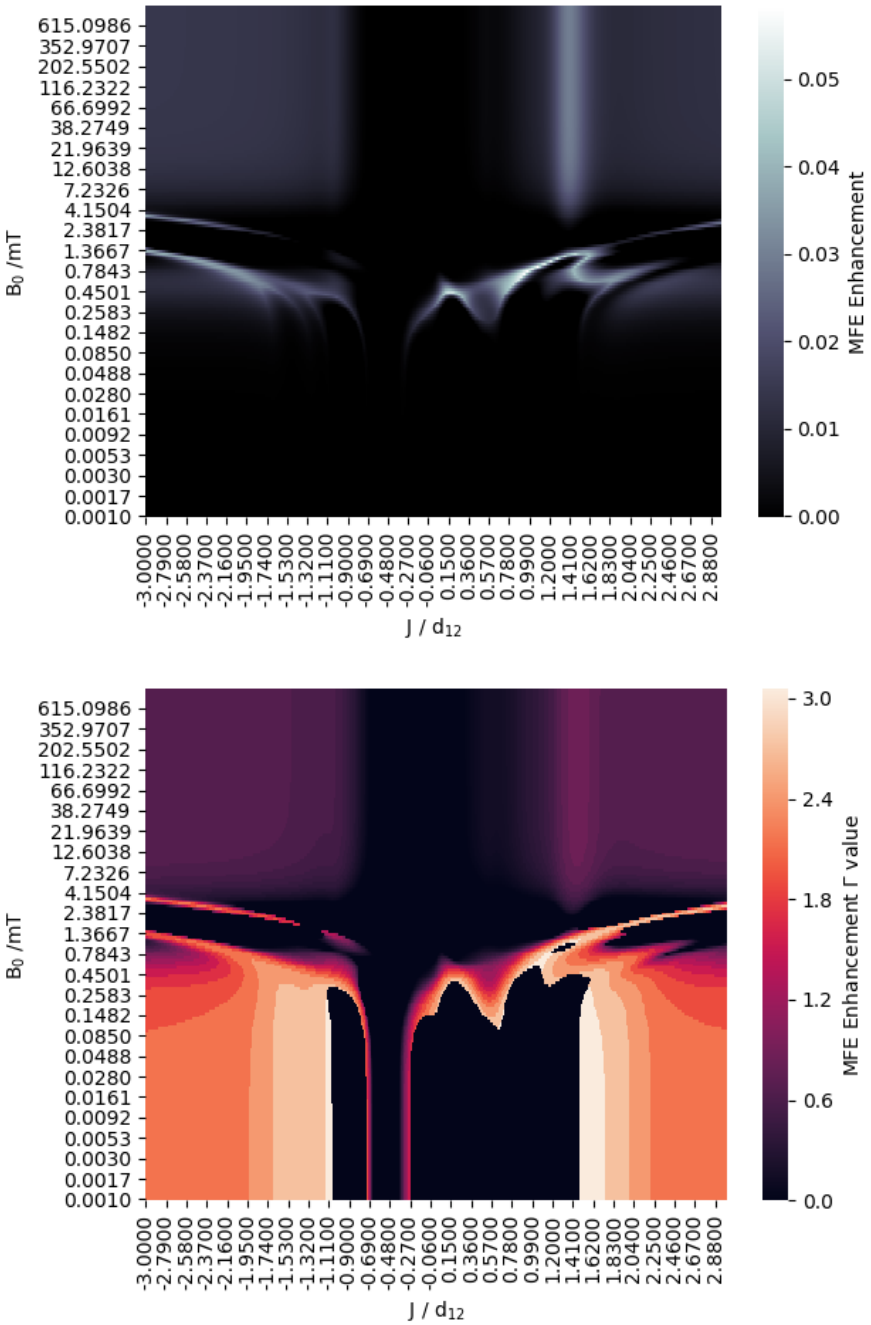

Figure 9.16: Square system (D_4), under the DnM formalism and in the presence of exchange and xyz-uncorrelated noise. The top panel shows regions where the presence of noise can gives an enhanced MFE relatively to the no-noise system. The bottom panel shows the value of the noise parameter, Γ (in MHz), that produced the corresponding enhanced MFE in the upper panel.

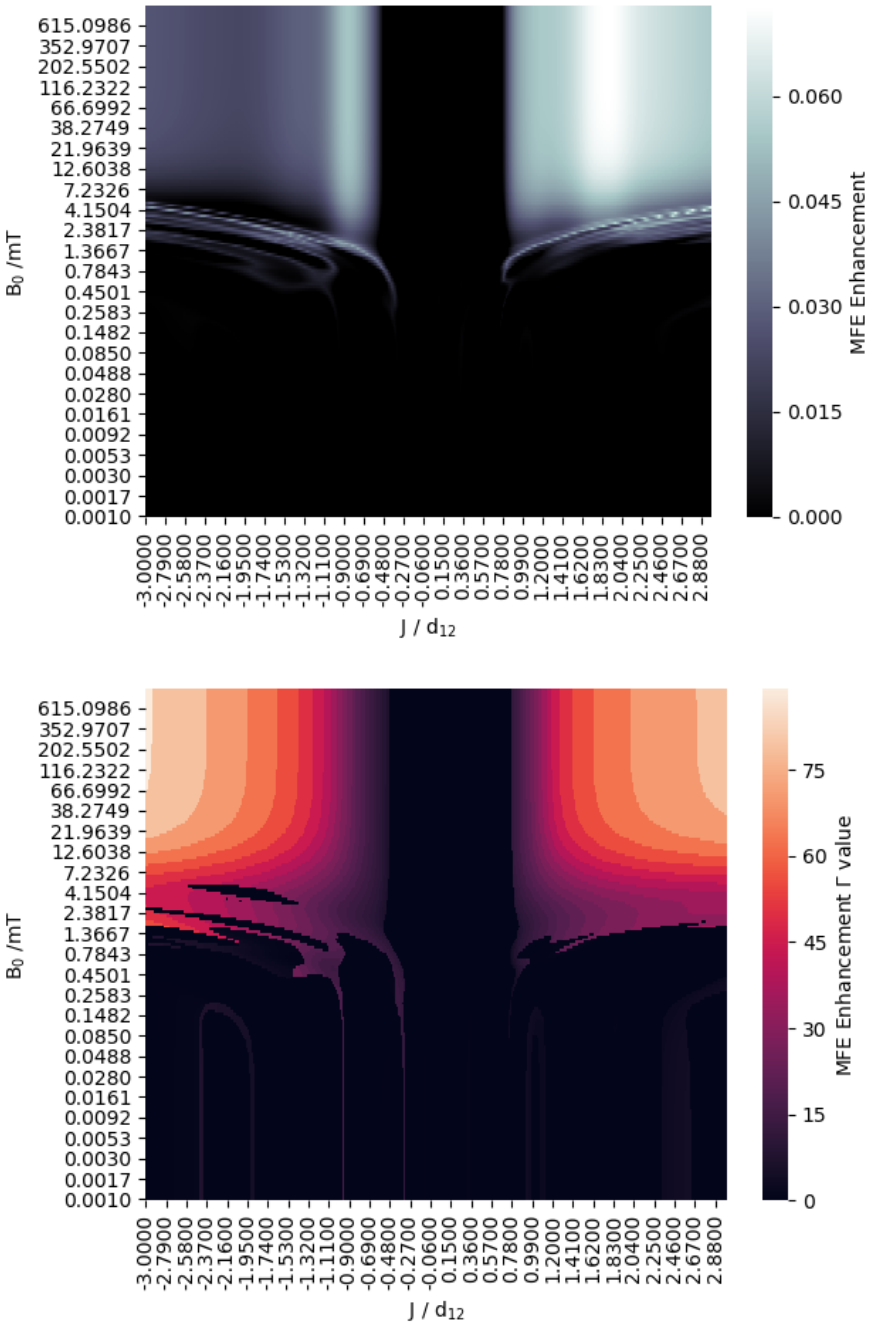

Figure 9.17: Pentagonal system (D_5), under the DnM formalism and in the presence of exchange and S-T dephasing. The top panel shows regions where the presence of noise can gives an enhanced MFE relatively to the no-noise system. The bottom panel shows the value of the noise parameter, Γ (in MHz), that produced the corresponding enhanced MFE in the upper panel.

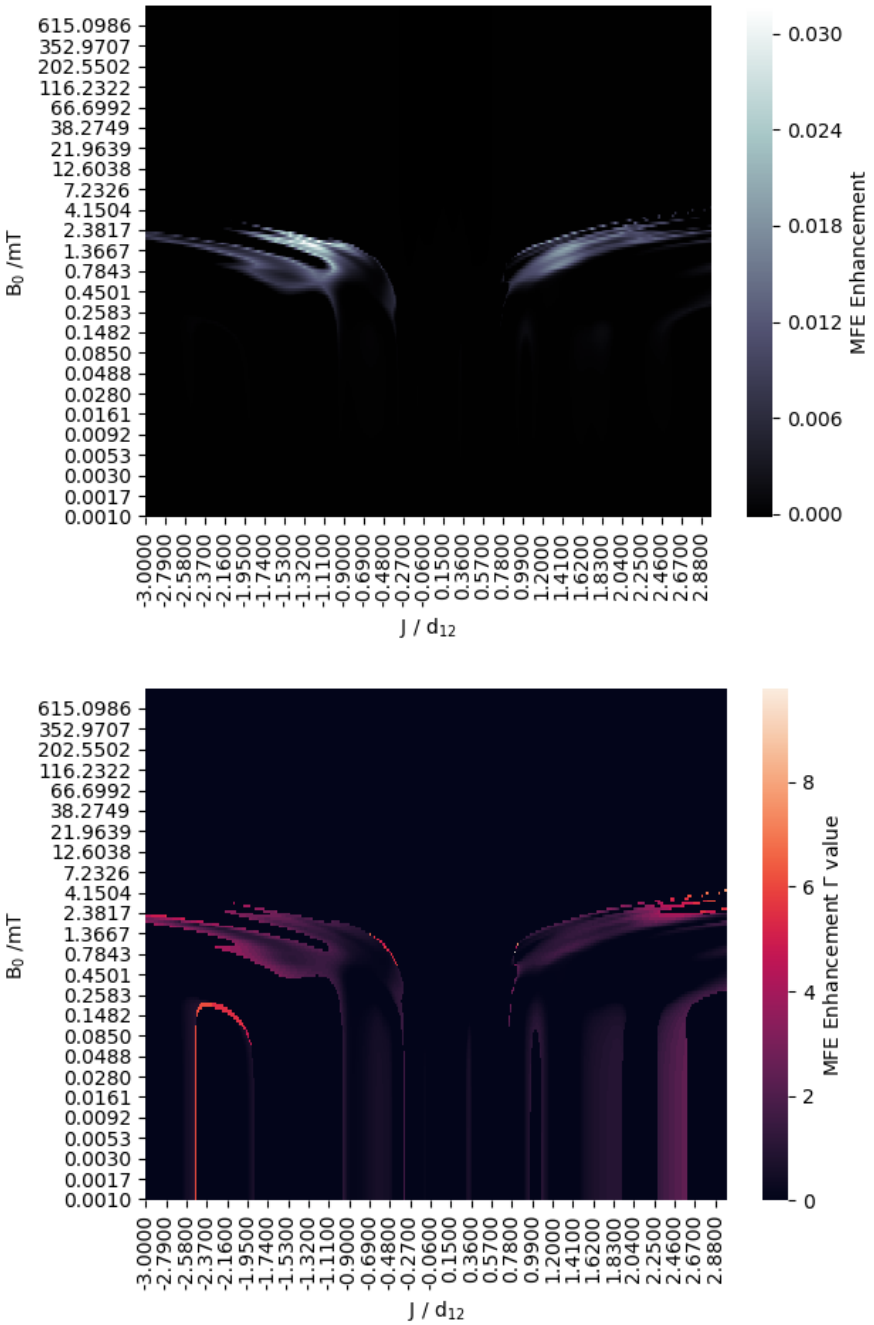

Figure 9.18: Pentagonal system (D_5), under the DnM formalism and in the presence of exchange and xyz-uncorrelated noise. The top panel shows regions where the presence of noise can gives an enhanced MFE relatively to the no-noise system. The bottom panel shows the value of the noise parameter, Γ (in MHz), that produced the corresponding enhanced MFE in the upper panel.

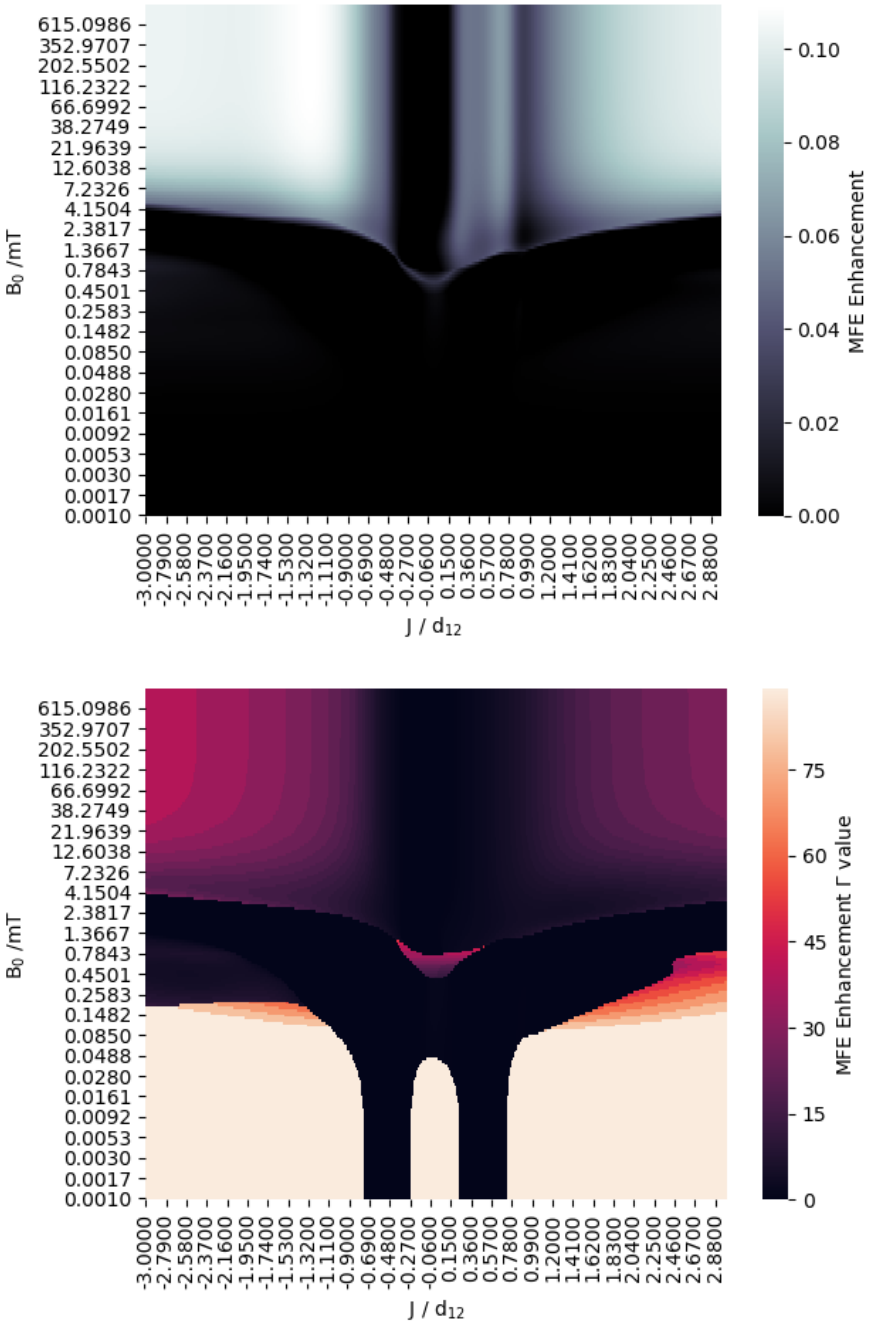

Figure 9.19: Planar Diamond system (coordinates: $[0,0,0],[2r,0,0],[r,r\sqrt{3},0],[r,-r\sqrt{3},0]$), under the D$n$M formalism and in the presence of exchange and S-T dephasing. The top panel shows regions where the presence of noise can gives an enhanced MFE relatively to the no-noise system. The bottom panel shows the value of the noise parameter, Γ (in MHz), that produced the corresponding enhanced MFE in the upper panel.

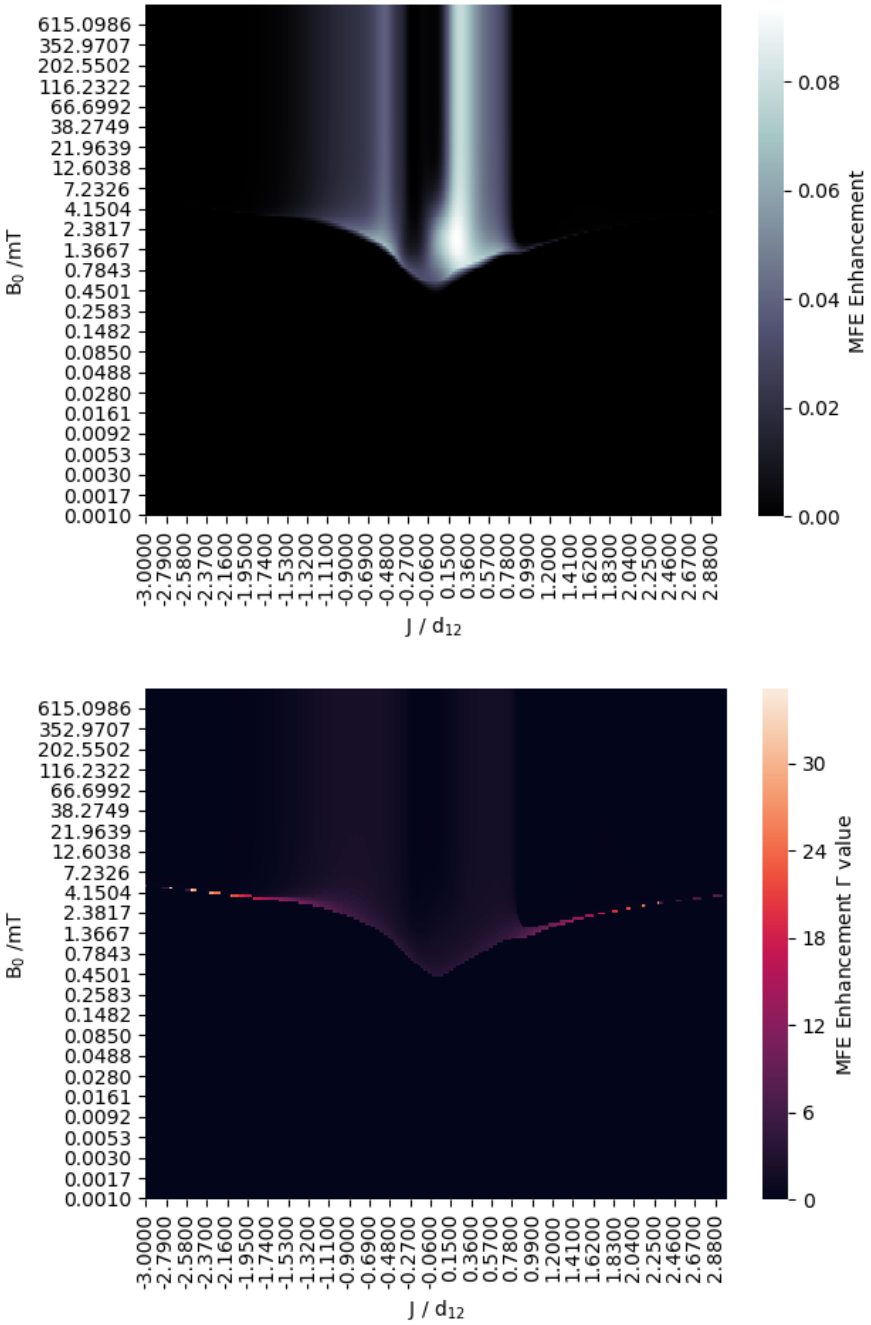

Figure 9.20: Planar Diamond system (coordinates: $[0,0,0],[2r,0,0],[r,r\sqrt{3},0],[r,-r\sqrt{3},0]$), under the D$n$M formalism and in the presence of exchange and xyz-uncorrelated noise. The top panel shows regions where the presence of noise can gives an enhanced MFE relatively to the no-noise system. The bottom panel shows the value of the noise parameter, Γ (in MHz), that produced the corresponding enhanced MFE in the upper panel.

9.12 Distortion-Dephasing Additional Results

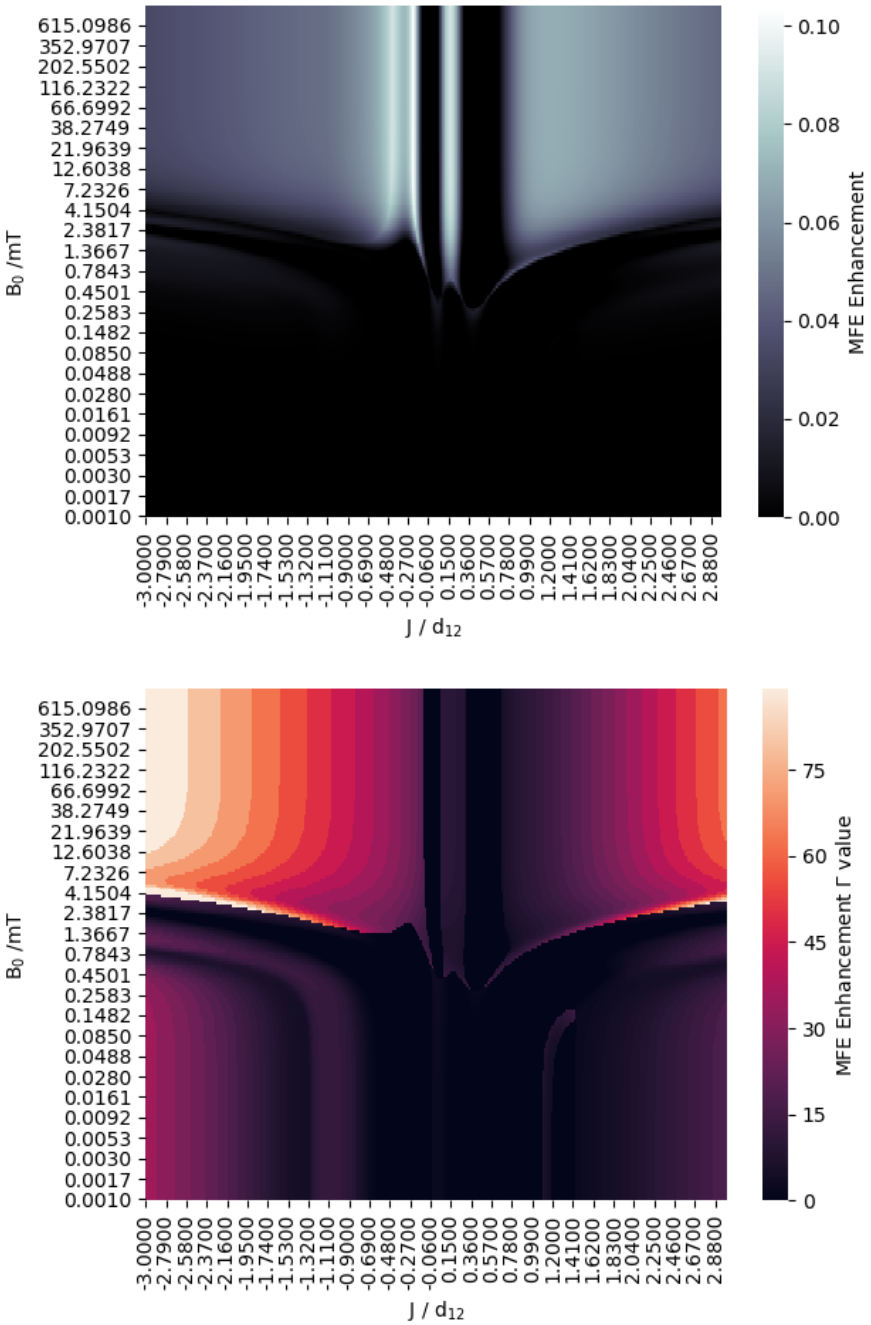

Figure 9.21: Three-spin distorted linear system ($L_{3,2y}$), under the DnM formalism and in the presence of exchange and S-T dephasing. The top panel shows regions where the presence of noise can gives an enhanced MFE relatively to the no-noise system. The bottom panel shows the value of the noise parameter, Γ (in MHz), that produced the corresponding enhanced MFE in the upper panel.

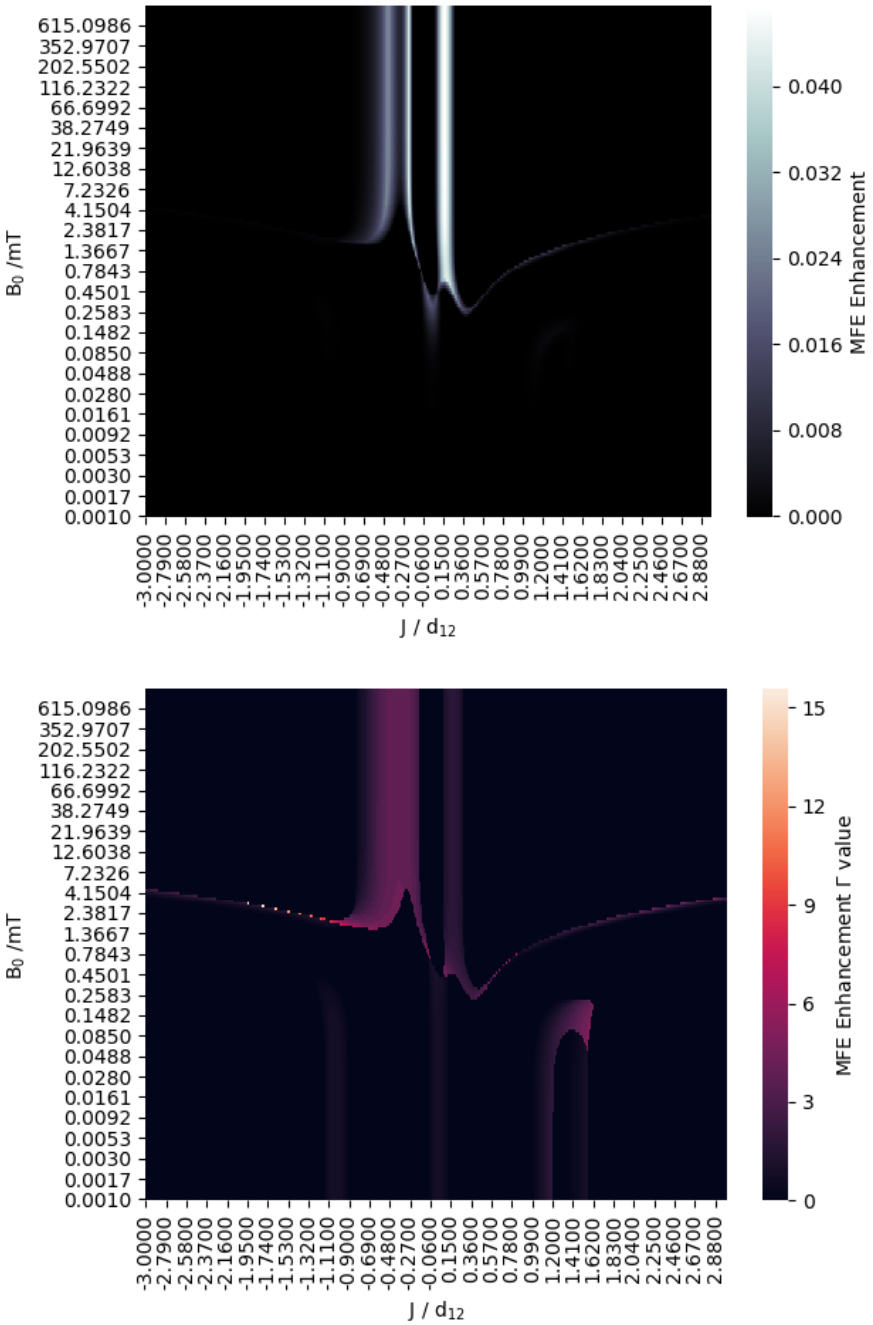

Figure 9.22: Three-spin distorted linear system ($L_{3,2y}$), under the DnM formalism and in the presence of exchange and xyz-uncorrelated noise. The top panel shows regions where the presence of noise can gives an enhanced MFE relatively to the no-noise system. The bottom panel shows the value of the noise parameter, Γ (in MHz), that produced the corresponding enhanced MFE in the upper panel.

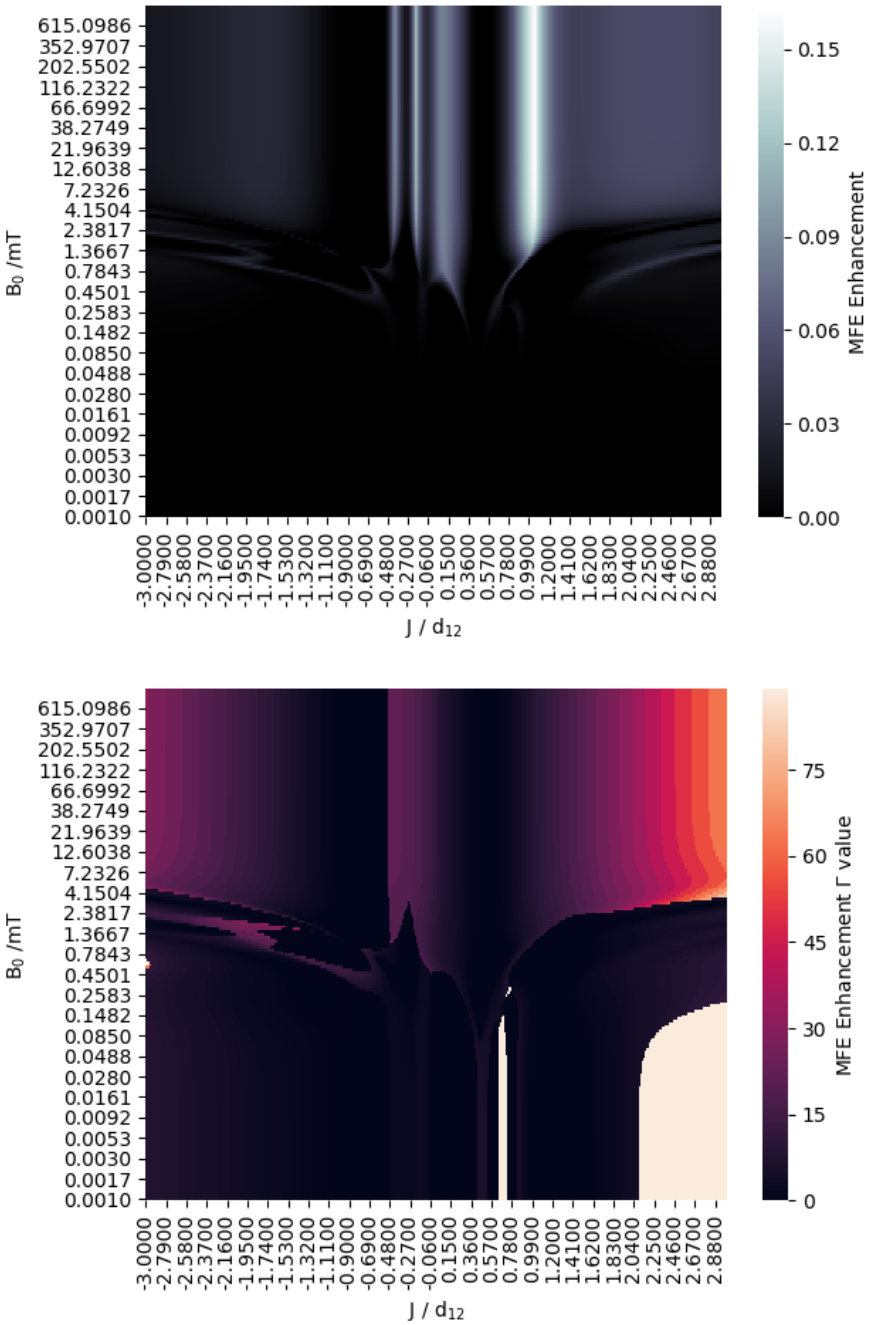

Figure 9.23: Four-spin distorted linear system ($L_{4,3x}$), under the DnM formalism and in the presence of exchange and S-T dephasing. The top panel shows regions where the presence of noise can gives an enhanced MFE relatively to the no-noise system. The bottom panel shows the value of the noise parameter, Γ (in MHz), that produced the corresponding enhanced MFE in the upper panel.

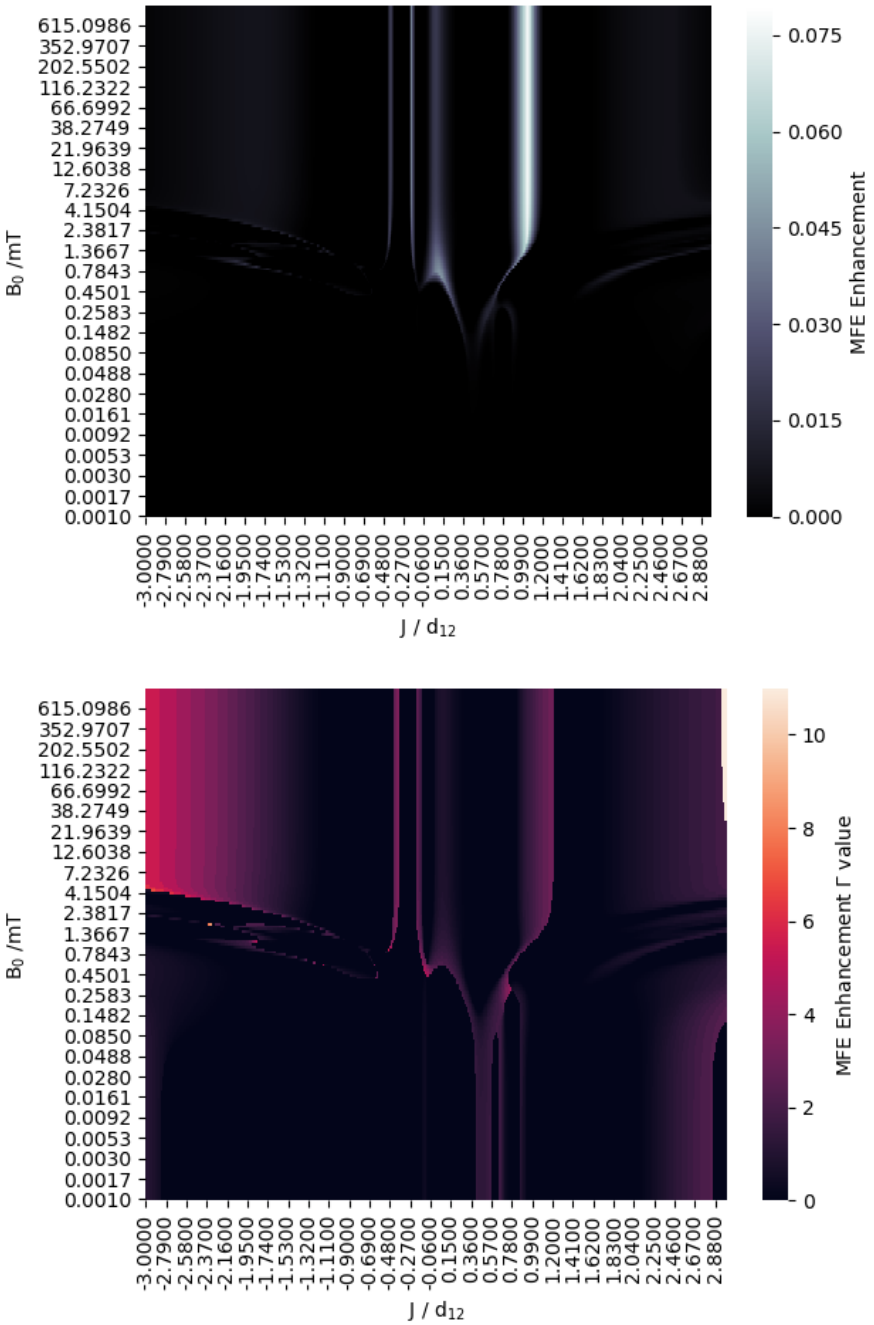

Figure 9.24: Four-spin distorted linear system ($L_{4,3x}$), under the DnM formalism and in the presence of exchange and xyz-uncorrelated noise. The top panel shows regions where the presence of noise can gives an enhanced MFE relatively to the no-noise system. The bottom panel shows the value of the noise parameter, Γ (in MHz), that produced the corresponding enhanced MFE in the upper panel.

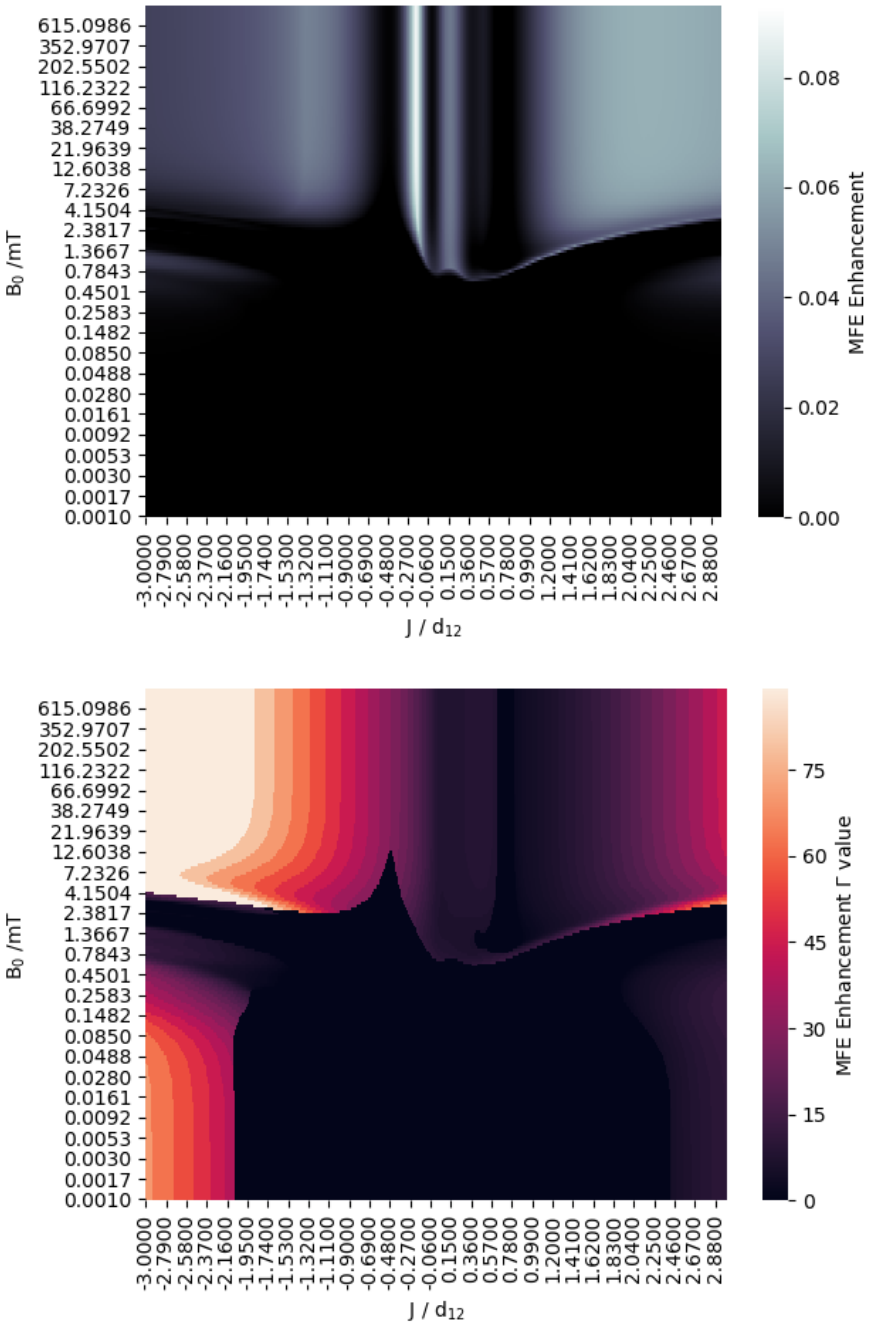

Figure 9.25: Four-spin distorted linear system ($L_{4,4x}$), under the DnM formalism and in the presence of exchange and S-T dephasing. The top panel shows regions where the presence of noise can gives an enhanced MFE relatively to the no-noise system. The bottom panel shows the value of the noise parameter, Γ (in MHz), that produced the corresponding enhanced MFE in the upper panel.

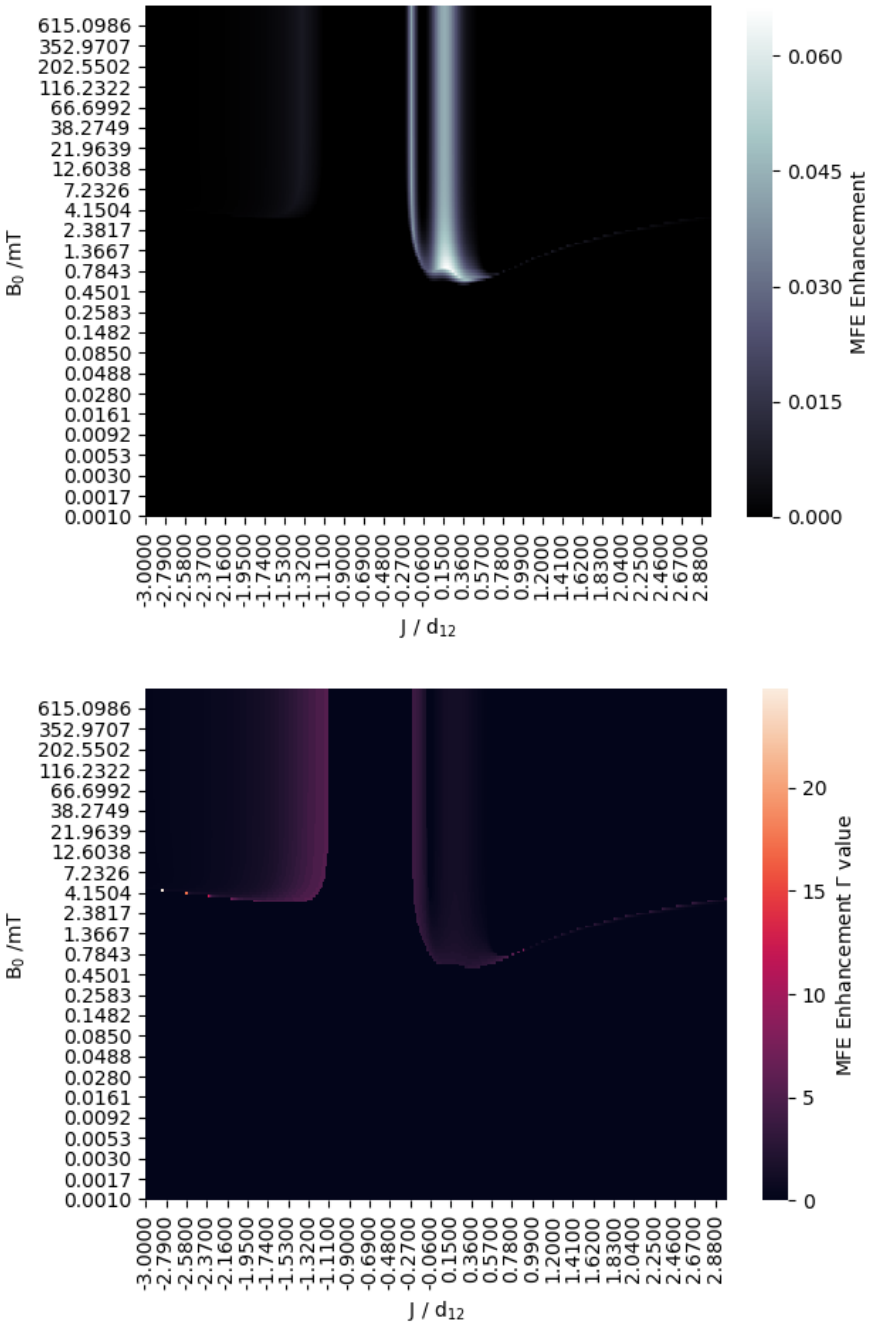

Figure 9.26: Four-spin distorted linear system ($L_{4,4x}$), under the DnM formalism and in the presence of exchange and xyz-uncorrelated noise. The top panel shows regions where the presence of noise can gives an enhanced MFE relatively to the no-noise system. The bottom panel shows the value of the noise parameter, Γ (in MHz), that produced the corresponding enhanced MFE in the upper panel.

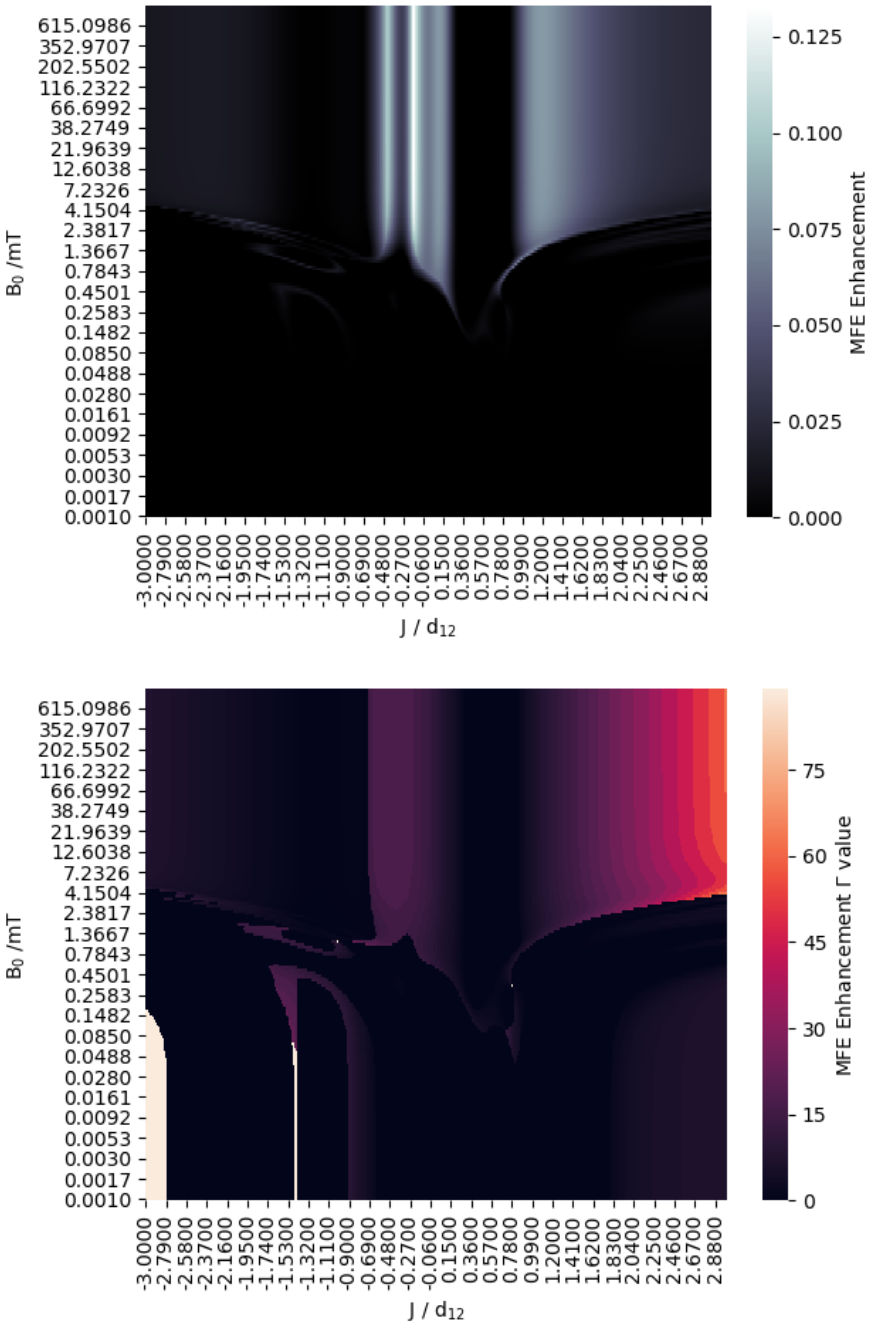

Figure 9.27: Five-spin distorted linear system ($L_{5,3x}$), under the DnM formalism and in the presence of exchange and S-T dephasing. The top panel shows regions where the presence of noise can gives an enhanced MFE relatively to the no-noise system. The bottom panel shows the value of the noise parameter, Γ (in MHz), that produced the corresponding enhanced MFE in the upper panel.

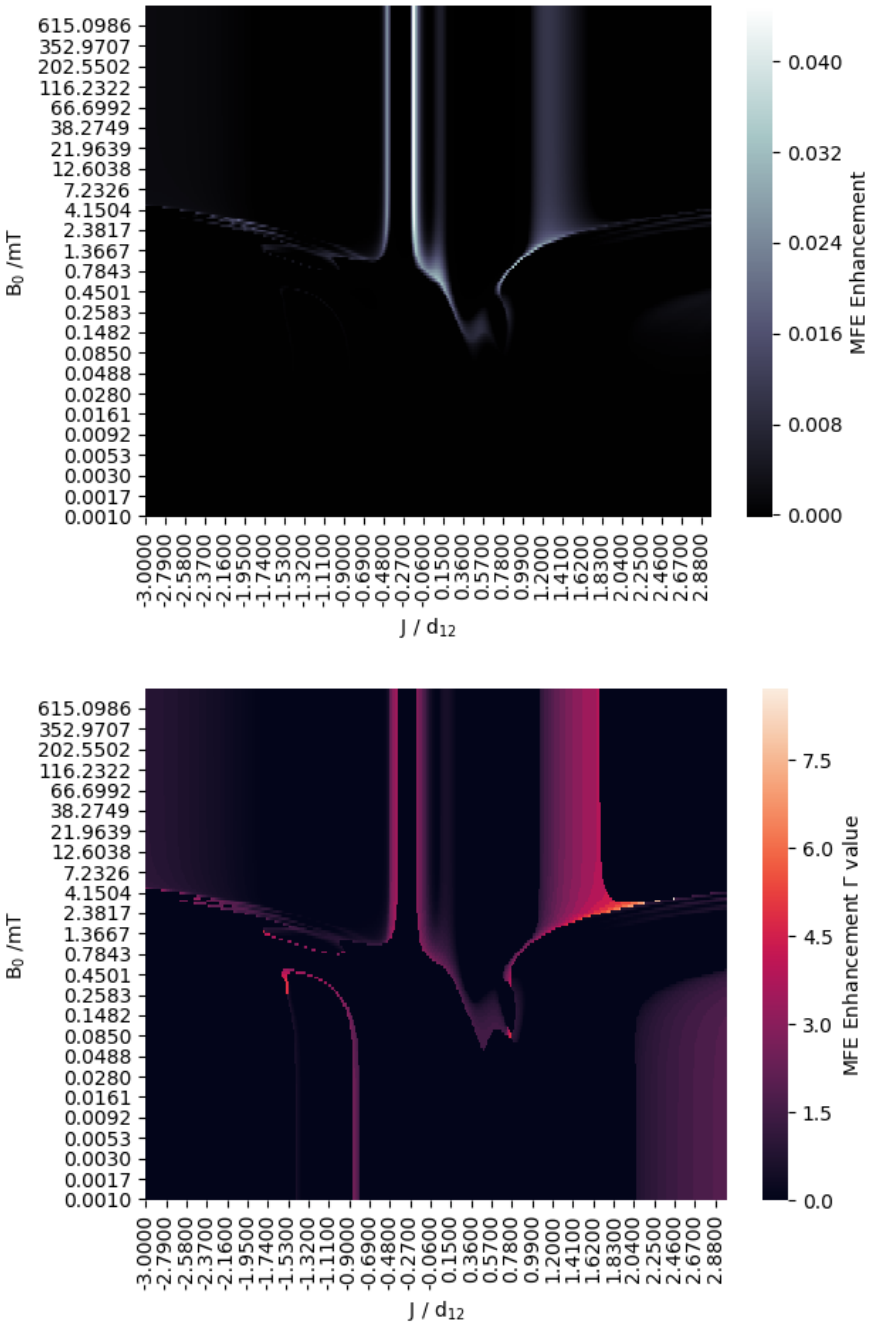

Figure 9.28: Five-spin distorted linear system ($L_{5,3x}$), under the DnM formalism and in the presence of exchange and xyz-uncorrelated noise. The top panel shows regions where the presence of noise can gives an enhanced MFE relatively to the no-noise system. The bottom panel shows the value of the noise parameter, Γ (in MHz), that produced the corresponding enhanced MFE in the upper panel.

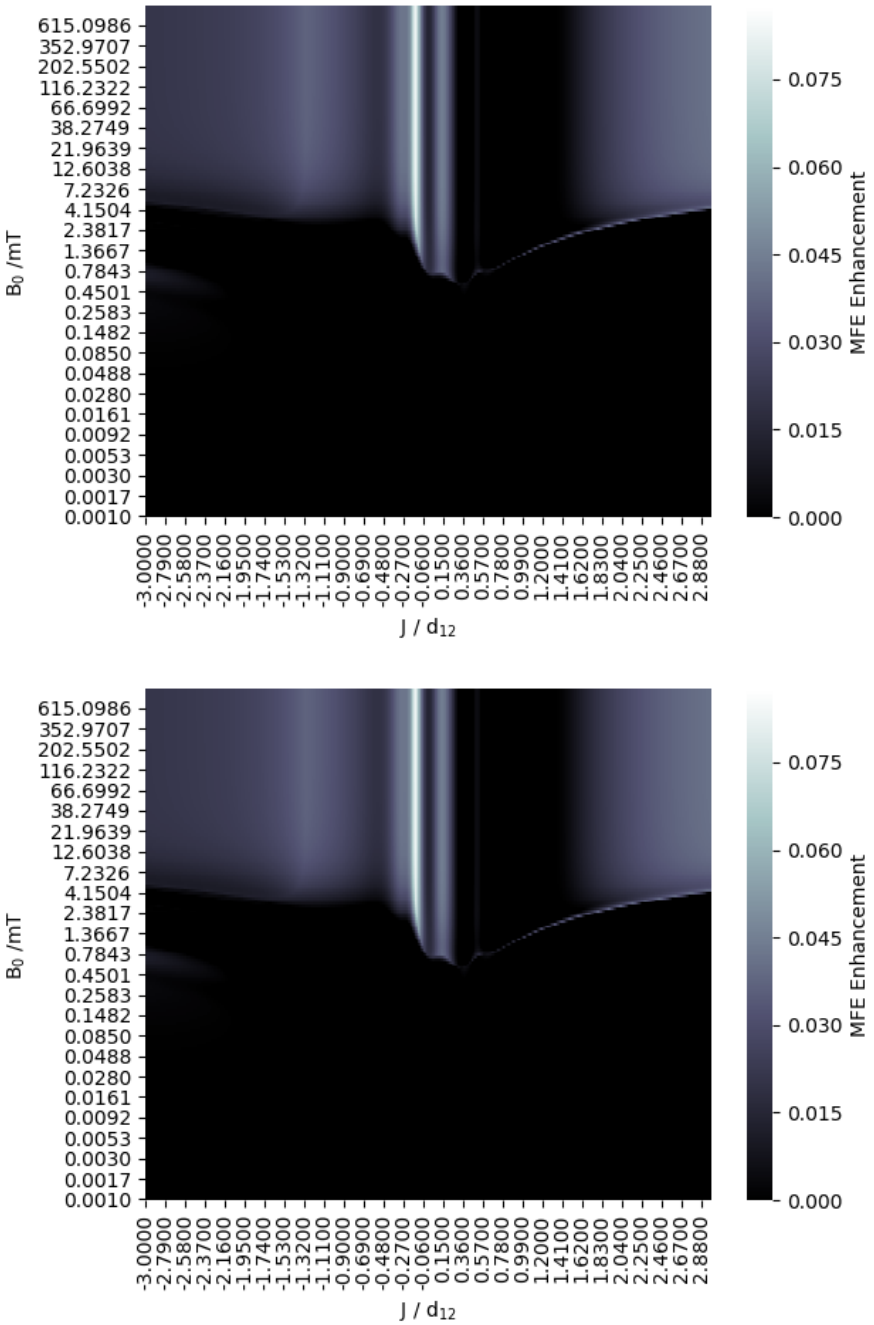

Figure 9.29: Five-spin distorted linear system ($L_{5,5x}$), under the DnM formalism and in the presence of exchange and S-T dephasing. The top panel shows regions where the presence of noise can gives an enhanced MFE relatively to the no-noise system. The bottom panel shows the value of the noise parameter, Γ (in MHz), that produced the corresponding enhanced MFE in the upper panel.

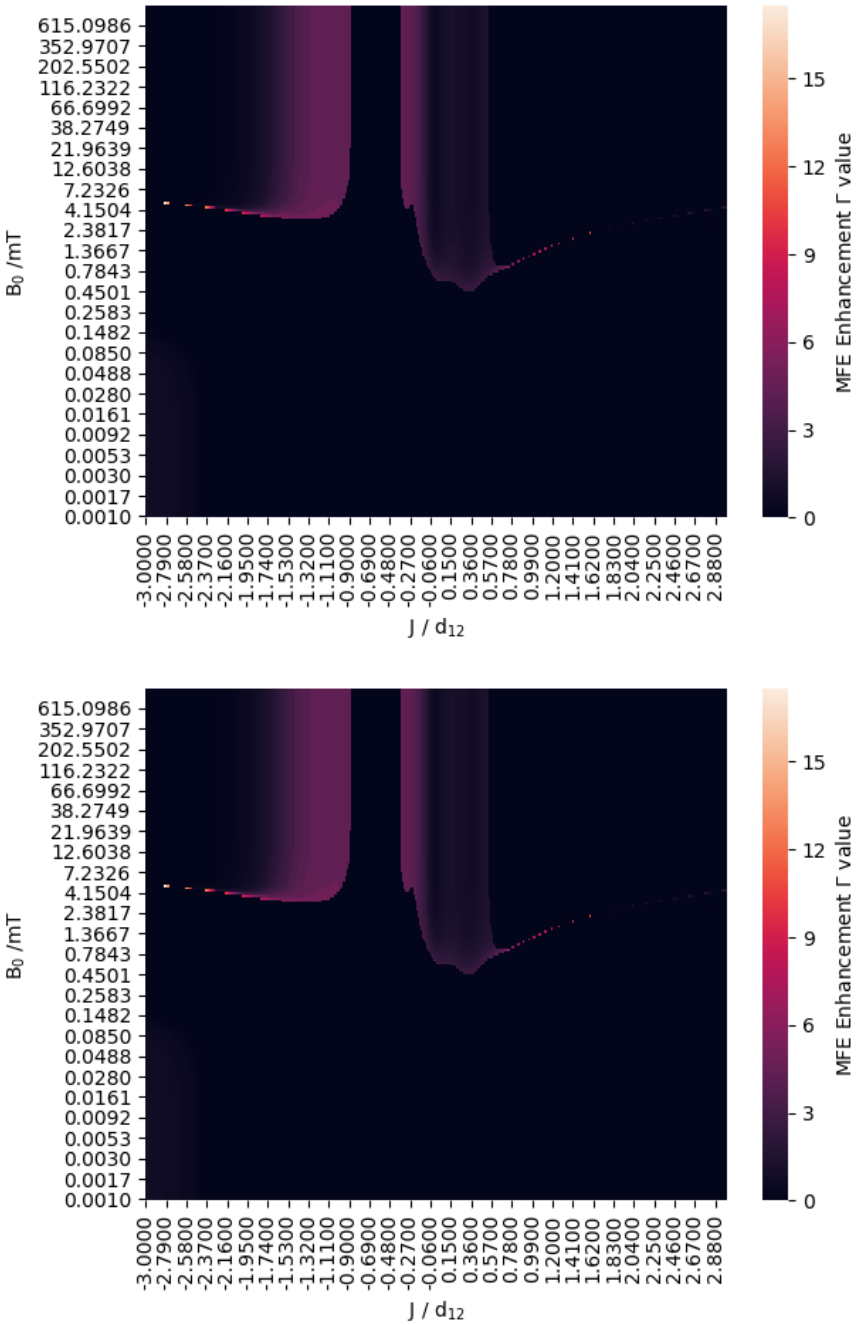

Figure 9.30: Five-spin distorted linear system ($L_{5,5x}$), under the DnM formalism and in the presence of exchange and xyz-uncorrelated noise. The top panel shows regions where the presence of noise can gives an enhanced MFE relatively to the no-noise system. The bottom panel shows the value of the noise parameter, Γ (in MHz), that produced the corresponding enhanced MFE in the upper panel.

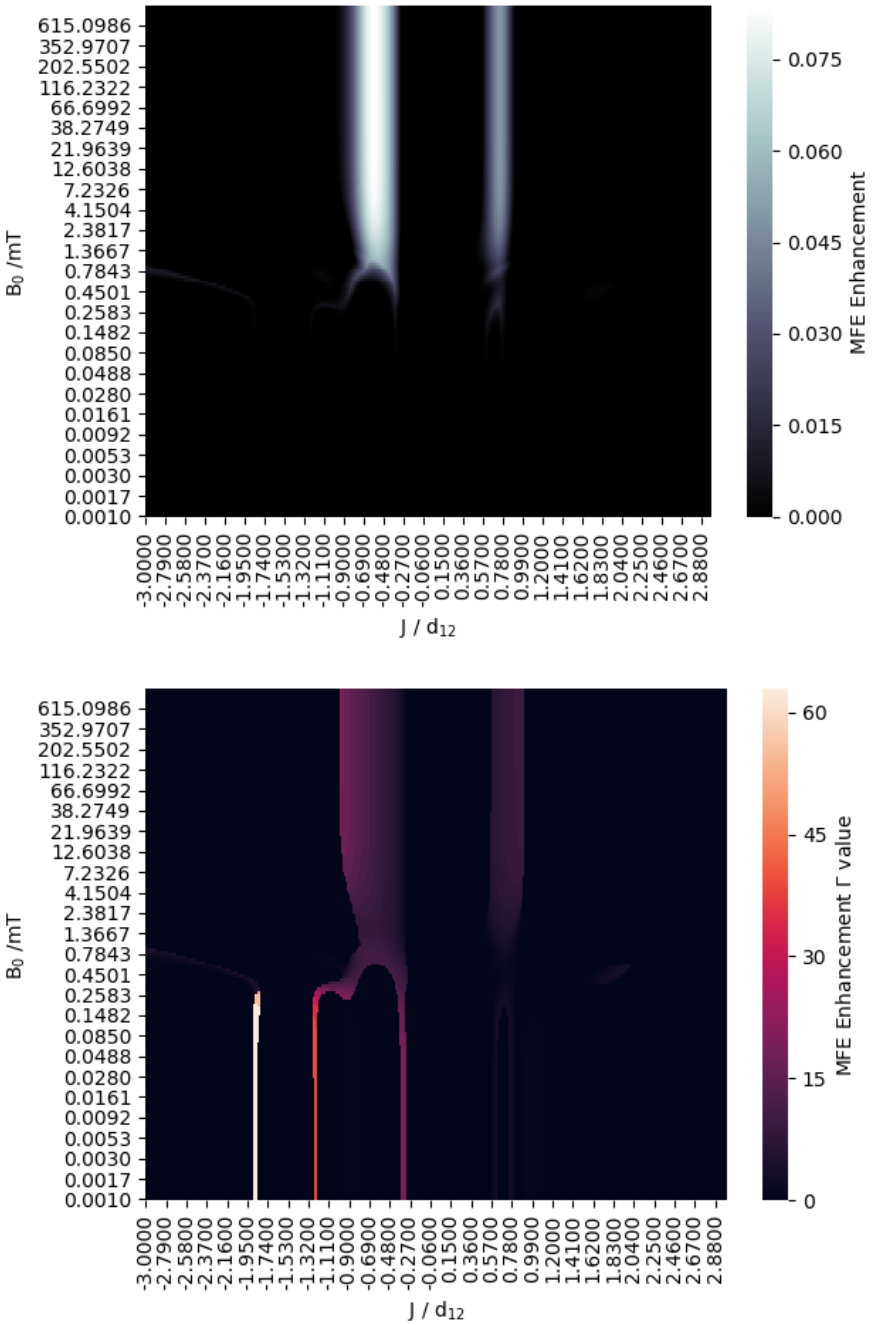

Figure 9.31: Distorted pentagon system ($D_{5,t}$), under the DnM formalism and in the presence of exchange and S-T dephasing. The top panel shows regions where the presence of noise can gives an enhanced MFE relatively to the no-noise system. The bottom panel shows the value of the noise parameter, Γ (in MHz), that produced the corresponding enhanced MFE in the upper panel.

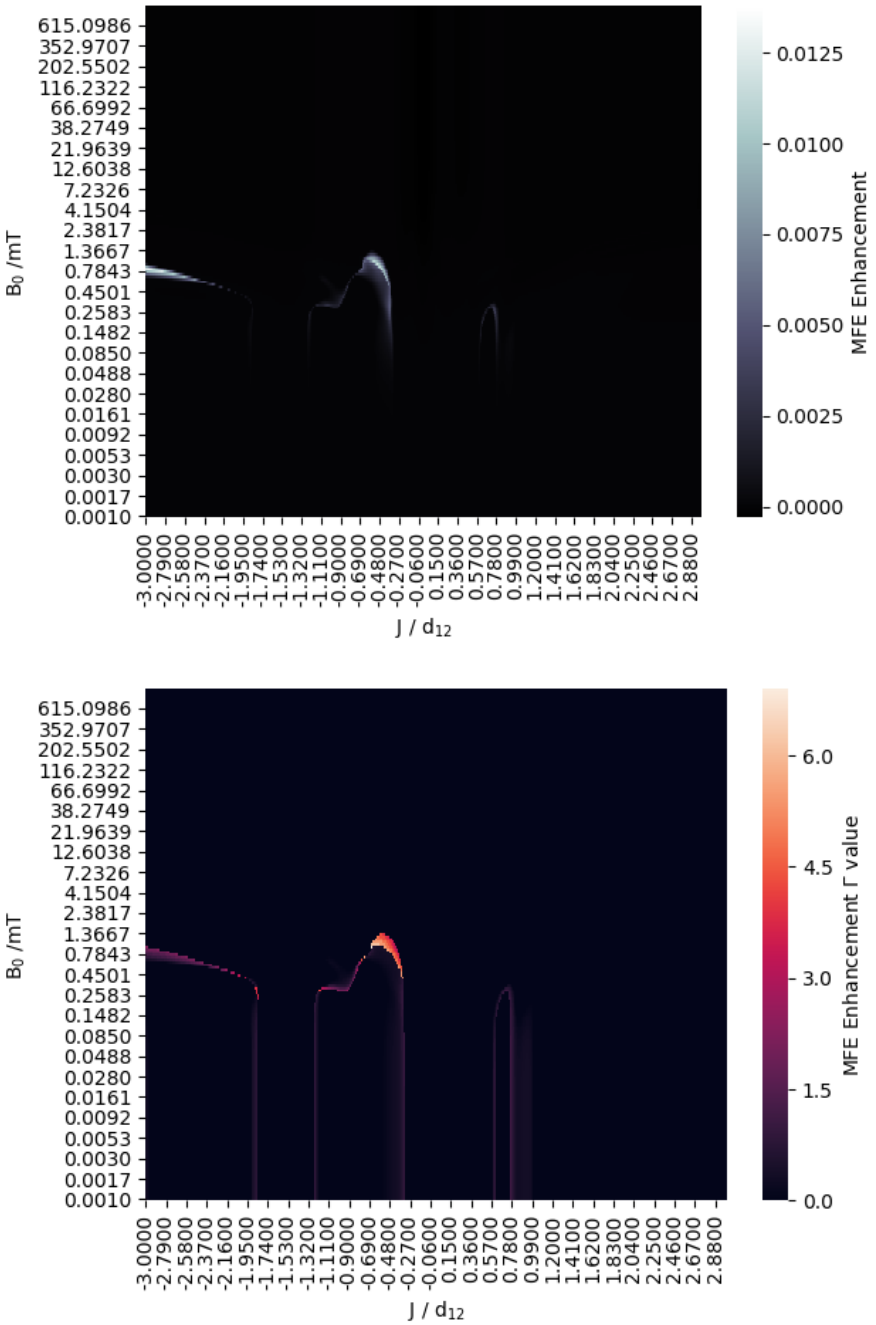

Figure 9.32: Distorted pentagon system ($D_{5,t}$), under the DnM formalism and in the presence of exchange and xyz-uncorrelated. The top panel shows regions where the presence of noise can gives an enhanced MFE relatively to the no-noise system. The bottom panel shows the value of the noise parameter, Γ (in MHz), that produced the corresponding enhanced MFE in the upper panel.

9.13 Additional data from Chapter 7

Here is presented supporting data for chapter 7. First, the hyperfine coupling constants used for FAD are shown, followed by those for the W radical, and finally the computational resources used for this study are detailed.

9.13.1 Hyperfine Coupling Constants for FAD radical (MHz)

$$\text{"N5"}: \begin{bmatrix} -2.848 & 0.074 & -1.757 \\ 0.074 & -2.567 & 0.327 \\ -1.757 & 0.327 & 53.686 \end{bmatrix}$$

$$\text{"N10"}: \begin{bmatrix} -0.098 & 0.002 & 1.804 \\ 0.002 & -0.513 & -0.509 \\ 1.804 & -0.509 & 19.109 \end{bmatrix}$$

$$3 \times \text{"H7"}: \begin{bmatrix} -3.779 & 0.000 & 0.000 \\ 0.000 & -3.779 & 0.000 \\ 0.000 & 0.000 & -3.779 \end{bmatrix}$$

$$3 \times \text{"H8"}: \begin{bmatrix} 11.872 & 0.000 & 0.000 \\ 0.000 & 11.872 & 0.000 \\ 0.000 & 0.000 & 11.872 \end{bmatrix}$$

$$\text{"H}\beta\text{1"}: \begin{bmatrix} 8.486 & -0.878 & -1.223 \\ -0.878 & 5.566 & 0.299 \\ -1.223 & 0.299 & 5.348 \end{bmatrix}$$

$$\text{"H}\beta\text{2"}: \begin{bmatrix} 5.301 & 1.024 & -1.091 \\ 1.024 & 2.321 & -0.270 \\ -1.091 & -0.270 & 1.939 \end{bmatrix}$$

$$\text{"H9"}: \begin{bmatrix} 2.377 & 0.861 & -0.022 \\ 0.861 & 4.165 & 0.178 \\ -0.022 & 0.178 & 0.325 \end{bmatrix}$$

$$\text{"H6"}: \begin{bmatrix} -5.314 & -1.034 & 0.256 \\ -1.034 & -13.393 & -0.201 \\ 0.256 & -0.201 & -11.632 \end{bmatrix}$$

9.13.2 Hyperfine Coupling Constants for W radical cation (MHz)

$$\text{"N1"}: \begin{bmatrix} -1.954 & -1.606 & 1.158 \\ -1.606 & 9.788 & -10.461 \\ 1.158 & -10.461 & 7.082 \end{bmatrix}$$

$$\text{"H1"}: \begin{bmatrix} -19.481 & -3.858 & -3.772 \\ -3.858 & -9.593 & 6.495 \\ -3.772 & 6.495 & -6.716 \end{bmatrix}$$

$$\text{"H2"}: \begin{bmatrix} -13.680 & 6.217 & 7.082 \\ 6.217 & -13.304 & 2.204 \\ 7.082 & 2.204 & -14.512 \end{bmatrix}$$

$$\text{"H}\beta\text{1"}: \begin{bmatrix} 10.543 & 0.268 & -1.718 \\ 0.268 & 5.184 & 0.292 \\ -1.718 & 0.292 & 5.733 \end{bmatrix}$$

$$\text{"H}\beta\text{2"}: \begin{bmatrix} 24.207 & -0.125 & -1.419 \\ -0.125 & 22.955 & 1.756 \\ -1.419 & 1.756 & 27.181 \end{bmatrix}$$

$$\text{"H4"}: \begin{bmatrix} -18.561 & -4.989 & -5.445 \\ -4.989 & -14.908 & 2.997 \\ -5.445 & 2.997 & -13.069 \end{bmatrix}$$

$$\text{"H5"}: \begin{bmatrix} 4.817 & 0.552 & 0.251 \\ 0.552 & 1.315 & 0.752 \\ 0.251 & 0.752 & 1.545 \end{bmatrix}$$

$$\text{"H6"}: \begin{bmatrix} -3.659 & 2.102 & 1.570 \\ 2.102 & -12.960 & -2.362 \\ 1.570 & -2.362 & -14.366 \end{bmatrix}$$

$$\text{"H7"}: \begin{bmatrix} -7.268 & -1.930 & -2.309 \\ -1.930 & -5.385 & 2.476 \\ -2.309 & 2.476 & -4.267 \end{bmatrix}$$

9.13.3 Computational resources used

Computing system used in this study:

- CPU: Intel(R) Xeon(R) CPU E5-2640 v3
- CPU frequency: 2601 MHz
- Cache size: 20480 KB
- Memory: 128 GB
- Programming language: Julia 1.3

9.14 Code written to implement D3M and DnM simulations

This section contains the fundamental source code, written independently by the author, used to implement the new models discussed in the main chapters and to generate the results published in works contributing. Note: Some lines of code have been artificially split, as they were too long to fit within a single line of the verbatim container that LaTeX provides.

9.14.1 Core Class File

```
import HFI_Dense
import numpy as np
from joblib import Parallel, delayed
import multiprocessing
import Zeeman_Dense
import Dipole_MKII_Dense
import Exchange_MKII_Dense
from point_dipole_dipole_coupling import point_dipole_dipole_coupling
from numpy.linalg import norm
from Linalg_Yields_Dense import Yield
import Projectors_Dense
from Set_up_spin_ops import calculateDoubleSpinOperator


_eps_ = 2.2204460492503131e-16 #Machine epsilon; used for zero-comparisons.


class Particle(object):
```

```
    def __init__(self, j2, index, type, position=None):
        self.j2 = j2 # Doubled angular momentum; can handle
        1 (spin-1/2) or 2 (spin-1).
        self.index = index
        self.type = type  #'e' or 'n', standing for electron or nucleus.
        self.position = position


class Operator(object):
    def __init__(self, j_2):
        self.dimension = j_2 + 1 #The matrix is square, and this is its side length


#Basic-grade spin operator components.
class SpinOp(Operator):
    def Spawn(self, index, j2_list, total_spins):
        self.index = index
        self.components = {'xcom': calculateDoubleSpinOperator(['x'],
        [self.index -1], j2_list, total_spins),
        'ycom' : calculateDoubleSpinOperator(['y'], [self.index -1],
        j2_list, total_spins),
        'zcom' : calculateDoubleSpinOperator(['z'], [self.index -1],
        j2_list, total_spins)}


#Dot products of spin operators used in interactions.
#Only electron-electron Exchange uses currently opDP,
so this has not been updated for spin-1.
class SpinOpDP(Operator):
    def DPSpawn(self, labels, j2_list, total_spins):
        self.PlusMinus = calculateDoubleSpinOperator(['p', 'm'],
        [labels[0]-1,labels[1]-1], j2_list, total_spins)
        self.MinusPlus = calculateDoubleSpinOperator(['m', 'p'],
```

```
        [labels[0]-1,labels[1]-1], j2_list, total_spins)
        self.ZZ = calculateDoubleSpinOperator(['z', 'z'],
        [labels[0]-1,labels[1]-1], j2_list, total_spins)
        self.OoDat = labels

#Similarly here, we only assume e- to combine, so spin-1 not considered.
class RecOp(Operator):
    def RecSpawn(self, Spins, RecomData, ND):
        j_2vals = [Spins['ES%d'% RecomData[0]].j2,
        Spins['ES%d'% RecomData[1]].j2]
        indices = [RecomData[0], RecomData[1]]
        self.name = 'k%d%d' % (RecomData[0], RecomData[1])
        self.matrix = (0.5 * RecomData[3] *
        np.transpose(Projectors_Dense.Singlet_Projector(j_2vals,
        indices, self.dimension, ND)))#, dtype=np.complex  )

#For setting up the parts of the Hamiltonian.
class Hamiltonian(Operator):
#This is my idea for avoiding unnecessary calculations in the Hamiltonain setup.
#Essentially, give it a list of characters for the interactions you
#want calculated, and they will be included. For example ['D', 'H', 'Z']
#would give Dipolar, Hyperfine, and Zeeman terms.

    def Jester(self, mask):
        self.Mask = mask
        self.Faces = {}

    def Zeeman(self, SysData, Electrons, Nuclei, Bz, ND):
        self.Faces['Z'] = Zeeman_Dense.ZInt(SysData, Electrons, Nuclei,
        ND, Bz=Bz)#Bx=Bz/np.sqrt(2), By=Bz/np.sqrt(2))
```

```
    def Exchange(self, SysData, SystemSize, ND):
        self.Faces['E'] = Exchange_MKII_Dense.ExInt_MKII(SysData,
        SystemSize, ND)

    def Dipolar(self, SysData, SystemSize, ND):
        self.Faces['D'] = Dipole_MKII_Dense.ddInt_MKII(SysData,
        SystemSize, ND)

    def Hyperfine(self, SysData, Electrons, Nuclears, SystemSize, ND):
        self.Faces['H'] = HFI_Dense.HFInt(SysData, Electrons, Nuclears,
        SystemSize, ND)

class Interactions(object):
    def __init__(self):
        pass

    def Dipolar_Data(self, Spins, Electrons):
        self.dipolar = {}
        for i in range(Electrons):
            for j in range(Electrons):
                if (i < j):
                    self.dipolar['D_%d%d' % (i+1, j+1)] = np.array(
                    [point_dipole_dipole_coupling(np.array(Spins['ES%d' % (i + 1)].
                    - np.array(Spins['ES%d' % (j + 1)].position)) * (2e-3*np.pi)])

    def Exchange_Data(self, Spins, J0, dcon_MHz, beta, r, Electrons):
        self.exchange = {}
        for i in range(Electrons):
```

```
            for j in range(Electrons):
                if (i < j):
                    self.exchange['J_%d%d' % (i+1, j+1)] = [J0 * dcon_MHz *
                    (2e-3*np.pi)* np.exp(-beta*
                    (norm(np.array(Spins['ES%d' % (i + 1)].position)
                    - np.array(Spins['ES%d' % (j + 1)].position))
                    - 2*r)), i+1 , j+1]

    #Currently assumes only singlet recombination.
    def Recombination_Data(self, Spins, kS0, kSc, beta, r, Electrons):
        self.RecomS = {}
        #if 'All' in Targeted_Recom_Pairs:
        for i in range(Electrons-1):

            self.RecomS['k_%d%d' % (i+1, i+2)] = [i+1 , i+2, 's', kS0]

        self.Scav = [0, 0, 'X', kSc]

    def Hyperfine_Data(self, Spins, Partners, a_iso):
        self.hyperfine = {}
        for i in range(len(Partners)):
            self.hyperfine['A_%d%d' %
            (Spins['ES%d' % Partners[i][0]].index,
            Spins['NS%d' % Partners[i][1]].index)]
            = a_iso*2e-3*np.pi*np.identity(3)#np.ones((3,3))

class Engine(object):
    def __init__(self):
        pass
```

```
    def CalcYield(H_tot, RecomData, Electrons,
    Nuclei, Dimensions,
    ND, Starting_Singlet=None, Targeted_Yield=None):
        yields, Evals = Yield(H_tot, RecomData, Electrons,
        Nuclei, Dimensions,
        ND, Starting_Singlet, Targeted_Yield)
        return yields, Evals




def Geometry(r, Electrons, Nuclei, j_2list):
    #The j_2 list is a generalisation to allow spin-1
    #to be implemented - j_2 can now be either 1 or 2.

        Spins = {} #A dictionary for the spins in the system.
        Electrons should
        #go first, then nuclei, so that the indexing is definitely correct.
        """
        The Pentagon:
        """
        #Spins['ES1'] =  Particle(j_2list[0], 1, 'e', [0, 0, 0])
        #Spins['ES2'] =  Particle(j_2list[1], 2, 'e', [2 * r, 0, 0])
        #Spins['ES3'] =  Particle(j_2list[2], 3, 'e', [(2 * r) - (r/2) *
        (1 - np.sqrt(5)), 2 * r * np.sqrt((5/8) + (np.sqrt(5))/8), 0])
        #Spins['ES4'] =  Particle(j_2list[3], 4, 'e',
        [r, r * np.sqrt(5 + (2 * np.sqrt(5))), 0])
        #Spins['ES5'] =  Particle(j_2list[4], 5, 'e', [(r/2) *
        (1 - np.sqrt(5)), 2 * r * np.sqrt(5/8 + np.sqrt(5)/8), 0])
```

```
"""
6-spin planar card-tower case:
"""

#Spins['ES1'] =  Particle(j_2list[0], 1, 'e', [0, 0, 0])
#Spins['ES2'] =  Particle(j_2list[1], 2, 'e', [2 * r, 0, 0])
#Spins['ES3'] =  Particle(j_2list[2], 3, 'e', [4 * r, 0, 0])
#Spins['ES4'] =  Particle(j_2list[3], 4, 'e', [r, r * np.sqrt(3), 0])
#Spins['ES5'] =  Particle(j_2list[4], 5, 'e', [3 * r, r * np.sqrt(3), 0])
#Spins['ES6'] =
Particle(j_2list[5], 6, 'e', [2* r, 2 * r * np.sqrt(3), 0])

"""
Hexagonal case:
"""
#Spins['ES1'] =
Particle(j_2list[0], 1, 'e', [0, 0, 0])
#Spins['ES2'] =
Particle(j_2list[1], 2, 'e', [2 * r, 0, 0])
#Spins['ES3'] =
Particle(j_2list[2], 3, 'e', [3 * r, r * np.sqrt(3), 0])
#Spins['ES4'] =
Particle(j_2list[3], 4, 'e', [2 * r, 2 * r * np.sqrt(3), 0])
#Spins['ES5'] =
Particle(j_2list[4], 5, 'e', [0, 2* r * np.sqrt(3), 0])
#Spins['ES6'] =
Particle(j_2list[5], 6, 'e', [-r, r * np.sqrt(3), 0])

"""
6-spin Crystal (Octahedron):
```

```
"""

#Spins['ES1'] =
Particle(j_2list[0], 1, 'e', [0, 0, 0])
#Spins['ES2'] =
Particle(j_2list[1], 2, 'e', [2 * r, 0, 0])
#Spins['ES3'] =
Particle(j_2list[2], 3, 'e', [0, 2 * r, 0])
#Spins['ES4'] =
Particle(j_2list[3], 4, 'e', [2 * r, 2 * r, 0])
#Spins['ES5'] =
Particle(j_2list[4], 5, 'e', [r, r * np.sqrt(2), r * np.sqrt(2)])
#Spins['ES6'] =
Particle(j_2list[5], 6, 'e', [r, r * np.sqrt(2), -r * np.sqrt(3)])

"""
Square-based pyramid (SBP) case:
"""

#Spins['ES1'] =
Particle(j_2list[0], 1, 'e', [0, 0, 0])
#Spins['ES2'] =
Particle(j_2list[1], 2, 'e', [2 * r, 0, 0])
#Spins['ES3'] =
Particle(j_2list[2], 3, 'e', [0, 2 * r, 0])
#Spins['ES4'] =
Particle(j_2list[3], 4, 'e', [2 * r, 2 * r, 0])
#Spins['ES5'] =
Particle(j_2list[4], 5, 'e', [r, r * np.sqrt(2), r * np.sqrt(2)])
"""
```

```
True Diamond (i.e. 5-spins in 3D) case:
"""

#Spins['ES1'] =
Particle(j_2list[0], 1, 'e', [0, 0, 0])
#Spins['ES2'] =
Particle(j_2list[1], 2, 'e', [2 * r, 0, 0])
#Spins['ES3'] =
Particle(j_2list[2], 3, 'e',
[r, r * np.sqrt(3), 0])
#Spins['ES4'] =
Particle(j_2list[3], 4, 'e',
[r, r * np.sqrt(3)/3, (2/3) * r * np.sqrt(2)])
#Spins['ES5'] =
Particle(j_2list[4], 5, 'e',
[r, r * np.sqrt(3)/3, -(2/3) * r * np.sqrt(2)])

"""
Planar Diamond case:
"""
#Spins['ES1'] =
Particle(j_2list[0], 1, 'e', [0, 0, 0])
#Spins['ES2'] =
Particle(j_2list[1], 2, 'e', [2 * r, 0, 0])
#Spins['ES3'] =
Particle(j_2list[2], 3, 'e', [r, r * np.sqrt(3), 0])
#Spins['ES4'] =
Particle(j_2list[3], 4, 'e', [r, -r * np.sqrt(3), 0])
"""
Tetrahedral case:
```

```
"""
#Beware integer division if using this in python2.

#Spins['ES1'] =
Particle(j_2list[0], 1, 'e', [0, 0, 0])
#Spins['ES2'] =
Particle(j_2list[1], 2, 'e', [2 * r, 0, 0])
#Spins['ES3'] =
Particle(j_2list[2], 3, 'e',
[r, r * np.sqrt(3), 0])
#Spins['ES4'] =
Particle(j_2list[3], 4, 'e',
[r, r * np.sqrt(3)/3, (2/3) * r * np.sqrt(2)])

"""
Square case:
"""

#Spins['ES1'] =
Particle(j_2list[0], 1, 'e', [0, 0, 0])
#Spins['ES2'] =
Particle(j_2list[1], 2, 'e', [2 * r, 0, 0])
#Spins['ES3'] =
Particle(j_2list[2], 3, 'e', [0, 2 * r, 0])
#Spins['ES4'] =
Particle(j_2list[3], 4, 'e', [2 * r, 2 * r, 0])

"""
Equilateral triangle case:
"""
```

```
#Spins['ES1'] =
Particle(j_2list[0], 1, 'e', [0, 0, 0])
#Spins['ES2'] =
Particle(j_2list[1], 2, 'e', [2 * r, 0, 0])
#Spins['ES3'] =
Particle(j_2list[2], 3, 'e', [r, r * np.sqrt(3), 0])
#Spins['NS1'] =
Particle(j_2list[3], 1, 'n', [0, 0, 2 * r])
"""
Almost Square case:
"""

#Spins['ES1'] =
Particle(j_2list[0], 1, 'e', [0, 0, 0])
#Spins['ES2'] =
Particle(j_2list[1], 2, 'e', [2.1 * r, 0, 0])
#Spins['ES3'] =
Particle(j_2list[2], 3, 'e', [0, 2 * r, 0])
#Spins['ES4'] =
Particle(j_2list[3], 4, 'e', [2 * r, 2 * r, 0])

"""
UnEquilateral triangle case:
"""
#Spins['ES1'] =
Particle(j_2list[0], 1, 'e', [0, 0, 0])
#Spins['ES2'] =
Particle(j_2list[1], 2, 'e', [2 * r, 0, 0])
#Spins['ES3'] =
Particle(j_2list[2], 3, 'e', [r, r * np.sqrt(4), 0])
```

```
        #Spins['NS1'] =
        Particle(j_2list[3], 4, 'n', [0, 0, 2 * r])

        """
        This code is for the (special) linear case:
        """
        for i in range(Electrons):
             Spins['ES%d' % (i + 1)] =
             Particle(1, i+1, 'e', [2 * i * r, 0, 0])

        #for i in range(Nuclei): #Check this for j2_list usage.
        #     Spins['NS%d' % (i + 1)] =
        Particle(j2_list[i + Electrons], i+1+Electrons, 'n',
        [2 * i * r, 2 * r, 0])

        return Spins

def Interaction(Spins, J0, beta, r, a_iso, Partners):
    dipolar_constant = -4*np.pi*1e-7 *
    (2.0023193043617 * 9.27400968e-24)**2
    /(4*np.pi*1e-30)/6.62606957e-34/1e6 #MHz * A^3
    dcon_MHz = dipolar_constant/((norm(np.array(Spins['ES1'].position)
    - np.array(Spins['ES2'].position)))**3)
    Friends = Interactions()
    Friends.Dipolar_Data(Spins)
    Friends.Exchange_Data(Spins, J0, dcon_MHz, beta, r, Electrons)
    Friends.Hyperfine_Data(Spins, Partners, a_iso)
    return Friends

def ND_ops(Electrons, Nuclei, j2_list):
```

```
    #Sets up the spin operators.
    #j_2 list is the list of j_2 values corresponding to the sysm spins.
    ND = {}
    total_spins = Electrons + Nuclei
    for spin_number in range(total_spins):
       temp = SpinOp(j2_list[spin_number]) #Sets the dimension of the operator.
       temp.Spawn(spin_number+1, j2_list, total_spins) #Sets up the operator.
       ND["S%s" % str(spin_number+1)] = temp

    for counter in range(Electrons-1):
       counter+=1
       counter2=counter+1
       while counter2<=Electrons:
          temp2 = SpinOpDP(j2_list[counter])
          temp2.DPSpawn([counter, counter2], j2_list, total_spins)
          ND['S%sdotS%s' % (str(counter), str(counter2))] = temp2
          counter2+=1

    return ND

def Recom(Spins, kS0, kSc, beta, r, Friends, ND, Electrons, SystemSize):
    Friends.Recombination_Data(Spins, kS0, kSc, beta, r, Electrons)
    for RecDat in Friends.RecomS:
        temp3 = RecOp(SystemSize-1)
        #This is only for Electrons, so j_2 hard-coded to 1.
        temp3.RecSpawn(Spins, Friends.RecomS[RecDat], ND)
        ND['k_%s%s' % (str(Friends.RecomS[RecDat][0]),
        str(Friends.RecomS[RecDat][1]))] = temp3

    return Friends, ND
```

9.14.2 Main function

```
from numpy.linalg import norm
from Sensible_Scratch import Engine
from Sensible_Scratch import Geometry
from Sensible_Scratch import ND_ops
from Sensible_Scratch import Interactions
from Sensible_Scratch import Recom
import numpy as np
from Sensible_Scratch import Hamiltonian
import copy
from joblib import Parallel, delayed
import multiprocessing
import os

"""
This function is for the linear spin chain - specifically the uneven case.
Feed it the spins as set up from the class file, which one you want moved
(it expects just an integer) and how far in the x-direction as a function of
r. To move in the y-direction rather than x, change the option to True.
"""

def uneven_chain(Spinlist, WhichOne, HowFar, r, ymove = False):

    if ymove == True:
        Spinlist['ES%d' % WhichOne].position =
        Spinlist['ES%d' % WhichOne].position + np.asarray([0, r * HowFar, 0])
        print(Spinlist['ES%d' % WhichOne].position)
        return
```

```
    elif WhichOne == 1 or WhichOne == 2:
        print('Unable to move spins 1 and 2, due to the D_12 metric.')
        exit()


    else:
        for i in range(1, WhichOne):
            print(Spinlist['ES%d' % i].position)
        for i in range(WhichOne,len(Spinlist)+1):
            Spinlist['ES%d' % i].position =
            Spinlist['ES%d' % i].position + np.asarray([r * HowFar, 0, 0])
            print(Spinlist['ES%d' % i].position)
        return


_eps_ = 2.2204460492503131e-16

Outfile_Stem = '041119_3Spin_LinearChain_Uneven_Spin1move_0p1r'
#The name of the file to which the simulation results will be saved.
#The naming system I use is a base stem (e.g. 'SpinChain_Targeted') and then in the
#parallel loop append the target pair to the end (cont.'SpinChain_Targeted_12').
a_i = 0 #The isotropic hyperfine coupling constant. Anisotropy not implemented yet.
r = 7.5  #The assumed radius of a radical, in Angstroms.
beta = 1.4 #The decay parameter that goes into all exponentials used.
kS0 = 0.005 #Singlet recombination rate constant, in inverse ns.
kSc = 0.001 #Scavenging rate constant, AKA lifetime.
J0 = -1 #NEW: this should be multiplied by
something NON-POSITIVE to be relevant to LP.
Isotropic exchange coupling strength.
```

```
_Test_Ang_Freq_ =  0.176085970872945  #Dimensional conversion factor.

B0 = np.append(0, np.logspace(-3, 3, 1000))  #Values here in mT.

B0 = _Test_Ang_Freq_* B0  #And now they're in rad/ns (I think).
num_cores = multiprocessing.cpu_count()
Electrons = 3 #Number of electrons in the system.
Nuclei = 0  #Number of nuclei in the system.
Hyperfine_Pairs = [] #Which electrons and nuclei hyperfine interact.
Targeted_Recom_Pairs = [['All']]#, [2,3]], [3,4]],
[4,5], [5,6], [6,7], [7,8]] #Default is all on,
but this specifies pairs of sites that are allowed to recombine
for specific use-cases.

mask = ['D']  #Sets the parts of the Hamiltonian that will be calculated.
#Options: 'H' : Hyperfine, 'D': Dipolar, 'E': Exchange, 'Z': Zeeman (assumed).
#Order not important.

nuclear_j2vals = []
#A list of the j2-values of any coupled nuclei in the system.
#This is a separate parameter, because we now allow spin-1.
#Acceptable entries here are 1 and 2.
j2_list = []
for i in range(Electrons):
    j2_list.append(1)
for j in range(Nuclei):
    j2_list.append(nuclear_j2vals[j])
print(j2_list)
SystemSize = 0
for j2 in j2_list:
```

```
    if SystemSize == 0:
        SystemSize = j2 + 1
    else:
        SystemSize *= (j2 +1)
print('Side length of Hamiltonian should be: %d' % SystemSize)

class Data(object):
    def __init__(self):
        self.Field_SYield = []
    def Add_Result(self, J, B, Answer):
        self.Field_SYield.append([J, B, Answer[0]])

def Abbatoir(J, Ham, Rec, H_Base, E_spins, Electrons,
Nuclei, B0, ND, Results, Outfile_Stem, SS=None, Target=None):
    Clone = copy.deepcopy(Ham)
    Data_Clone = copy.deepcopy(Results)
    #print(Outfile_Name)
    H_total = H_Base
    Outfile_Name = Outfile_Stem + "J_%s_d12units" % J


    for B in B0:

        Clone.Zeeman(E_spins, Electrons, Nuclei, B, ND)
        H_total = np.add(H_Base, Clone.Faces['Z'])

        Answer, Evals = Engine.CalcYield(H_total, [Rec[0],
        Rec[1]], Electrons, Nuclei, SystemSize, ND, Starting_Singlet=SS,Targeted_Yi
        Data_Clone.Add_Result(J, B, Answer)
        File_Format = np.array([J, B])
```

```
        File_Format = np.append(File_Format, Evals)

    np.savetxt("%s.csv" % Outfile_Name,
    Data_Clone.Field_SYield, delimiter=",")



def Interaction(Spins, beta, r, a_iso, Partners):
    dipolar_constant = -4*np.pi*1e-7 * (2.0023193043617 *
    9.27400968e-24)**2 /(4*np.pi*1e-30)/6.62606957e-34/1e6 #MHz * A^3
    dcon_MHz = dipolar_constant/((norm(np.array(Spins['ES1'].position)
    - np.array(Spins['ES2'].position)))**3)
    Friends = Interactions()
    Friends.Dipolar_Data(Spins, Electrons)
    #Friends.Exchange_Data(E_spins, J0, dcon_MHz, beta, r)
    Friends.Hyperfine_Data(Spins, Partners, a_iso)

    return Friends



Spins = Geometry(r, Electrons, Nuclei, j2_list)

uneven_chain(Spins, 3, 0.1, r)

Friends = Interaction(Spins, beta, r, a_iso=a_i,
Partners=Hyperfine_Pairs)
ND = ND_ops(Electrons, Nuclei, j2_list)
Friends, ND = Recom(Spins, kS0, kSc, beta, r,
Friends, ND, Electrons, SystemSize)
```

```
Ham = Hamiltonian(SystemSize-1)
#The -1 is just to make the size consistent
#with how the operator class is currently set up.


Ham.Jester(mask)


if 'D' in Ham.Mask:
    Ham.Dipolar([Spins, Friends.dipolar], SystemSize, ND)

if 'H' in Ham.Mask:
    Ham.Hyperfine([Spins, Friends.hyperfine], Electrons,
    Nuclei, SystemSize, ND)



H_Base = []
for face in Ham.Mask:
    if H_Base == []:
        H_Base = Ham.Faces[face]
    else:
        if face in Ham.Faces:
            H_Base = np.add(H_Base, Ham.Faces[face])



BYield_Array = []
Jset = np.arange(-3, 3.01, 0.01)
dipolar_constant = -4*np.pi*1e-7 * (2.0023193043617
```

```
* 9.27400968e-24)**2 /(4*np.pi*1e-30)/6.62606957e-34/1e6 #MHz * A^3
dcon_MHz = dipolar_constant/((norm(np.array(Spins['ES1'].position)
- np.array(Spins['ES2'].position)))**3)
for J in Jset:
    print(J)
    ExtraClone = copy.deepcopy(Ham)
    Friends.Exchange_Data(Spins, J, dcon_MHz, beta, r, Electrons)
    ExtraClone.Exchange([Spins, Friends.exchange], SystemSize, ND)
    H_Base_Jvar = np.add(H_Base, ExtraClone.Faces['E'])
    Results = Data()
    Abbatoir(J, Ham, [Friends.RecomS, Friends.Scav],
    H_Base_Jvar, Spins, Electrons, Nuclei, B0, ND, Results, Outfile_Stem)
```

9.14.3 Absolute MFE measure used in Chapter 5

```
from Plot_BvarMFE import ReorderColumns
import matplotlib.pyplot as plt
import pandas as pd
import numpy as np
import scipy

"""
This integral measure is designed to average over the J-dependence of the
heatplots we made and show that, for the subtraction dataframe calculated
between a distorted geometry and its perfect counterpart
"""

def MakeNewOrder(MFE_df):
```

```
    cols = MFE_df.columns.tolist()
    cols = np.sort(cols)
    #print(cols)
    #print(df)
    negatives = []
    positives = []
    for col in cols:
        #col = col.split('_')[0]
        if float(col) < 0:
            negatives.append(col)
        else:
            positives.append(col)
    neworder = []
    for i in range(len(negatives)):
        neworder.append(negatives[len(negatives) - i - 1])
    for i in range(len(positives)):
        neworder.append(positives[i])



    return neworder


#The second name in names is the J-value corresponding to a column of singlet yield
def Make_MFEdf():
    counter = 0
    for File in os.listdir():
        if File.endswith('.csv'):
            with open(File, 'r') as data:
                #headers = ['J', 'Field', 'Singlet_Yield']
                if counter == 0:
                    MFE_df = pd.read_csv(File,
```

```
                names=['Field', '%s' % File.split('_')[-2]],
                usecols=[1, 2])
                MFE_df = MFE_df.set_index('Field')
                counter += 1
            else:
                newcol = pd.read_csv(File,
                names=['Field', '%s' % File.split('_')[-2]],
                usecols=[1, 2])
                newcol = newcol.set_index('Field')
                MFE_df.insert(len(MFE_df.columns),
                '%s' % File.split('_')[-2], newcol)
                counter += 1


neworder = MakeNewOrder(MFE_df)
MFE_df = ReorderColumns(MFE_df, neworder)

counter2 = 0
#print(df)
for column in MFE_df.columns:
    newcol = (MFE_df.loc[0:, column]
    - MFE_df.loc[0, column])/MFE_df.loc[0, column]
    if counter2 == 0:
        ActualMFEs = pd.DataFrame(newcol)
        #print(MFEdf)
        counter2 += 1
    else:
        ActualMFEs.insert(len(ActualMFEs.columns),
        column, newcol)
```

```
    #print(ActualMFEs.head())
    return ActualMFEs


#Plot the subtraction df to make sure it looks like
the difference of two heatplots.
def Sanity_Check(MFEdf, Title):
    fig = plt.figure('%s' % Title)
    maxMFE = []
    minMFE = []

    min_five_percent = [0,0,0,0]
    for column in MFEdf.columns:
        #print(column)
        #print(MFEdf)
        maxMFE.append(np.max(MFEdf.loc[0:, column]))
        minMFE.append(np.min(MFEdf.loc[0:, column]))

    actualmax = np.max(maxMFE)
    actualmin = np.min(minMFE)
    limit = np.max([actualmax, np.absolute(actualmin)])
    h = plt.pcolor(MFEdf, cmap='RdBu', vmin=-0.15, vmax=0.15)
    plt.xlabel('J (d_12 units)')
    plt.ylabel('B (mT)')
    plt.title(Title)
    cbar = fig.colorbar(h)
    cbar.ax.set_ylabel('MFE')
    #print(MFEdf.index)
    plt.xticks(np.arange(0, len(MFEdf.columns), step=100),
    MFEdf.columns[0::100])
```

```
    #['{:.4f}'.format(x) for x in
    MFEdf.index[0::167]/0.176085970872945])
    #plt.yticks(10**np.logspace(-3, 3, 7))
    #plt.yscale('log')

    path = '[PATH REDACTED]'
    plt.savefig(path + Title + '.png', format='png')

    plt.show()


def MFE_Measure(Subtraction, title):
    fields = []
    measures = []
    for row in Subtraction.itertuples():
        fields.append(row[0]/0.176085970872945)
        M = scipy.integrate.simps(row[1:])
        measures.append(M)
    return fields, measures


if __name__ == '__main__':
    import sys
    import os
    #dirs = []
    title = sys.argv[1]
    #dirs.append(sys.argv[2:])

    dirs = [PERSONAL DIRECTORIES REDACTED]
    MFEdf_dict = {}
```

```
for dir in dirs:
    os.chdir(dir)  #Make sure it is a filepath,
    rather than pardir() - it's just easier.
    #Second argument none because the zero case
    has already been handled for the data.
    MFEdf_dict['{}'.format(dir.split('/')[-1])]
    = Make_MFEdf()
    #MFEdf_dict['%s' % dir.split('/')[-1]]
    = HeatPlot('MFE_plot_%s' % dir.split('/')[-1], None)
#print(MFEdf_dict.keys())
"""
for i in range(len(MFEdf_dict['3_Spin'].columns)):

    column1 = MFEdf_dict['Spin3Move0p1r'].columns[i]
    column2 = MFEdf_dict['3_Spin'].columns[i]
    column3 = MFEdf_dict['Spin2Move'].columns[i]

    col1 = MFEdf_dict['Spin3Move0p1r'].loc[:,
    column1].abs() - MFEdf_dict['3_Spin'].loc[:, column2].abs()
    col2 = MFEdf_dict['Spin2Move'].loc[:,
    column3].abs() - MFEdf_dict['3_Spin'].loc[:, column2].abs()
    colname1 = column1
    colname2 = column3

    if i == 0:
        subtraction1 = pd.DataFrame(col1)
        subtraction2 = pd.DataFrame(col2)
    else:
        subtraction1.insert(len(subtraction1.columns),
        colname1, col1)
```

```
        subtraction2.insert(len(subtraction2.columns),
        colname2, col2)
 """

Sanity_Check(MFEdf_dict['4_Spin'], '4_Spin')
Sanity_Check(MFEdf_dict['Spin4Move'], 'Spin4Move')
Sanity_Check(MFEdf_dict['Spin3Move'], 'Spin3Move')
#fields, s2move = MFE_Measure(subtraction1, 's2move')
#fields, s3move = MFE_Measure(subtraction2, 's3move')
#The MFEdf here is the new_measure_to_be df,
from the subtraction above.



"""
plt.semilogx(fields, s2move, label='Spin3Move0p1r')
plt.semilogx(fields, s3move, label='Spin2Move')
plt.legend()
plt.xlabel('B (mT)')
plt.ylabel('MFE measure')
path = ''
plt.savefig(path + title + '.pdf', format='pdf')
plt.show()
"""
```

9.14.4 Primary plotting function for MFE profiles

```
"""
Arguments expected: A file stem for the output template, and a graph title stem.
By file stem, I mean something like 22719_Linear_3Spin_BfixedEarth_Jvar_
```

```
which is descriptive of the simulation and should be present in all files of
a given simulation.
And by title stem, I mean something similar but that can apply to the graph(s)
that this will produce:
- The position (in terms of Jvalues) of the maximum MFE as a function of field.
- As above, but the minimum MFE.
- The MFE profile as a function of the exchange for a given field.

If you feed it just two files, the MFE profile will run.
If you feed it a set of files, it will run the other two comparative cases.
"""

import matplotlib.pyplot as plt
import pandas as pd
import numpy as np
import seaborn as sns

#Takes an array of csv files, and some labels, then makes a graph.


def Makedf(Files):  #Creates a DataFrame from a bunch of files for processing.
    counter = 0
    for File in Files:
        with open(File,'r') as data:
            if counter == 0:
                headers = ['J', 'Field', 'Zero Yield']
                df = pd.read_csv(File, names=headers)

                counter += 1
                #df = ReorderColumns(df, ['Field', 'J', 'Singlet_Yield'])
```

```
            else:
                pass




    return df




def Profile(df, x_axis, y_axis, Title):



    MFEs = []
    for i in range(len(df)):
        mfe = (df.loc[i, "Singlet Yield"]
        - df.loc[i, "Zero Yield"]) / df.loc[i, "Zero Yield"]
        MFEs.append(mfe)
    fig = plt.figure('%s_MFEs' % Title)


    plt.plot(df.loc[0:, 'J'], MFEs)
    plt.xlabel(x_axis)
    plt.ylabel(y_axis)
    plt.title(Title + "_MFEprofile")
    plt.legend()
    plt.show()
```

```
def ReorderColumns(df, column_order):
#Feed me a DataFrame and an array containing
#the names of the columns in the order you want them.
    df = df[column_order]
    return df


def HeatPlot(Title, stem): #The graph title you want, that is.
    Files = []
    import os
    """
    This section has been commented for use in integral measure.
    if (stem + "J_0.0_d12units.csv") in os.listdir():
        Files.append(stem + "J_0.0_d12units.csv")


    else:
        print("You're going to get an error.
        Problem: a lack of a zero file.")
    print(stem + "J_0.0_d12units.csv")
    """
    for File in os.listdir():
        """
        if File == Files[0]:
            pass
        else:
            Files.append(File)
        """
        Files.append(File)
    df = Makedf(Files)
    df = df.drop('J', axis=1)
    df = df.set_index('Field')
```

```
cols = df.columns.tolist()
cols = np.sort(cols)

negatives = []
positives = []
for col in cols:
    #col = col.split('_')[0]
    if float(col) < 0:
        negatives.append(col)
    else:
        positives.append(col)
neworder = []
for i in range(len(negatives)):
    neworder.append(negatives[len(negatives) - i - 1])
for i in range(len(positives)):
    neworder.append(positives[i])

df = ReorderColumns(df, neworder)
counter2 = 0

for column in df.columns:
    newcol = (df.loc[0:, column] - df.loc[0, column])/df.loc[0, column]

    if counter2 == 0:
        MFEdf = pd.DataFrame(newcol)
        #print(MFEdf)
        counter2 += 1
    else:
        MFEdf.insert(len(MFEdf.columns), column, newcol)
        #print(MFEdf)
```

```
    fig = plt.figure('%s' % Title)
    maxMFE = []
    minMFE = []
    for column in MFEdf.columns:

        maxMFE.append(np.max(MFEdf.loc[0:, column]))
        minMFE.append(np.min(MFEdf.loc[0:, column]))
    actualmax = np.max(maxMFE)
    actualmin = np.min(minMFE)
    limit = np.max([actualmax, np.absolute(actualmin)])
    h = plt.pcolor(MFEdf, cmap='RdBu', vmin=-limit, vmax=limit)
    plt.xlabel('J (d_12 units)')
    plt.ylabel('B (mT)')
    plt.title(Title)
    cbar = fig.colorbar(h)
    cbar.ax.set_ylabel('MFE')

    plt.xticks(np.arange(0, len(MFEdf.columns), step=100),
    df.columns[0::100])
    plt.yticks(np.arange(0, len(MFEdf.index), step=125),
    ['{:.4f}'.format(x) for x in MFEdf.index[0::125]/0.176085970872945])
    plt.show()

    return MFEdf

#Plot MFEs across a spectrum of J-values
for a multitude of fields on the same graph.
#Changes into each dir in dirs to look for files to use.
#Expects pathways to folders containing MFE
```

```
data that needs to be on the same graph.
def MultiProfile(dirs, Title):
    for dir in dirs:
        os.chdir(dir)
        aSortMe = []
        bSortMe = []
        cSortMe = []
        for file in os.listdir():

            with open(file, 'r') as File:
                Jval = float(file.split('_')[-2])
                #The J-value of relevance
                counter = 0
                for line in File:
                    if counter == 0:
                        zeroval = float(line.split(',')[2])
                        counter +=1

                    #elif re.search('8.81910383420236852e-03',line):
                        #aTargetVal = float(line.split(',')[2])
                        #FiftyuTmfe = (aTargetVal - zeroval)  /  zeroval

                    #elif re.search('8.80296345656722712e-02',line):
                    #    bTargetVal = float(line.split(',')[2])
                    #    Zp5mTmfe = (bTargetVal - zeroval)  /  zeroval

                    elif re.search('8.81910383420237309e-01',line):
                        cTargetVal = float(line.split(',')[2])
                        FivemTmfe = (cTargetVal - zeroval)  /  zeroval
```

```
        #aSortMe.append((FiftyuTmfe, Jval))
        #bSortMe.append((Zp5mTmfe, Jval))
        cSortMe.append((FivemTmfe, Jval))
    #aSortMe.sort(key=lambda x:x[1])
    #bSortMe.sort(key=lambda x:x[1])
    cSortMe.sort(key=lambda x:x[1])
    FiftyuT_MFEs = []
    Zp5mT_MFEs = []
    FivemT_MFEs = []
    Jvals = []
    #for item in aSortMe:
    #    FiftyuT_MFEs.append(item[0])

    for item in cSortMe:
        FivemT_MFEs.append(item[0])
        Jvals.append(item[1])
    #for item in bSortMe:
    #    Zp5mT_MFEs.append(item[0])

    labelstem = dir.split('/')[-1]
    alabel = labelstem + '50uT'
    blabel = labelstem + '0p5mT'
    clabel = labelstem + '5mT'
    #plt.plot(Jvals, FiftyuT_MFEs, label=alabel)
    plt.plot(Jvals, FivemT_MFEs, label=clabel)
    #plt.plot(Jvals, FivemT_MFEs, label=clabel)
plt.xlabel('J_d12Units')
plt.ylabel('MFE')
plt.legend()
plt.title(Title)
```

```
    plt.show()
#This function now reproduces the graphs as in the paper.


if __name__ == '__main__':
    import sys
    import os
    import re

    stem = sys.argv[1]  #This should be the Outfile_Stem from the run file.
    Title = sys.argv[2]
    Order = sys.argv[3]
    Location = sys.argv[4] #Target directory
    dirs = [Location]
    if Order == 'heat' or Order == 'Heat':
        HeatPlot(Title, stem)

    elif Order == 'Profile':
        Files = []
        for item in sys.argv[4:]:
            Files.append(item)
        df = Makedf(Files)
        Profile(df, 'J', 'MFE', Title)

    elif Order == 'FixB':
        Files = []
        for item in sys.argv[4:]:
            Files.append(item)
        df = Makedf(Files)

    else:
```

```
        MultiProfile(dirs, Title)
```

9.14.5 Hamiltonian Components

Hyperfine

```
"""
The overall purpose of this function is to
calculate the hyperfine contribution
to the Hamiltonian and return it,
in matrix form, to main for processing.
"""


import numpy as np
import SXS_Dense
from Die_KeyError_Die import KeyBlade

_eps_ = 2.2204460492503131e-16

def HFInt(SysData, Electrons, Nuclears, SystemSize, ND):
    if not(SysData):
        print("Error - please provide coupling data.")
        exit(-1)
    #print(SysData)
    idxpairs = []
    j_2vals = [-1]
    #newDict = {**SysData[0], **SysData[1]}
    for item in SysData[0]:
        print(item)
```

```
    print(SysData[0]['%s' % item].index)
        #if not(item[0] == 'N'):
        Nuclear exchange interaction to be neglected.
    if j_2vals[0] == -1:
        j_2vals[0] = SysData[0]['%s' % item].j2
        #This uses nuclear J - assume e- is always 1.
    else:
        j_2vals = np.insert(j_2vals,
        len(j_2vals), SysData[0]['%s' % item].j2)


counter = 0
XcomParts = {}
for item in SysData[1]:
    counter += 1
    NameEnding = '%d' % counter
    Name = 'Part' + NameEnding

    XcomParts[Name] = SysData[1]['%s' % item]#.reshape(3,3)



for i in range(Nuclears):
#Currently assumes ESi interacts with NSi.
    if idxpairs == []:

        idxpairs = np.array([SysData[0]['ES%s' %
        (i + 1)].index, SysData[0]['NS%s' % (i + 1)].index])

    else:
        #key = list(SysData[1]['%s' % nucleus].index)
        idxpairs = np.append(idxpairs, np.array([SysData[0]
```

```
            ['ES%s' % (i + 1)].index, SysData[0]
            ['NS%s' % (i + 1)].index]))
        idxpairs = idxpairs.reshape(int(len(idxpairs)/2), 2)
        print(idxpairs)
        print(j_2vals)
        #print(XcomParts)
    H_hyp = SXS_Dense.SXSTensorProd(XcomParts, j_2vals,
    idxpairs, SystemSize, ND)
    for i in range(SystemSize):
        for j in range(SystemSize):
            if np.absolute(H_hyp[i][j]) > _eps_:
                print(i, j, H_hyp[i][j])
    return H_hyp
```

Zeeman

```
"""
The overall purpose here is to set up the Zeeman
part of the Hamiltonian.
Assumes isotropy of g-factor.

"""

import numpy as np
from scipy import sparse


def ZInt(SysData, Electrons, Nuclears, ND, Bx=0, By=0, Bz=0):
```

```
    Ziamat = []

    for spin in SysData:
        if 'e' in SysData['%s' % spin].type:
            for component in ['x', 'y', 'z']:
                FCom = eval("B%s" % component)
                Zcom = sparse.csr_matrix(-FCom *
                ND["S%d" % SysData['%s' % spin].index].
                components['%scom' % component])
                if Ziamat == []:
                    Ziamat = np.asfortranarray(Zcom.todense())
                else:
                    Ziamat = np.add(Ziamat,
                    np.asfortranarray(Zcom.todense()),
                    dtype=np.complex_)

            typevec = np.full((1,Electrons + Nuclears),'')
    return Ziamat
```

Dipolar

```
"""
User manual for ddInt_MKII:

The overall purpose of this function is
to calculate the Hamiltonian element
that corresponds to the electron-electron
magnetic dipolar interaction.
```

```
"""

import numpy as np
import SXS_Dense


_eps_ = 2.2204460492503131e-16

def ddInt_MKII(SysData, SystemSize, ND, IdxPairs=[]):
    if not(SysData):
        print("Error - please provide dipolar coupling data.")
        exit(-1)

    idxpairs = []
    j_2vals = [-1]
    for item in SysData[0]:
        if j_2vals[0] == -1:
            j_2vals[0] = SysData[0]['%s' % item].j2
        else:
            j_2vals = np.insert(j_2vals, len(j_2vals),
            SysData[0]['%s' % item].j2)

    counter = 0
    XcomParts = {} #As in, components of the matrix
    X in the SXS tensor product.
    for item in SysData[1]:
        counter += 1
        NameEnding = '%d' % counter
        Name = 'Part' + NameEnding
```

```
        XcomParts[Name] = SysData[1]['%s' % item].reshape(3,3)
        if IdxPairs == []:
            if idxpairs == []:
                idxpairs = np.array([int(item[2]),
                int(item[3])])
            else:
                idxpairs = np.append(idxpairs,[int(item[2]),
                int(item[3])])
            idxpairs = idxpairs.reshape(int(len(idxpairs)/2), 2)
        else:
            idxpairs = IdxPairs
    H_dd = SXS_Dense.SXSTensorProd(XcomParts, j_2vals,
    idxpairs, SystemSize, ND)
    return H_dd
```

Exchange

```
"""

Calculates the exchange interaction Hamiltonian, given system data.
"""

import numpy as np
from scipy import sparse
from OpDotProd_Dense import opdotprod


def ExInt_MKII(SysData, SystemSize, ND):
```

```
if not(SysData):
    print("Error - please provide information about the spin system.")
    exit(-1)
j_2vals = [-1] #Sets the doubled quantum number to an unphysical default.
for item in SysData[0]:
    if j_2vals[0] == -1:
        j_2vals[0] = SysData[0]['%s' % item].j2
    else:
        j_2vals = np.insert(j_2vals, len(j_2vals), SysData[0]['%s' % item].j2)
Hex = [] #To become the exchange Hamiltonian matrix.
for item in SysData[1]:
    SysData[1]['%s' % item][0]
    if Hex == []:
        Hex = np.asfortranarray(SysData[1]['%s' % item][0] *
        (0.5 * np.asfortranarray(sparse.identity(SystemSize).todense())
        + 2* opdotprod([j_2vals[SysData[1]['%s' % item][1]-1],
        j_2vals[SysData[1]['%s' % item][2]-1]],
        [SysData[1]['%s' % item][1], SysData[1]['%s' % item][2]], ND)))

    else:
        Hex = Hex + np.asfortranarray(SysData[1]['%s' % item][0] *
        (0.5 * np.asfortranarray(sparse.identity(SystemSize).todense())
        + 2* opdotprod([j_2vals[SysData[1]['%s' % item][1]-1],
        j_2vals[SysData[1]['%s' % item][2]-1]],
        [SysData[1]['%s' % item][1], SysData[1]['%s' % item][2]], ND)))

return Hex
```

9.14.6 Utility Functions

```
#Calculate the point-dipole coupling
import numpy as np
from numpy.linalg import norm


def point_dipole_dipole_coupling(r):
   """Takes in a 3x1 vector (in list format)
   distance between 2 points
   and returns a 3x3 matrix for the dipolar
   coupling between the 2 points"""

   dipolar_constants = -4*np.pi*1e-7 * (2.0023193043617 *
   9.27400968e-24)**2 /(4*np.pi*1e-30)/6.62606957e-34/1e6

   if np.isscalar(r):
      dipolar_distance_constants = dipolar_constants/r**3
      dipolar_matrix = np.diag([-dipolar_distance_constants,
      - dipolar_distance_constants, 2*dipolar_distance_constants])
   else:
      norm_r = norm(r)
      dipolar_distance_constants = dipolar_constants/norm_r**3
      normalised_vector_r = (r / norm_r).reshape(3, 1)
      dipolar_matrix = dipolar_distance_constants *
      (3*np.kron(normalised_vector_r, normalised_vector_r.transpose())
      - np.identity(3))

   return dipolar_matrix

#Calculate composite spin operators
```

```
def calculateDoubleSpinOperator(spin_op, pos, j2_list, number_of_spins):
   """Takes in an array of spin operators (each being a character),
   an array of positions and the total number of spins
   returns the correctly set up spin operator"""

   op = {}
   posit = {}

   for counter in range(len(spin_op)):
       if j2_list[pos[counter]] == 1:
           op["op%d" % counter] = SpinOp(spin_op[counter])
       elif j2_list[pos[counter]] == 2:
            op["op%d" % counter] = Spin1(spin_op[counter])
   I  = SpinOp('I')
   I3 = Spin1('I')

   for counter in range(len(pos)):
       posit["pos%d" % counter] = pos[counter]

   if len(posit)<2:
       posit["pos1"] = np.nan
   #print(posit)
   #print("Nan?")
   #print(np.isnan(posit["pos1"]))
   if posit["pos0"]==0 and posit["pos1"]==1:
      #print("case1")
      ops = np.kron(op["op0"], op["op1"])
   elif posit["pos0"]==0 and posit["pos1"]!=1:
      if not(np.isnan(posit["pos1"])) and
      j2_list[posit["pos1"]] == 2:
```

```
        #print("case2a")
        ops = np.kron(op["op0"], I3)
    elif not(np.isnan(posit["pos1"])) and
    j2_list[posit["pos1"]] == 1:
        #print("case2b")
        ops = np.kron(op["op0"], I)
    else:
        if j2_list[1] == 1:
            ops = np.kron(op["op0"], I)
        elif  j2_list[1] == 2:
            ops = np.kron(op["op0"], I3)

elif posit["pos0"]==1:
    if j2_list[posit["pos0"]] == 1:
        #print("case3a")
        ops = np.kron(I, op["op0"])
    elif j2_list[posit["pos0"]] == 2:
        #print("case3b")
        ops = np.kron(I3, op["op0"])
    else:
        print("Case3 failed.")
else:
    if not(np.isnan(posit["pos1"])):

        if j2_list[posit["pos0"]] == 1 and
        j2_list[posit["pos1"]] == 1:
            ops = np.kron(I, I)
        elif j2_list[posit["pos0"]] == 1 and
        j2_list[posit["pos1"]] == 2:
            ops = np.kron(I, I3)
```

```
        elif j2_list[posit["pos0"]] == 2 and
        j2_list[posit["pos1"]] == 1:
            ops = np.kron(I3, I)
        elif j2_list[posit["pos0"]] == 2 and
        j2_list[posit["pos1"]] == 2:
            ops = np.kron(I3, I3)
    else:
        if j2_list[0] == 1 and j2_list[1] == 1:
            ops = np.kron(I, I)
        elif j2_list[0] == 2 and j2_list[1] == 2:
            ops = np.kron(I3, I3)
        elif j2_list[0] == 1 and j2_list[1] == 2:
           ops = np.kron(I, I3)
        elif j2_list[0] == 2 and j2_list[1] == 1:
            ops = np.kron(I3, I)
        else:
            print("Something has gone horribly wrong.")
            exit()

#print("ops before the larger loop is:")
#print(ops)

if number_of_spins>2:
   #print("Spins: %d" % number_of_spins)
   #print(len(j2_list))
   counter=2
   #print(len(ops))
   while counter<number_of_spins:
      if posit["pos0"]==counter:
         ops = np.kron(ops, op["op0"])
```

```
            elif posit["pos1"]==counter:
                ops = np.kron(ops, op["op1"])
            else:
                if j2_list[counter] == 1:
                    ops = np.kron(ops, I)
                elif j2_list[counter] == 2:
                    ops = np.kron(ops, I3)
            #print(len(ops))
            counter+=1
    #print(spin_op)
    #print(ops)


    return ops

#Linear Algebra function for calculating yield

import numpy as np
from scipy import sparse
from scipy import linalg
import math
import Projectors_Dense
_eps_ = 2.2204460492503131e-16

def Yield(H, Sysdata, Electrons, Nuclears, Dimensions,
ND, Starting_Singlet, Targeted_Yield):
    K1_total = []
    #K2_total = []
    for k in Sysdata[0]:
        #print(k)
```

```
    if K1_total == []:
        K1_total = ND['%s' % k].matrix
        #print(k)
    else:
        K1_total = np.add(K1_total, ND['%s' % k].matrix)
        #print(k)


#K_ST = K1_total + K2_total
#Triplet recom (K2) is currently assumed nonpresent
- generalise at some point.
H_eff = H - (1j * K1_total) #+ ND['K2']))
Evecs = np.linalg.eig(H_eff)[1]
Evals = np.linalg.eig(H_eff)[0]
Lambda = np.asfortranarray(sparse.spdiags(Evals, 0,
Dimensions, Dimensions).todense())
Evec_Inverse = np.linalg.inv(Evecs)

if Starting_Singlet == None:
    rho_0 = np.reshape(np.matmul(Evec_Inverse,
    np.transpose(np.conj(Evec_Inverse))),
    (len(Evecs)**2, 1))
else:
    rho_0_soon = Evec_Inverse @ ND['k_%d%d' %
    (Starting_Singlet[0], Starting_Singlet[1])].matrix
    rho_0 = np.reshape(rho_0_soon @
    np.transpose(np.conj(Evec_Inverse)) ,
    (len(Evecs)**2, 1))
    #rho_0 = np.reshape(np.matmul(Evec_Inverse,
    np.transpose(np.conj(Evec_Inverse))),
```

```
    (len(Evecs)**2, 1))

G = np.full((len(Evals), len(Evals)), 0.0 + 0.0j)
for i in range(len(Evals)):
    for j in range(len(Evals)):
        testG = 1j *(Evals[i] - np.conj(Evals[j]))
        G[i][j] = testG
G = np.reshape(G, (len(Evecs)**2, 1)) + Sysdata[1][3]
LS_rhoS = np.divide(rho_0,G)
rho_S = np.reshape(LS_rhoS, (int(math.sqrt(len(LS_rhoS))),
int(math.sqrt(len(LS_rhoS)))))
temp = np.matmul(rho_S, np.conj(np.transpose(Evecs)))
rho_S = np.matmul(Evecs, temp)
yields = np.zeros(2)

if Targeted_Yield == None:
    yields[0] = 2 * np.sum(np.real(np.sum(np.multiply(
    K1_total, np.transpose(rho_S)))))
else:
    yields[0] = 2 * np.sum(np.real(np.sum(np.multiply(
    ND['k_%d%d' % (Targeted_Yield[0],
    Targeted_Yield[1])].matrix, np.transpose(rho_S)))))
#yields[1] = 2 * np.sum(np.real(np.sum(np.multiply(
K2_total, np.transpose(rho_S)))))
yields[1] = Sysdata[1][3] *
np.trace(np.real(rho_S))
yields = np.divide(yields, Dimensions)
#print("Yields: %s" % yields)

Maybe_Evals = []
```

```
    for i in range(len(Evals)):
        Maybe_Evals.append(np.real(rho_S[i][i]))
    #print(Maybe_Evals)
    return yields, Maybe_Evals

#Projectors

import numpy as np
from scipy import sparse


_eps_ = 2.2204460492503131e-16
def Singlet_Projector(j_2, idx, SysSize, ND):

    P_s = ((0.25 * np.asfortranarray(sparse.identity(SysSize).todense()))
    - ND["S%sdotS%s" % (str(idx[0]), str(idx[1]))].ZZ
    - 0.5 * ( ND["S%sdotS%s" % (str(idx[0]), str(idx[1]))].PlusMinus
    + ND["S%sdotS%s" % (str(idx[0]), str(idx[1]))].MinusPlus ))
    #print(P_s)
    return P_s

def Triplet_Projector(j_2, idx, SysSize, ND):

    P_t = (0.75 * np.asfortranarray(sparse.identity(SysSize).todense())
    + ND["S%sdotS%s" % (str(idx[0]), str(idx[1]))].ZZ
    + 0.5 * ( ND["S%sdotS%s" % (str(idx[0]), str(idx[1]))].PlusMinus
    + ND["S%sdotS%s" % (str(idx[0]), str(idx[1]))].MinusPlus ))

    return P_t
```

Bibliography

F. J. Adrian (1979). 'Principles of the radical pair mechanism of chemically induced nuclear and electron spin polarization'. In: *Res. Chem. Intermed.* 3, pp. 3–43 (Cited on page 79).

S. Akesson, J. Morin, R. Muheim and U. Ottosson (2001). 'Avian orientation at steep angles of inclination: experiments with migratory white-crowned sparrows at the magnetic North Pole'. In: *Proceedings of the Royal Society B-Biological Sciences* 268.1479, pp. 1907–1913 (Cited on page 8).

C. Atkins, K. Bajpai, J. Rumball and D. R. Kattnig (2019). 'On the optimal relative orientation of radicals in the cryptochrome magnetic compass'. In: *J. Chem. Phys.* 151.6, p. 065103 (Cited on page 185).

P. W. Atkins and R. S. Friedman (2011). *Molecular quantum mechanics*. Oxford university press (Cited on page 38).

N. S. Babcock and D. R. Kattnig (2020). 'Electron–Electron Dipolar Interaction Poses a Challenge to the Radical Pair Mechanism of Magnetoreception'. In: *J. Phys. Chem. Lett.* 11.7, pp. 2414–2421 (Cited on pages 29, 108 and 173).

A. J. Baldwin, T. P. Knowles, G. G. Tartaglia, A. W. Fitzpatrick, G. L. Devlin, S. L. Shammas, C. A. Waudby, M. F. Mossuto, S. Meehan, S. L. Gras et al. (2011). 'Metastability of native proteins and the phenomenon of amyloid formation'. In: *Journal of the American Chemical Society* 133.36, pp. 14160–14163 (Cited on page 22).

F. Barnes and B. Greenebaum (2018). 'Role of radical pairs and feedback in weak radio frequency field effects on biological systems'. In: *Environ. Res.* 163, pp. 165 –170 (Cited on pages 23 and 102).

D. Becker, T. La Vere and M. Sevilla (Nov. 1994). 'ESR Detection at 77 K of the Hydroxyl Radical in the Hydration Layer of Gamma-Irradiated DNA'. In: *Radiat. Res.* 140, pp. 123–9 (Cited on page 200).

V. I. Borovkov, I. S. Ivanishko, V. A. Bagryansky and Y. N. Molin (2013). 'Spin-Selective Reaction with a Third Radical Destroys Spin Correlation in the Surviving Radical Pairs'. In: *J. Phys. Chem. A* 117.8 (Cited on page 17).

A. Bradlaugh, A. L. Munro, A. R. Jones and R. A. Baines (2021). 'Exploiting the Fruit-fly, Drosophila melanogaster, to Identify the Molecular Basis of Cryptochrome-Dependent Magnetosensitivity'. In: *Quantum Reports* 3.1, pp. 127–136 (Cited on page 10).

C. A. Brasil, F. F. Fanchini and R. d. J. Napolitano (Mar. 2013). 'A simple derivation of the Lindblad equation'. en. In: *Revista Brasileira de Ensino de FÃsica* 35, pp. 01 –09. ISSN: 1806-1117. URL: `http://www.scielo.br/scielo.php?script=sci_arttext&pid=S1806-11172013000100003&nrm=iso` (Cited on page 30).

H.-P. Breuer, F. Petruccione et al. (2002). *The theory of open quantum systems*. Oxford University Press on Demand (Cited on pages 159, 163 and 184).

B. Brocklehurst (2002). 'Magnetic fields and radical reactions: recent developments and their role in nature'. In: *Chem. Soc. Rev.* 31.5, pp. 301–311 (Cited on pages 27, 28 and 159).

B. Brocklehurst and K. A. McLauchlan (1996). 'Free radical mechanism for the effects of environmental electromagnetic fields on biological systems'. In: *International journal of radiation biology* 69.1, pp. 3–24 (Cited on page 8).

J. C. Brookes (2017). 'Quantum effects in biology: golden rule in enzymes, olfaction, photosynthesis and magnetodetection'. In: *Proceedings of the Royal Society A: Mathematical, Physical and Engineering Sciences* 473.2201, p. 20160822 (Cited on page 1).

A. L. Buchachenko and V. L. Berdinsky (1996). 'Spin Catalysis of Chemical Reactions'. In: *J. Phys. Chem.* 100.47, pp. 18292–18299 (Cited on page 17).

A. L. Buchachenko and V. L. Berdinsky (2002). 'Electron Spin Catalysis'. In: *Chem. Rev.* 102.3, pp. 603–612 (Cited on page 16).

C. Y. Cai, Q. Ai, H. T. Quan and C. P. Sun (2012). 'Sensitive chemical compass assisted by quantum criticality'. In: *Phys. Rev. A* 85 (2), p. 022315. DOI: 10.1103/PhysRevA.85.022315 (Cited on page 1).

J. M. Cai, F. Caruso and M. B. Plenio (2012). 'Quantum limits for the magnetic sensitivity of a chemical compass'. In: *Physical Review A* 85.4. ISSN: 1050-2947. DOI: ARTN04030410.1103/PhysRevA.85.040304. URL: <GotoISI>://WOS:000302602500001https://journals.aps.org/pra/abstract/10.1103/PhysRevA.85.040304 (Cited on pages 6 and 32).

J. M. Cai, G. G. Guerreschi and H. J. Briegel (2010). 'Quantum Control and Entanglement in a Chemical Compass'. In: *Physical Review Letters* 104.22. ISSN: 0031-9007. DOI: ARTN22050210.1103/PhysRevLett.104.220502. URL: <GotoISI>://WOS:000278477500002https://journals.aps.org/prl/abstract/10.1103/PhysRevLett.104.220502 (Cited on pages 6, 9, 31 and 32).

J. M. Canfield, R. L. Belford, P. G. Debrunner and K. J. Schulten (1994). 'A Perturbation-Theory Treatment of Oscillating Magnetic-Fields in the Radical Pair Mechanism'. In: *Chemical Physics* 182.1, pp. 1–18. ISSN: 0301-0104. DOI: Doi10.1016/0301-0104(93)E0442-X. URL: <GotoISI>://WOS:A1994NF44100001 (Cited on page 32).

J. M. Canfield, R. L. Belford, P. G. Debrunner and K. Schulten (1995). 'A Perturbation Treatment of Oscillating Magnetic-Fields in the Radical Pair Mechanism Using the Liouville Equation'. In: *Chemical Physics* 195.1-3, pp. 59–69. ISSN: 0301-0104. DOI: Doi10.1016/0301-0104(95)00049-T. URL: <GotoISI>://WOS:A1995RE02300005 (Cited on page 32).

A. Carrington and A. D. McLachlan (1967). 'Introduction to magnetic resonance: with applications to chemistry and chemical physics'. In: (Cited on page 37).

A. M. Chagovetz and C. B. Grissom (1993). 'Magnetic Field Effects in adenosylcob (III) alamin photolysis: relevance to B12 enzymes'. In: *Journal of the American Chemical Society* 115.25, pp. 12152–12157 (Cited on page 14).

N. Chhabra, M. L. Aseri and D. Padmanabhan (2013). 'A review of drug isomerism and its significance'. In: *International journal of applied and basic medical research* 3.1, p. 16 (Cited on page 21).

E. Ciejka and A. Goraca (Feb. 2008). 'Influence of low magnetic field on lipid peroxidation'. In: *Pol. Merkuriusz Lek.* 24, pp. 106–8 (Cited on pages 11 and 13).

E. Ciejka, P. Kleniewska, B. Skibska and A. Goraca (2011). 'Effects of extremely low frequency magnetic field on oxidative balance in brain of rats'. In: *J. Physiol. Pharmacol.* 62, pp. 657–661 (Cited on page 13).

F. Cintolesi, T. Ritz, C. W. M. Kay, C. R. Timmel and P. J. Hore (2003). 'Anisotropic recombination of an immobilized photoinduced radical pair in a 50-mu T magnetic field: a model avian photomagnetoreceptor'. In: *Chemical Physics* 294.3, pp. 385–399. ISSN: 0301-0104. DOI: 10.1016/S0301-0104(03)00320-3. URL: <GotoISI>://WOS:000186265200015 (Cited on pages 7, 19 and 32).

J. Clausen, G. G. Guerreschi, M. Tiersch and H. J. Briegel (2014). 'Multiple re-encounter approach to radical pair reactions and the role of nonlinear master equations'. In: *J. Chem. Phys.* 141.5, p. 054107 (Cited on page 1).

A. Córdova-Palomera, T. Kaufmann, K. Persson, D. Alnæs, N. T. Doan, T. Moberget, M. J. Lund, M. L. Barca, A. Engvig, A. Brækhus et al. (2017). 'Disrupted global metastability and static and dynamic brain connectivity across individuals in the Alzheimer's disease continuum'. In: *Scientific reports* 7, p. 40268 (Cited on page 22).

Ş. Coşkun, B. Balabanlı, A. Canseven and N. Seyhan (July 2008). 'Effects of Continuous and Intermittent Magnetic Fields on Oxidative Parameters textitIn vivo'. In: *Neurochem. Res.* 34, pp. 238–43 (Cited on page 13).

O. Desouky and G. Zhou (2016). 'Biophysical and radiobiological aspects of heavy charged particles'. In: *JTUSCI* 10.2, pp. 187–194 (Cited on page 103).

G.-R Ding, T. Nakahara, H. Hirose, S. Koyama, Y. Takashima and J. Miyakoshi (2004). 'Extremely low frequency magnetic fields and the promotion of H_2O_2-induced cell death in HL-60 cells'. In: *Int. J. Radiat. Biol.* 80.4, pp. 317–324 (Cited on page 14).

C. A. Dodson, P. J. Hore and M. I. Wallace (2013). 'A radical sense of direction: signalling and mechanism in cryptochrome magnetoreception'. In: *Trends in Biochemical Sciences* 38.9, pp. 435–446. ISSN: 0968-0004. DOI: 10.1016/j.tibs.2013.07.002. URL: <GotoISI>://WOS:000324284100006 (Cited on page 2).

A. Doktorov, N. N. Lukzen and J. Pedersen (Sept. 2008). 'Analysis of Lipid Peroxidation Kinetics. 1. Role of Recombination of Alkyl and Peroxyl Radicals'. In: *J. Phys. Chem. B* 112, pp. 11854–61. DOI: 10.1021/jp709921m (Cited on pages 11 and 12).

R. L. Donkers and D. G. Leaist (1997). 'Diffusion of Free Radicals in Solution. TEMPO, Diphenylpicrylhydrazyl, and Nitrosodisulfonate'. In: *J. Phys. Chem. B* 101.3, pp. 304–308 (Cited on page 199).

J. Dormand and P. Prince (1986). 'A reconsideration of some embedded Runge—Kutta formulae'. In: *J. Comput. Appl. Math.* 15.2, pp. 203–211 (Cited on page 169).

R. S. Drago (1992). *Physical methods for chemists*. Surfside Scientific Publishers (Cited on pages 30 and 75).

O. Efimova and P. Hore (2008). 'Role of exchange and dipolar interactions in the radical pair model of the avian magnetic compass'. In: *Biophys. J.* 94.5, pp. 1565–1574 (Cited on pages 7, 19, 29, 32, 95, 96 and 173).

N. M. Emanuel and A. B. Gagarina (1966). 'Critical Phenomena in Chain Brnaching Reactions with Degenerate Chain Branching'. In: *Russian Chem. Rev.* 35.4, p. 260 (Cited on page 12).

S. Engels, N. L. Schneider, N. Lefeldt, C. M. Hein, M. Zapka, A. Michalik, D. Elbers, A. Kittel, P. J. Hore and H. Mouritsen (2014). 'Anthropogenic electromagnetic noise disrupts magnetic compass orientation in a migratory bird'. In: *Nature* 509.7500, pp. 353–+. ISSN: 0028-0836. DOI: 10.1038/nature13290. URL: <GotoISI>://WOS:000336121200037http://www.nature.com/articles/nature13290http://www.nature.com/articles/nature13290.pdf (Cited on pages 6 and 7).

S. Engels, C. D. Treiber, M. C. Salzer, A. Michalik, L. Ushakova, D. A. Keays, H. Mouritsen and D. Heyers (2018). 'Lidocaine is a nocebo treatment for trigeminally

mediated magnetic orientation in birds'. In: *Journal of The Royal Society Interface* 15.145, p. 20180124 (Cited on page 4).

E. W. Evans, D. R. Kattnig, K. B. Henbest, P. Hore, S. R. Mackenzie and C. R. Timmel (2016). 'Sub-millitesla magnetic field effects on the recombination reaction of flavin and ascorbic acid radicals'. In: *J. Chem. Phys.* 145.8, p. 085101 (Cited on pages 7, 31, 32 and 186).

I. F. Benzie (June 1996). 'Lipid peroxidation: A review of causes, consequences, measurement and dietary influences'. In: *Int. J. Food Sci. Nutr.* 47, pp. 233–61 (Cited on page 11).

G. Falkenberg, G. Fleissner, K. Schuchardt, M. Kuehbacher, P. Thalau and H. Mouritsen (2010). 'Avian Magnetoreception: Elaborate Iron Mineral Containing Dendrites in the Upper Beak Seem to Be a Common Feature of Birds.' In: *PLoS ONE* 5.2 (Cited on page 3).

E. E. Farmer and M. J. Mueller (2013). 'ROS-Mediated Lipid Peroxidation and RES-Activated Signalling'. In: *Annu. Rev. Plant Biol.* 64, pp. 429–450 (Cited on page 11).

T. P. Fay, L. P. Lindoy and D. E. Manolopoulos (2018). 'Spin-selective electron transfer reactions of radical pairs: beyond the Haberkorn master equation'. In: *J. Chem. Phys.* 149.6, p. 064107 (Cited on pages 81, 159, 160 and 164).

T. P. Fay, L. P. Lindoy, D. E. Manolopoulos and P. Hore (2019). 'How quantum is radical pair magnetoreception?' In: *Faraday discussions* 221, pp. 77–91 (Cited on page 8).

G. Fedele, E. W. Green, E. Rosato and C. P. Kyriacou (2014a). 'An electromagnetic field disrupts negative geotaxis in Drosophila via a CRY-dependent pathway'. In: *Nature communications* 5.1, pp. 1–6 (Cited on page 11).

G. Fedele, M. D. Edwards, S. Bhutani, J. M. Hares, M. Murbach, E. W. Green, S. Dissel, M. H. Hastings, E. Rosato and C. P. Kyriacou (2014b). 'Genetic analysis of circadian responses to low frequency electromagnetic fields in Drosophila melanogaster'. In: *PLoS genetics* 10.12, e1004804 (Cited on page 11).

E. Fermi (1930). 'Magnetic moments of atomic nuclei'. In: *Nature* 125.3140, pp. 16–16 (Cited on page 36).

M. Forbes, N. Lebedeva, R. C. White, T. K. Chen, R. Macarthur, P. Caregnato and T. E. Hill (Aug. 2007). 'On the electron spin polarization observed in TREPR experiments involving hydroxyl and sulfate radicals'. In: *Mol. Phys.* 105, pp. 2127–2136 (Cited on page 200).

J. J. Frost, K. J. Pienta and D. S. Coffey (2018). 'Symmetry and symmetry breaking in cancer: a foundational approach to the cancer problem'. In: *Oncotarget* 9.14, p. 11429 (Cited on pages 21 and 135).

M. M. Gaschler and B. R. Stockwell (2017). 'Lipid peroxidation in cell death'. In: *Biochem. Biophys. Res. Commun.* 482(2), pp. 419–425 (Cited on pages 11 and 199).

E. M. Gauger, E. Rieper, J. J. Morton, S. C. Benjamin and V. Vedral (2011). 'Sustained quantum coherence and entanglement in the avian compass'. In: *Phys. Rev. Lett.* 106.4, p. 040503 (Cited on pages 1, 8, 9, 20, 32, 142 and 164).

R. J. Gegear, L. E. Foley, A. Casselman and S. M. Reppert (2010). 'Animal cryptochromes mediate magnetoreception by an unconventional photochemical mechanism'. In: *Nature* 463.7282, pp. 804–807 (Cited on pages 7 and 10).

R. J. Gegear, A. Casselman, S. Waddell and S. M. Reppert (2008). 'Cryptochrome mediates light-dependent magnetosensitivity in Drosophila'. In: *Nature* 454.7207, pp. 1014–1018 (Cited on page 10).

S. Ghodbane, A. Lahbib, M. Sakly and H. Abdelmelek (2013a). 'Bioeffects of Static Magnetic Fields: Oxidative Stress, Genotoxic Effects, and Cancer Studies'. In: *BioMed. Research International* 2013, p. 602987 (Cited on page 13).

S. Ghodbane, A. Lahbib, M. Sakly and H. Abdelmelek (2013b). 'Bioeffects of static magnetic fields: oxidative stress, genotoxic effects, and cancer studies'. In: *BioMed. Res. Internat.* 2013 (Cited on pages 1, 11, 23, 76 and 77).

C. N. Giachello, N. S. Scrutton, A. R. Jones and R. A. Baines (2016). 'Magnetic fields modulate blue-light-dependent regulation of neuronal firing by cryptochrome'. In: *Journal of Neuroscience* 36.42, pp. 10742–10749 (Cited on page 10).

M. Giorgio, M. Trinei, E. Migliaccio and P. G. Pelicci (Sept. 2007). 'Hydrogen peroxide: a metabolic by-product or a common mediator of ageing signals?' In: *Nat. Rev. Mol. Cell Biol.* 8, 722A–728 (Cited on page 11).

C. B. Grissom (1995). 'Magnetic Field Effects in Biology: A Survey of Possible Mechanisms with Emphasis on Radical-Pair Recombination'. In: *Chemical Reviews* 95.1, pp. 3–24. DOI: 10.1021/cr00033a001. eprint: http://dx.doi.org/10.1021/cr00033a001. URL: http://dx.doi.org/10.1021/cr00033a001 (Cited on page 41).

P. A. Guerra, R. J. Gegear and S. M. Reppert (2014). 'A magnetic compass aids monarch butterfly migration'. In: *Nature communications* 5.1, pp. 1–8 (Cited on page 10).

A. Günther, A. Einwich, E. Sjulstok, R. Feederle, P. Bolte, K.-W. Koch, I. A. Solov'yov and H. Mouritsen (2018). 'Double-cone localization and seasonal expression pattern suggest a role in magnetoreception for European robin cryptochrome 4'. In: *Current Biology* 28.2, pp. 211–223 (Cited on page 8).

J. M. C. Gutteridge (1986). 'Iron promoters of the Fenton reaction and lipid peroxidation can be released from haemoglobin by peroxides'. In: *FEBS Lett.* 201, pp. 291–295 (Cited on page 11).

R. Haberkorn (1976). 'Density matrix description of spin-selective radical pair reactions'. In: *Mol. Phys.* 32(5), pp. 1491–1493 (Cited on pages 30, 40, 81, 110, 141, 159 and 160).

B. Halliwell and J. M. Gutteridge (2015). *Free radicals in biology and medicine*. Oxford University Press, USA (Cited on page 27).

M Hammad, M Albaqami, M Pooam, E Kernevez, J Witczak, T Ritz, C Martino and M Ahmad (2020). 'Cryptochrome mediated magnetic sensitivity in Arabidopsis occurs independently of light-induced electron transfer to the flavin'. In: *Photochem. Photobiol. Sci.* 19.3, pp. 341–352 (Cited on page 172).

R. Hanini, A. Chatti, S. B. Ghorbel and A. Landoulsi (May 2017). 'Role of SOD Gene in Response to Static Magnetic Fields in Pseudomonas aeruginosa'. In: *Curr. Microbiol.* 74 (Cited on page 13).

K. Haume, P. de Vera, A. Verkhovtsev, E. Surdutovich, N. J. Mason and A. V. Solov'yov (June 2018). 'Transport of secondary electrons through coatings of ion-irradiated metallic nanoparticles'. In: *Eur. Phys. J. D* 72, p. 116 (Cited on page 103).

H. Hayashi (2004a). *Introduction to Dynamic Spin Chemistry*. World Scientific. DOI: 10.1142/5316. eprint: https://www.worldscientific.com/doi/pdf/10.1142/5316. URL: https://www.worldscientific.com/doi/abs/10.1142/5316 (Cited on pages 27 and 28).

H. Hayashi and S. Nagakura (1984). 'Theoretical study of relaxation mechanism in magnetic field effects on chemical reactions'. In: *Bulletin of the Chemical Society of Japan* 57.2, pp. 322–328 (Cited on pages 7, 31 and 128).

H. Hayashi (2004b). *Introduction to dynamic spin chemistry: magnetic field effects on chemical and biochemical reactions*. Vol. 8. World Scientific Publishing Company (Cited on page 39).

H. Hayashi and Y. Sakaguchi (2005). 'Magnetic field effects and CIDEP due to the d-type triplet mechanism in intra-molecular reactions'. In: *Journal of Photochemistry and Photobiology C: Photochemistry Reviews* 6.1, pp. 25–36 (Cited on page 15).

R. D. Hills Jr. and N. McGlinchey (2016). 'Model parameters for simulation of physiological lipids'. In: *J. Comput. Chem.* 37.12, pp. 1112–1118 (Cited on page 79).

H. G. Hiscock, H. Mouritsen, D. E. Manolopoulos and P. J. Hore (2017). 'Disruption of Magnetic Compass Orientation in Migratory Birds by Radiofrequency Electromagnetic Fields'. In: *Biophysical Journal* 113.7, pp. 1475–1484. ISSN: 0006-3495. DOI: 10.1016/j.bpj.2017.07.031. URL: <GotoISI>://WOS:000412551200011 (Cited on pages 8 and 32).

H. G. Hiscock, S. Worster, D. R. Kattnig, C. Steers, Y. Jin, D. E. Manolopoulos, H. Mouritsen and P. Hore (2016). 'The quantum needle of the avian magnetic compass'. In: *Proceedings of the National Academy of Sciences* 113.17, pp. 4634–4639 (Cited on pages 1, 6, 8, 69, 171 and 185).

H. Hiscock, T. Hiscock, D. Kattnig, T Scrivener, A. Lewis, D. Manolopoulos and P. Hore (2019). 'Navigating at night: fundamental limits on the sensitivity of radical pair magnetoreception under dim light'. In: *Quarterly reviews of biophysics* 52 (Cited on page 31).

H. M. Hoang, V. T. B. Pham, G. Grampp and D. R. Kattnig (2018). 'Magnetic Field-Sensitive Radical Pair Dynamics in Polymethylene Ether-Bridged Donor–Acceptor Systems'. In: *ACS omega* 3.8, pp. 10296–10305 (Cited on page 161).

H. J. Hogben, T. Biskup and P. J. Hore (2012). 'Entanglement and Sources of Magnetic Anisotropy in Radical Pair-Based Avian Magnetoreceptors'. In: *Phys. Rev. Lett.* 109 (22), p. 220501. DOI: 10.1103/PhysRevLett.109.220501 (Cited on page 1).

H. J. Hogben, O. Efimova, N. Wagner-Rundell, C. R. Timmel and P. Hore (2009). 'Possible involvement of superoxide and dioxygen with cryptochrome in avian magnetoreception: Origin of Zeeman resonances observed by in vivo EPR spectroscopy'. In: *Chem. Phys. Lett.* 480.1, pp. 118 –122 (Cited on pages 7 and 16).

H. Hogben, P. Hore and I. Kuprov (2010). 'Strategies for state space restriction in densely coupled spin systems with applications to spin chemistry'. In: *J. Chem. Phys.* 132.17, p. 174101 (Cited on page 186).

H. Hogben, M Krzystyniak, G. Charnock, P. Hore and I. Kuprov (2011). 'Spinach–a software library for simulation of spin dynamics in large spin systems'. In: *J. Magn. Reson.* 208.2, pp. 179–194 (Cited on page 186).

N. Hogg and B. Kalyanaraman (1999). 'Nitric oxide and lipid peroxidation'. In: *Biochim. Biophys. Acta* 1411, pp. 378–384 (Cited on page 11).

P. Hore and H. Mouritsen (2016). 'The radical-pair mechanism of magnetoreception'. In: *Annual review of biophysics* 45, pp. 299–344 (Cited on pages 1, 2, 6, 8, 27 and 28).

P. Hore, D. A. Hunter, F. G. van Wijk, T. J. Schaafsma and A. J. Hoff (1988). 'Electron spin polarization in the donor triplet state of bacterial photosynthetic reaction centres. II. Anisotropic inversion of electron spin polarization in a three-

spin model reaction centre'. In: *BBA-Bioenergetics* 936.2, pp. 249–258 (Cited on page 17).

K. Hornberger (2009). 'Introduction to decoherence theory'. In: *Entanglement and decoherence*. Springer, pp. 221–276 (Cited on page 142).

X. Huang, H. Sun, X. Yi et al. (2008). 'Non-Markovian quantum jump with generalized Lindblad master equation'. In: *Phys. Rev. E* 78.4, p. 041107 (Cited on page 163).

J. A. Hughes, S. J. Hardman, N. S. Scrutton, D. M. Graham, J. R. Woodward and A. R. Jones (2019). 'Observation of the Δ g mechanism resulting from the ultrafast spin dynamics that follow the photolysis of coenzyme B12'. In: *The Journal of chemical physics* 151.20, p. 201102 (Cited on page 15).

M. Inotani, S. Fukuyoshi and T. Kusumi (Oct. 2001). 'Autoxidation of linoleic acid in a strong magnetic field (9.4 T)'. In: *Tetrahedron Lett.* 42, pp. 7451–7452 (Cited on page 14).

K. L. Ivanov, M. V. Petrova, N. N. Lukzen and K. Maeda (2010). 'Consistent treatment of spin-selective recombination of a radical pair confirms the haberkorn approach'. In: *J. Phys. Chem. A* 114.35, pp. 9447–9455 (Cited on page 160).

J. Jajte, J. Grzegorczyk, M. Zmyślony and E. Rajkowska (2002). 'Effect of 7 mT static magnetic field and iron ions on rat lymphocytes: apoptosis, necrosis and free radical processes'. In: *Bioelectrochemistry* 57.2, pp. 107 –111 (Cited on page 13).

G. Jeschke (2016). 'Comment on "Quantum trajectory tests of radical-pair quantum dynamics in CIDNP measurements of photosynthetic reaction centers"[Chem. Phys. Lett. 640 (2015) 40–45]'. In: *Chem. Phys. Lett.* 648, pp. 200–203 (Cited on page 160).

S. Johnsen and K. J. Lohmann (2005). 'The physics and neurobiology of magnetoreception'. In: *Nature Reviews. Neuroscience* 6.9, p. 703 (Cited on page 8).

A. R. Jones (2016). 'Magnetic field effects in proteins'. In: *Molecular Physics* 114.11, pp. 1691–1702 (Cited on page 8).

A. R. Jones, J. R. Woodward and N. S. Scrutton (2009). 'Continuous wave photolysis magnetic field effect investigations with free and protein-bound alkylcobalamins'.

In: *Journal of the American Chemical Society* 131.47, pp. 17246–17253 (Cited on page 14).

A. R. Jones, S. Hay, J. R. Woodward and N. S. Scrutton (2007). 'Magnetic field effect studies indicate reduced geminate recombination of the radical pair in substrate-bound adenosylcobalamin-dependent ethanolamine ammonia lyase'. In: *Journal of the American Chemical Society* 129.50, pp. 15718–15727 (Cited on pages 14 and 15).

A. R. Jones, S. J. Hardman, S. Hay and N. S. Scrutton (2011a). 'Is there a dynamic protein contribution to the substrate trigger in coenzyme B12-dependent ethanolamine ammonia lyase?' In: *Angewandte Chemie International Edition* 50.46, pp. 10843–10846 (Cited on page 14).

J. A. Jones and P. J. Hore (2010a). 'Spin-selective reactions of radical pairs act as quantum measurements'. In: *Chemical Physics Letters* 488.1-3, pp. 90–93. ISSN: 0009-2614. DOI: 10.1016/j.cplett.2010.01.063. URL: <GotoISI>://WOS:000275142000019 (Cited on pages 30, 32, 141 and 157).

J. Jones, K. Maeda, U. Steiner and P. Hore (2011b). 'Reply to comment on 'spin-selective reactions of radical pairs act as quantum measurements''. In: *Chem. Phys. Lett.* 508.1-3, pp. 184–185 (Cited on page 160).

J. A. Jones and P. J. Hore (2010b). 'Spin-selective reactions of radical pairs act as quantum measurements'. In: *Chem. Phys. Lett.* 488.1-3, pp. 90–93 (Cited on pages 159, 160 and 164).

J. A. Jones, K. Maeda and P. J. Hore (2011). 'Reaction operators for spin-selective chemical reactions of radical pairs'. In: *Chem. Phys. Lett.* 507.4-6, pp. 269–273 (Cited on pages 159, 160 and 164).

J. Juutilainen, M. Herrala, J. Luukkonen, J. Naarala and P. Hore (2018a). 'Magnetocarcinogenesis: is there a mechanism for carcinogenic effects of weak magnetic fields?' In: *Proc. R. Soc. B* 285.1879, p. 20180590 (Cited on page 1).

J. Juutilainen, M. Herrala, J. Luukkonen, J. Naarala and P. Hore (2018b). 'Magnetocarcinogenesis: is there a mechanism for carcinogenic effects of weak magnetic

fields?' In: *Proceedings of the Royal Society B: Biological Sciences* 285.1879, p. 20180590 (Cited on page 23).

H. Kabuto, I. Yokoi, N. Ogawa, A. Mori and R. P. Liburdy (2001). 'Effects of magnetic fields on the accumulation of thiobarbituric acid reactive substances induced by iron salt and H2O2 in mouse brain homogenates or phosphotidylcholine'. In: *Pathophys.* 7.4, pp. 283–288 (Cited on pages 1, 7, 13, 14, 23, 77 and 103).

C. Kahler, B. Grimm, E. Schleussner, A. Schneider, U. Schneider, H. Nowak, L. Vogt and H.-J. Seewald (2001). 'The application of fetal magnetocardiography (FMCG) to investigate fetal arrhythmias and congenital heart defects (CHD)'. In: *Prenatal Diagnosis* 21.3, pp. 176–182. ISSN: 1097-0223. DOI: 10.1002/1097-0223(200103)21:3<176::AID-PD22>3.0.CO;2-W. URL: http://dx.doi.org/10.1002/1097-0223(200103)21:3<176::AID-PD22>3.0.CO;2-W (Cited on page 9).

K. Kannan and S. K. Jain (2000). 'Oxidative stress and apoptosis'. In: *Pathophysiology* 7.3, pp. 153–163 (Cited on page 11).

T. Y. Karogodina, S. V. Sergeeva, D. V. Stass and U. E. Steiner (2011a). 'Magnetic field effect on recombination of nitric oxide and superoxide anion in high magnetic field'. In: *Dokl. Phys. Chem.* 436.1, pp. 5–7 (Cited on page 16).

T. Y. Karogodina, I. G. Dranov, S. V. Sergeeva, D. V. Stass and U. E. Steiner (2011b). 'Kinetic Magnetic-Field Effect Involving the Small Biologically Relevant Inorganic Radicals NO and O2.-'. In: *ChemPhysChem* 12.9, pp. 1714–1728 (Cited on page 15).

D. Kattnig, J. Sowa, I. A. Solov'yov and P. J. J. Hore (June 2016a). 'Electron spin relaxation can enhance the performance of a cryptochrome-based magnetic compass sensor'. In: *New J. Phys.* 18, p. 063007 (Cited on pages 1, 162 and 184).

D. R. Kattnig (2017a). 'Radical-Pair-Based Magnetoreception Amplified by Radical Scavenging: Resilience to Spin Relaxation'. In: *J. Phys. Chem. B* 121.44, pp. 10215–10227 (Cited on page 16).

D. R. Kattnig and P. J. Hore (2017a). 'The sensitivity of a radical pair compass magnetoreceptor can be significantly amplified by radical scavengers'. In: *Scientific Reports* 7. ISSN: 2045-2322. DOI: ARTN1164010.1038/s41598-017-09914-7. URL:

<GotoISI>://WOS:000410739000138http://www.nature.com/articles/s41598-017-09914-7.pdf (Cited on pages 7, 17, 18, 29 and 31).

D. R. Kattnig and P. J. Hore (2017b). 'The sensitivity of a radical pair compass magnetoreceptor can be significantly amplified by radical scavengers'. In: *Sci. Rep.* 7, p. 11640 (Cited on pages 16 and 28).

D. R. Kattnig (2017b). 'Radical-pair-based magnetoreception amplified by radical scavenging: resilience to spin relaxation'. In: *The Journal of Physical Chemistry B* 121.44, pp. 10215–10227 (Cited on pages 2, 7, 17, 18, 21, 32, 64, 135 and 142).

D. R. Kattnig (2017c). 'Radical-pair-based magnetoreception amplified by radical scavenging: resilience to spin relaxation'. In: *J. Phys. Chem. B* 121.44, pp. 10215–10227 (Cited on pages 162, 171, 173 and 185).

D. R. Kattnig and P. Hore (2017c). 'The sensitivity of a radical pair compass magnetoreceptor can be significantly amplified by radical scavengers'. In: *Sci. Rep.* 7.1, p. 11640 (Cited on pages 17, 18 and 185).

D. R. Kattnig, C. Nielsen and I. A. Solov'yov (2018). 'Molecular dynamics simulations disclose early stages of the photo-activation of cryptochrome 4'. In: *New J. Phys.* 20.8, p. 083018 (Cited on page 173).

D. R. Kattnig, A. Rosspeintner and G. Grampp (2011). 'Magnetic field effects on exciplex-forming systems: the effect on the locally excited fluorophore and its dependence on free energy'. In: *PCCP* 13.8, pp. 3446–3460 (Cited on page 160).

D. R. Kattnig, I. A. Solov'yov and P. Hore (2016). 'Electron spin relaxation in cryptochrome-based magnetoreception'. In: *Physical Chemistry Chemical Physics* 18.18, pp. 12443–12456 (Cited on pages 21, 31, 135, 142, 162 and 173).

D. R. Kattnig, E. W. Evans, V. Déjean, C. A. Dodson, M. I. Wallace, S. R. Mackenzie, C. R. Timmel and P. Hore (2016b). 'Chemical amplification of magnetic field effects relevant to avian magnetoreception'. In: *Nat. Chem.* 8.4, p. 384 (Cited on pages 2 and 171).

K. V. Kavokin (2009). 'The puzzle of magnetic resonance effect on the magnetic compass of migratory birds'. In: *Bioelectromagnetics* 30.5, pp. 402–410 (Cited on page 7).

R. H. Keens, S. Bedkihal and D. R. Kattnig (2018). 'Magnetosensitivity in dipolarly coupled three-spin systems'. In: *Physical review letters* 121.9, p. 096001 (Cited on pages 16, 19, 20, 22, 23, 24, 79, 86, 100, 104, 105, 108, 109, 112, 121, 122 and 136).

R. H. Keens and D. R. Kattnig (2020). 'Monte-Carlo wavefunction approach for the spin dynamics of recombining radicals'. In: *arXiv preprint arXiv:2005.04417* (Cited on pages 26 and 112).

R. H. Keens, C. Sampson and D. R. Kattnig (2021). 'How symmetry-breaking can amplify the magnetosensitivity of dipolarly coupled n-radical systems'. In: *J. Chem. Phys* 154.9, p. 094101. DOI: 10.1063/5.0041552. eprint: https://doi.org/10.1063/5.0041552. URL: https://doi.org/10.1063/5.0041552 (Cited on pages 20 and 25).

S. M. Kelly, T. J. Jess and N. C. Price (2005). 'How to study proteins by circular dichroism'. In: *Biochimica et Biophysica Acta (BBA)-Proteins and Proteomics* 1751.2, pp. 119–139 (Cited on page 22).

Y. Kim, F. Bertagna, E. M. D'Souza, D. J. Heyes, L. O. Johannissen, E. T. Nery, A. Pantelias, A. Sanchez-Pedreño Jimenez, L. Slocombe, M. G. Spencer et al. (2021). 'Quantum Biology: An Update and Perspective'. In: *Quantum Rep.* 3.1, pp. 80–126 (Cited on pages 1, 2, 8 and 36).

A. Kipriyanov Jr., A. Doktorov and P. Purtov (2015). 'Magnetic field effects on bistability and bifurcation phenomena in lipid peroxidation'. In: *Bioelectromagnetics* 36.7, pp. 485–493 (Cited on pages 12, 79, 83, 98 and 200).

J. Kirschvink (1981). 'Biogenic magnetite as a basis for magnetic field sensitivity in animals'. In: *Biosystems* 13, pp. 181–201. URL: http://ci.nii.ac.jp/naid/10029117395/en/ (Cited on pages 2 and 3).

D. A. Kishkinev and N. S. Chernetsov (2015). 'Magnetoreception systems in birds: A review of current research'. In: *Biology Bulletin Reviews* 5.1, pp. 46–62. ISSN: 2079-0872. DOI: 10.1134/S2079086415010041. URL: https://doi.org/10.1134/S2079086415010041 (Cited on page 8).

E. G. Kıvrak, K. K. Yurt, A. A. Kaplan, I. Alkan and G. Altun (2017). 'Effects of electromagnetic fields exposure on the antioxidant defense system'. In: *J. Microsc. Ultrastruct.* 5.4, pp. 167 –176 (Cited on page 14).

J. B. Klauda, M. F. Roberts, A. G. Redfield, B. R. Brooks and R. W. Pastor (2008). 'Rotation of Lipids in Membranes: Molecular Dynamics Simulation, 31P Spin-Lattice Relaxation, and Rigid-Body Dynamics'. In: *Biophys. J.* 94.8, pp. 3074 –3083 (Cited on page 200).

M. J. Klein (1952). 'On a degeneracy theorem of kramers'. In: *Am. J. Phys.* 20.2, pp. 65–71 (Cited on page 46).

R. Kohen and A. Nyska (2002). 'Oxidation of Biological Systems: Oxidative Stress Phenomena, Antioxidants, Redox Reactions, and Method for Their Quantification'. In: *Toxicol. Pathol.* 30, pp. 620–650 (Cited on pages 76, 77 and 78).

I. K. Kominis (2009). 'Quantum Zeno effect explains magnetic-sensitive radical-ion-pair reactions'. In: *Phys. Rev. E* 80.5, p. 056115 (Cited on page 160).

I. K. Kominis (2015). 'The radical-pair mechanism as a paradigm for the emerging science of quantum biology'. In: *Modern Phys. Lett. B* 29.Supplement 1, p. 1530013 (Cited on page 160).

I. Kominis (2016). 'Reply to the comment on "Quantum trajectory tests of radical-pair quantum dynamics in CIDNP measurements of photosynthetic reaction centers" by G. Jeschke'. In: *Chem. Phys. Lett.* 648, pp. 204–207 (Cited on page 160).

M. Kornyik and A. Vukics (2019). 'The Monte Carlo wave-function method: A robust adaptive algorithm and a study in convergence'. In: *Comput. Phys. Commun.* 238, pp. 88–101 (Cited on pages 159, 161, 162 and 169).

K. Krasulova, M. Siller, O. Holas, Z. Dvorak and P. Anzenbacher (2016). 'Enantiospecific effects of chiral drugs on cytochrome P450 inhibition in vitro'. In: *Xenobiotica* 46.4, pp. 315–324 (Cited on page 21).

M Kritsotakis and I. Kominis (2014). 'Retrodictive derivation of the radical-ion-pair master equation and Monte Carlo simulation with single-molecule quantum trajectories'. In: *Phys. Rev. E* 90.4, p. 042719 (Cited on page 161).

S. Kryszewski and J. Czechowska-Kryszk (2008). 'Master equation - tutorial approach'. In: (Cited on page 142).

I. Kuprov, N. Wagner-Rundell and P. Hore (2007). 'Polynomially scaling spin dynamics simulation algorithm based on adaptive state-space restriction'. In: *J. Magn. Reson.* 189.2, pp. 241–250 (Cited on page 186).

U. Lalo, Y. Pankratov and O. Mykhaylyk (1994). 'Steady Magnetic-Fields Effect on Lipid-Peroxidation Kinetics'. In: *Redox Rep.* 1, pp. 71–75. DOI: 10.1080/13510002.1994.11746959 (Cited on pages 1, 11, 12, 14, 23, 77 and 103).

N. Lambert, Y.-N. Chen, Y.-C. Cheng, C.-M. Li, G.-Y. Chen and F. Nori (2013). 'Quantum biology'. In: *Nat. Phys.ics* 9.1, pp. 10–18 (Cited on pages 1, 31 and 32).

A. A. Lee, J. C. Lau, H. J. Hogben, T. Biskup, D. R. Kattnig and P. Hore (2014). 'Alternative radical pairs for cryptochrome-based magnetoreception'. In: *J. R. Soc. Interface* 11.95, p. 20131063 (Cited on pages 171 and 185).

B. Lee, H. Johng, J. Lim, J. H. Jeong, K. Y. Baik, T. J. Nam, J. H. Lee, J. Kim, U. D. Sohn, G. Yoon et al. (2004). 'Effects of extremely low frequency magnetic field on the antioxidant defense system in mouse brain: a chemiluminescence study'. In: *J. Photochem. Photobiol., B* 73.1, pp. 43 –48 (Cited on page 13).

N. Lefeldt, D. Dreyer, N. L. Schneider, F. Steenken and H. Mouritsen (2015). 'Migratory blackcaps tested in Emlen funnels can orient at 85 degrees but not at 88 degrees magnetic inclination'. In: *Journal of Experimental Biology* 218.2, pp. 206–211 (Cited on page 8).

A. S. Letuta and V. L. Berdinskii (2015). 'Chemical Zeno effect—A new mechanism of spin catalysis in radical triads'. In: *Dokl. Phys. Chem.* 463.2, pp. 179–181 (Cited on pages 16, 17 and 28).

C. Levy, B. D. Zoltowski, A. R. Jones, A. T. Vaidya, D. Top, J. Widom, M. W. Young, N. S. Scrutton, B. R. Crane and D. Leys (2013). 'Updated structure of Drosophila cryptochrome'. In: *Nature* 495.7441, E3–E4 (Cited on page 8).

A. M. Lewis, T. P. Fay, D. E. Manolopoulos, C. Kerpal, S. Richert and C. R. Timmel (2018a). 'On the low magnetic field effect in radical pair reactions'. In: *J. Chem. Phys.* 149.3, p. 034103 (Cited on pages 27, 28, 85 and 86).

A. M. Lewis, T. P. Fay and D. E. Manolopoulos (2016). 'An efficient quantum mechanical method for radical pair recombination reactions'. In: *J. Chem. Phys.* 145.24, p. 244101 (Cited on pages 161, 170, 178 and 184).

A. M. Lewis, D. E. Manolopoulos and P. Hore (2014). 'Asymmetric recombination and electron spin relaxation in the semiclassical theory of radical pair reactions'. In: *J. Chem. Phys.* 141.4, p. 044111 (Cited on pages 19, 183 and 184).

A. M. Lewis, T. P. Fay, D. E. Manolopoulos, C. Kerpal, S. Richert and C. R. Timmel (2018b). 'On the low magnetic field effect in radical pair reactions'. In: *The Journal of chemical physics* 149.3, p. 034103 (Cited on pages 15 and 32).

E. H. Lieb (1973). 'The classical limit of quantum spin systems'. In: *Commun. Math. Phys.* 31.4, pp. 327–340 (Cited on page 170).

M. Liedvogel and H. Mouritsen (2010). 'Cryptochromes—a potential magnetoreceptor: what do we know and what do we want to know?' In: *Journal of The Royal Society Interface* 7.Suppl 2 (Cited on page 6).

M. Liedvogel, K. Maeda, K. Henbest, E. Schleicher, T. Simon, C. R. Timmel, P. J. Hore and H. Mouritsen (2007a). 'Chemical magnetoreception: bird cryptochrome 1a is excited by blue light and forms long-lived radical-pairs'. In: *PloS one* 2.10, e1106 (Cited on page 32).

M. Liedvogel, G. Feenders, K. Wada, N. F. Troje, E. D. Jarvis and H. Mouritsen (2007b). 'Lateralized activation of Cluster N in the brains of migratory songbirds'. In: *European Journal of Neuroscience* 25.4, pp. 1166–1173 (Cited on page 6).

C. T. Lin and T. Todo (2005). 'The cryptochromes'. In: *Genome Biology* 6.5. ISSN: 1465-6914. DOI: ARTN22010.1186/gb-2005-6-5-220. URL: <GotoISI>://WOS:000228864300005https://genomebiology.biomedcentral.com/track/pdf/10.1186/gb-2005-6-5-220?site=genomebiology.biomedcentral.com (Cited on pages 6 and 9).

V. Lobo, A. Patil, A. Phatak and N Chandra (2010). 'Free radicals, antioxidants and functional foods: impact on human health'. In: *Pharmacogn. Rev.* 4 (8), pp. 118–26 (Cited on page 101).

H. A. Lowenstam (1962). 'Magnetite in Denticle Capping in Recent Chitons (Polyplacophora)'. In: *Geological Society of America Bulletin* 73, p. 435. DOI: 10.1130/0016-7606(1962)73[435:MIDCIR]2.0.CO;2 (Cited on page 2).

N. N. Lukzen, K. L. Ivanov, V. M. Sadovsky and R. Z. Sagdeev (2020). 'Magnetic field effect on recombination of radicals diffusing on a two-dimensional plane'. In: *The Journal of chemical physics* 152.3, p. 034103 (Cited on page 13).

R. Macháň and M. Hof (2010). 'Lipid diffusion in planar membranes investigated by fluorescence correlation spectroscopy'. In: *Biochim. Biophys. Acta, Biomembr.* 1798.7, pp. 1377–1391 (Cited on page 199).

K. Maeda, P. Liddell, D. Gust and P. J. Hore (2013). 'Spin-selective recombination reactions of radical pairs: Experimental test of validity of reaction operators'. In: *Journal of Chemical Physics* 139.23. ISSN: 0021-9606. DOI: Artn23430910.1063/1.4844355. URL: <GotoISI>://WOS:000329191300024http://aip.scitation.org/doi/pdf/10.1063/1.4844355 (Cited on page 31).

K. Maeda, K. B. Henbest, F. Cintolesi, I. Kuprov, C. T. Rodgers, P. A. Liddell, D. Gust, C. R. Timmel and P. Hore (2008). 'Chemical compass model of avian magnetoreception'. In: *Nature* 453.7193 (Cited on page 2).

K. Maeda, A. J. Robinson, K. B. Henbest, H. J. Hogben, T. Biskup, M. Ahmad, E. Schleicher, S. Weber, C. R. Timmel and P. Hore (2012). 'Magnetically sensitive light-induced reactions in cryptochrome are consistent with its proposed role as a magnetoreceptor'. In: *Procs. Nat. Acad. Sci.* 109.13 (Cited on pages 2, 7, 21 and 171).

I. M. Magin, P. A. Purtov, A. I. Kruppa and T. V. Leshina (2005). 'Peculiarities of magnetic and spin effects in a biradical/stable radical complex (three-spin system). Theory and comparison with experiment'. In: *J. Phys. Chem. A* 109.33, pp. 7396–7401 (Cited on page 17).

I. Magin, P. Purtov, A. Kruppa and T. Leshina (2004). 'Modeling magnetic field effects in multispin systems'. In: *Appl. Magn. Reson.* 26.1-2, p. 155 (Cited on page 17).

D. E. Manolopoulos and P. Hore (2013). 'An improved semiclassical theory of radical pair recombination reactions'. In: *The Journal of chemical physics* 139.12, p. 124106 (Cited on page 184).

R. Marley, C. N. Giachello, N. S. Scrutton, R. A. Baines and A. R. Jones (2014). 'Cryptochrome-dependent magnetic field effect on seizure response in Drosophila larvae'. In: *Scientific reports* 4.1, pp. 1–4 (Cited on page 10).

E. N. G. Marsh and G. D. R. Meléndez (2012). 'Adenosylcobalamin enzymes: Theory and experiment begin to converge'. In: *Biochimica et Biophysica Acta (BBA)-Proteins and Proteomics* 1824.11, pp. 1154–1164 (Cited on page 14).

M.-O. Mattsson and M. Simkó (2014). 'Grouping of experimental conditions as an approach to evaluate effects of extremely low-frequency magnetic fields on oxidative response in in vitro studies'. In: *Frontiers in public health* 2, p. 132 (Cited on page 13).

J. McConathy and M. J. Owens (2003). 'Stereochemistry in drug action'. In: *Primary care companion to the Journal of clinical psychiatry* 5.2, p. 70 (Cited on page 21).

K. A. McLauchlan and U. Steiner (1991). 'Invited article: the spin-correlated radical pair as a reaction intermediate'. In: *Molecular Physics* 73.2, pp. 241–263 (Cited on page 159).

A. V. Melkikh and A. Khrennikov (2015). 'Nontrivial quantum and quantum-like effects in biosystems: Unsolved questions and paradoxes'. In: *Progress in Biophysics and Molecular Biology* 119.2, pp. 137–161 (Cited on page 1).

H. L. Messiha, T. Wongnate, P. Chaiyen, A. R. Jones and N. S. Scrutton (2015). 'Magnetic field effects as a result of the radical pair mechanism are unlikely in redox enzymes'. In: *Journal of the Royal Society Interface* 12.103, p. 20141155 (Cited on page 14).

K. Mølmer, Y. Castin and J. Dalibard (1993). 'Monte Carlo wave-function method in quantum optics'. In: *JOSA B* 10.3, pp. 524–538 (Cited on pages 159, 161, 162 and 164).

P. Müller, J. Yamamoto, R. Martin, S. Iwai and K. Brettel (2015). 'Discovery and functional analysis of a 4th electron-transferring tryptophan conserved exclusively in animal cryptochromes and (6-4) photolyases'. In: *Chemical Communications* 51.85, pp. 15502–15505 (Cited on page 8).

U. Munro, J. A. Munro, J. B. Phillips, R. Wiltschko and W. Wiltschko (1997). 'Evidence for a magnetite-based navigational "map" in birds'. In: *Naturwissenschaften* 84.1, pp. 26–28. ISSN: 0028-1042. DOI: DOI10.1007/s001140050343. URL: <GotoISI>://WOS:A1997WJ11700006https://link.springer.com/content/pdf/10.1007%2Fs001140050343.pdf (Cited on page 3).

C. Mylonas and D. Kouretas (1999). 'Lipid peroxidation and tissue damage'. In: *In Vivo* 13(3), pp. 295–309 (Cited on page 11).

R. Naaman and D. H. Waldeck (2015). 'Spintronics and chirality: Spin selectivity in electron transport through chiral molecules'. In: *Annual review of physical chemistry* 66, pp. 263–281 (Cited on page 21).

L. A. Nguyen, H. He and C. Pham-Huy (2006). 'Chiral drugs: an overview'. In: *International journal of biomedical science: IJBS* 2.2, p. 85 (Cited on page 21).

C. Niessner, S. Denzau, K. Stapput, M. Ahmad, L. Peichl, W. Wiltschko and R. Wiltschko (2013). 'Magnetoreception: activated cryptochrome 1a concurs with magnetic orientation in birds'. In: *Journal of the Royal Society Interface* 10.88. ISSN: 1742-5689. DOI: UNSP2013063810.1098/rsif.2013.0638. URL: <GotoISI>://WOS:000330301300018http://rsif.royalsocietypublishing.org/content/royinterface/10/88/20130638.full.pdf (Cited on page 7).

C. Niessner, S. Denzau, L. Peichl, W. Wiltschko and R. Wiltschko (2014). 'Magnetoreception in birds: I. Immunohistochemical studies concerning the cryptochrome cycle'. In: *Journal of Experimental Biology* 217.23, pp. 4221–4224. ISSN: 0022-0949. DOI: 10.1242/jeb.110965. URL: <GotoISI>://WOS:000345900300021http:

//jeb.biologists.org/content/jexbio/217/23/4221.full.pdf (Cited on page 8).

D. Nohr, B. Paulus, R. Rodriguez, A. Okafuji, R. Bittl, E. Schleicher and S. Weber (2017). 'Determination of Radical-Radical Distances in Light-Active Proteins and Their Implication for Biological Magnetoreception'. In: *Angewandte Chemie-International Edition* 56.29, pp. 8550–8554 (Cited on pages 19 and 29).

D. Nohr, S. Franz, R. Rodriguez, B. Paulus, L.-O. Essen, S. Weber and E. Schleicher (2016). 'Extended electron-transfer in animal cryptochromes mediated by a tetrad of aromatic amino acids'. In: *Biophysical journal* 111.2, pp. 301–311 (Cited on page 8).

G. C. Nordmann, T. Hochstoeger and D. A. Keays (2017). 'Magnetoreception-A sense without a receptor'. In: *PLoS Biol* 15.10, e2003234. ISSN: 1545-7885 (Electronic) 1544-9173 (Linking). DOI: 10.1371/journal.pbio.2003234. URL: https://www.ncbi.nlm.nih.gov/pubmed/29059181http://journals.plos.org/plosbiology/article/file?id=10.1371/journal.pbio.2003234&type=printable (Cited on page 3).

Y. I. Novitskii, G. V. Novitskaya, Y. A. Serdyukov, T. K. Kocheshkova, D. R. Molokanov and M. V. Dobrovolskii (2015). 'Influence of weak permanent magnetic field on lipid peroxidation in radish seedlings'. In: *Russ. J. Plant Physiol.* 62.3, pp. 375–380 (Cited on pages 11 and 13).

A. R. O'Dea, A. F. Curtis, N. J. B. Green, C. R. Timmel and P. J. Hore (2005). 'Influence of Dipolar Interactions on Radical Pair Recombination Reactions Subject to Weak Magnetic Fields'. In: *J. Phys. Chem. A* 109.5, pp. 869–873. DOI: 10.1021/jp0456943 (Cited on page 19).

H. Okano (2008). 'Effects of static magnetic field in biology: role of free radicals'. In: *Front. Biosci.* 13, pp. 6106–6125 (Cited on page 13).

J. W. Orton (1969). *Electron paramagnetic resonance: an introduction to transition group ions in crystals*. Gordon and Breach (Cited on pages 30 and 75).

J. A. Pauls, Y. Zhang, G. P. Berman and S. Kais (2013). 'Quantum coherence and entanglement in the avian compass'. In: *Phys. Rev. E* 87 (6), p. 062704. DOI: 10.1103/PhysRevE.87.062704 (Cited on pages 1 and 2).

J. Phillips and O Sayeed (1993). 'Wavelength-dependent effects of light on magnetic compass orientation in Drosophila melanogaster'. In: *Journal of Comparative Physiology A* 172.3, pp. 303–308 (Cited on page 10).

J. B. Phillips and S. C. Borland (1992). 'Behavioural evidence for use of a light-dependent magnetoreception mechanism by a vertebrate'. In: *Nature* 359.6391, pp. 142–144 (Cited on page 10).

J. B. Phillips, P. E. Jorge and R. Muheim (2010). 'Light-dependent magnetic compass orientation in amphibians and insects: candidate receptors and candidate molecular mechanisms'. In: *Journal of the Royal Society Interface* 7.suppl_2, S241–S256 (Cited on page 10).

M. B. Plenio and P. L. Knight (1998). 'The quantum-jump approach to dissipative dynamics in quantum optics'. In: *Rev. Mod. Phys.* 70.1, p. 101 (Cited on pages 159, 161, 162 and 168).

E. M. Pliss, A. M. Grobov, A. K. Kuzaev and A. L. Buchachenko (2017). 'Magnetic field effect on the oxidation of hydrocarbons by molecular oxygen'. In: *Mendeleev Commun.* 27.3, pp. 246 –247 (Cited on pages 12, 77, 79, 83 and 98).

M. Pooam, L.-D. Arthaut, D. Burdick, J. Link, C. F. Martino and M. Ahmad (2019). 'Magnetic sensitivity mediated by the arabidopsis blue-light receptor cryptochrome occurs during flavin reoxidation in the dark'. In: *Planta* 249.2, pp. 319–332 (Cited on pages 8 and 172).

V. S. Poonia, D. Saha and S. Ganguly (2015). 'State transitions and decoherence in the avian compass'. In: *Physical Review E* 91.5, p. 052709 (Cited on page 142).

M. Portnoi, M Rosenau da Costa, O. Kibis and I. Shelykh (2009). 'Magnetically controlled terahertz absorption and emission in carbon nanotubes'. In: *International Journal of Modern Physics B* 23.12n13, pp. 2846–2850 (Cited on page 135).

D. A. Pratt, K. A. Tallman and N. A. Porter (2011). 'Free Radical Oxidation of Polyunsaturated Lipids: New Mechanistic Insights and the Development of Peroxyl Radical Clocks'. In: *Acc. Chem. Res.* 44.6, pp. 458–467 (Cited on page 13).

M. Procopio and T. Ritz (2016). 'Inhomogeneous ensembles of radical pairs in chemical compasses'. In: *Scientific Reports* 6 (Cited on page 32).

M. Procopio and T. Ritz (2020). 'The reference-probe model for a robust and optimal radical-pair-based magnetic compass sensor'. In: *J. Chem. Phys.* 152.6, p. 065104 (Cited on page 171).

P. Purtov (2010). 'To the theory of Zeno chemical effect: The exactly solvable model'. In: *Chem. Phys. Lett.* 496.4-6, pp. 335–338 (Cited on page 160).

C. Rackauckas and Q. Nie (2017). 'Differentialequations. jl–a performant and feature-rich ecosystem for solving differential equations in julia'. In: *J. Open Res. Softw.* 5.1 (Cited on page 169).

J. Radcliffe (1971). 'Some properties of coherent spin states'. In: *J. Phys. A: Gen. Phys.* 4.3, p. 313 (Cited on page 170).

T. Ritz, S. Adem and K. Schulten (2000). 'A model for photoreceptor-based magnetoreception in birds'. In: *Biophysical Journal* 78.2, pp. 707–718. ISSN: 0006-3495. URL: <GotoISI>://WOS:000085249300015https://www.ncbi.nlm.nih.gov/pmc/articles/PMC1300674/pdf/10653784.pdf (Cited on pages 1, 2, 3 and 6).

C. T. Rodgers and P. J. Hore (2009). 'Chemical magnetoreception in birds: The radical pair mechanism'. In: *Proceedings of the National Academy of Sciences of the United States of America* 106.2, pp. 353–360. ISSN: 0027-8424. DOI: 10.1073/pnas.0711968106. URL: <GotoISI>://WOS:000262804000003https://www.ncbi.nlm.nih.gov/pmc/articles/PMC2626707/pdf/zpq353.pdf (Cited on pages 1, 6, 7, 19, 27, 28 and 31).

C. T. Rodgers, S. A. Norman, K. B. Henbest, C. R. Timmel and P. J. Hore (2007). 'Determination of Radical Re-encounter Probability Distributions from Magnetic Field Effects on Reaction Yields'. In: *J. Am. Chem. Soc.* 129.21, pp. 6746–6755 (Cited on page 86).

C. T. Rodgers (2009). 'Magnetic field effects in chemical systems'. In: *Pure and Applied Chemistry* 81.1, pp. 19–43 (Cited on page 27).

B. Rosenstein and D. Li (2010). 'Ginzburg-Landau theory of type II superconductors in magnetic field'. In: *Reviews of modern physics* 82.1, p. 109 (Cited on pages 21 and 134).

B. K. Rugg, M. D. Krzyaniak, B. T. Phelan, M. A. Ratner, R. M. Young and M. R. Wasielewski (2019). 'Photodriven quantum teleportation of an electron spin state in a covalent donor–acceptor–radical system'. In: *Nat. Chem.* 11.11, pp. 981–986 (Cited on pages 17 and 108).

G. A. Russell (1957). 'Deuterium-isotope Effects in the Autoxidation of Aralkyl Hydrocarbons. Mechanism of the Interaction of PEroxy Radicals'. In: *J. Am. Chem. Soc.* 79.14, pp. 3871–3877 (Cited on page 79).

S. W. Ryter, H. P. Kim, A. Hoetzel, J. W. Park, K. Nakahira, X. Wang and A. M. Choi (2007). 'Mechanisms of cell death in oxidative stress'. In: *Antioxidants & redox signaling* 9.1, pp. 49–89 (Cited on page 11).

K. M. Salikhov, J. H. Golbeck and D. Stehlik (2007). 'Quantum teleportation across a biological membrane by means of correlated spin pair dynamics in photosynthetic reaction centers'. In: *Appl. Magn. Reson.* 31.1, pp. 237–252 (Cited on pages 17 and 108).

K. M. Salikhov, Y. N. Molin, R. Sagdeev and A. Buchachenko (1984). 'Spin polarization and magnetic effects in radical reactions'. In: (Cited on page 159).

C. Sampson, R. H. Keens and D. R. Kattnig (2019). 'On the magnetosensitivity of lipid peroxidation: two-versus three-radical dynamics'. In: *Physical Chemistry Chemical Physics* (Cited on pages 25, 108, 109, 135 and 142).

G. D. Scholes, G. R. Fleming, L. X. Chen, A. Aspuru-Guzik, A. Buchleitner, D. F. Coker, G. S. Engel, R. Van Grondelle, A. Ishizaki, D. M. Jonas et al. (2017). 'Using coherence to enhance function in chemical and biophysical systems'. In: *Nature* 543.7647, pp. 647–656 (Cited on page 1).

K. Schulten (1982). 'Magnetic-Field Effects in Chemistry and Biology'. In: *Festkorperprobleme Advances in Solid State Phyics* 22, pp. 61–83. ISSN: 0430-3393. DOI:

DOI10.1007/BFb0107935. URL: <GotoISI>://WOS:A1982QE45200004https://link.springer.com/chapter/10.1007%2FBFb0107935 (Cited on pages 4 and 29).

K. Schulten, C. E. Swenberg and A. Weller (1978). 'A biomagnetic sensory mechanism based on magnetic field modulated coherent electron spin motion'. In: *Zeitschrift für Physikalische Chemie* 111.1, pp. 1–5 (Cited on page 2).

K. Schulten and P. G. Wolynes (1978). 'Semiclassical description of electron spin motion in radicals including the effect of electron hopping'. In: *J. Chem. Phys.* 68.7, pp. 3292–3297 (Cited on page 184).

H.-R. Schwarz and N. Köckler (2013). *Numerische mathematik*. Springer-Verlag (Cited on page 169).

S. Schwarze, N.-L. Schneider, T. Reichl, D. Dreyer, N. Lefeldt, S. Engels, N. Baker, P. Hore and H. Mouritsen (2016). 'Weak broadband electromagnetic fields are more disruptive to magnetic compass orientation in a night-migratory songbird (Erithacus rubecula) than strong narrow-band fields'. In: *Frontiers in behavioral neuroscience* 10, p. 55 (Cited on page 7).

J. Shaver, J. Kono, O. Portugall, V. Krstić, G. L. Rikken, Y. Miyauchi, S. Maruyama and V. Perebeinos (2007). 'Magnetic brightening of carbon nanotube photoluminescence through symmetry breaking'. In: *Nano letters* 7.7, pp. 1851–1855 (Cited on pages 20 and 134).

A. Shushin (1991). 'The effect of the spin exchange interaction on SNP and RYDMR spectra of geminate radical pairs'. In: *Chem. Phys. Lett.* 181.2-3, pp. 274–278 (Cited on pages 160 and 161).

R. B. Sidje (1998). 'Expokit: A software package for computing matrix exponentials'. In: *ACM T Math Software* 24.1, pp. 130–156 (Cited on page 185).

I. A. Solov'yov, D. E. Chandler and K. Schulten (2007). 'Magnetic field effects in Arabidopsis thaliana cryptochrome-1'. In: *Biophysical Journal* 92.8, pp. 2711–2726. ISSN: 0006-3495. DOI: 10.1529/biophysj.106.097139. URL: <GotoISI>://WOS:000245164000011https://www.ncbi.nlm.nih.gov/pmc/articles/PMC1831705/pdf/2711.pdf (Cited on pages 7 and 9).

I. A. Solov'yov, D. E. Chandler and K. Schulten (2008). 'Exploring the possibilities for radical pair effects in cryptochrome'. In: *Plant Signal Behav* 3.9, pp. 676–7. ISSN: 1559-2316 (Print) 1559-2316 (Linking). URL: https://www.ncbi.nlm.nih.gov/pubmed/19704823https://www.ncbi.nlm.nih.gov/pmc/articles/PMC2634554/pdf/psb0309_0676.pdf (Cited on pages 6, 7 and 32).

I. A. Solov'yov, H. Mouritsen and K. Schulten (2010). 'Acuity of a Cryptochrome and Vision-Based Magnetoreception System in Birds'. In: *Biophysical Journal* 99.1, pp. 40–49. ISSN: 0006-3495. DOI: 10.1016/j.bpj.2010.03.053. URL: <GotoISI>://WOS:000279720800010https://www.ncbi.nlm.nih.gov/pmc/articles/PMC2895366/pdf/main.pdf (Cited on pages 2 and 8).

I. A. Solov'yov and K. Schulten (2009). 'Magnetoreception through Cryptochrome May Involve Superoxide'. In: *Biophysical Journal* 96.12, pp. 4804–4813. ISSN: 0006-3495. DOI: 10.1016/j.bpj.2009.03.048. URL: <GotoISI>://WOS:000267194600005https://www.ncbi.nlm.nih.gov/pmc/articles/PMC2712043/pdf/main.pdf (Cited on page 6).

D. V. Sosnovsky, G. Jeschke, J. Matysik, H.-M. Vieth and K. L. Ivanov (2016). 'Level crossing analysis of chemically Induced dynamic nuclear polarization: Towards a common description of liquid-state and solid-state cases'. In: *J. Chem. Phys.* 144.14, p. 144202 (Cited on pages 69 and 81).

G. Spiteller (1998). 'Linoleic acid peroxidation - the dominant lipid peroxidation process in low density lipoprotein - and its relationship to chronic diseases'. In: *Chem. Phys. Lipids* 95.2, pp. 105–162 (Cited on pages 11 and 84).

U. Steiner (1984). 'K. M. Salikhov, Yu. N. Molin, R. Z. Sagdeev, A. L. Buchachenko: Spin Polarization and Magnetic Effects in Radical Reactions, Vol. 22 aus "Studies in Physical and Theoretical Chemistry", Elsevier Scientific Publ. Comp., Amsterdam, Oxford, New York, Tokyo 1984. 419 Seiten, Preis: DM 225,-'. In: *Ber. Dtsch. Chem. Ges.* 88.11, 1168B–1169. DOI: 10.1002/bbpc.198400037. eprint: https://onlinelibrary.wiley.com/doi/pdf/10.1002/bbpc.198400037. URL: https://onlinelibrary.wiley.com/doi/abs/10.1002/bbpc.198400037 (Cited on pages 27 and 28).

U. E. Steiner, J. Sch afer, N. N. Lukzen and C. Lambert (2018). 'J-Resonance Line Shape of Magnetic Field-Affected Reaction Yield Spectrum from Charge Recombination in a Linked Donor-Acceptor Dyad'. In: *J. Phys. Chem. C* 122.22, pp. 11701–11708 (Cited on page 95).

U. E. Steiner and T. Ulrich (1989). 'Magnetic field effects in chemical kinetics and related phenomena'. In: *Chem. Rev.* 89.1, pp. 51–147. DOI: 10.1021/cr00091a003 (Cited on pages 1, 8, 27, 28, 37 and 159).

T. Suzuki, T. Miura, K. Maeda and T. Arai (2005). 'Spin Dynamics of the Radical Pair in a Low Magnetic Field Studied by the Transient Absorption Detected Magnetic Field Effect on the Reaction Yield and Switched External Magnetic Field'. In: *J. Phys. Chem. A* 109.44. PMID: 16838907, pp. 9911–9918. DOI: 10.1021/jp053989q (Cited on page 2).

M. C. R. Symons (1969). 'Electron Spin Resonance Spectra of Organic Oxy radicals. The radical $(CH_3)_3CO_3$'. In: *J. Am. Chem. Soc.* 91, p. 5924 (Cited on page 200).

I. Tejero, À. González-Lafont, J. M. Lluch and L. A. Eriksson (2007). 'Theoretical Modeling of Hydroxyl-Radical-Induced Lipid Peroxidation Reactions'. In: *J. Phys. Chem. B* 111.20, pp. 5684–5693 (Cited on page 11).

M. Terazima, K. Okamoto and N. Hirota (1993). 'Transient radical diffusion in photoinduced hydrogen abstraction reactions of benzophenone probed by the transient grating method'. In: *J. Phys. Chem.* 97.50, pp. 13387–13393 (Cited on page 199).

M. Tiersch and H. J. Briegel (2012). 'Decoherence in the chemical compass: the role of decoherence for avian magnetoreception'. In: *Philosophical Transactions of the Royal Society A: Mathematical, Physical and Engineering Sciences* 370.1975, pp. 4517–4540 (Cited on pages 1, 21 and 142).

M. Tiersch, U. E. Steiner, S. Popescu and H. J. Briegel (2012). 'Open quantum system approach to the modeling of spin recombination reactions'. In: *J. Phys. Chem. A* 116.16, pp. 4020–4028 (Cited on page 160).

C. R. Timmel and K. B. Henbest (2004). 'A study of spin chemistry in weak magnetic fields'. In: *Philosophical Transactions of the Royal Society of London. Series A:*

Mathematical, Physical and Engineering Sciences 362.1825, pp. 2573–2589 (Cited on page 2).

C. Timmel, U. Till, B. Brocklehurst, K. Mclauchlan and P. Hore (1998). 'Effects of weak magnetic fields on free radical recombination reactions'. In: *Mol. Phys.* 95.1, pp. 71–89. DOI: 10.1080/00268979809483134 (Cited on pages 2, 7, 16, 20, 27, 28, 41, 63 and 85).

K Tsampourakis and I. Kominis (2015). 'Quantum trajectory tests of radical-pair quantum dynamics in CIDNP measurements of photosynthetic reaction centers'. In: *Chem. Phys. Lett.* 640, pp. 40–45 (Cited on pages 160 and 161).

C. Tsitouras (2011). 'Runge–Kutta pairs of order 5 (4) satisfying only the first column simplifying assumption'. In: *Comput. Math. Appl.* 62.2, pp. 770–775 (Cited on page 169).

N. J. Turro and B. Kraeutler (1980). 'Magnetic field and magnetic isotope effects in organic photochemical reactions. A novel probe of reaction mechanisms and a method for enrichment of magnetic isotopes'. In: *Acc. Chem. Res.* 13.10, pp. 369–377 (Cited on page 95).

G. S. Uhrig (2008). 'Exact results on dynamical decoupling by π pulses in quantum information processes'. In: *New Journal of Physics* 10.8, p. 083024 (Cited on page 35).

R. J. Usselman, I. Hill, D. J. Singel and C. F. Martino (2014). 'Spin biochemistry modulates reactive oxygen species (ROS) production by radio frequency magnetic fields'. In: *PloS one* 9.3, e93065 (Cited on page 11).

R. J. Usselman, C. Chavarriaga, P. R. Castello, M. Procopio, T. Ritz, E. A. Dratz, D. J. Singel and C. F. Martino (2016). 'The quantum biology of reactive oxygen species partitioning impacts cellular bioenergetics'. In: *Scientific reports* 6.1, pp. 1–6 (Cited on page 11).

M. Valko, D. Leibfritz, J. Moncol, M. T. Cronin, M. Mazur and J. Telser (2007). 'Free radicals and antioxidants in normal physiological functions and human disease'. In: *Int. J. Biochem. Cell Biol.* 39.1, pp. 44–84 (Cited on pages 76, 77 and 101).

J. H. Van Vleck (1932). *The theory of electric and magnetic susceptibilities*. Clarendon Press (Cited on pages 38 and 39).

N. C. Verma and R. W. Fessenden (1976). 'Time reolved ESR spectroscopy. IV. Detailed measurement and analysis of the ESR time profile'. In: *J. Chem. Phys.* 65, p. 2139 (Cited on page 200).

L. Visscher (2002). 'Post Dirac-Hartree-Fock Methods-Electron Correlation'. In: *Theoretical and Computational Chemistry*. Vol. 11. Elsevier, pp. 291–331 (Cited on page 35).

P. W. Atkins and D. Kivelson (Jan. 1966). 'ESR Linewidths in Solution. II. Analysis of Spin-Rotational Relaxation Data'. In: *J. Chem. Phys.* 44, pp. 169–174 (Cited on page 199).

X. Wei, T. Tanaka, Y. Yomogida, N. Sato, R. Saito and H. Kataura (2016). 'Experimental determination of excitonic band structures of single-walled carbon nanotubes using circular dichroism spectra'. In: *Nature communications* 7, p. 12899 (Cited on page 22).

J. A. Weil and J. R. Bolton (2007). *Electron paramagnetic resonance: elementary theory and practical applications*. John Wiley & Sons (Cited on pages 38 and 39).

A. Weiße, G. Wellein, A. Alvermann and H. Fehske (2006). 'The kernel polynomial method'. In: *Rev. Mod. Phys.* 78.1, p. 275 (Cited on page 170).

R. Wiltschko and W. Wiltschko (2013). 'The magnetite-based receptors in the beak of birds and their role in avian navigation'. In: *Journal of Comparative Physiology a-Neuroethology Sensory Neural and Behavioral Physiology* 199.2, pp. 89–98. ISSN: 0340-7594. DOI: 10.1007/s00359-012-0769-3. URL: <GotoISI>://WOS:000315042900001https://www.ncbi.nlm.nih.gov/pmc/articles/PMC3552369/pdf/359_2012_Article_769.pdf (Cited on page 3).

R. Wiltschko and W. Wiltschko (2014). 'Sensing magnetic directions in birds: radical pair processes involving cryptochrome'. In: *Biosensors (Basel)* 4.3, pp. 221–42. ISSN: 2079-6374 (Print) 2079-6374 (Linking). DOI: 10.3390/bios4030221. URL: https://www.ncbi.nlm.nih.gov/pubmed/25587420https://www.ncbi.nlm.

nih.gov/pmc/articles/PMC4264356/pdf/biosensors-04-00221.pdf (Cited on page 6).

R. Wiltschko, D. Gehring, S. Denzau, C. Niessner and W. Wiltschko (2014). 'Magnetoreception in birds: II. Behavioural experiments concerning the cryptochrome cycle'. In: *Journal of Experimental Biology* 217.23, pp. 4225–4228. ISSN: 0022-0949. DOI: 10.1242/jeb.110981. URL: <GotoISI>://WOS:000345900300022http://jeb.biologists.org/content/jexbio/217/23/4225.full.pdf (Cited on pages 6 and 8).

R. Wiltschko, P. Thalau, D. Gehring, C. Niessner, T. Ritz and W. Wiltschko (2015). 'Magnetoreception in birds: the effect of radio-frequency fields'. In: *Journal of the Royal Society Interface* 12.103. ISSN: 1742-5689. DOI: UNSP2014110310.1098/rsif.2014.1103. URL: <GotoISI>://WOS:000353394100010http://rsif.royalsocietypublishing.org/content/royinterface/12/103/20141103.full.pdf (Cited on pages 3, 7 and 8).

R. Wiltschko, M. Ahmad, C. Niessner, D. Gehring and W. Wiltschko (2016). 'Light-dependent magnetoreception in birds: the crucial step occurs in the dark'. In: *Journal of the Royal Society Interface* 13.118. ISSN: 1742-5689. DOI: ARTN2015101010.1098/rsif.2015.1010. URL: <GotoISI>://WOS:000378313200001http://rsif.royalsocietypublishing.org/content/royinterface/13/118/20151010.full.pdf (Cited on pages 8 and 172).

W. Wiltschko and R. Wiltschko (1972). 'Magnetic Compass of European Robins'. In: *Science* 176.4030, pp. 62–64 (Cited on page 6).

J. Woodward (2002). 'Radical pairs in solution'. In: *Progress in Reaction Kinetics and Mechanism* 27.3, pp. 165–207 (Cited on pages 27 and 37).

S. Worster, D. R. Kattnig and P. Hore (2016). 'Spin relaxation of radicals in cryptochrome and its role in avian magnetoreception'. In: *J. Chem. Phys.* 145.3, p. 035104 (Cited on page 162).

B.-M. Xu, J. Zou, J.-G. Li and B. Shao (2013). 'Estimating the hyperfine coupling parameters of the avian compass by comprehensively considering the available

experimental results'. In: *Phys. Rev. E* 88 (3), p. 032703. DOI: 10.1103/PhysRevE.88.032703 (Cited on page 1).

J. Xu, L. E. Jarocha, T. Zollitsch, M. Konowalczyk, K. B. Henbest, S. Richert, M. J. Golesworthy, J. Schmidt, V. Déjean, D. J. Sowood et al. (2021). 'Magnetic sensitivity of cryptochrome 4 from a migratory songbird'. In: *Nature* 594.7864, pp. 535–540 (Cited on page 9).

H. Yin, L. Xu and N. A. Porter (Aug. 2011). 'Free Radical Lipid Peroxidation: Mechanisms and Analysis'. In: *Chem. Rev.* 111, pp. 5944–72 (Cited on page 11).

M. Zapka, D. Heyers, M. Liedvogel, E. D. Jarvis and H. Mouritsen (2010). 'Night-time neuronal activation of Cluster N in a day-and night-migrating songbird'. In: *European Journal of Neuroscience* 32.4, pp. 619–624 (Cited on page 6).

M. Zarea, R. Carmieli, M. A. Ratner and M. R. Wasielewski (2014). 'Spin Dynamics of Radical Pairs with Restricted Geometries and Strong Exchange Coupling: The Role of Hyperfine Coupling'. In: *J. Phys. Chem. A* 118.24, pp. 4249–4255. DOI: 10.1021/jp5039283 (Cited on page 19).

Y. T. Zhang, G. P. Berman and S. Kais (2015). 'The radical pair mechanism and the avian chemical compass: Quantum coherence and entanglement'. In: *International Journal of Quantum Chemistry* 115.19, pp. 1327–1341. ISSN: 0020-7608. DOI: 10.1002/qua.24943. URL: <GotoISI>://WOS:000359732200007http://onlinelibrary.wiley.com/store/10.1002/qua.24943/asset/qua24943.pdf?v=1&t=j9odwn2k&s=b22696b55653948910d5a233ffde472e37125612 (Cited on pages 6 and 9).

M. Zmyslony, E. Rajkowska, P. Mamrot, P. Politanski and J. Jajte (2004). 'THe effect of weak 50 Hz magnetic field on the number of free oxygen radicals in rat lymphocytes *in vitro*'. In: *Bioelectromagnetics* 25, pp. 607–612 (Cited on page 13).

B. D. Zoltowski, A. T. Vaidya, D. Top, J. Widom, M. W. Young and B. R. Crane (2011). 'Structure of full-length Drosophila cryptochrome'. In: *Nature* 480.7377, pp. 396–399 (Cited on page 8).

B. D. Zoltowski, Y. Chelliah, A. Wickramaratne, L. Jarocha, N. Karki, W. Xu, H. Mouritsen, P. J. Hore, R. E. Hibbs, C. B. Green et al. (2019). 'Chemical and structural analysis of a photoactive vertebrate cryptochrome from pigeon'. In: *Proceedings of the National Academy of Sciences* 116.39, pp. 19449–19457 (Cited on page 9).